UNIVERSITY OF SOUTHAMPTON

FACULTY OF ENGINEERING AND THE ENVIRONMENT

Civil, Maritime and Environmental Engineering and Sciences

Volume [1] of [1]

INVESTIGATION OF WAVE IMPACTS ON POROUS STRUCTURES FOR COASTAL DEFENCES

By

ROBERT BRIAN MAYON

Thesis for the degree of Doctor of Philosophy

October 2017

UNIVERSITY OF SOUTHAMPTON

ABSTRACT

FACULTY OF ENGINEERING AND THE ENVIRONMENT

Fluid Structure Interactions

Thesis for the degree of Doctor of Philosophy

INVESTIGATION OF WAVE IMPACTS ON POROUS STRUCTURES FOR COASTAL DEFENCES

Robert Brian Mayon

There is great scientific interest in further understanding the underlying wave impact dynamics on solid and/or permeable structures for coastal defences. The accurate and validated simulation of the dynamics of the flow at microsecond temporal scale prior to, at, and after impact is an outstanding and challenging numerical problem in CFD. More advanced numerical models of free surface flow processes which include entrapment of large air pockets is required. These models will yield more insight into the trends of pulse-like forces involved at impact with solid and/or porous material and will enable the understanding of the mechanical stability and integrity of defence structures. Furthermore, the development of advanced numerical models for solving such problems will need to be made accessible as information systems to a wider community of civil engineers in order to achieve integrated design of structural defences (coastal, offshore oil and gas, hydraulic dams etc.). This research is on the development of free surface flow simulations, flow visualisation, analyses of forces of impact, and analyses of the integrity of offshore structures in an information system environment.

A large dataset of compressible (and incompressible) numerical models have been generated to simulate waves impacting at solid and porous structures. Initial studies focus on the behaviour of wave impacts with a solid structure in a 2 dimensional domain. The simulations data are verified through a grid independence study. Numerical results are validated against two sets of experimental data. Air bubble entrapment and consequential multi-modal oscillatory pressure response trends are observed in the compressible simulations during wave

impact. Frequency domain analyses of the oscillatory impact pressure responses are undertaken. The numerical model data sets are compared with results generated from analytic methods and experimental data with good agreement.

These initial findings confirm the robustness of our numerical model predictions concerning the simulated air bubble formations when compared with theories on air bubbles at impact and their resonance frequency modes.

The compressible numerical model is extended to a 3 dimensional simulation. A range of porous structure morphologies are incorporated into the domain to replace solid wall impact interface. A brief overview of previous research on the subject of fluid flow in porous media is presented. The characterisation of the porous model morphologies is examined. Various permeability flow models are discussed in detail. The methods for the generation of the various porous structures and their integration into the CFD model are described. The results from a soliton wave impact at the porous structure morphologies both with and without air entrainment effects at the free surface is investigated in detail.

Finally future work to develop an experimentation specification for the analysis of fluid flow thorough a porous structure is discussed. It is envisioned that this experimental work with have dual outcomes. Firstly it will serve to validate the numerical models created over the course of this study and secondly the potential for clean, renewable energy harvesting from oscillatory pressures through the incorporation of smart sensor hardware within the porous structure will be investigated.

Contents

List of Figures

List of Tables

Declaration of Authorship

I, Robert Brian Mayon declare that this thesis and the work presented in it are my own and has been generated by me as the result of my own original research. *Investigation of Wave Impacts on Porous Structures for Coastal Defences.*

I confirm that:

1. This work was done wholly or mainly while in candidature for a research degree at this University;
2. Where any part of this thesis has previously been submitted for a degree or any other qualification at this University or any other institution, this has been clearly stated;
3. Where I have consulted the published work of others, this is always clearly attributed;
4. Where I have quoted from the work of others, the source is always given. With the exception of such quotations, this thesis is entirely my own work;
5. I have acknowledged all main sources of help;
6. Where the thesis is based on work done by myself jointly with others, I have made clear exactly what was done by others and what I have contributed myself;
7. Parts of this work have been published as:

   MAYON, R., SABEUR, Z., TAN, M.-Y. & DJIDJELI, K. 2016. Free surface flow and wave impact at complex solid structures. *12th International Conference on Hydrodynamics*.
   MAYON, R., BRIAN, SABEUR, Z., TAN, M. & DJIDJELI, K. 2017a. Analysis of fluid flow impact oscillatory pressures with air entrapment at structures. *In: Proceedings of 35th Conference on Coastal Engineering, Antalya, Turkey, 2016.* Coastal Engineering Research Council.

Signed: .....

Date: .....

Acknowledgements

Firstly I wish to express my gratitude to my supervisors Dr Zoheir Sabeur, Dr Mingyi Tan and Dr Kamal Djidjeli for the wealth of knowledge and experience which they imparted to me over the duration of this study. I would like to acknowledge all my colleagues and the great friends who I have met over the last three years at the University of Southampton. The staff at the Faculty of Engineering and Environment, especially in the Fluid Structures Interaction Group, and the staff at IT Innovation Centre proved most helpful from the time I arrived in Southampton. I would like to thank my examiners Professor Arthur Veldman and Dr Dominic Taunton. Finally I wish to thank my family without whose help support this would not have been possible.

Nomenclature

a	Simulation water column initial half base width
a_b	Radius of entrapped air bubble
$\boldsymbol{B}$	Body force
C_n	Courant number
C_o	Order of convergence
E_k	Fluid kinetic energy
E_p	Fluid potential energy
F	Field value representing proportion of cell occupied by fluid
F_s	Safety factor
f_{ap}	Pressure oscillation frequency
g	Gravity acceleration
h	Water depth at the trough of a wave
h_a	Absolute enthalpy
h_e	System enthalpy
h_f^i	Heat of formation of phase i
h_s	Standard internal energy
h_w	Simulation water column initial height
H	Wave height
H_b	Maximum height of breaking wave
k	Thermal conductivity
l	Bubble diameter
L_c	Characteristic wave length
$\boldsymbol{n}$	Unit normal vector
p	Pressure
q	Heat flux vector
p_{max}	Maximum peak pressure

p_{maxnd}	Non-dimensional maximum peak pressure
P_0	Hydrostatic liquid pressure outside the bubble
P_{ipnd}	Non-dimensional impact pressure impulse
r	Grid refinement ratio
r_a	Volumetric fraction of a constituent fluid in a free surface cell in a multiphase simulation
R	Universal Gas Constant
Re	Reynolds Number
Rt	Rise time
R_{tnd}	Non-dimensional rise time
S	Control surface
T	Temperature
t	Time
t_{nd}	Non-dimensionalised time
u	Velocity component in x direction
$\boldsymbol{U}$	Flow velocity
V	Velocity component in y direction
V	Control volume
X	Horizontal distance
Y_i	Mass fraction of phase i
z	Vertical distance

δ	Logarithmic decrement
γ	Ratio of specific heat of a gas at constant pressure to that at constant volume
ρ	Density
ν	Kinematic viscosity
$\boldsymbol{\tau}$	Stress tensor
$\boldsymbol{\varphi}$	Tensor field of considered parameter
ζ	Damping ratio

Abbreviations

AIAA	American Institute of Aeronautics and Astronautics
ALE	Arbitrary Lagrangian –Eulerian
CAD	Computer Aided Design
CFD	Computational Fluid Dynamics
CFL	Courant-Friedrichs-Lewy Condition
DIC	Diagonal Incomplete Cholesky
FCT	Flux Corrected Transport
FFT	Fast Fourier Transform
GCI	Grid Convergence Index
HPC	High Performance Computing
LES	Large-eddy Simulation
LHS	Left Hand Side
LNG	Liquid Natural Gas
MAC	Marker and Cell
MARIN	Maritime Research Institute Netherlands
MULES	Multidimensional Universal Limiter with Explicit Solution
NOAA	National Oceanic and Atmospheric Administration
PCG	Preconditioned Conjugate Gradient
PDE	Partial Differential Equation
PDI	Power Dissipation Index
RAS	Reynolds-averaged Stress
REV	Representative Elementary Volume
RHS	Right Hand Side
SST	Sea Surface Temperature
stl	stereolithographic
VOF	Volume Of Fluid

Chapter 1

Introduction

This first chapter sets out the project motivation, as well as the aims and objectives of the study. Also, it includes a brief overview of the methodology describing how these objectives will be achieved. The layout of the report and the novelty of the undertaken research work is subsequently described.

1.1 Research motivation

There has been an observed trend in global sea level rise which has persisted for decades. This is mainly attributed to thermal expansion as a consequence of ocean warming and the loss of polar ice sheets. As climate change continues to cause global mean temperatures to increase it is forecast that ocean levels will continue to rise. However, there is much ambiguity associated with quantifying the levels of increase, and this is mainly due to the uncertainty surrounding the rate and magnitude of melting of the polar ice caps. A report published by the National Oceanic and Atmospheric Administration (NOAA), presents four scenarios for the predicted rise in the global mean sea level (Parris et al., 2012). Each scenario has been calculated based on the findings from previous studies and also using semi-empirical data to extrapolate the future mean sea level increases. Figure 1.1.1 displays each of these scenarios up to the year 2100. The largest projected increase in sea level of 2 meters has been computed based on the assumption that the issue of climate change is ignored. This forecast assumes the sustained construction of power plants for the combustion of fossil fuels continuing unabated in line with increasing population demands, continued rainforest harvesting, and the further exploitation of other natural resources.

The fourth scenario is the best case outlook in which environmental conservation becomes the most important topic for governments around the globe when deciding new environment policies and regulations. Even with this best case scenario the projected mean sea level will increase by approximately 200mm. Recent research has shown however that the maximum predicted sea level rise of 2 meters may be an underestimation. Dewi Le et al. (2017)

employed a probabilistic process-based model to determine the rate of Antarctic ice sheet melt and they have projected a possible sea level rise of close to 3 meters by the end of this century.

In the Paris Agreement ratified in 2015, efforts to limit the global temperature increase to 1.5^{o} C above pre industrial levels were agreed. However recent research suggests that this may be an unattainable target (Hulme, 2016), even more so in the context of recent global political uncertainty.

It is therefore more prudent to consider that an intermediate rise in sea level between the projected extremes (and closer to the upper bound) will be realised. Thus a minimum global sea level rise of 1.5 meters should be expected over the next century.

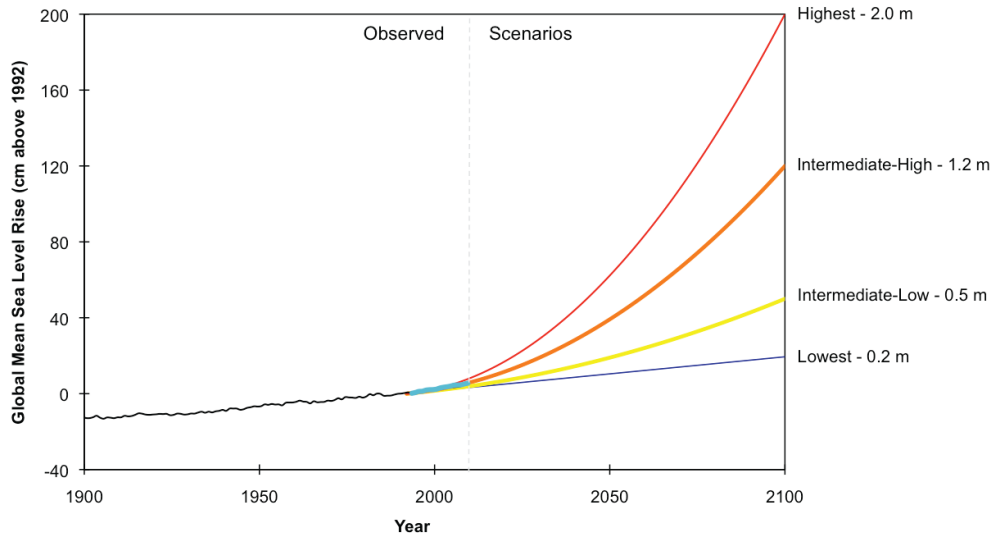

Figure 1.1.1 Predicted elevation of global mean sea level, (Parris et al., 2012).

In addition, studies on storm intensity and duration in the Atlantic Ocean have been conducted by numerous researchers including Emanuel (2005) and Coumou and Rahmstorf (2012). In many of these studies, strong correlations between increasing intensity and duration of hurricanes and that of increasing mean sea surface temperature (SST) have been found. Indeed the recent hyperactive hurricane season in the Atlantic region is in keeping with this trend.

Emanuel (2005), introduced an index for the total destructiveness of storm events based on the energy expended by a storm integrated over the duration of the storm. He calls this the power dissipation index (PDI). Figure 1.1.2, (Coumou and Rahmstorf, 2012), illustrates a plot of the calculated PDI recorded since 1948 for the case of North Atlantic tropical storms. This is compared with the annual tropical Atlantic mean SST. Strong correlations between the PDI and SST with a general upward trend are clearly observed.

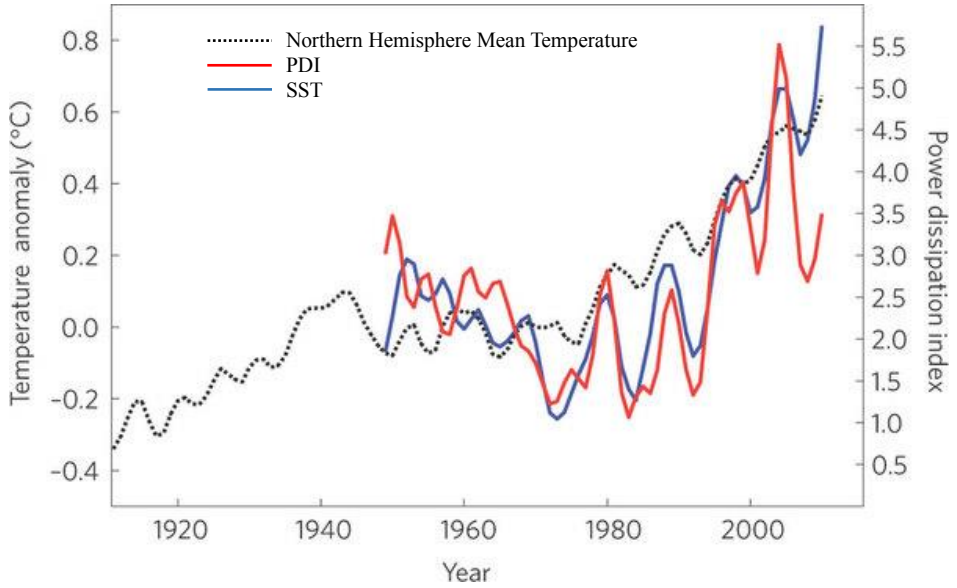

Figure 1.1.2 PDI and SST for period between 1948 and 2012. Also included is the northern hemisphere mean temperature evolution for the past century, (Coumou and Rahmstorf, 2012).

The problems associated with climate change outlined above are also predicted to have a major impact on a regional scale, for example see Figure 1.1.3 for wave damage inflicted on the UK coastline during recent storm events. A report compiled by the UK Met Office by Gosling et al. (2011) notes that by the 2080's the annual number of people whose homes will be flooded in the UK could be around 986,300 should a higher sea level rise scenario be realised.

Research using tide gauges has found that the recorded mean sea level rise around the UK has been increasing by about 1mm per year during the 20th century. However during the 1990's and 2000's this rate has been accelerating (Jenkins et al., 2008). Research using the coastline of East Anglia as a case study suggests that in the event of the higher sea level rise scenario the significant wave height having a 100 year return period also becomes more frequent, (Chini et al., 2010). The projected re-occurrence of these significant waves escalates at the rate of 2% increase in 100 year return period for a 3.5mm sea level rise per annum, 4% for a 7mm rise per annum, and 12% increase in return frequency of a significant wave for a 19mm per annum sea level increase. These increasing frequencies in extreme wave conditions will have adverse effects on unprotected shorelines and also on the design life duration of pre-existing coastal defences which have been constructed to withstand these historically less extreme events, both in terms of magnitude and frequency of reoccurrence.

Figure 1.1.3 Wave impact damage sustained on the south coast of Devon during storm events in 2014, (NCE, 2014).

Severe damage can be inflicted on coastal defence structures as a result of high intensity wave forces during storm events. Many laboratory experiments have been undertaken to gain an understanding of the physical processes which occur at the wave impact interface, (Topliss et al., 1993), (Bullock et al., 2006), (Bullock et al., 2007), (Bredmose et al., 2009). The damage is often caused by transient wave impact pressures which are at present not fully understood (Oumeraci et al., 1993). Also, depending on the profile of the impacting wave, a shock-wave which may have a velocity and pressure magnitude much larger than that associated with the propagation of ordinary waves under gravitational forces may be observed (Peregrine, 2003). Whilst laboratory experiments have yielded many valuable results and insights into the wave impacting process there still remains the problem of repeatability of experimental results. Many authors have previously commented on the difficulty in achieving reliable, well controlled and repeatable results from experimental studies, (Chan and Melville, 1988), (Schmidt et al., 1992). This is due to the wave breaking process being highly non-linear, transient and in some cases chaotic in nature. Thus, the ability to confidently predict wave breaking forces whilst relying on previously published experimental data is currently inadequate. With the recent development and advances in computational fluid dynamics (CFD), it is now possible to simulate wave breaking with realistic free surface flow processes that replicate the results from independent simulations with identical initial conditions. This allows the investigator to confidently analyse how the variation of a certain parameter within the simulation will influence the free surface flow profile development and the associated wave impact pressures.

Many coastal protective structures such as breakwaters or sea defence walls are empirically designed. These installations are often constructed as a rubble mound breakwaters or may be formed through the relatively random placement of prefabricated tetrahedral concrete units (Figure 1.1.4), (Zhang and Li, 2014), (British Standards Institution, 1991). Because of the construction techniques employed in these methods of coastal defence breakwaters the resulting structure is inherently permeable (porous).

(a) (b)

Figure 1.1.4 Typical construction methods for coastal defences,
(a) Rock-armour (Weems Brothers, 2013) (b) concrete tetrapod units (Betonform, 2015)

The above mentioned examples of sea level rise, intensification in total storm energy, and empirical approaches to designing these protective structures highlights the necessity for readdressing the manner in which shoreline defences are designed and planned to augment their resilience in the years to come. While the current trends in climate change persists, coastal defences will inevitably face an increasing threat of destruction from inundation and from waves impacting during more powerful and ever more frequent storm events.

1.2 Aims and objectives

This study aims to augment our knowledge of the process of ocean wave impact forces on protective coastal edifices whilst developing novel concepts and methods for the design of more resilient structures. This will be achieved by developing a methodology which allows a deeper understanding of the mechanism(s) of energy transfer at the wave impact interface with static porous coastal defences and structures. In so doing, the ability to design these structures for optimal impacting wave energy attenuation can be realised. The advanced numerical models developed in the course of this study will also be made accessible to the wider community of engineers and scientists thus permitting the integrated design of the next

generation of robust and resilient structural defences (coastal, offshore oil and gas, hydraulic dams etc.) for the protection against wave impacts.

The first objective of this study is the development of a numerical 2D/3D free surface flow model using the open source CFD modelling software OpenFOAM (Weller et al., 1998). The model is created by incrementally building on the complexity of an initially simplified model. The early simulations take the form of 2D investigations using dam-break modelling. Much experimental (Martin and Moyce, 1952), and numerical, (Sabeur et al., 1996, Sabeur et al., 1997), (Kleefsman et al., 2005) investigation has been carried out into this model setup and it is often used as a benchmark test case for numerical simulations. In the early simulations compressibility effects of air pockets entrapped within the flow are neglected and the flow front impacts a non-porous vertical wall. In this study the use of the term entrained air bubble refers to larger air voids whereas entrapped air bubbles indicates those smaller bubbles which occur during turbulent wave breaking resulting in the formation of a bubble cloud.

A spatial grid analysis based on a technique developed by Roache (1997) is carried out to verify the model at this stage. The model is subsequently validated by comparison of the flow front displacement with the experimental results published by Martin and Moyce (1952). When the grid independence and the validity of the model has been established the simulation is updated to include the effects of air as a compressible gas which can be entrapped within the liquid flow during wave impact. By comparison between the results from the simulation with the compressible air phase included, with those from the simulation without the compressible air phase, the influence of the compressible air entrainment on the impacting pressures is established and observed. The oscillatory pressure response recorded in the compressible simulation is analysed in the frequency domain. The oscillating frequencies of the air pockets entrapped within the liquid phase are then compared to values computed from an analytic expression developed by Minnaert (1933) and an experimentally derived formula by Hattori et al. (1994).

Once the contribution of entrapped air to the impulse pressures has been identified, the vertical wall on which the wave breaks is replaced by structures of varying porosity and varying topology. The compressible simulations are then repeated whilst varying the morphological parameters of the porous structure upon which the wave impacts. These parameters include porosity, specific surface area, permeability and tortuosity. It is thus projected that by varying the geometry of the permeable structure, relationships can then be postulated and established between the wave energy attenuation and the durability of the protective structure, and its geometric topology.

Concurrent work to investigate the feasibility of integrating clean, state of the art wave energy harvesting technologies into breakwater structures without impairing their effectiveness to act as coastal protective structures is also being undertaken. This aim of this separate study is to develop an experimental specification for the validation of the transient wave impact dynamics at the porous structure and to quantify the energy which is available for harvesting and conversion to usable forms. It is envisaged that this separate work will also concentrate on the data retrieved from embedded sensors within the porous structures, non-intrusive image and video analysis of the free surface flow evolution both outside and in the interior of the porous media. This concurrent study will yield data which will serve to further validate the numerical model in the future. Furthermore, this study should provide proof of concept for energy harvesting applications from wave impacts on breakwater structures which has previously been overlooked.

The final objective of this research will be to make the model accessible to the engineering community as an open, web-accessible CFD service based system. This can be achieved through the publication of the OpenFOAM solver and the simulations data which was developed throughout the course of this study.

1.3 Layout of report and novelty of research

A thorough literature review constitutes Chapter 2. The progressive advances which have been made in understanding the effects of wave impacts on vertical surfaces is initially presented. This begins with some of the earliest research in this field which was performed by Bagnold (1939) and concludes with recent experimental research carried out by Wemmenhove et al. (2015). Also included in the literature review is a brief summary of research into acoustic bubble dynamics and more significantly for this study, a discussion on the oscillatory vibrations of entrapped pockets due to an external excitation force. Finally the literature review includes some remarks on the structure of porous topologies and the flow of fluids through those permeable media.

Following Chapter 2, a section on numerical modelling methods employed in the CFD simulations is described. It includes an analysis of numerical discretisation schemes which are adopted in this study and a summary of the volume of fluid method for free surface flow modelling. Chapter 3 closes with a description of the OpenFOAM model case structure.

Chapter 4 presents an overview of the CFD model developed for the study of wave impacts. The model geometry is reported while aspects of temporal and spatial discretisation are discussed. This chapter concludes with a discussion on the parameters used to define both

free surface flow modelling with incompressible air and simulations with air included as a compressible medium.

Results from early stages of this research obtained from the OpenFOAM CFD simulations are presented and analysed in Chapter 5. The procedure for verification and validation of the CFD model is detailed. A frequency domain investigation of the oscillatory impact pressures is performed and a comparison of the pressure results obtained from models with incompressible air and models with compressible air is documented. Finally, analysis and discussion on the observed oscillatory pressure signals from air pockets entrapped within the fluid subsequent to the wave impacting with the obstructing structure and overturning is presented.

Chapter 6 documents an analysis of the characterisation of porous topologies and hydraulic conductivity through permeable media. The concepts of homogeneity and isotropy of permeable assemblies are investigated. Parameters such as porosity, specific surface, tortuosity and permeability which can be used to describe the degree of complexity of a porous structure morphology are discussed in depth. Darcian seepage flow and Darcy-Forcheimer inertial flow regimes are examined. Finally the different approaches to modelling fluid flow through porous media are discussed.

The next chapter describes the 3 dimensional porous model simulation setup. The different sphere packing models and their generation are described. The varying porosity fibrous type structures are analysed. The procedural steps in Fortune's Algorithm which is used to develop a Voronoi diagram in 2 dimensions are presented, the method to extend this algorithm to 3 dimensions for the construction of a random multidirectional fibrous network topology is then explained. The OpenFOAM simulation model geometry for the investigation of 3 dimensional wave impact at a porous structure is reviewed. The intricate meshing procedure to incorporate the porous geometries into the CFD model is investigated.

Chapter 8 presents the results from the 3 dimensional simulations of wave impact with the porous structures. The results for the various morphology sphere based porous media simulations are first analysed followed by the results from the fibrous media simulations. The evolution of the free surface flow profile before, at and after wave impact with the different structures is examined. This is followed by an investigation into the influence of the porous morphology characteristics introduced in Chapter 6 on the flow field dynamics.

The final chapter summarises the results and comments on the findings from the various model simulations. Proposals for future research programmes are also highlighted.

Some of the key findings of this research have been that we have shown that OpenFOAM is a suitable software to simulate free surface flow waves impacting porous structures. The

entrapment of air pockets is confirmed to be the source of oscillatory fluctuations within the pressure response signal during wave impacts which has been previously observed in experimental research. Additionally, we have demonstrated that the amplitude of the first pressure wave cycle during the entrapped bubble induced oscillatory pressure phase can be as energetic as the surging flow front impulse impact. This work also proves that by modifying the topology of the porous structure the amplitude of these oscillatory waves can be precisely controlled and attenuated. By varying the porous structure topologies we have demonstrated that different packing systems and different constituent element sizes damp the wave impact energy more effectively. This research has also proven that there is viable energy harvesting opportunity to be realised from waves impacting on porous structures. Also, the foundations of a new numerical method which has the capability to accurately predict the response of porous coastal protective structures under varying spectra wave impact loading has been developed.

Until now the design of coastal protective structures such as breakwaters has been based predominantly on empirical knowledge or experimental data, because of this it has proven difficult to validate if the optimal design has been employed in their construction. By conducting these rigorous numerical simulations additional information on the mechanism of wave energy transfer at the impact interface has been achieved. This data has improved our understanding of the wave impact process and can be used to augment the design method for coastal defence installations.

Chapter 2

Literature review

2.1 introduction

The main geometrical characteristics of breaking waves are initially described. Breaking waves at a solid interface and the generation of large impact pressure impulses is discussed. The process of wave "flip-through" is explained. An in-depth discussion on oscillatory pressure signals observed during previous wave impact experimental research follows. Finally a brief overview of the characteristics of a porous media are delivered, and those spatial features of the medium which are relevant to this study are described.

2.2 Breaking wave geometries

A strong correlation exists between breaking wave profiles and the quantity of air entrapped at the impact interface, (Schmidt et al., 1992). A comprehensive investigation into breaking wave classifications was first presented by Galvin (1968). In his study, the geometric parameters of the beach upon which the waves break were examined to determine its influence on the developing wave profiles. The wave breaking profiles can be classified into four groups; spilling, plunging, collapsing or surging as shown on Figure 2.1.1.

A spilling wave occurs when the wave crest becomes unstable. Turbulent white water results at the crest and spills forward and downwards on the face of the inclined wave front. Plunging waves result when the wave crest becomes much steeper than that of a spilling breaker. The wave crest falls forward and curls into the base of the wave with a violent impact. Plunging breakers will usually trap a large air pocket which may fragment and be ejected through the crest creating a turbulent flow field forward of the wave. A surging wave results when the wave crest does not break and the toe of the wave flows up the beach with some very minor breaking. The surging wave has a relatively flat, horizontal profile and yields little or no white water. A collapsing breaker exhibits flow properties of both the plunging and spilling breakers. The crest of the wave does not break but rather remains

somewhat flat, while the bottom of the forward face of the wave steepens and collapses in the flow direction creating a turbulent flow which glides up the beach.

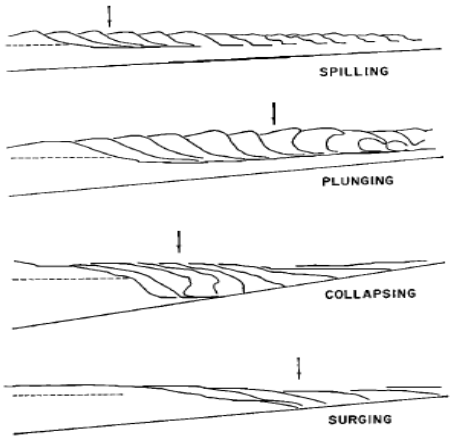

Figure 2.2.1 Breaking wave profiles, (Galvin, 1968).

2.3 Wave impact at solid interface

Experimental work has shown that incident waves on vertical structures can produce impact pressure values which are greatly in excess of pressures which would normally be expected from calculations adopting shallow water theory (Peregrine, 2003). Experimental results have recorded pressures which can commonly exceed $10\rho g(h+H)$ where H is the wave height and h is the water depth at the trough of the wave. Bagnold (1939)found that these pressures reach their greatest value as the amount of air entrapped by the advancing wave front tends towards a minimum value, but not reaching zero. This indicates that the evolving geometry of the wave front prior to, and at impact strongly influences the velocity and pressure records at the impact interface. In the case of a wave crest having developed a forward jet just prior to impact (i.e. a plunging wave which is beginning to overturn), a large bubble will be entrapped within the flow. Also, if a plunging wave has collapsed prior to impact, the flow region immediately forward of the wave may be very turbulent and result in the entrainment of many smaller bubbles. In each case the trapped air will alter the observed flow field response to impact (Peregrine, 2003). In most experimental work the difficulty with repeatability of results from identical model set-ups has been extensively documented. These difficulties in achieving repeatable results may be due to the randomness of the trapped-air dynamics during wave breaking (Chan and Melville, 1988), turbulence left behind by a preceding wave, or strong interaction with the reflection of the preceding wave (Kisacik et al., 2011). Chan and Melville (1988) provide a comparison of pressure time histories for an experiment repeated four times with identical initial conditions yielding significantly varying results. Schmidt et al. (1992) also cite the highly transient and complex

nature of two phase flow in addition to the scale effects of entrapped air as a difficulty in obtaining repeatability of results. Although recent experimental research has employed more accurate and sensitive equipment to record the velocity and pressure fields, repeatability of results is still very difficult due to the highly transient and complex nature of the wave as it impinges upon an obstacle. In order to accurately record the impulse pressure signal resulting from the wave impact, sampling rates at 10kHz or above are usually required (Peregrine, 2003). Despite these difficulties which are associated with the replication of results and accuracy of recorded data, a number of experimental investigations have identified some common traits which are observed when examining the pressure response at the impact interface. Figure 2.3.1 displays a typical solitary wave impact pressure trace sampled at a point adjacent to the impacting wave tip location. It should be noted that the maximum pressure impulse value in Figure 2.3.1 is approximately $17(\rho gh)$ where (ρgh) is the hydrostatic pressure. However, for this impact record no information was provided on the impinging wave height, *H* or the geometry of the impacting wave.

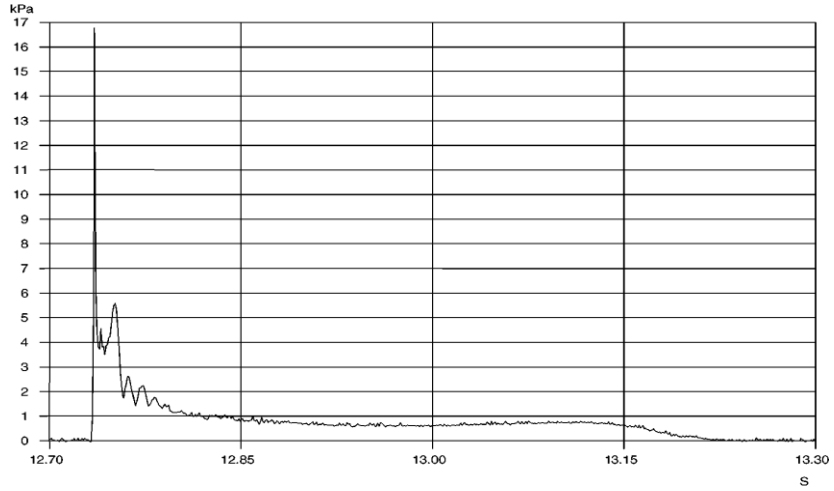

Figure 2.3.1 Pressure time series from a single wave impact at a solid wall- Plymouth University laboratory flume, (Peregrine, 2003)

The pressure observed at the wall interface can be categorised into three temporal phases. At the instant of impact, the horizontal momentum at the crest of the impinging wave is transferred into vertical momentum and the wave is forced vertically upwards through the formation of a thin jet. The tall narrow pressure impulse of approximately 16.75 kPa on Figure 2.3.1 is responsible for the formation and upwards acceleration of this water jet when the wave impacts the wall. It can be observed that the peak duration of this impulse pressure is very short (in the order of 1-2 milliseconds). The jet however may continue to form and accelerate upwards for a longer duration due to inertial effects. As the pressure impulse rapidly decreases the inertial force resulting in the upward displacement of the jet diminishes thus allowing deceleration in its velocity. The jet will reach its point of maximum upwards

velocity, and because the pressure impulse is no longer exerting a vertical force on the water jet it begins to collapse.

As the jet crest falls back its velocity will be decelerated by the fluid beneath. This results in a pressure increase within the fluid below the jet which can be observed as the smaller amplitude (5.5 kPa), longer duration pressure impulse on Figure 2.3.1. After the subsidence of the jet some oscillatory pressure effects can be observed. It has been suggested that these oscillations may be due to the irregular shape of the wave after impacting with the wall (Peregrine, 2003). However the regularity in both the period of oscillations and the uniform manner in which they are damped would seem to be at variance with this hypothesis. Much more likely is the alternative suggestion that these oscillations result from air bubbles entrained within the flow as it breaks up subsequent to impact (Schmidt et al., 1992) however until now this theory has not been validated by numerical investigations.

After these pressure oscillations have been damped the pressure plot records the hydrostatic loading from the fluid as it is in contact with the wall.

The high impulse pressure peaks evident on Figure 2.3.1 cannot be explained using the commonly applied shallow water-wave theories, thus some additional phenomenon must be present to which these large pressures can be attributed. Research performed by Longuet-Higgins and Cokelet (1976), and more recently by Dold (1992) and Peregrine (2003) have made some advances to explain these high pressure impulses. The phenomenon to which they attribute these high pressures has been termed wave "flip-through" and can be explained according to Figure 2.3.2.

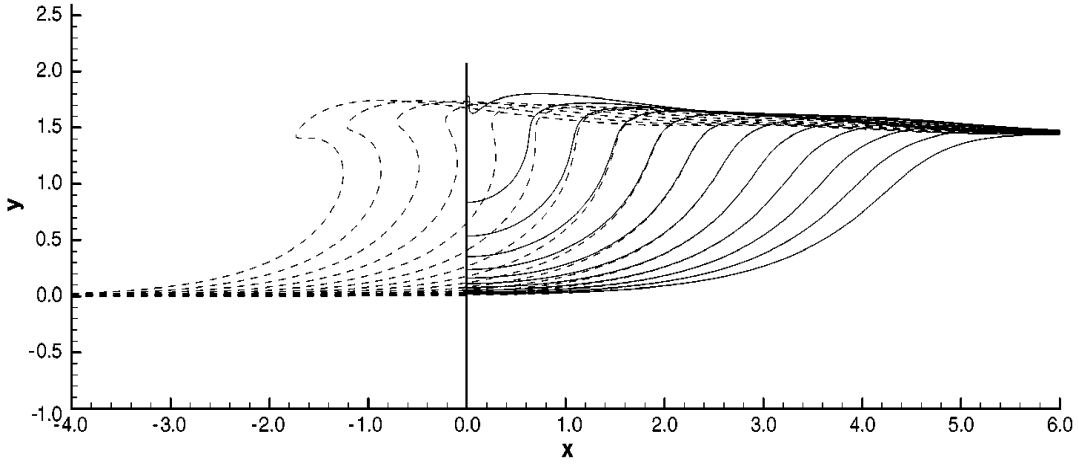

Figure 2.3.2 The development of wave "flip-through" in the presence of a flow inhibiting obstacle (Peregrine, 2003).

The dashed line in Figure 2.3.2 represents the evolution of a large amplitude plunging wave which in the absence of an obstacle would collapse forward forming a horizontal jet. If a structure such as a vertical wall or a breakwater is located in the path of the breaking wave

such that the wave will impact it at the precise time that the wave begins to overturn, i.e. when the wave has developed a vertical profile at its advancing face, then the wave is prevented from collapsing forward and the physics of how the wave breaks is very much altered. Such a flow obstacle is represented by the solid vertical line positioned at X = 0 in Figure 2.3.2. The solid wave profile lines display the manner in which the wave shape evolves in the presence of an obstacle in the wave's path. The obstacle causes the water at the trough of the wave to accelerate rapidly in a vertically upward direction. As the trough depth diminishes the horizontal thrust at the crest of the wave is maintained and the free surface converges to a point thus tending towards a stress singularity at the position of impact. Peregrine (2003) notes that the vertical acceleration of the water in the trough of the wave can be as high as $1000g$. This high vertical acceleration of the water must result in a correspondingly high pressure gradient being transferred to the wall face ($1000\rho g$), thus explaining the high pressure impulse such as that recorded on Figure 2.3.1. A large vertical jet and associated high pressures can therefore form in the absence of any clear impact of the crest of the wave with the wall but rather with the impact having a smooth irrotational flow action. This effect is illustrated on Figure 2.3.3. Experimental research conducted by Chan and Melville (1988) supports the existence of the "flip-through" action at wave impact for certain wave breaking profiles. Free surface instabilities such as Kelvin-Helmholtz instability are less influential on the flow behaviour than the geometry in which the development of the "flip through" profile phenomenon occurs. For example, wave "flip-through" will generally occur only in the presence of a vertical obstacle which causes a rapid vertical acceleration of the water constituting the trough of the breaking wave. In this case the geometry of the environment in which the wave breaks is the dominant factor influencing the profile development of the flow. Likewise, a nearshore plunging breaker wave will usually form due to a depth profile change at a beach. Once the wave has broken, some further turbulent dispersion of energy may occur during spillage due to Kelvin-Helmholtz or other such instabilities (Ikeda et al., 2014). In deep water environments wherein the seabed is non-influential on free surface flow profile, instability effects such as Raleigh-Taylor or Kelvin Helmholtz may be the dominant factor in the development and breaking of waves. These instabilities can be induced by a velocity differential between the ocean water and wind blowing across the surface. This creates a shear velocity flow profile in the uppermost layers of the ocean water leading to the generation of surface waves. In this study we focus on waves breaking on obstacles, and the influence theses obstacles have on the development of the flow profile, thus we neglect the effects of free surface instabilities such as Kelvin-Helmholtz or Raleigh-Taylor.

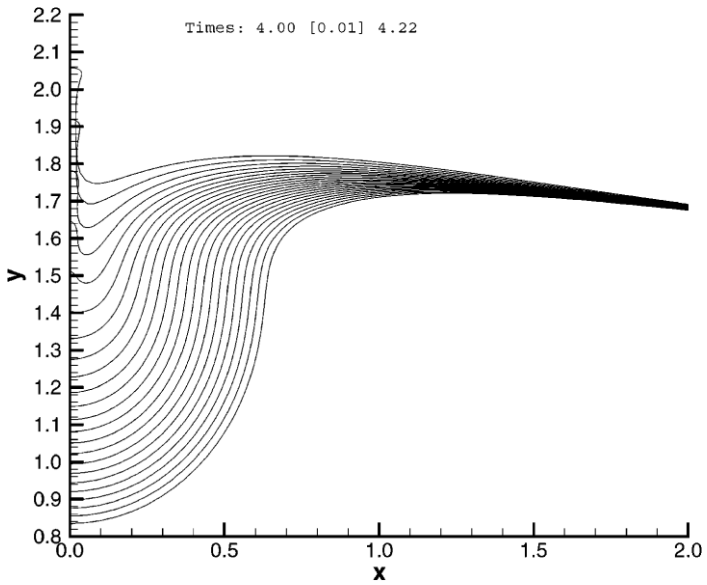

Figure 2.3.3 Development of a vertical jet at the impact interface through the process of "flip-through" (Peregrine, 2003).

2.4 Pressure oscillation

According to Peregrine (2003) "in two-dimensional laboratory experiments on a rigid wall, well- defined oscillations are not uncommon and are clearly related to pockets of trapped air". He also states that the effect of air entrapment is to cushion the impact, the results of our numerical simulations do not agree with this as discussed in Chapter 5. Chan and Melville (1988) conducted a detailed experimental investigation into plunging wave pressures at vertical walls. In their research they initially determined the zone of wave breaking for their experimental setup. They then incrementally varied the wall location in the breaking zone relative to the impinging wave whilst maintaining the geometric parameters of the oncoming wave constant. Thus they were able to obtain a detailed insight into the characteristics of wave impact pressures in the wave breaking zone. In their findings they observed high amplitude pressure oscillations at impact when the vertical wall was located between the positions $3.638L_c \leq x \leq 3.659L_c$. Where x is the distance from the wave-maker to the wall and L_c is the characteristic wavelength of the generated wave. These pressures had a frequency oscillation in the range of 300-800 Hz and coincided with the wave breaking profiles in which maximum air entrainment was observed. Higher frequency, lower amplitude pressure oscillations were also recorded at various other wall positions, most significantly when the wall was positioned such that the wave had broken prior to impact and the flow was more turbulent with the quantity of air entrainment reduced. The entrapped air pockets were also fragmented into smaller bubbles in these cases. By comparing averaged pressure maximum results over 23 experimental runs with the averaged pressure maximum results from 9 experimental runs with the wall position at $x/L_c = 3.643$

and $x/L_c = 3.659$ respectively at the wall elevation $z/L_c = 0.057$ (where z/L_c is the elevation with respect to the still water level) Chan and Melville (1988) also suggest that the oscillatory pressures due to an entrapped air pocket may contribute to the maximum pressure impulse at wave impact. They contend that the pressure oscillations may be due to resonance effects within the air pocket entrapped just below the crest of the impinging wave.

Schmidt et al. (1992) also conducted large scale experimental analysis of wave impacts and observed low frequency impact force oscillations which occurred immediately subsequent to the impingement of a plunging breaker with a large entrapped bubble. They attributed these oscillations to the cyclic compression and expansion of the bubble. Furthermore they found that the frequency of oscillation can be related to the bubble diameter. Additional discussion on this subject is included in Chapter 5. It is also significant that the period of the force oscillations recorded by Schmidt et al. (1992) in their large scale experiments were within the range of natural frequencies for typical caisson breakwater construction designs. This could result in resonant excitation in the structure thus accelerating damage and deterioration of the structure which would otherwise have been attributed to the influence of wave impacts alone. Figure 2.4.1, displays the key features of a typical impact force plot for a plunging breaker type wave with the associated flow profiles at the key temporal points of interest indicated.

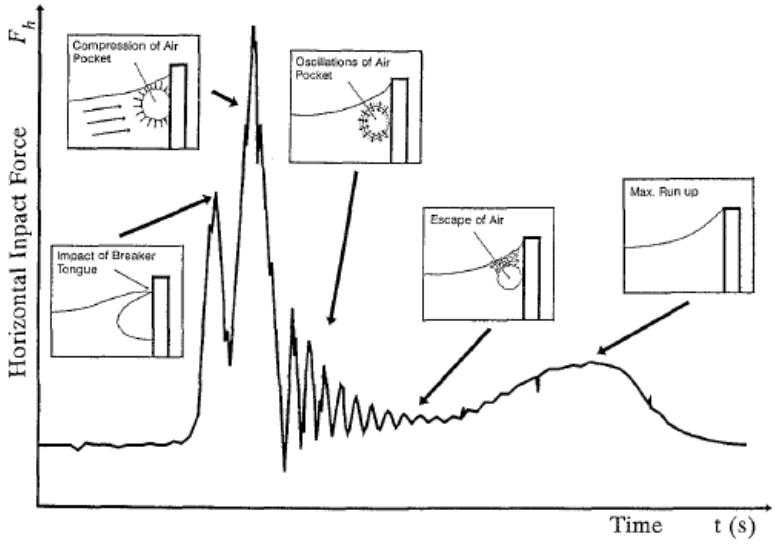

Figure 2.4.1 Typical horizontal impact force observed during plunging breaker impact, (Schmidt et al., 1992).

Mitsuyasu (1966) studied these pressure oscillations and concluded that the characteristic damping mechanism observed in his earlier experimental work and in previous studies (Bagnold, 1939), (Ross, 1955) was due to leakage of air from the main bubble entrapped within the flow subsequent to impact. However in simulations conducted in the course of

this study the damped oscillations were observed without major leakage of air from the entrapped air pocket, this would seem to contradict Mitsuyasu's conjecture. Whilst Zhang et al. (1996) also recorded the vertical dissipation of air from the entrapped bubble in their numerical study, the damping of the pressure oscillations in their opinion was attributed to a transfer of fluid kinetic energy E_k to fluid potential energy E_p as the wave front moved upwards along the wall.

Hattori et al. (1994), have also conducted experiments to investigate impact pressures from a wave impinging on a vertical wall. By varying the wall location relative to the breaking wave they were able to capture and analyse the effects of 4 distinct geometries of breaking wave. High speed video recording at the impact interface was captured, from which still images were provided. The first generated wave broke against the wall exhibiting the phenomenon of flip through without the entrainment of bubbles and thus no oscillatory effects in the time–pressure history plot were observed. The second wave impacted the wall having developed a vertically flat wave front. This type of breaker yielded a very high impact pressure $\frac{p_{max}}{\rho g H_b} = 108.2$. In this case there were groups of small air bubbles trapped near the crest of the impacting wave. These bubbles appeared to be ejected upwards as the crest impacted the wall. The time-pressure record for this impact displayed a very high impact impulse followed by a series of high frequency (1.1kHz) oscillations which decayed rapidly. See Figure 2.4.2 for the wave breaking still images and the pressure plot. The results from the second wave experiment would appear to support the findings of Chan and Melville (1988) for the case when the wave broke just prior to impact resulting in a quantity of small air bubbles being entrained in a very turbulent flow.

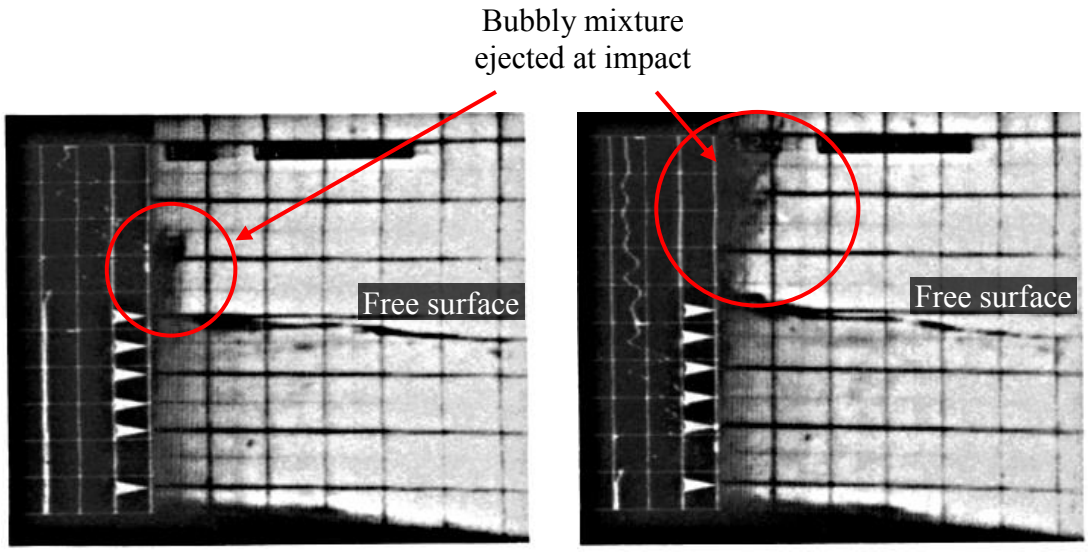

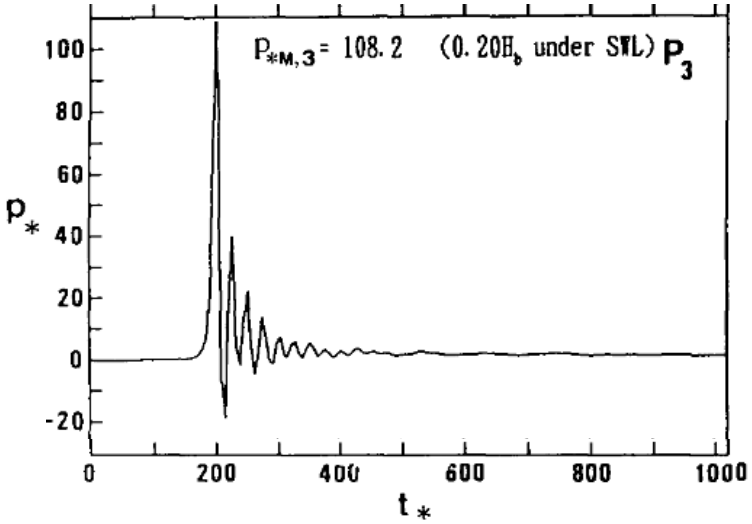

Figure 2.4.2 Wave breaking with associated high frequency rapidly decaying oscillation pressure, (Hattori et al., 1994)

The third type of breaking wave geometry analysed was that of a plunging breaker with a thin lens of air trapped at the interface. Again relatively high impulse pressures were recorded $\frac{p_{max}}{\rho g H_b} = 51.9$. Subsequent to the initial impact pressure oscillations with a frequency of about 250 Hz were observed. Hattori et al. (1994) note that the main bubble fragments in to a number of smaller bubbles immediately after impact at elapsed time 835ms (Figure 2.4.3). However, on the pressure plot Figure 2.4.3, the oscillation are recorded with a very uniform frequency which persists after the fragmentation of the main bubble. This point requires further investigation as smaller bubble sizes should oscillate at higher resonant frequencies. Therefore unless all the bubbles were resonating in a synchronised phase manner the recorded pressure plot should display a non-uniform oscillation after elapsed time 835ms. The oscillations continue until the bubbles escape upwards through the wave crest and Hattori et al. (1994) suggest this to be a source of the damping. It should also be noted that there are some high frequency, low amplitude oscillations recorded on the pressure plot Figure 2.4.3 between 870 and 880 ms which may be due to residual smaller air pockets which remain after the majority of bubbles have escaped through the wave crest. Unfortunately there are no corresponding photographs presented for this time period. It is also suggested that the high velocity rotation of the bubbles may result in some of their energy loss thus contributing to the damping of the pressure oscillation signal.

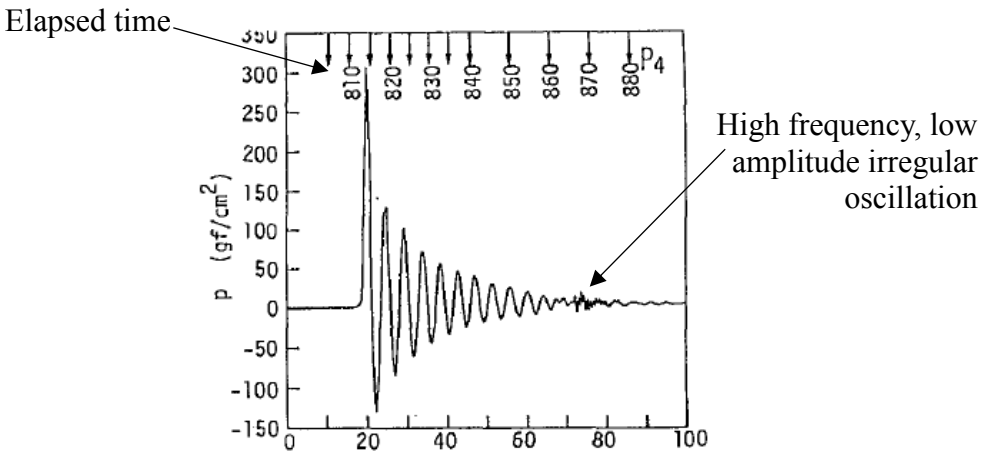

Figure 2.4.3 Regular pressure oscillation resulting from air pocket entrapped within the flow, (Hattori et al., 1994).

The final wave profile investigated by Hattori et al. (1994) was that of a plunging breaker with a large trapped air bubble. They found that an increase in the diameter *l* of the entrapped bubble resulted in a decrease in both the peak impulse pressure and an associated decrease in the oscillating pressure frequencies recorded. The relationship between the bubble diameter and peak pressure, and also the bubble diameter and the mono-polar resonant oscillation frequency was found to vary inversely. Figures 2.4.4 and 2.4.5 show the relationship between the bubble diameter and the peak pressure and the bubble diameter and the resonant oscillation frequency respectively for a range of experiments conducted. It is noted that the approximate envelope curve for the oscillating pressure frequency is represented by

$$f_{ap} = 180 l^{-\frac{1}{2}} \qquad (2.4.1)$$

where l is the bubble diameter. Equation *(2.4.1)* yields a very similar result to the theoretical relationship predicted by the Minnaert resonance frequency given in Equation *(2.4.2),* (Minnaert, 1933). This analytic equation will be further discussed in Chapter 5.

$$\upsilon = \frac{1}{2\pi a_b}\left(\frac{3\gamma P_0}{\rho}\right)^{0.5} \qquad (2.4.2)$$

where γ is the ratio of specific heat of a gas at constant pressure to that at constant volume, P_0 is taken to be the hydrostatic liquid pressure outside the bubble (assumed to be atmospheric pressure in this case) and ρ is the density of the fluid, and a_b is the radius of the entrapped bubble, (Leighton, 1994).

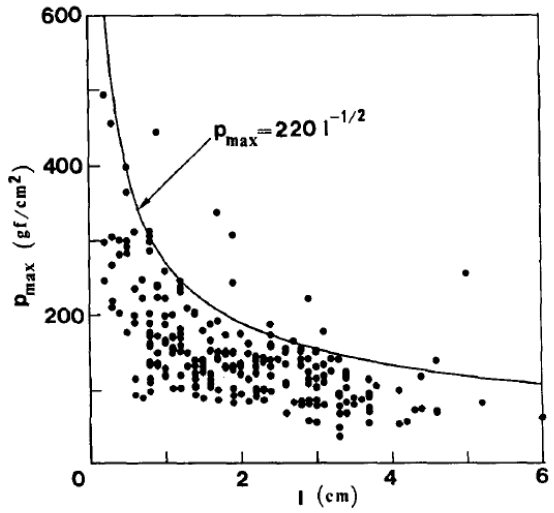

Figure 2.4.4 Entrapped bubble diameter versus maximum pressure, (Hattori et al., 1994).

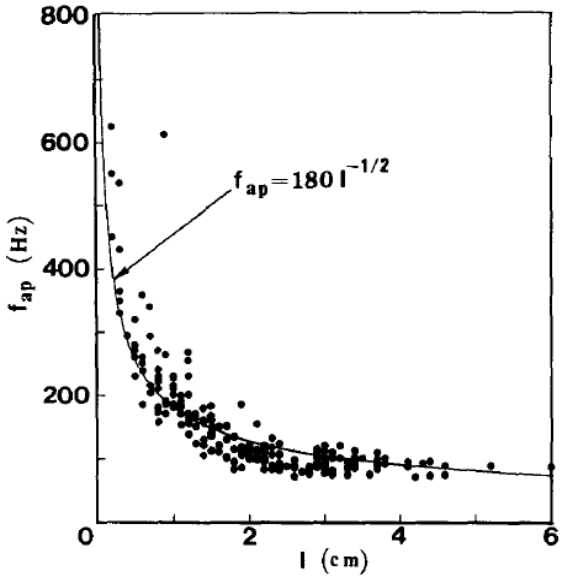

Figure 2.4.5 Entrapped bubble diameter versus oscillating frequency, (Hattori et al., 1994).

From their experimental data and based on previous research results from Bagnold (1939), Hattori et al. (1994) also created a predictive model which relates the observed trapped bubble diameter to the maximum impact pressure and the observed bubble diameter to the oscillating pressure frequency. Figure 2.4.6(a) and Figure 2.4.6(b) present the predicted model results and the observed experimental results. At smaller bubble diameter dimensions there is a high variability in the observed peak pressure in comparison to the predicted peak pressure, however the comparison is more favourable as the observed bubble diameter increases. The comparison between the measured frequency of the pressure oscillation and the predicted frequency of oscillation is quite favourable.

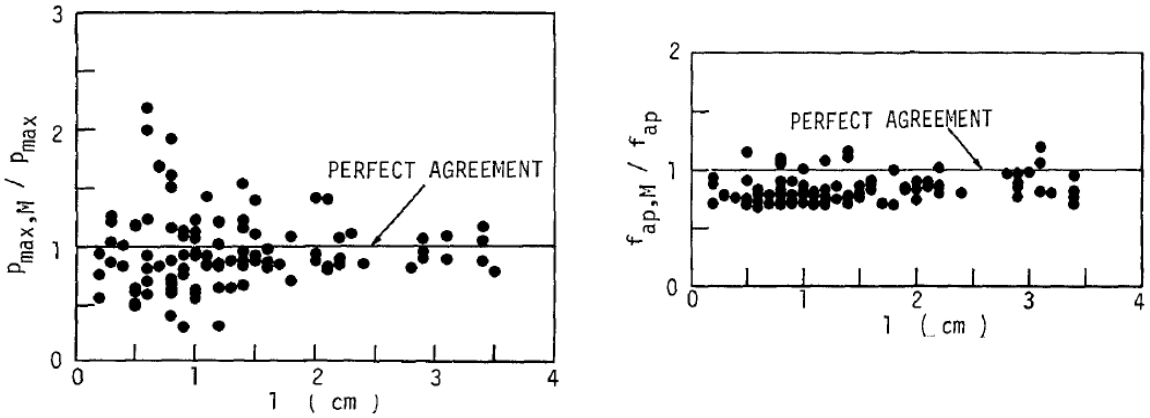

Figure 2.4.6 Hattori et al. (1994) model results (a) Predicted max pressure.
(b) Predicted oscillating pressure frequency.

Topliss et al. (1993) present mathematical models for the analysis of the high frequency pressure oscillations recorded during a wave impact at a vertical wall. They first analysed the oscillating pressure frequency of a bubbly mixture in proximity to the impact surface. Expressions were derived for the frequency of oscillation as a function of depth of the fluid and aeration percentage and also for frequency of oscillation as a function of the distance which the bubbly mixture extends from the wall and aeration percentage. A potential flow model for the analysis of a relatively large single bubble trapped at the impact interface was also developed. The mathematical models were compared to three sets of experimental results provided by Hattori et al. (1994), Witte (1998), and Graham and Hewson (1992). The mathematical models developed by Topliss et al. (1993) compare reasonably favourably for frequency oscillation measurements for large air bubbles, however the mathematical model in most cases over estimates the oscillating pressure frequency experimental results obtained by Hattori et al. (1994).

More recently a study carried out by Kleefsman et al. (2005) using the ComFlow software developed jointly by MARIN, the University of Delft and the University of Groningen investigated the flow of an incompressible viscous fluid. The numerical method was based on the Navier-Stokes equations which were discretised on a fixed Cartesian grid using the finite volume method. The free surface evolution was described by the volume of fluid method. To validate their software they performed a dam-break numerical simulation. They then compared the numerical results with results generated from a dam-break experiment. The vertical water height in the reservoir was monitored in both the experimental setup and the numerical simulation as the water column collapsed. Also pressure time histories were recorded on an obstacle located in the path of the advancing wave front for both the numerical and the experimental setup. Good general agreement was found when the results from the simulation were compared to the experimental results. However because the

simulation only considered incompressible fluids there was no oscillatory pressure response observed in the numerical results. In contrast there were some small irregular pressure oscillations recorded in the experimental results immediately subsequent to the wave front impacting the obstacle. The oscillations may result from the free surface breaking up or may be due to small diameter bubble entrainment. Nevertheless some oscillatory pressure response is expected as the air bubbles entrained within the liquid phase undergo cyclic compression and dilation as previously discussed thus generating the oscillations in the recorded signal.

Wemmenhove et al. (2015) used an updated version of the ComFlow software to investigate both single and two-phase wave impacts with air modelled as a compressible gas. Two sets of numerical simulations were performed, the first set of simulations modelled sloshing behaviour inside a LNG (liquid natural gas) tank; the second study examined wave run-up behaviour at impact with a partially immersed structure. In both cases single and two phase simulations were completed with both sets of numerical results also compared against experimental data in order to validate the numerical models. Only the first set of simulations which concentrated on the sloshing behaviour within the tank will be considered here. The experimental results in the case of the sloshing study were obtained over a 20 minute experiment duration. It was found that wave run-up height simulated with the two phase model agreed quite well with the experimental data in contrast to the single phase model which overestimated the wave run-up at the tank wall. The overestimated wave run-up height simulated by the single phase model resulted in peak pressures which were excessive when compared to the two phase model and the experimental results.

The effect of air entrainment on the simulated model were also investigated. A single wave which exhibited the geometrical characteristics of a plunging breaker at impact from the experimental setup was selected for this part of the study. The simulation pressure results for the single and two phase models were compared to the corresponding wave pressure results from the experiment study. The entrapped air pocket had a diameter of order $O(10^{-1})$ and lasted for at time duration $O(10^{-1})$ before being compressed, fragmenting and ejected out through the impacting wave crest. The pressures were monitored at two locations in the experimental setup; a point below the entrapped air pocket and at a point above the entrapped air pocket located at the same elevation as the as the horizontal jet formed by the plunging breaker. At both locations the simulation results from the two phase model correlated better with the experimental results, in terms of impact pressure magnitude and also in terms of a temporal evolution of the impact pressure. However there was no evidence of a high frequency pressure oscillation exhibited in the two phase model as would be expected with

an entrapped air pocket at impact. The experimental results did however exhibit some irregular oscillations in the pressure response signal as would be expected during wave breaking with air entrapment.

2.5 Porous media

In this section we present a brief introductory description of a porous assembly. Further analysis and an in-depth discussion on porous topologies is included in Chapter 6. A porous material can be considered as an assemblage of matter which consists of two or more materials being composed of a minimum of two material phases. Thus a porous medium is usually a solid matrix containing void spaces filled with a fluid which may be a liquid, a gas or both. Notwithstanding this, foams may also be considered as porous materials in which case a solid matrix may not be a constituent of the material. Examples of porous media both naturally occurring and synthetic are numerous and the characteristics which can be used to classify them are very diverse. Properties of these porous media which are often used for their classification include density, permeability, and electrical conductance. These parameters however depend not only on the morphology of the medium, but also on the properties of the material which constitute the porous medium. Material independent measures can be better used to classify the topology of such structures. These material independent classifiers include the level of porosity of the assemblage itself, specific surface area and the sample tortuosity.

In general all materials examined at an atomistic scale are porous, therefore a limit on the minimum constituent particle size must be established. A soil classification system presented by Brewer (1964) defines the lower limit of macroporous soil at 75 microns. This investigation will be restricted to studying porous materials at a macroscopic level using a direct numerical simulation method. Other modelling techniques include methods employing a continuum approaches. In adopting the continuum method homogenisation approaches are employed such as adopting a representative elementary volume (REV) of the material to characterise the porous assembly. Material properties such as levels of porosity, velocity of fluids through the porous material, entrained fluid pressures etc. are all averaged over this representative elementary volume.

A comprehensive description and characterisation of porous media is presented by Bear (1988). He recognises that while the previous description of a porous media may be technically accurate, using these guidelines a hollow cylinder would satisfy the requirements to be considered porous. Obviously in the context of this study a hollow cylinder cannot be

representative of the porous medium, therefore the description of a porous medium presented above is somewhat deficient and needs additional constraints. According to Bear (1988) the solid phase should be distributed relatively uniformly throughout the material with each REV containing an amount of solid material. The specific surface of the material should be relatively high, and the interstices comprising the voids should be relatively narrow. Finally a proportion of the void spaces must be interconnected. This study will concentrate on developing a relationship between the characteristics used to describe the porous assembly topology at the impact interface and the attenuation of the oscillating pressure energy resulting from the impinging wave and air entrainment. It will be seen that these characteristics are highly influential to damp the resonant pressures which specific frequencies resulting from wave impacts with entrapped air pockets.

Chapter 3

Numerical modelling methods

3.1 Introduction

The CFD software package OpenFOAM (Weller et al., 1998) has been selected for the fluid flow simulation and analysis of the wave-structure interface region during the impact event. OpenFOAM is an open source software program which computes the flow field variables such as pressure, velocity, temperature etc. through the application of the finite volume method.

In the early stage of this research a review of the various CFD packages was undertaken. Proprietary CFD software packages such as Ansys Fluent, Star CCM+ and Ansys CFX were considered. However these programmes are all closed source software and the user is very restricted in their ability to modify the underlying programme code upon which these programs are built. The creation of a new bespoke code to model compressible fluid flow through porous structures was also briefly considered; this however was determined to be too large a challenge in the timeframe permitted by this research. Additionally, it was determined that OpenFOAM possessed much the modelling requirements which this study demanded. Nevertheless for those situations which could not be modelled with the pre-existing software, modification of the source code was required to suit the particular cases analysed in this research. Because OpenFOAM is an open source platform the code can be modified to suit the user's needs with relative ease once the essential physics of the problem are understood.

The procedure to create an OpenFOAM model is quite straightforward. First the problem domain is discretised into a set of contiguous volumetric cells. These cells are defined by a set of interconnected faces, the number of which will depend on the shape of the volumetric cell. For example a hexahedral volumetric cell is defined by six faces whilst a tetrahedral cell has four faces. These faces are in turn defined by a series of interconnected points forming the domain mesh or grid. Thus the basic building blocks of a volumetric mesh to define a computational domain is a set of points or nodes. The values of the discrete flow

fields are computed and stored at the volumetric cell centres. The values at the cell faces must be computed through interpolation between the cell centred values.

3.2 Governing equations of fluid flow

Because OpenFOAM relies on a finite control volume representation of the problem domain, the governing flow equations which describe the mathematical model are represented in integral form. The form of these equations can be manipulated to indirectly obtain the equivalent set of partial differential equations (PDEs) (Anderson, 1995). The system of governing integral equations which exactly describe the spatial and temporal flow evolution cannot be solved analytically and so are discretised across a mesh which represents the problem domain. Then a numerical approximation can be achieved by substituting the integrals with a system of algebraic equations which are solved at the volumetric cell centre. The integral equations to be substituted are typically the continuity equation, the momentum conservation equation and the energy conservation equation; these are each presented as Equations *(3.2.1)*, *(3.2.2)* and *(3.2.3)* respectively.

$$\frac{\partial}{\partial t}\iiint_V \rho \, dV + \iint_S \rho \boldsymbol{U} \cdot \boldsymbol{dS} = 0 \qquad \text{Continuity equation} \quad (3.2.1)$$

In Equation *(3.2.1)*, V is the control volume, ρ the density of the fluid (an alternative flow field variable could be used), $\boldsymbol{U}$ is the flow velocity at a point on the control volume surface and $\mathbf{d}\boldsymbol{S}$ is the vector elemental surface area defined as $\boldsymbol{n} \cdot dS$, with $\boldsymbol{n}$ being the unit vector perpendicular to surface dS.

$$\frac{\partial}{\partial t}\iiint_V \rho \boldsymbol{U} \, dV + \iint_S \rho \boldsymbol{U}\boldsymbol{U} \cdot \boldsymbol{dS} = \iint_S \boldsymbol{\tau} \cdot \boldsymbol{dS} + \iiint_V \rho \boldsymbol{b} \, dV \qquad \text{Momentum equation} \quad (3.2.2)$$

In the momentum Equation *(3.2.2)* the right hand side represents the forces which act directly on the fluid element. These forces can be sub-divided into body forces and surface forces. Body forces act upon the volumetric mass of the control volume, Gravitational and magnetic field forces are two such examples of these body forces. The term $\boldsymbol{b}$ in Equation *(3.2.2)* represents the body forces. Surface forces act upon the surface of the control volume, shear stresses and surface tension forces are examples of such surface forces. $\boldsymbol{\tau}$ is a stress tensor representing the surface forces. These act to alter the geometry of the control volume.

$$\frac{\partial}{\partial t}\iiint_V \rho h_e \, dV + \iint_S \rho h_e \boldsymbol{U} \cdot \boldsymbol{dS} = \iint_S k \nabla T \cdot \boldsymbol{dS}$$
$$+ \iiint_V (\boldsymbol{U} \cdot \nabla p + \tau \cdot \nabla \boldsymbol{U}) dV + \frac{\partial}{\partial t}\iiint_V p dV \qquad \text{Energy equation} \quad (3.2.3)$$

Equation *(3.2.3)* presents the energy conservation equation. Here h_e represents the enthalpy of the system, k is the thermal conductivity of the fluid, ∇ is the gradient, T is the temperature, τ is the viscous shear stress and p is the pressure.

Through the application of the divergence theorem Equations *(3.2.1 - 3.2.3)* can be transformed into an equivalent set of partial differential equations given by

$$\frac{\partial \rho}{\partial t} + \boldsymbol{\nabla} \cdot (\rho \boldsymbol{U}) = 0 \qquad \text{Continuity equation} \quad (3.2.4)$$

$$\frac{\partial}{\partial t}(\rho \boldsymbol{U}) + \boldsymbol{\nabla} \cdot (\rho \boldsymbol{U}\boldsymbol{U}) = \boldsymbol{\nabla} \cdot \boldsymbol{\tau} + \rho \boldsymbol{b} \qquad \text{Momentum equation} \quad (3.2.5)$$

$$\frac{\partial}{\partial t}(\rho h_e) + \nabla \cdot (\rho h_e \boldsymbol{U} + \boldsymbol{q})$$
$$= \nabla \cdot (\boldsymbol{\tau} \boldsymbol{U}) + \boldsymbol{U} \cdot \rho \boldsymbol{b} \qquad \text{Energy equation} \quad (3.2.6)$$

$\boldsymbol{q}$ is the heat flux vector.

3.3 Numerical discretisation schemes

Following on from spatially discretising the domain into a set of control volumes, the governing equations can be replaced by a system of algebraic equations which are solved at the cell centres. This is also termed equation discretisation. As an example consider the continuity equation in vector notation.

$$\frac{\partial \rho}{\partial t} + \boldsymbol{\nabla} \cdot (\rho \boldsymbol{U}) = 0 \qquad (3.3.1)$$

This equation contains of two terms, a temporal term and a spatial advection term which must be integrated in time and space respectively.

$$\int_t^{t+\Delta t} \iiint_V \left(\frac{\partial \rho}{\partial t} + \boldsymbol{\nabla} \cdot (\rho \boldsymbol{U}) \right) dV dt = 0 \qquad (3.3.2)$$

The discretised spatial advection term is obtained by applying Gauss' divergence theorem

$$\int_t^{t+\Delta t} \iiint_V \boldsymbol{\nabla} \cdot (\rho \boldsymbol{U}) \, dV dt = \int_t^{t+\Delta t} \oiint_{\partial S} \rho \boldsymbol{U} \cdot \boldsymbol{ds} dt \approx \left(\sum_f \rho_f \boldsymbol{U}_f \boldsymbol{S}_f \right) dt \qquad (3.3.3)$$

where ∂S represents the total surface enclosing the cell volume *V,* the subscript *f* indicates that the summation is over the faces which bound the cell volume.

The discretised temporal term can be approximated by a first order algebraic equation as

$$\int_{t}^{t+\Delta t} \iiint_{V} \frac{\partial \rho}{\partial t} dV dt \approx V\,(\rho^{n+1} - \rho^{n}) \qquad (3.3.4)$$

where the superscript *n+1* and *n* represent the new and old time steps respectively.

Combining Equation *(3.3.3)* and (*3.3.4)* result a discrete algebraic approximation for the differential equation

$$\frac{\partial \rho}{\partial t} + \boldsymbol{\nabla} \cdot (\rho \boldsymbol{U}) \approx V \frac{\rho^{n+1} - \rho^{n}}{\Delta t} + \sum_{f} \rho_f \boldsymbol{U}_f \boldsymbol{S}_f \approx 0 \qquad (3.3.5)$$

3.3.1 Time schemes

In this study numerical models were analysed with both first order and second order discretisation schemes applied to the time derivative. These time marching schemes are pre-coded into the OpenFOAM software and are selected at runtime. The finite volume method is applied to the flow domain and the integral form of the conservation equations result. The derivative $\partial/\partial t$ is integrated over a control volume according to

$$\frac{\partial}{\partial t} \iiint_{V} \rho \varphi \, dV \qquad (3.3.6)$$

For a first order backward discretisation scheme the partial derivative is replaced by

$$\frac{(\rho_P \varphi_P V)^{n+1} - (\rho_P \varphi_P V)^{n}}{\Delta t} \qquad (3.3.7)$$

Whilst this scheme is unconditionally stable due to the dependence of the projected time-step value on the value from the current time-step only, thus eradicating the progressive accumulation of errors, the accuracy of this scheme is seldom sufficient and most guides advise the use of a higher order scheme (Ivings et al., 2004).

In the second order scheme which is also programmed in OpenFOAM the partial derivative is replaced by the second order backward difference equation

$$\frac{3(\rho_P \varphi_P V)^{n+1} - 4(\rho_{P\emptyset} \varphi_P V)^{n} + (\rho_{P\emptyset} \varphi_P V)^{n-1}}{2\Delta t} \qquad (3.3.8)$$

where the superscript n indicts the current time-step. Whilst the first order scheme is more stable, the second order scheme conserves the flow field properties more accurately and thus second or higher order schemes are usually employed for CFD analyses.

3.3.2 Gradient Schemes

The gauss linear gradient (∇) discretisation scheme is specified for all scalar field variables in each simulation in this study. By applying Gauss' Theorem to the volume integral it can be transformed to a surface integral according to

$$\iiint_V \nabla\varphi \, dV = \iint_S \varphi \, d\boldsymbol{S} = \sum_f \boldsymbol{S}_f \varphi_f \qquad (3.3.9)$$

In the above expression φ represents a tensor field for any parameter under consideration, and $\boldsymbol{S}$ is the surface area vector.

The `gauss` keyword is used in the OpenFOAM code to specify the standard finite volume discretisation of Gaussian integration which requires the interpolation of values from volumetric cell centres to face centres (The openFOAM Foundation, 2013) thus in the case of the gradient scheme defined for this study the interpolation from cell centres to face centres is a linear interpolation.

3.3.3 Divergence Schemes

The divergence term ($\nabla \cdot$) is integrated over the control volume and linearized according to

$$\iiint_V \nabla \cdot \boldsymbol{\phi} dV = \iint_S \boldsymbol{\phi} \cdot d\boldsymbol{s} = \sum_f \varphi_f \cdot \boldsymbol{S}_f \qquad (3.3.10)$$

(The openFOAM Foundation, 2013). The divergence scheme for each of the flow field variables was defined as second order accurate except in the case of the thermal flow fields which were specified as first order accurate. The thermal flow fields were only required to be specified in the case of the compressible flow simulations and not for the incompressible simulations. This is because the fluid temperature was a variable which needed to be included within the ideal gas equation which governed the compressive behaviour of the fluid. `CompressibleInterFoam`, the CFD Solver used to model the compressible simulations in this study is capable of modelling flows in which cavitation is present. However, because the degree to which the air is compressed is relatively low in this research the thermal change resulting from the fluid compressing is negligible. Thus a first order

scheme can be used to discretise the thermal flow fields in the energy equation for the compressible simulations.

3.3.4 Laplacian Schemes

The Laplacian term is integrated over the control volume and is linearized according to

$$\iiint_V \nabla \cdot (\Gamma \nabla \varphi)\, dV = \iint_S (\Gamma \nabla \varphi) \cdot d\boldsymbol{s} = \sum_f (\nabla \varphi)_f \cdot \boldsymbol{S}_f\, \Gamma_f \qquad (3.3.11)$$

(The openFOAM Foundation, 2013). A second order accurate uncorrected Gauss linear discretisation scheme was specified for the Laplacian terms. The linear interpolation from cell volume centre to face centre was performed using a central differencing scheme. Because the domain mesh was hexahedral the vector joining cell centres was coincident with the surface normal vector, therefore a correction term was not required to be applied to the interpolation scheme values. In the case of a tetrahedral mesh the vector joining adjacent cell centres may not be orthogonal to the cell faces. In this case a correction factor may be required to be applied to the interpolation value.

3.4 Volume of Fluid Method

The volume of fluid (VOF) method originally developed by Hirt and Nichols (1981) is a numerical technique used to model complex free surface flows. It is based on an Eulerian approach wherein the movement of the fluid is tracked across a static mesh which defines the problem domain. It is a particularly suitable method for those simulations in which the free surface boundary undergoes large deformations where a Lagrangian approach is unsuitable. The transformation of the flow and the subsequent evolution of the free surface is achieved by using a finite volume discretisation to solve a transport equation for the fluid in each cell (Godderidge, 2009), (Hirt and Nichols, 1981). The method was primarily developed to overcome the inherent low resolution problem which occurs at a free surface boundary interface in a multiphase flow analysis which arises due to convective flux averaging of flow properties across cell boundaries when pure Eulerian or Arbitrary Lagrangian-Eulerian (ALE) techniques are employed. Hirt and Nichols (1981) set out 3 types of problems which arise in the treatment of free boundaries and how these are managed in the VOF method.

1. Their discrete representation.
2. Their evolution in time
3. The manner in which the boundary conditions are imposed on them.

1. The discrete representation of free boundary surfaces

In the volume of fluid method a function $F(x, y, t)$is introduced at each grid cell in the domain. The value of this function is defined as unity at any cell entirely occupied by the fluid and zero at any cell completely devoid of fluid. Thus cells with an intermediate value $0 < F < 1$ are those the cells which the free surface boundary crosses or indeed cells which are intersected by the surface of an entrained air bubble. Thus a cell which at least one empty neighbour cell ($F = 0$) is by definition a free surface cell and a cell must contain a droplet when that cell has a value $0 < F \leq 1$ and is surrounded by cells with a value of $F = 0$ (Sabeur et al., 1995). This method allows for the determination of the fluid proportion in each cell through the storage of only a single variable. Previously the Marker and Cell (MAC) method devised by Harlow and Welch (1965) required the fluid spatial representation through the positioning of marker particles which moved with the fluid flow. This required the storage of the velocity components of each particle which was updated at each time-step in the calculation. Because the VOF method requires only the value of the *F* function to determine the fluid spatial representation the computational storage requirements are considerably reduced compared to the MAC method.

2. The evolution of the free boundary in time.

Although those cells which contain the free surface are determined from the *F* function, the orientation of the surface requires additional computation. By calculating the derivatives of the *F* function at each cell boundary the free surface normal can be established (Sabeur et al., 1995). The normal direction to the free surface is then the direction in which the *F* function varies most rapidly (i.e.∇F). From the value of the *F* function and the direction of the normal to the boundary a line cutting the cell can be drawn which represents the free surface boundary. The temporal evolution of the *F* function and thus the advection of the flow in two dimensional space is governed by the transport equation

$$\frac{\partial F}{\partial t} + u\frac{\partial F}{\partial x} + v\frac{\partial F}{\partial y} = 0 \qquad (3.4.1)$$

Where $u$and v are the velocities in the component $x$and y directions respectively. Then as the simulation proceeds in time the value of function *F* moves with the fluid. The fluxes across each cell in the fluid domain are then obtained from Equation *(3.4.1)*. The value of *F* is then recorded and the simulation is advanced in time by the amount ∂t at which stage the value of $F(x, y, t)$ is re-computed. In OpenFOAM version 2.3.0 the advection of the free surface in the InterFOAM solver is controlled by the explicit Multidimensional Universal

Limiter with Explicit Solution (MULES) algorithm, which is a variation of the Flux Corrected Transport (FCT) scheme (Dianat et al., 2017). The MULES algorithm relies in a straightforward upwind scheme to computed advection in the interfacial cells (Deshpande et al., 2012). The MULES schemes ensures the fluxes into or out of a cell are limited to maintain boundedness of the VOF method, thus ensuring stability of the numerical code.

3. The manner in which the boundary conditions are imposed on the free surface.

Because *F* is a step function having a value of zero or unity in the single phase cells, certain considerations must be made for those cells which contain the free surface to ensure the discontinuous nature of the *F* function and prevent smearing of the boundary interface. Hirt and Nichols (1981) propose the implementation of a Donor-Acceptor scheme for the flux approximation across cells, this ensures those cells containing the free surface boundary maintain a sharp interface.

Due to the restriction that fluid can only be advected to its nearest neighbour cell in a single time-step when implementing the Donor-Acceptor Scheme a stability time-step constraint follows that

$$\partial t < \min\left\{\frac{\partial x_i}{|u_{ij}|}, \frac{\partial y_i}{|v_{ij}|}\right\} \qquad (3.4.2)$$

Where $\partial x_i$and ∂y_i are the mesh size increments in the respective *x* and *y* directions. Also when a non-zero value of kinematic viscosity v is applied, the flow momentum may not diffuse more than a single mesh cell in a single time-step and for stability to be ensured the following limitation is applied

$$v\partial t < \frac{1}{2}\frac{\partial x_i^2 \partial y_j^2}{\partial x_i^2 + \partial y_j^2} \qquad (3.4.3)$$

Godderidge (2009) lists some of the advantages and disadvantages of the VOF method. The main benefit includes the possibility of analysing the flow of multiple fluids (multi-phase flow) within a single simulation whilst including the interactive effects between the discrete fluids. However it is not a trivial process to incorporate these interactions. A frequently observed problem is the smearing of the fluid boundary. This occurs as a result of diffusion of the transport equation over the mesh cell in which the boundary is located. This problem can be addressed by specifying a high resolution mesh in the region where the fluid interface will occur. Figure 3.4.1 clearly shows the effects of increased mesh resolution on the sharpness of the fluid interfacial boundary. The mesh on the left hand side is a 1mm cubic

tetrahedral mesh, the mesh on the right hand side is a 0.5mm tetrahedral mesh. Whilst the smearing on the fluid interface extends over a single mesh cell in each case, the fluid interface is sharper on the right hand side as it is restricted to 0.5mm thickness.

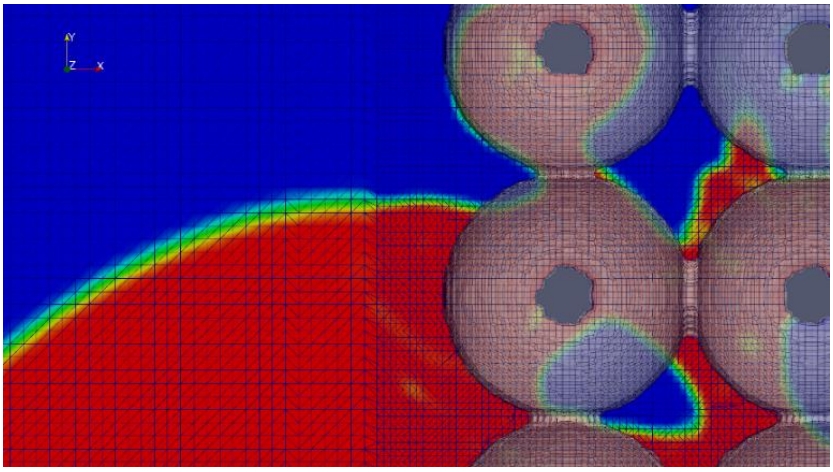

Figure 3.4.1 Fluid interfacial sharpening through mesh refinement.

The interaction between the individual fluid phase constituents in the model is important as the pressure transfer across the free surface boundary which defines an entrained air bubble is central to this study. Multiphase CFD models can be implemented using either a homogeneous or an inhomogeneous approach. For a given transport process, the homogeneous model assumes that the transported quantities (with the exception of volume fraction or F function value) for that process are the same for all phases (ANSYS, CFX 2013). Thus a common flow field for velocities, temperature, pressures etc. is applied to all fluids within the domain. This simplifies the underlying code which defines the interaction of the fluids at the boundary as a single mass conservation and momentum conservation equation is applied to both fluid as opposed to individual conservation equations being applied to each fluid in an inhomogeneous model approach at the fluid interface. The conservation of mass and momentum equations are formulated by summing the averaged fluid properties according to their constituent proportion in the boundary cell. For a two phase flow, density ρ in the boundary cells is given by

$$\rho = \sum_{a=1}^{2} r_a \rho_a \qquad (3.4.4)$$

where r_a is the volumetric fraction of each constituent fluid in the free surface boundary cell. The conservation of mass equation for an incompressible fluid in tensor notation is

$$\frac{\partial(\rho)}{\partial t} + \frac{\partial(\rho u_i)}{\partial x_i} = 0 \qquad (3.4.5)$$

and the conservation of momentum for an incompressible fluid is

$$\frac{\partial(\rho u_i)}{\partial t} + \frac{\partial\left(\rho u_i u_j\right)}{\partial x_j} = -\frac{\partial p}{\partial x_i} + \frac{\partial \tau_{ij}}{\partial x_j} + f_i \qquad (3.4.6)$$

where ρ is given in Equation *(3.4.4)*

In the domain cells where $F = 1$ or r $F = 0$ these equations reduce to the mass and momentum conservation equations for a single phase fluid. The Homogeneous model approach is incorporated into the OpenFOAM multiphase solvers. This limits the relative motion between individual fluids at the boundary interface cells to zero. This is analogous to a "no-slip" boundary condition between the individual fluids at the cells in which the fluid interface is located.

3.5 OpenFOAM model case structure

Each OpenFOAM simulation case is organised and structured within a hierarchical directory system (The openFOAM Foundation, 2013). The directories and their sub-directories contain files which are used to define the model flow field initial conditions and boundary conditions, the geometry, the fluid specifications, the solver controls and the post-processing commands. Figure 3.5.1 displays the basic structure of a typical OpenFOAM case simulation.

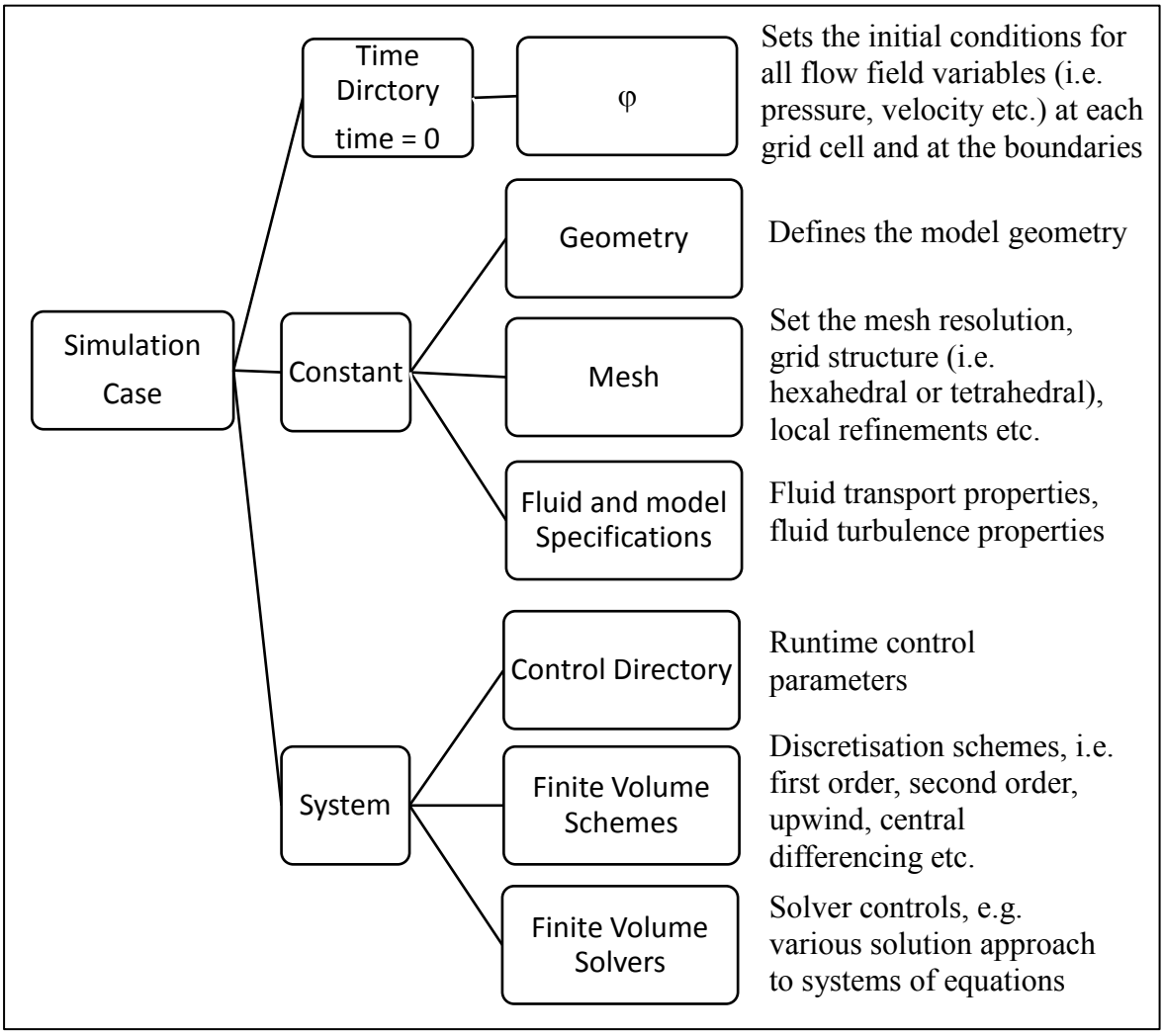

Figure 3.5.1 Typical OpenFOAM case structure.

Chapter 4

2 Dimensional CFD dam-break model definition

4.1 Introduction

This chapter describes the key parameters and some aspects of the underpinning theory which must be programmed in order to create the CFD model analysed in this study. The specific criteria for the incompressible simulations and the compressible simulations are also described.

4.2 Dam-break model geometry

The OpenFOAM model geometry consists of a 300mm long by 200 mm high tank with an initial 4 mm square spatial mesh discretisation resolution. All OpenFOAM models are initially generated in three dimensions, thus the solutions are produced in three dimensions by default (The openFOAM Foundation, 2013). Nevertheless, the model can be reduced to a two dimensional study by specifying a model thickness of 1 grid cell and applying certain boundary conditions on the third dimension (in the direction of the model thickness) for which no solution is required, i.e. an `empty` boundary condition. The initial study comprises of a two dimensional analysis of the flow.

The tank contains a column of water at the left hand side (LHS). The dimensions of the water column are specified as 57.15 mm wide by 114.3 mm high. These dimensions were selected to reflect the collapsing water column experimental research conducted by Martin and Moyce (1952). A no-slip boundary condition is prescribed at the tank base and at the vertical walls. As the top of the tank is considered to be open to the atmosphere the inflow and outflow of the fluid is permitted across this boundary. In the incompressible simulation a combination of boundary conditions are specified at this edge for the pressure and velocity terms of the fluid flow governing equations to model this inflow and outflow behaviour

whilst maintaining stability of the simulation. A `fixedValue` boundary condition with a value of zero is specified for the pressure term whilst a `pressureInletOutletVelocity` boundary condition is applied to the velocity term at the boundary edge representing the top of the tank. The boundary conditions on the air phase permit the inflow and outflow behaviour, however, the water phase is restricted to outflow only

In the case of the incompressible model, the inflow and outflow of the air phase is permitted across this upper boundary, however the liquid phase is again restricted to outflow condition only. Then, in the case of the compressible simulation the numerical value of the `calculated` boundary condition is set to atmospheric pressure across the edge which represents the top of the tank for the initial pressure term. This allows the compressibility effects of the phases to be modelled within the domain of the simulation. The velocity boundary condition is unchanged from the incompressible setup with a `pressureInletOutletVelocity` boundary condition is applied. The liquid fluid phase has an `inletOutlet` boundary condition applied which permits only the outflow of the water, whilst the air phase has an `inletOutlet` boundary condition which allows both the inflow and outflow of air.

Four grid points P1, P2, P3, and P4 on the impact interface are selected at which to sample the pressures. These points are located at the intersection of the tank base and vertical wall and also at 8 mm, 20 mm and 40 mm above the tank base respectively. Figure 4.2.1 displays the initial model setup and sampling points. Also visible on this figure is the 4mm square discretisation mesh. The liquid phase is represented by the red grid cells and the air phase by the blue cells. Because a low resolution mesh is applied to the model in Figure 4.2.1 the interface between the liquid and gas phase is not sharply defined. As the mesh is incrementally refined in later simulations this interface between the fluids is more sharply defined.

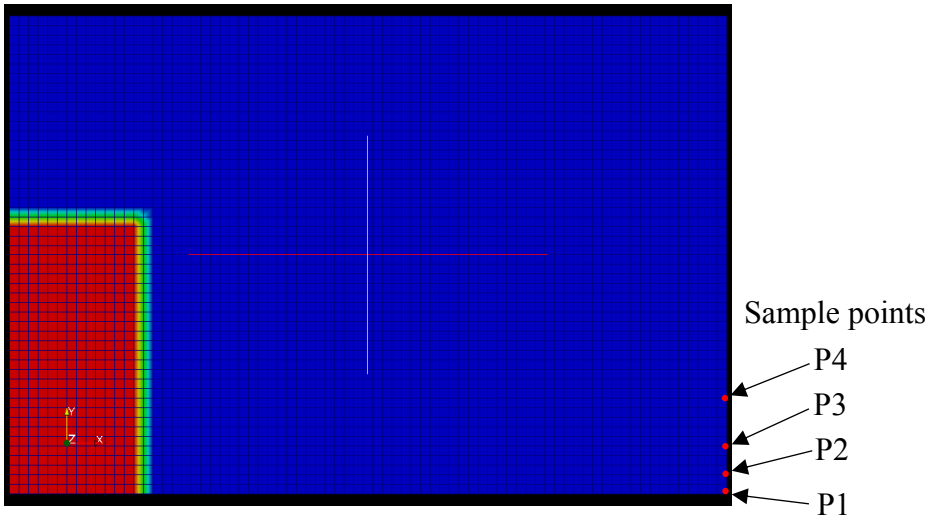

Figure 4.2.1 Initial CFD OpenFOAM model setup and sampling points.

4.3 Spatial discretisation

The spatial domain was initially discretised using a structured 4mm mesh. This initial mesh resolution was subsequently refined three times as part of the grid independence study. The grid independence was determined using the incompressible first order temporal and second order spatial discretisation scheme only. The spatial discretisation analysis was performed by calculating the maximum impulse force at initial wave impact for each level of refinement (see Section 5.2.1). These results were then compared to verify that with progressive mesh refinement the solution was trending towards convergence. Table 4.3.1 records the grid resolutions and associated geometrical properties applied to the model for this section of the study. Because two dimensional simulations in OpenFOAM are defined with a model thickness of a single three dimensional element as described in Section 4.2 and illustrated on Figure 4.3.1 then the total number of nodes for these simulations is calculated according to

$$n_n = 2e + 2 \qquad (4.5.1)$$

where n_n is the total number of nodes and e is the total number of elements.

Grid [mm]	Total number of nodes	Number of nodes in x direction	Number of nodes in y direction	Total number of elements	Number of elements in x direction	Number of elements in y direction
4X4	7752	152	102	3750	75	50
2X2	30502	302	202	15000	150	100
1X1	121002	602	402	60000	300	200
0.5X0.5	482002	1202	802	240000	600	400

Table 4.3.1 Grid statistics for varying levels of grid resolution

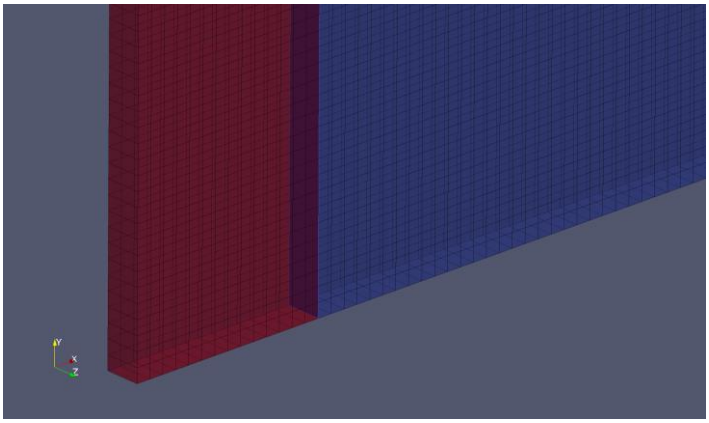

Figure 4.3.1 Two dimensional simulation mesh showing elements and nodes

4.4 Temporal discretisation

The OpenFOAM `controlDict` file within the project case `constant` directory contains the input data which controls the temporal functioning of the simulation. This file contains a command for specifying the simulation time step duration. It also contains a command which allows the user to define the maximum Courant number value. Furthermore there is an `adjustTimeStep` function which automatically over-rides and reduces the time step duration should the specified time-step cause the maximum Courant value to be exceeded. This ensures stability of the model during the simulation runtime by limiting the maximum Courant number value to 1. By limiting the courant number thus, Von Neumann stability is ensured. Initial simulations were conducted using a specified maximum Courant number of 1.0 and an initial time-stepping length of 0.00001 sec. For the first order time and spatial discretisation schemes with low level grid resolution this time-step duration was sufficiently short to allow the Courant value to be maintained below 1.0. However as the grid was progressively refined and more accurate higher order temporal and spatial discretisation schemes were applied to the model it was observed that the program automatically reduced the time-step duration to enforce stability and ensure convergence of the solution. This reduction in time step length increased the computational cost and associated simulation wall-clock time. Also, as the fluid flow velocity varied during the simulation the time-step duration was varied accordingly.

The `controlDict` file also allows the user to define the time intervals at which the simulation results are recorded or sampled. From preliminary simulations it was observed that subsequent to the water column collapse the wave front impacted the right hand side after approximately 0.2 seconds as shown on Figure 4.4.1 (a). During the initial simulation phase prior to impact the results data was sampled at 200 Hz intervals up to 0.195 seconds elapsed simulation time. The wave front impact generates a sharp pressure pulse on the

pressure history plot (see Figure 4.4.2), this causes the formation of a jet which accelerates vertically upwards (Figure 4.4.1(b)). Because the pressure impulse is of short duration the upwards acceleration of the jet is mainly due to inertial forces as described in Section 2.3. Then to capture these impulsive, short duration effects, the simulation was halted at 0.195 seconds and the programme code defining the time-step sampling interval was altered to increase the sampling frequency from 200 Hz to 1 kHz during this phase of the simulation. The simulation was restarted using the results from the 0.195 seconds time-step as the simulation initial conditions. This sampling frequency was maintained until 0.5 seconds elapsed simulation time. This allowed the rapidly varying pressure impulse to be more accurately recorded. The pressure data from this time period was used for the grid convergence study as described in Section 5.2.1. As these inertial forces dissipate the velocity of the jet decelerates, the direction of flow reverses and the jet collapses as shown on Figure 4.4.1(c). During this stage of the flow simulation a quantity of the gas phase is trapped within the liquid phase. This is manifested as air bubbles or pockets of air trapped within the liquid as shown on Figure 4.4.1(d). Because this period of the flow development is of particular interest especially when observing the oscillatory pressure effects with the compressible simulation the sampling frequency interval is further reduced (by code modification as describe before) to 10 kHz from (0.5s to 0.7s elapsed simulation time). This ensures the oscillatory pressure behaviour is accurately captured. This high frequency sampling rate is maintained until the entrapped bubble dissipates through the free surface, or fragments into smaller bubbles or migrates away from the impact interface such that the oscillations in the observed pressures are damped out.

Following this simulation period the time step sampling rate is increased back to 0.001s (1 kHz) until the completion of the simulation. These alterations to the sampling frequency required that the simulation was halted and restarted a number of times, with each restart using the results from the previous time step as the initial conditions. The pressure history plot for the incompressible simulation is shown on Figure 4.4.2 with the approximate corresponding flow simulation profile visualisations from Figure 4.4.1 indicated.

The profile of the collapsing jet and the entrainment of gas bubbles within the liquid varies depending on the equation discretisation schemes used for the temporal and spatial terms within the fluid flow governing equations. Also, with a higher mesh resolution discretisation, the entrainment of small bubbles of the air phase within the liquid phase is more accurately captured and the interface between the fluid phases is more sharply defined. It should also be noted that Figure 4.4.2 was plotted using data obtained from an incompressible simulation.

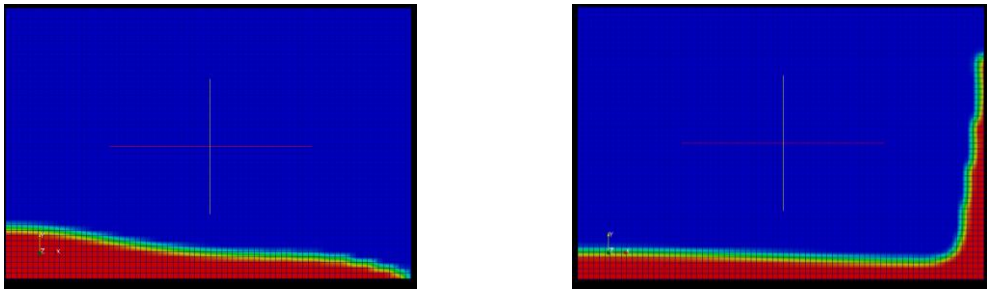

(a) t = 0.208s (b) t = 0.306s

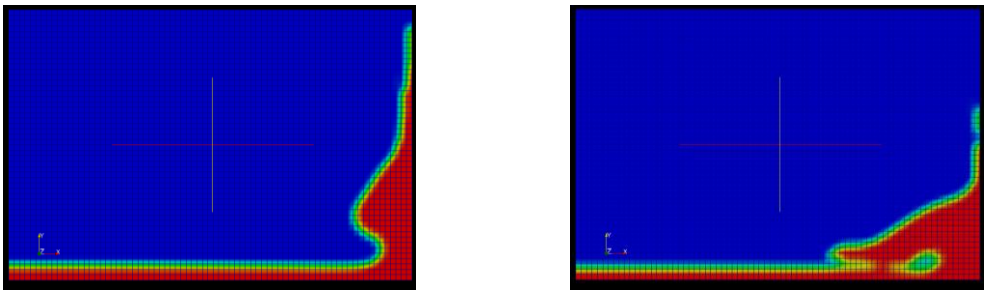

(c) t = 0.456s (d) t = 0.5356s

Figure 4.4.1 Free surface spatial evolution and bubble entrainment (4mm mesh resolution)

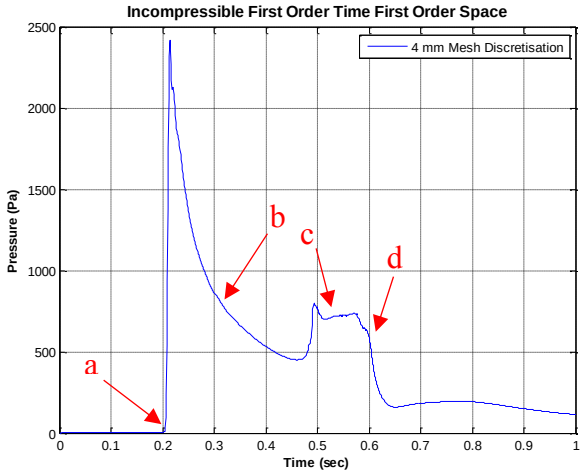

Figure 4.4.2 Time-Pressure plot for incompressible 4mm spatial discretisation simulation (see Figure 4.4.1 for the corresponding flow profile images at points a, b, c and d).

4.5 Dam-break flow simulation with incompressible air phase

The series of simulations performed can be broadly categorised into two groups, those in which air compressibility effects were neglected and those in which air was considered as a compressible fluid. The simulation settings for the incompressible model are described in this sub-section. In the next sub-section the modifications to the model which are required to incorporate the effects of compressible air are described.

4.5.1 Solver controls

The OpenFOAM solver `interFoam` uses Navier-Stokes equation in a single field formulation to model the two phase flow of two immiscible, incompressible fluid phases (Maric et al., 2015).Using the discretisation methods previously described in Section 3.3 a system of equations for each of the discretised terms in the fluid flow governing equations can be generated in the form

$$[\boldsymbol{A}][\boldsymbol{x}] = [\boldsymbol{b}] \qquad (4.5.2)$$

Where $\boldsymbol{A}$ is a square matrix of coefficients, the size of which is directly proportional to the number of grid cells comprising the model domain, it is usually sparsely populated and diagonally dominant. The sparsity of the matrix depends on the order of discretisation stencil used for the equation term under consideration, i.e. pressure, velocity, F function etc. $\boldsymbol{x}$ is a vector of values for which the solution is sought and $\boldsymbol{b}$ is a vector of values which represents the known boundary condition values or source terms. The solution to $\boldsymbol{x}$ is obtained by employing either a direct or an iterative method for the solution of a linear system of equations to the coefficient matrix $\boldsymbol{A}$ in Equation *(4.5.2)*. Gaussian elimination is an example of a direct method which involves row swapping, multiplication and addition operations in order to create an upper triangular matrix of coefficients which can then be used to solve for the unknown vector matrix $\boldsymbol{x}$ through back substitution. This method of solving the system of algebraic equations has an arithmetic complexity of $O(n^3)$ where n is proportional to the number of grid cells. Using this technique, the coefficient matrix is diagonally dominant and usually sparse prior to the row swapping operation, however, afterwards the matrix is no longer diagonally dominant. This results in additional memory requirements and can also be a source of slow algorithm solution times. It is much more efficient to employ an iterative method or a technique which can exploit the initial diagonal dominance of the coefficient matrix.

One such technique is to utilise the direct solver in combination with a runtime updated iterative over relaxation scheme such as the Gauss-Seidel method. To improve accuracy a solution residual is introduced and computed at predefined iteration steps. An upper tolerance bound must be specified for the residual and this parameter is included within the `fvSolution` file in the case system directory.

Alternatively an iterative technique such as a preconditioned conjugate gradient (PCG) method can be adopted with a runtime selectable matrix preconditioner such as the Diagonal Incomplete Cholesky (DIC) technique applied.

In order to obtain an approximate solution to the Navier-Stokes equations which contain both pressure and velocity terms a coupling algorithm must be also specified. This algorithm uses the values computed from the linear systems of equations to advance the flow of fluid through the model domain as the simulation proceeds. For this study the PIMPLE algorithm is used to couple the pressure and velocity terms to produce an approximate solution to the Navier-Stokes equations.

4.5.2 Fluid constants and flow control settings

Both the air and water phases were defined as Newtonian fluids. The kinematic viscosity ν, was defined as 1.0×10^{-6} m^2/s and 1.48×10^{-5} m^2/s for water and air respectively while assuming a temperature of approximately 293k. These values reflect typical laboratory condition properties of water and air during experimental investigations (Seiffert et al., 2015), (Koch et al., 2016). The density ρ, of water and air was set to 1027 kg/m^3 and $1kg/m^3$ respectively[1]. A model to describe the flow regime (i.e. laminar flow, turbulent RANS, turbulent LES model) must also be included in the `Constant` directory of the simulation case.

As described in Section 4.4 the water wave front travels 242.85 mm (300mm-57.15mm) reaching the impact interface at approximately 0.2 seconds. Thus its average velocity is 1.21 m/s.

Defining Reynolds number as

$$Re = \frac{\boldsymbol{U}L}{\nu} \qquad (4.5.3)$$

Where $\boldsymbol{U}$ is the flow front velocity, L is the distance the flow front traverses (the characteristic linear dimension) and ν is the kinematic viscosity.

Using the above values the Reynolds number for this simulation is approximately 2.94×10^5. Because the simulation is two dimensional with the no slip boundary condition specified only at the tank bottom the calculated *Re* value can be directly compared to the case of flow over a flat plate. A representative value of $Re \leq 5\times10^5$ is often used as the critical transitional value for laminar to turbulent flow over a flat plate (Incropera and DeWitt, 2002). In this simulation the flow regime has a Reynolds number value below this critical value and a laminar flow model is adopted for the simulation. As this study progresses various model geometries may be investigated in which the flow no longer behaves in a laminar manner. In those cases turbulent flow effects will be included in the simulation by specifying a turbulence model such as RANS or LES.

4.6 Dam-break flow simulation with compressible air phase

The flow model which takes account of the compressibility of the air phase is created in a similar manner to the incompressible flow model. The OpenFOAM solver `compressibleInterFoam` is used to model the effects of compressibility in the phases which constitute the problem domain. In this model the characteristics of the liquid phase are defined such that it is practically an incompressible phase in comparison to the air phase is.

The following modifications and additions to the incompressible case directory and its constituent files are required to include the simulation of the air phase as a compressible material. Whilst the geometrical layout is maintained identical to the incompressible simulation, the region of the domain not occupied by the water phase must now be explicitly defined as the air phase and the properties of air must also be declared. The internal pressure fields for both phases are initialised to atmospheric pressure rounded to 1.0×10^5 Pa. The liquid and gas phase temperature are also initialised to 293 Kelvin.

The surface tension value at the water/air interface is set 0.07 Nm^{-1}. This parameter is particularly important in describing the behaviour of the entrained air bubbles formed subsequent to the liquid phase striking the impact interface. In addition to the flow regime model described in Section 4.5.2 additional thermophysical models must be defined for each fluid phase.

A thermophysical model is constructed in OpenFOAM as a pressure-temperature system from which other properties can be computed (The openFOAM Foundation, 2013). It is necessary to include a thermophysical model because the energy conservation equation (in addition to the mass and momentum conservation equations) is included in the PIMPLE algorithm when simulating the effects of compressibility within the model. The pre-programmed thermophysical model, `herhoThermo` is selected for both fluid phases. This model is explicitly constructed for the simulation of a multiphase flow interaction. It computes the basic thermophysical properties of the constituent simulation phases based on the density of those phases which varies as the temperature within the domain changes. Thus, as this is a near isothermal simulation the density variation due to thermal fluctuations within each phase will be small and subsequently the thermophysical properties of the two fluids is relatively unchanged.

[1] Since this study is concerned with oceanic waves breaking on coastal defensive structures the liquid phase is programmed as sea water which has an average density of 1027 kg/m^3 (Roquet et al., 2015).

For the water phase the Perfect Fluid equation of state is selected. This model which is based on the ideal gas equation of state neglects shear stress, viscosity and heat conduction within the fluid. The equation of state which defines the behaviour of a perfect fluid is (The openFOAM Foundation, 2013),

$$\rho = \frac{1}{RT}p + \rho_0 \qquad (4.6.1)$$

Where ρ is the fluid density, R is the universal gas constant, T is the temperature p is pressure and ρ_0 is the density at the reference pressure. In this equation the value of R (usually taken to be approximately 8.314 J $K^{-1}mol^{-1}$) is set artificially high with a value of 3000 $JK^{-1}mol^{-1}$. This emphasises the incompressibility of the liquid phase in contrast to the gas phase within the program code. The perfect gas equation of state is used for the air phase.

The mixture model is specified as `pureMixture` which dictates that the composition of the two phases in the simulation remain unaltered and no chemical change occurs in either fluid as a result of their physical interaction. The transport model is defined as `constant` for both phases which limits the dynamic viscosity and the Prandtl number to fixed values throughout the simulation. The thermodynamic model `hConst` is applied to both phases. This model computes the system enthalpy assuming a constant pressure specific heat value of 4195J $kmol^{-1}$ K^{-1} and 1007J $kmol^{-1}$ K^{-1} for water and air respectively.

The final parameter which must be defined in the thermophysical properties directory is the form of energy to be used in the thermodynamic solution. For both phases the `sensibleInternalEnergy` behaviour for the fluids is selected. Thus the behaviour of both phases is defined by the standard internal energy state function. The absolute enthalpy equation is given as

$$h_a = h_s + \sum_i Y_i \Delta h_f^i \qquad (4.6.2)$$

Where h_a is the absolute enthalpy, h_s is the standard internal energy, Y_i is the mass fraction of phase i, h_f^i is the heat of formation of phase I (The openFOAM Foundation, 2013).The inclusion of the `sensible` term in the keyword specification refers to the omission of the heat of formation term from the absolute enthalpy equation. Then the absolute energy of the system is simply equal to the sensible energy.

$$h_a = h_s \qquad (4.6.3)$$

Sensible energy is typically used in simulations where chemical reactions are not present or where large energy changes in a system are easily attributable to chemical reactions (The openFOAM Foundation, 2013).

4.7 Domain decomposition and parallel solution over distributed processors

Many factors influence the OpenFOAM simulation wall clock runtime, the most obvious being the mesh discretisation resolution, the discretisation scheme employed for the governing equations, and the OpenFOAM solver employed to compute the flow field results. A larger number of grid cells requires greater memory storage space and additional computational operations to produce a solution. Also, the particular solver employed will necessitate the computation of a particular set of equations. For example the incompressible `interFoam` solver computes the approximate solution to the Navier-Stokes equations. To generate a solution which incorporates the effects of fluid compressibility within the model the solver `compressibleInterFoam` additionally solves equations of state for each fluid and the energy equation which must also be incorporated into the PIMPLE algorithm.
The temporal and spatial equation discretisation schemes also have a significant impact on the runtime. For example the implicit second order backward discretisation temporal scheme uses the grid cell values from the two previous time steps to project the value at the next time step. In contrast the first order time scheme uses only the values from the previous time step to compute the value at the next time step. Thus the latter scheme has less terms in the solution equation simplifying the algorithm and requiring less computer RAM space and processing time. This is a very important consideration especially when investigating models with high mesh resolution and fine time stepping.
By default the OpenFOAM solvers are executed on a single processor in serial execution mode (Maric et al., 2015). However the facility to carry out parallel processing is incorporated into OpenFOAM through the implementation of the standard message passing interface (MPI). This allows the simulation to be decomposed and concurrently run across a number of processors thus allowing a significant saving in wall clock computation time. The parallelisation of the simulation is achieved by first decomposing the model domain into a number of sub-domains. The number of subdomains must correspond to the number of processors on which the computation is to be carried out. The calculations are then carried out on each subdomain in parallel time. The OpenFOAM `reconstructPar` command is invoked to reconstruct the decomposed fields and mesh across the sub-domain boundaries

into a single overall solution once the simulation has completed. The case `System` directory within the project folder hierarchy (see Figure 3.5.1) contains the `decomposeParDict` file which can be modified to define the parameters for running the simulation in parallel.

The incompressible, low mesh resolution, first order spatial and temporal discretisation simulations in this study were completed using serial processing. As the simulations became more computationally expensive the model domain was discretised into 8 subdomains to achieve a solution on a 64 bit, 2.5GHz, 8 CPU laptop with 12 GB of RAM. The most computationally expensive simulations were decomposed into 64 subdomains and run in parallel on 64 processors on the University of Southampton high performance computing (HPC) cluster Iridis 4.

Chapter 5

2 Dimensional simulation with solid wall impact results

5.1 Introduction

Results from the model verification process are initially presented. By performing a grid independence study it is determined that a satisfactorily high mesh resolution has been applied to the model. The model is next validated through an analysis of the time varying collapsing fluid column leading edge position. The results from this analysis are then compared to the well-recognised benchmarking experimental work performed by Martin and Moyce (1952). As the results from the numerical model agree well with the experimental case it is determined that the simulation is behaving in an accurate manner. Further validation is provided through comparison of the impact pressure history with impact pressure signal results produced through a dam-break experiment conducted at MARIN in the Netherlands. Again a satisfactory comparison is achieved.

Finally the pressure responses at a number of positions are analysed in simulations in which the air phase is modelled as both an incompressible and a compressible medium. The influence of air entrapped within the liquid phase is examined to determine its effect on oscillatory pressure fluctuations. The pressure signals are analysed in both the time and frequency domains. A comparison of the simulated oscillatory pressure response is made with both the analytic Minnaert resonant frequency response of a single bubble in an infinite domain of water, and a single bubble resonant frequency expression developed experimentally by Hattori et al. (1994). Again satisfactory results are achieved for the numerical model.

5.2 Model verification and validation

In order to ensure confidence in the accuracy of the simulation and the data generated from it, it is important to determine the correctness of the model through comparison with previously substantiated studies. The simulation results should be compared to data obtained from previous research conducted through both experimental and, or numerical means. There are two recognised stages in establishing the integrity of a numerical model, first the model should first be verified, then validated.

The American Institute of Aeronautics and Astronautics (AIAA) define verification as "the process of determining that a model implementation accurately represents the developer's conceptual description of the model and the solution to the model" and validation as "The process of determining the degree to which a model is an accurate representation of the real world from the perspective of the intended uses of the model"(American Institute of Aeronautics and Astronautics., 1998). Roache (1997) also presents a very concise definition for verification and validation in the application of those terms to CFD analyses; verification is "solving the equations right" whilst validation is "solving the right equations". Thus to verify the model is to ensure that the correct numerical schemes to solve the discretised partial differential equations are applied, and also a sufficiently high discretisation resolution is adopted for both the temporal and spatial domains. Model validation is achieved by comparison of the model results with accepted benchmarking test cases or by comparison with research results which have been previously substantiated. Modelling factors which may invalidate the model include the selection of wrong boundary conditions, incorrect geometry data, erroneous fluid property parameters etc.

A thorough analysis of numerical schemes was conducted at the initial stage of investigation. This was achieved by applying both first and second order solution schemes to both the temporal and spatial equation discretisation schemes. For each simulation then four levels of mesh refinement were investigated to ensure a solution which was independent of grid resolution. Simulations were performed using a variable time-step with an upper limit bounded by the Courant number. This process was repeated for two sets of simulations, the first neglecting the effects of compressibility of the air phase within the model whilst the second set of simulations incorporated the effects of compressibility for the air phase. In total then there were 32 simulation completed (16 with air compressible and 16 with air incompressible) with the impact pressures sampled at four positions at the impact interface for each simulation thus yielding 64 data sets for the incompressible simulation and 64 data sets for the compressible simulation. Consequently by comparing the two sets of results the influence of the air compressibility on the oscillatory impact pressure could be observed.

Spatial discretisation of the model was analysed by performing a grid independence study which compared the impact pressure impulse as the wave front impinged upon the right hand side wall of the tank for four levels of mesh resolution. The pressure impulse for the grid independence study was measured at the bottom right-hand corner of the tank, position P1 on Figure 4.2.1.

5.2.1 Impact pressure impulse

To verify the model, a grid independence study was performed. For this analysis the results set from the incompressible first order in time, second order in space simulation were utilised. To allow for direct comparison of the results, the simulation times and pressures were first converted to a non-dimensional quantities. Time series values were non-dimensionalised according to $t_{nd} = nt\sqrt{(g/a)}$, where a is the half base width of the water column in its initial position, g is the acceleration due to gravity, t is time. n is calculated according to $n = \sqrt{(h/a)}$ where h is the initial height of the water column. The pressure series values were non-dimensionalised according to $P = p/\rho gh$, where p is the impulse pressure and ρ is the density of water. The non-dimensionalised time-pressure plots for the time period equivalent from 0.19 s to 0.25 s simulation time are shown on Figure 5.2.1 for the four levels of grid resolution. The impact pressure impulse value was obtained for each grid resolution by integrating the pressure over the peak rise time (Peregrine, 2003)

$$I(\boldsymbol{x}) = \int_{Rise\ time} P(\boldsymbol{x}, t)dt \qquad (5.2.1)$$

The peak rise time which for this study is taken as the duration of impact was determined for each of the four levels of mesh discretisation in the manner shown on Figure 5.2.2. The baseline time adopted for the calculation of the peak rise time was set at 0.19 seconds elapsed simulation time for all levels of grid discretisation as this was the time at which any significant rise in pressure was registered at P1. This small pressure increase was detected at location P1 (Figure 4.2.1) before the water phase impacted the wall. This pressure increase was due to the collapsing water phase applying pressure to the incompressible air phase which in turn transmitted some fraction of the pressure to the RHS wall. Thus, the peak rise time was computed from the time of maximum impulse impact minus 0.19 seconds elapsed simulation time. The impact pressure impulse for each level of discretisation is shown on Table 5.2.1. The grid independence study was conducted using a data set obtained from the incompressible simulation

Temporal discretisation was governed by the Courant-Friedrichs-Lewy Condition (CFL Conditioning). In applying the CFL condition each time step is bounded by an upper limit value according to $C_n = u_i \frac{\Delta t}{\Delta x_i}$ where C_n is the courant number, usually set to a maximum value of 1.0 to ensure Von Neumann stability of the finite volume time scheme. u_i is the flux field value under consideration at node i, Δt is the time step duration and Δx_i is the grid spacing. OpenFOAM allows an adaptive time-stepping option which reduces the time-step duration automatically during runtime to ensure the CFL condition is observed.

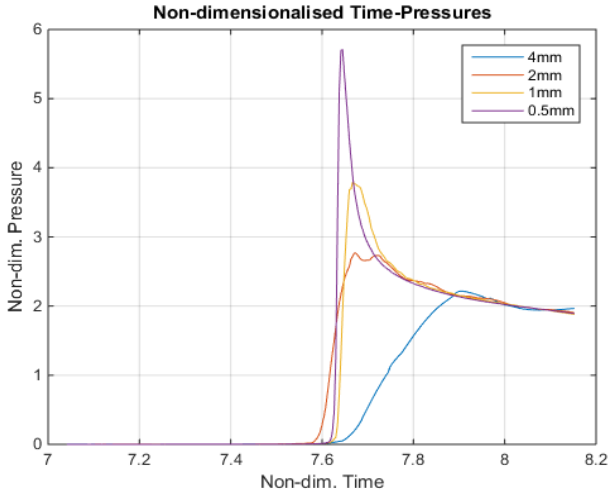

Figure 5.2.1 Non-dimensionalised pressure rise time plot for four levels of mesh resolution

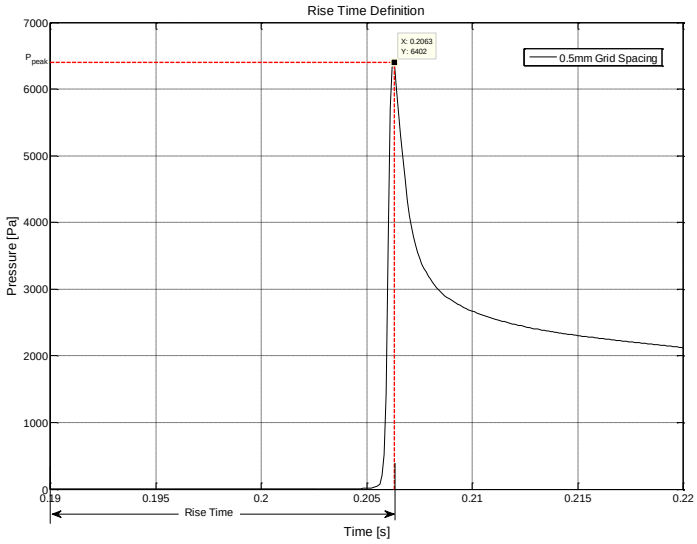

Figure 5.2.2 Peak rise time definition for 0.5mm grid spacing simulation
(note values are not non-dimensionalised)

As the grid is progressively refined the rise time decreases and the pressure peak increases as observed on Figure 5.2.1. The non-dimensional impact pressure impulse is obtained by integrating the non-dimensional pressures over the non-dimensional rise time. This value is recorded in the final column of Table 5.2.1

Grid	Dimensions mm x mm	Rise Time [Rt]	Non-Dim. Rise Time [R_{tnd}]	Peak pressure [p_{max}]	Non-Dim. Peak Pressure [p_{maxnd}]	Non-Dim. Impact pressure impulse [P_{ipnd}]
1	0.5 x 0.5	0.0163	0.6040	6402.7	5.7102	0.0717
2	1 x 1	0.0169	0.6263	4259.7	3.7990	0.0852
3	2 x 2	0.0170	0.6300	3105.9	2.7700	0.1283
4	4 x 4	0.0233	0.8634	2484.8	2.2160	0.3276

Table 5.2.1 Impact pressure values at peak rise times

Because the rise time duration decreases as the grid resolution increases the gradient of the time-pressure response plot sharpens with a finer mesh. This results in the non-dimensional impact pressure impulse integral value decreasing as the grid resolution increases. This indicates that the pressure values are more highly dependent on the spatial discretisation resolution than the temporal resolution. A plot of the non-dimensional grid spacing versus 1 minus the non-dimensional pressure impulse values is shown on Figure 5.2.3.

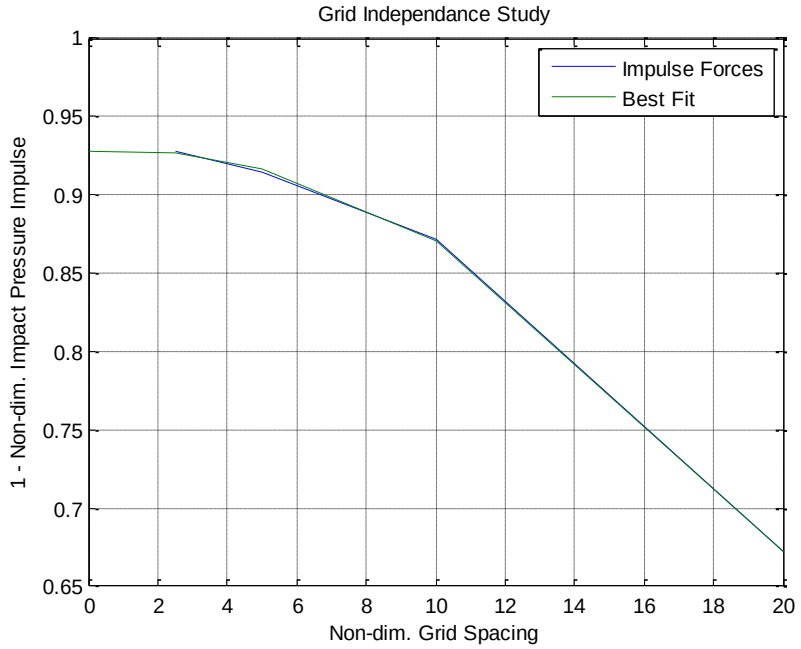

Figure 5.2.3 1 - Non dimensional impact pressure impulse Vs Non dimensional grid spacing

Also included on the graph is a second order best fit line extrapolated to a zero value non-dimensional grid spacing. The equation of this line is $y = -0.0007x^2 + 0.0012x + 0.9283$. Thus a theoretical extrapolated value for $[1- P_{ipnd}]_{0.0mm} = 0.9283$ is obtained. This yields a non-dimensional impact pressure impulse value of 0.0717. Note that this value is identical to $[P_{ipnd}]_{0.5mm}$ (from Table 5.2.1) indicating that a satisfactory level of grid convergence has been achieved. To further verify the grid independence results the order of

convergence C_o determined from an algorithm developed by Richardson and Gaunt (1927) can be computed from

$$C_o = \frac{ln\left(\frac{\left[1-P_{ipnd}\right]_{2mm}-\left[1-P_{ipnd}\right]_{1mm}}{\left[1-P_{ipnd}\right]_{1mm}-\left[1-P_{ipnd}\right]_{0.5mm}}\right)}{ln(r)} \qquad (5.2.2)$$

In Equation *(5.2.2)* only the finest 3 grid resolution results are considered. r is the grid refinement ratio which should be constant for each progressive grid resolution refinement for ease of computation. By employing a grid doubling scheme for refinement the value of r is 2. The order of grid convergence using Equation *(5.2.2)* above was established to be C_o = 1.676 for the finest 3 grids. This value is approximately 16.2% below a theoretical value of C_o = 2 which is expected for second order spatial discretisation.

The next stage in the model verification is to compute the Grid Convergence Index (GCI). This is a method for uniformly documenting grid convergence tests developed by Roache (1997) whilst also providing a means to determine if the solutions for each progressive grid refinement are approaching the asymptotic range of convergence. Again the three highest levels of grid resolution are considered. From Roache (1997), $GCI_{12} = F_s|E_{12}|$ where F_s is a safety factor with a recommended value of 1.25 for a study comparing two levels of grid resolution and

$$|E_{12}| = \frac{\left(\frac{\left[1-P_{ipnd}\right]_{0.5mm}-\left[1-P_{ipnd}\right]_{1mm}}{\left[1-P_{ipnd}\right]_{0.5mm}}\right)}{(2^{c_o}-1)} \qquad (5.2.3)$$

This yields a GCI value of 0.827% for grids 1 and 2 and 2.683% for grids 2 and 3. Using these two values one can check that the solution is within the asymptotic range of convergence according to $\frac{GCI_{23}}{r^{C_o}GCI_{12}} \approx 1$. For this study a value of 1.015 was computed thus indicating a satisfactory level of grid refinement has been applied at 1mm grid size resolution.

5.2.2 Collapsing fluid column leading edge location

Once the model has been verified through the grid independence study as outlined in Section 5.2.1, the next stage is to validate the results obtained. This is first achieved by comparison of the time varying leading edge position of the collapsing fluid column with experimental results from a study performed by Martin and Moyce (1952). The model is further verified by comparison of the non-dimensionalised time pressure response plots with experimental

data published by Kleefsman et al. (2005) obtained from their research conducted at MARIN Institute in the Netherlands.

In the dambreak study conducted by Martin and Moyce (1952), five initial water column geometries were selected as listed on Table 5.2.2. a is a dimensional characteristic defined as half the base length of each water column, n is a constant. The height of the water columns are calculated according to $n^2 a$. The CFD simulations conducted for this study were all performed using an initial water column geometry corresponding to that of experiment 5. Figure 5.2.4 displays plots of the non-dimensional surge front displacement from the original water column centreline as a function of non-dimensional time for each of the five initial water column geometries analysed by Martin and Moyce (1952).

				Width		Height	
Experiment	***n***	***n*²**	***a***	**[Inches]**	**[mm]**	**[Inches]**	**[mm]**
1	1	1	$2\,1/4$	$4\,1/2$	114.3	$2\,1/4$	57.15
2	1	1	$4\,1/2$	9	228.6	$4\,1/2$	114.3
3	$\sqrt{2}$	2	$1\,1/8$	$2\,1/4$	57.15	$2\,1/4$	57.15
4	$\sqrt{2}$	2	$2\,1/4$	$4\,1/2$	114.3	9	228.6
5	2	4	$1\,1/8$	$2\,1/4$	57.15	$4\,1/2$	114.3

Table 5.2.2 Initial water column geometries for Martin and Moyce experimental setup

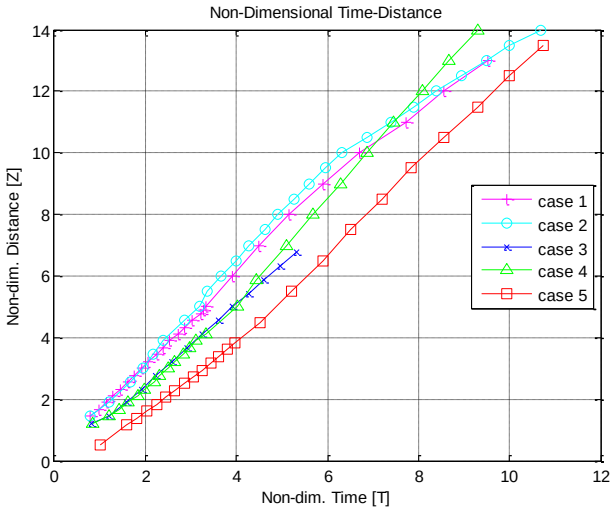

Figure 5.2.4 Martin and Moyce surge front displacement experimental results.

Using the incompressible second order time, second order spatial discretisation scheme results, the surge front location was extracted from the CFD simulation and was plotted for each of the four levels of grid resolution. The results are shown on Figure 5.2.5. The Figure demonstrates that the flow front displacement shows very good agreement between the different CFD mesh resolution models in the early phase of the simulation (up to 3 units, non-dimensional time). Thereafter the solutions diverge slightly displaying a slightly higher

velocity for the finer grid spacing. It is clearly evident that the 4mm grid spacing simulation reaches the impact interface later than the higher resolution grid simulations (indicated by a later levelling off on the graphs). This is supported by the data presented in Figure 5.2.1 wherein the maximum impact impulse amplitude occurs later for the coarser grid meshes. Also included on Figure 5.2.5 is a plot of the fluid front leading edge position sampled during experiment 5 conducted by Martin and Moyce (1952). The initial geometry of the water column in the experiment corresponds to the initial water column geometry in the CFD simulation. There is a small discrepancy between the numerical and experimental flow front position at low values of T. This may be explained due to the dam break release mechanism employed in the experimental setup transmitting a drag force to the water column as it collapses. However in the latter stages of the comparative study there is very good agreement between the experimental results of Martin and Moyce and CFD simulation results.

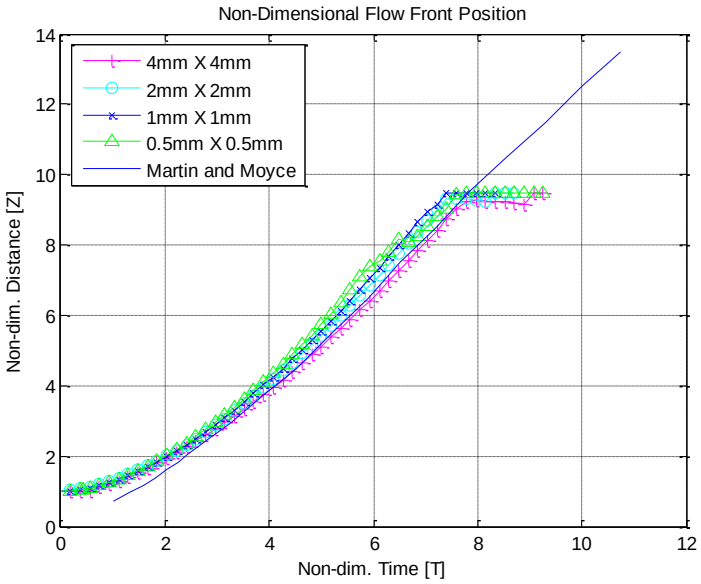

Figure 5.2.5 surge front location for four levels of mesh resolution obtained from CFD simulation

5.2.3 Comparison with MARIN experimental results

To further validate the CFD model a comparison of the pressure history results were made with experimental results from a dam-break study published by Kleefsman et al. (2005) at MARIN in the Netherlands. In this study an impact pressure analysis was also undertaken using a numerical model developed at University of Groningen, Kleefsman et al. (2005), however the experimental results only will be considered here. The geometrical set up of this experiment consisted of a 1.22 metre wide by 0.55 metre high water column which, when released impacted an obstacle located 1.77 metres from the nearside of the water column. The obstacle, shown on Figure 5.6.6 has a series of pressure sensors embedded

midway along its y –axis. This obstacle measured 0.16 metres wide and 0.16 meter high. Notwithstanding the geometry of this rectangular obstacle, if we consider a slice through the experiment at y = 0 the results of this study can be reduced to a 2 dimensional planar comparison with our simulation results. The MARIN experimental setup is shown on Figure 5.2.6. Thus it is clear that the geometry of the MARIN experimental setup is very different from the CFD model used in this numerical study. Nevertheless by non-dimensionalising the time and pressure results as described in accordance with Section 5.2.1 a direct comparison of Kleefsman's experimental results and our CFD numerical pressure history plots is possible. Figure 5.2.7 displays a plot of the experimental time pressure history results sampled at P1 on Figure 5.2.6 versus both the incompressible and the compressible numerical simulation results obtained using a second order time and second order spatial discretisation scheme with a 0.5 mm X 0.5 mm grid resolution modelled in OpenFOAM.

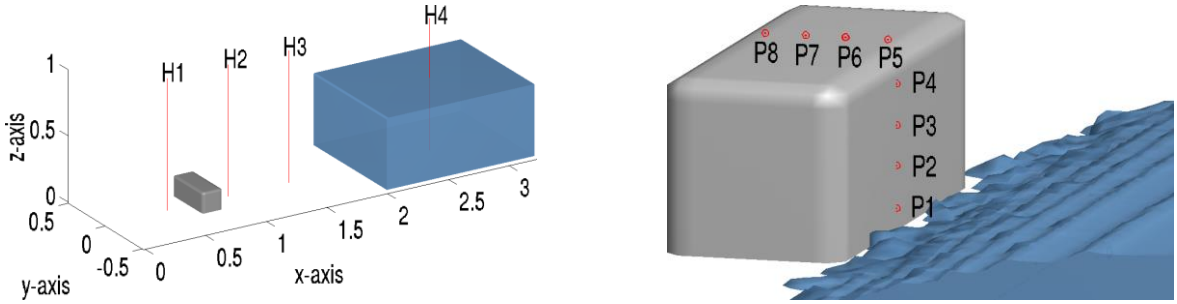

Figure 5.2.6 MARIN experimental setup and location of pressure sensors embedded into impact obstacle, (Kleefsman et al., 2005).

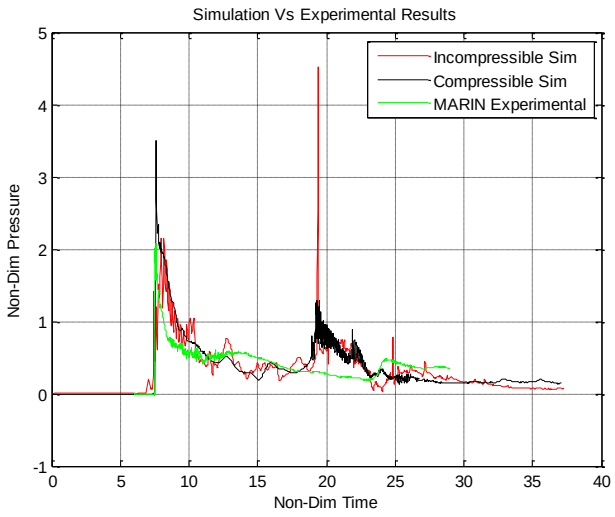

Figure 5.2.7 Comparison of numerical results with experimental results

It can be observed that there is good general agreement in the recorded pressure trend. However the impulse pressure from the compressible simulation is notably higher. This may be due to a small air bubble entrained at the leading edge of the surging wave in the numerical model or, alternatively, the sensors employed in the experimental set up may have a surface

contact area large enough which acts to cushions the impact. There is also an obvious discrepancy between the numerical CFD and experimental results from approximately 17.5 units non-dimensional time to 23.2 units non-dimensional time which is explained in the following paragraphs.

The flow front leading edge in our CFD numerical models impacts the side of the numerical tank wall which has a height greater than the initial height of the water column (262.5% higher), a jet is formed which rises vertically along the wall before collapsing back upon itself as shown in Figure 5.3.3 (a) and (b). This collapse of the jet yields the second pressure peak which can be observed at around 20 units non-dimensional time (see Figure 5.3.3(b) for the free surface profile development at the equivalent 20 units non dimensional time).

In contrast, the free surface flow evolution during the experimental investigation at MARIN has a different profile. The flow front impacts the rectangular obstacle which is centred at x = 0.75 and forms a jet. In the experiment the rectangular obstacle's height relative to the initial water column height is quite small (29%) thus the jet rises above the obstacle. At impact with this obstacle the fluid retains a proportion of its horizontal momentum causing the formed jet to lean forward and collapse onto the top of the rectangular obstacle. Thus in this experimental case a second pressure peak is not observed in the results at P1 on Figure 5.2.6 and Figure 5.2.7, (Kleefsman et al., 2005) as the jet does not collapse back onto the fluid as occurs in Figure 5.3.3 (b). See Figure 5.2.8 for the free surface flow evolution for both the numerical and experimental studies conducted at MARIN.

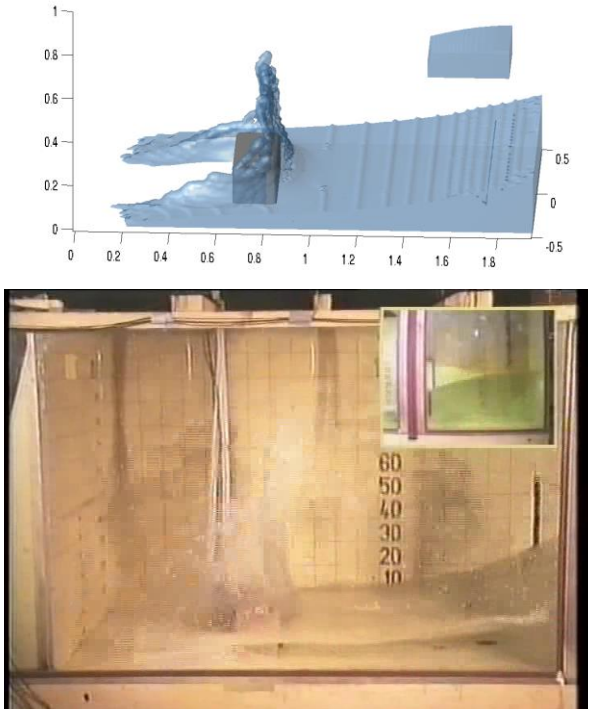

Figure 5.2.8 numerical and experimental free surface flow evolution from studies at MARIN, (Kleefsman et al., 2005).

Another feature which can be observed on the compressible simulation numerical results plot (Figure 5.2.7) is the high frequency damped oscillatory pressure fluctuation recorded just after the second impact peak. These oscillatory fluctuations are a consequence of air bubble(s) being entrained within the flow. Because the air is compressible these bubbles will contract and dilate rapidly thus applying a high frequency pressure wave to the wall. This pressure wave is transmitted through the incompressible liquid phase. As these bubbles migrate away from the impact interface and also escape through the free surface the amplitude of the pressure wave is damped in the current numerical simulation study. The oscillatory pressure fluctuations are discussed further in Section 5.3. The incompressible simulation results exhibit a much larger impact pressure than the compressible simulation when the fluid jet collapses at about 19 units non dimensional time. This could be attributable to the entrapped air bubble compressing in the compressible simulation (see Figure 5.3.3), thereby having a cushioning effect for the collapsing jet. In contrast the air phase cannot have this cushioning effect in the incompressible simulation thus yielding a higher impact pressure.

5.3 Numerical simulation results analysis

As previously discussed in Section 5.2 a total of 128 data sets have been obtained. This study will concentrate on two of these sets of data for further analysis. The first data set is from the 1mm X 1mm mesh resolution using the first order in time, first order in space equation discretisation scheme sampled a position P1 (Figure 4.2.1) The second data set is from the 0.5mm X 0.5mm mesh resolution using the second order in time, second order in space equation discretisation scheme again sampled at P1. We use a similar geometrical setup for our model as that used by Martin and Moyce, (1952).

5.3.1 First order in time, first order in space equation discretisation scheme results

The pressure variation as a function of time for both the incompressible air phase simulation and the compressible air phase simulation are shown on Figure 5.3.1. As discussed in Sections 4.2 and 4.6 atmospheric pressure is applied to both phases in the compressible simulation. Thus in order to facilitate a direct comparison between the compressible and incompressible pressure histories the value of atmospheric pressure is subtracted from the compressible simulation pressure record during post processing.

It can be observed that in general there is good agreement in the pressure trend results between the two simulations. However Figure 5.3.2 shows that between t = 0.5145 and t = 0.5895 a high amplitude oscillation is recorded in the pressure results for the compressible simulation. This is due to the entrapment of a large air pocket which occurs when the jet collapses as shown of Figure 5.3.3 (b). This air bubble has a cross sectional area of approximately 306 mm^2 which results in an equivalent spherical bubble of approximate radius 9.87 mm. Figure 5.3.3 shows the free surface evolution and corresponding pressure distributions. Figure 5.3.3 (a) and 5.3.3 (d) display the F function and pressure results respectively as the wave front impacts the wall at t = 0.207. This produces the first pressure peak on Figure 5.3.1. As the jet collapses and converges with the fluid below, a bubble is entrapped in the flow. This occurs at t = 0.5145 and yields the second pressure peak on Figure 5.3.1. The free surface geometry is shown on Figure 5.3.3 (b) with the associated pressure distribution displayed on Figure 5.3.3(e) The pressure gradient from the centre of the bubble across its boundary wall does not exhibit a large variation as the air cavity is just in the instant of being formed at this time step. The amplitude of the oscillating pressure signal is reduced in an underdamped manner until the oscillations are eliminated at approximately t = 0.5895 as shown on Figure 5.3.2. Figure 5.3.3(c) and 5.2.3(f) show the F function and pressure distribution at time t = 0.5895 respectively.

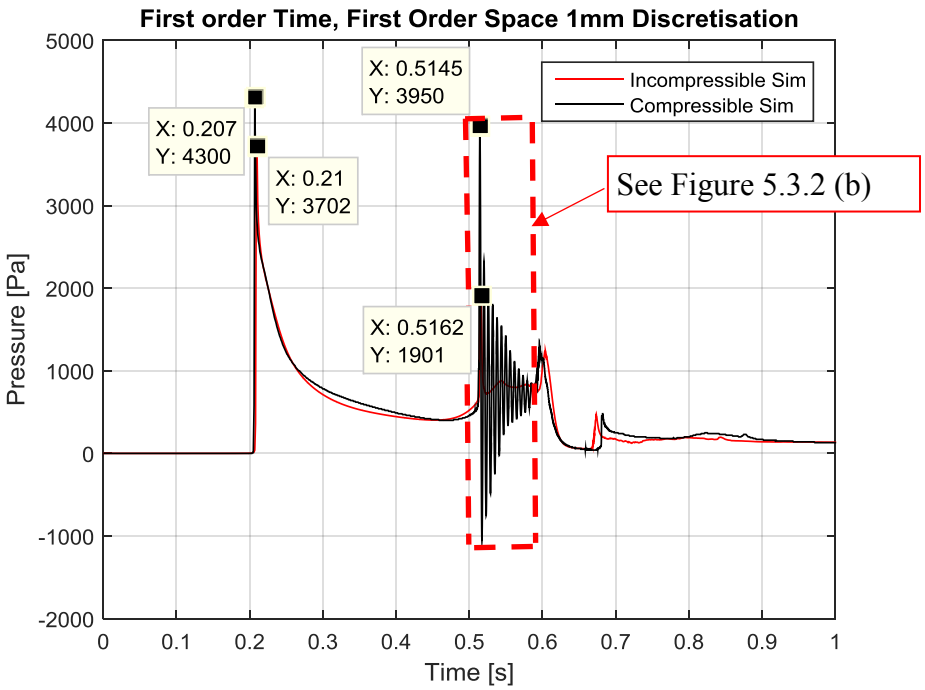

Figure 5.3.1 Pressure Vs Time for compressible and incompressible simulation recorded at P1

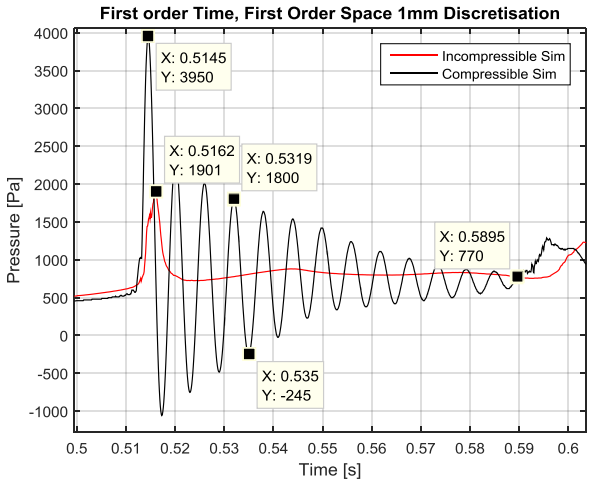

Figure 5.3.2 High amplitude pressure oscillation in compressible air phase model recorded at P1

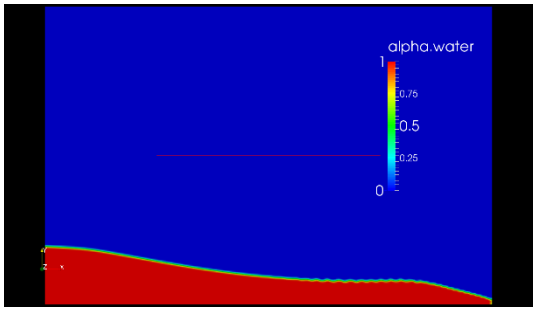

a. Free surface profile at t = 0.207 sec

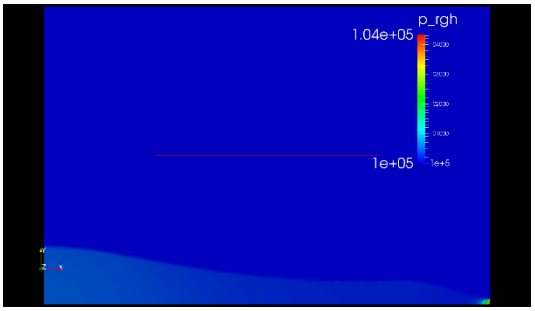

d. Pressure distribution at t = 0.207 sec

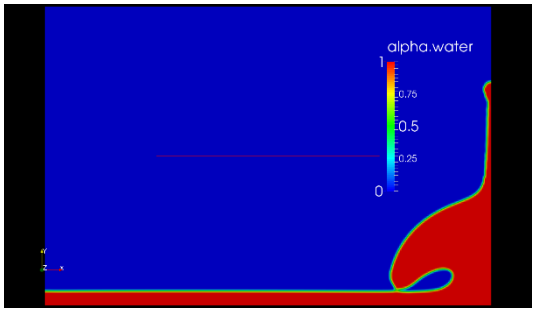

b. Free surface profile at t = 0.5145 sec

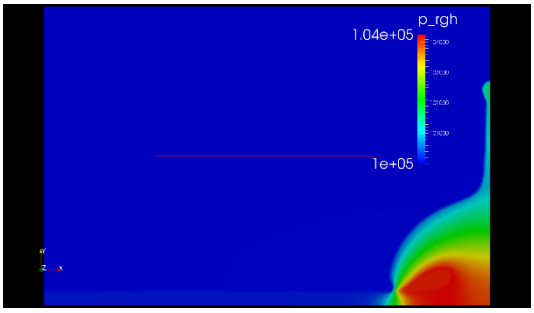

e. Pressure distribution at t = 0.5145 sec

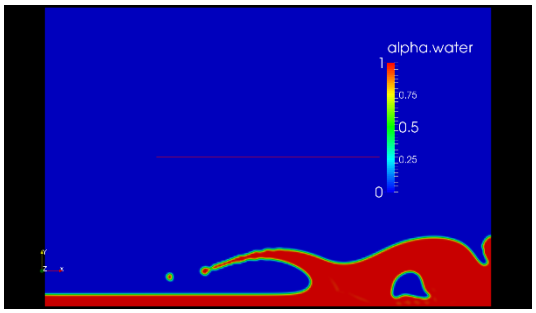

c. Free surface profile at t = 0.5895 sec

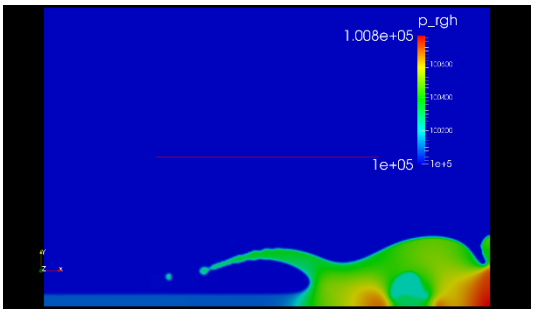

f. Pressure distribution at t = 0.5895 sec

Figure 5.3.3 Free surface evolution and associated pressure contour distributions for compressible simulation

The simulation time between $0.5145 < t < 0.5895$ for the compressible model is of significant interest to this study as the oscillatory pressures which occur within this time frame may be responsible for inflicting much damage on coastal protective structures. If these oscillations can be damped in a more effective manner fewer pressure impulses will be applied to the impact interface thereby reducing the damaging effect on the protective structure and increasing its design life duration. The behaviour of the entrapped air bubble must first be analysed to assess its influence on the observed pressure oscillation.

5.3.1.1 Frequency domain analysis

Firstly it must be ascertained that the oscillations are a direct consequence of the entrapped air pocket. To do this the pressure value within the entrapped air pocket is measured. This pressure should oscillate in a manner identical to the pressure oscillation recorded at P1. In a larger model a small time lag may be present as the resonant pressure within the bubble is transmitted through the liquid medium to point P1. The speed of a pressure wave in water is 1482 m/s. However this is a small scale model and the pressure wave induced by the bubble oscillation is transmitted through the water and registered at P1 almost instantaneously. The bubble edge radius is approximately 40mm from P1. Thus the pressure wave travels from the bubble to P1 in approximately 2.70×10^{-5} s. The time step sampling rate for this phase of the simulation is set to 0.0001s, which is not a high enough sampling rate to observe the time lag, therefore the pressure oscillations within the bubble and at P1 are in phase as shown on Figure 5.3.4. The amplitude of the oscillating signal from the pressure within the bubble is consistently larger than the pressure recorded at P1. This would also imply that the resonant contraction and expansion action of the entrapped bubble is the source of the pressure oscillation. The reduced amplitude of the pressure signal at P1 may be due to energy loss through the free surface, energy loss due to viscous effects within the liquid phase or energy loss due to surface tension effects at the bubble wall. The pressure oscillation within the bubble also persists for some time after the oscillations at P1 are damped, further supporting the argument that the oscillations emanate from the bubble.

From Figure 5.3.4 the pressure in the bubble can be seen to oscillate with a very regular frequency. The positive amplitude portion of the waveform measured inside the bubble represents contraction of the bubble whilst the negative amplitude of the waveform represents expansion of the bubble. This frequency of pressure oscillation can be compared with the adiabatic Minnaert (1933) resonant frequency given by

$$\upsilon = \frac{1}{2\pi a_b}\left(\frac{3\gamma P_0}{\rho}\right)^{0.5} \qquad (5.3.1)$$

where γ is the ratio of specific heat of a gas at constant pressure to that at constant volume, P_0 is taken to be the hydrostatic liquid pressure outside the bubble (assumed to be atmospheric pressure in this case) and ρ is the density of the fluid, and a_b is the radius of the entrapped bubble, (Leighton, 1994). It is assumed that the bubble is entrapped in an infinite domain of water. Whilst the analytic Equation (5.3.1) is applicable to spherical bubbles it has been argued that the oscillating frequency of non-spherical bubbles varies only slightly from the oscillating frequency of spherical bubbles (Strasberg, 1953).

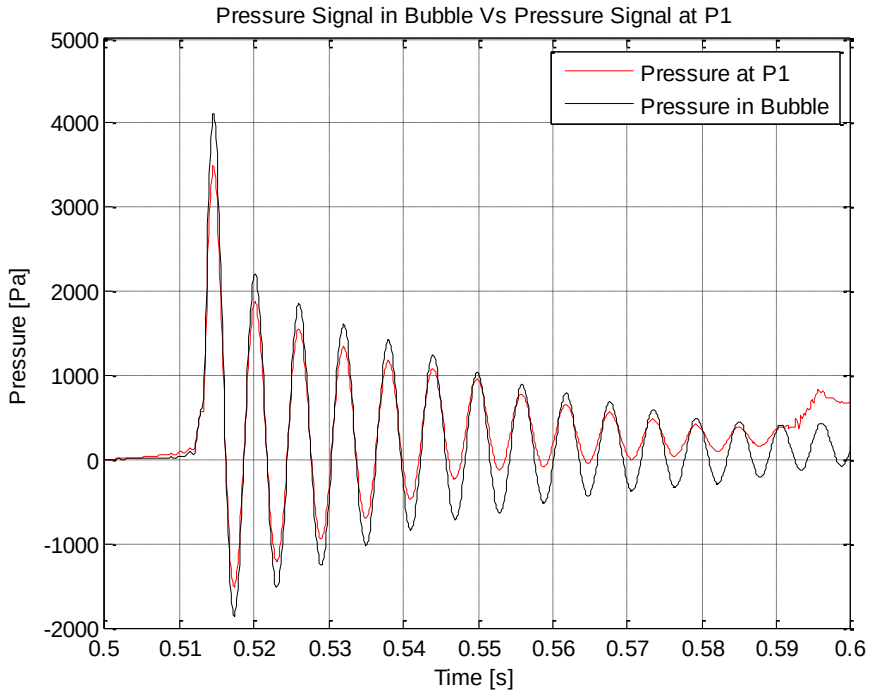

Figure 5.3.4 Pressure oscillations at the entrapped air bubble vs pressure oscillations at P1

The frequency is highly dependent on the volume of the bubble rather than its shape, (Strasberg, 1953). From their experimental research Hattori et al. (1994) developed the following alternative experimentally derived relationship between bubble size and oscillation frequency

$$f_{ap} = 180l^{-0.5} \qquad (5.3.2)$$

Where f_{ap} is the frequency of pressure oscillation and l is the bubble thickness or diameter in this case.

By applying a Fast Fourier Transform (FFT) to the simulation pressure signal recorded at point P1 in Figure 5.3.4 a dominant oscillating frequency of approximately 170 Hz was recorded as shown on Figure 5.3.5.

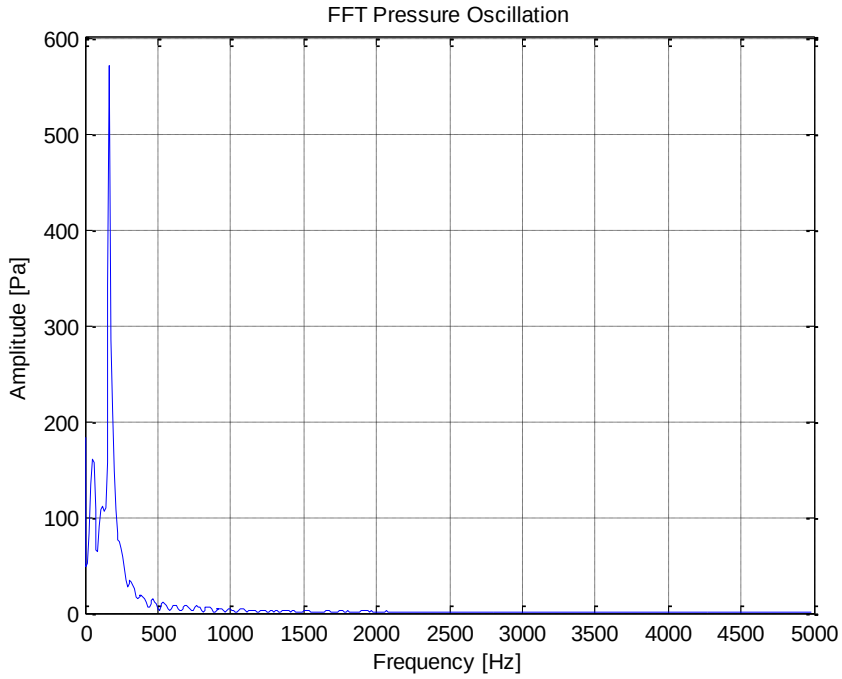

Figure 5.3.5 FFT of pressure oscillation

Table 5.3.1 summarises the oscillation frequencies computed by the various methods for a bubble having an equivalent diameter of 19.7 mm. Both the Minnaert resonance envelope and Hattori et al envelope for computing bubble oscillation are shown on Figure 5.3.6 along with the FFT computed oscillation frequency for this numerical simulation. Whilst the Minnaert analytic equation for oscillation resonance and the Hattori et. experimental results show good agreement at larger bubble diameters there is a large discrepancy when comparing the frequency of oscillation for smaller bubbles. This is shown on Figure 5.3.6. This may be due to small scale effects of bubble oscillation which the Hattori et al experiment setup could not capture. Nevertheless the results from our simulation agree well with both approaches.

Method	**Resonant Oscillating Frequency [Hz]**
Minnaert analytic equation	330
Hattori et al. experimental relationship	128
FFT	170

Table 5.3.1 Oscillation frequency values for 19.7mm diameter bubble

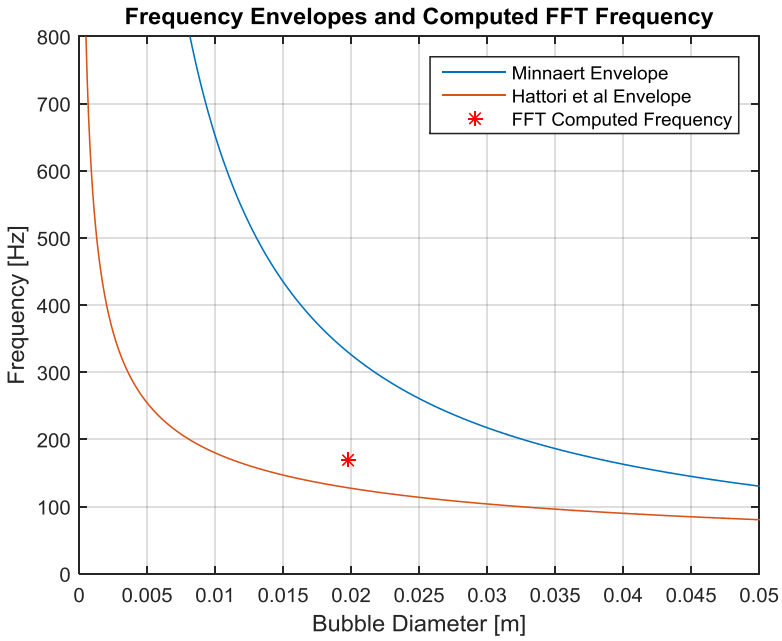

Figure 5.3.6 Frequency envelopes and computed FFT frequency

The pressure signals in Figure 5.3.4 are attenuated in an underdamped manner, i.e. the damping ratio is $0 \leq \zeta \leq 1$. The damping ratio can be calculated by applying a logarithmic decrement method to the amplitude of waves on the pressure plot. The logarithmic decrement is given by

$$\delta = \frac{1}{n} ln \frac{x(t)}{x(t+nT)} \tag{5.3.3}$$

Where n is any integer number, $x(t)$ is the signal amplitude at time t and $x(t+nT)$ is the peak signal amplitude of the wave at n periods away. This equation yields a logarithmic decrement value of 0.093 for the pressure signal measured at P1 on Figure 5.3.2. This value can then be used to calculate the damping ratio according to

$$\zeta = \frac{1}{\sqrt{1+\left(\frac{2\pi}{\delta}\right)^2}} \tag{5.3.4}$$

From Equation *(5.3.4)* a damping ratio of 0.015 is computed. The main sources of energy attenuation in a bubble oscillation pressure signal are due to thermal damping, radiation damping (through the emission of spherical sound waves) and viscous damping (Devin, 1959). Because the thermal effects due to phase compression in this simulation are negligible, thermal damping can be excluded as a main source of energy attenuation. Both the pressure signal measured at P1 and the pressure signal recorded inside the bubble are damped at approximately the same rate. However as the simulation proceeds the bubble migrates away

from the RHS wall. This would indicate that the position of the bubble relative to P1 is not a strongly influencing factor on the rate of damping. It is therefore likely that the reduction in the amplitude of the pressure wave both in the bubble and at P1 is due to viscous damping of the bubble wall membrane.

5.3.2 Second order in time, second order in space equation discretisation scheme results

The procedure outlined in Section 5.3.1 was repeated for the pressure response obtained from the 0.5 mm X 0.5 mm mesh resolution models (both incompressible and compressible) with second order temporal and second order spatial equation discretisation schemes. Figure 5.3.7 shows a comparison between the simulation pressure records for each model.

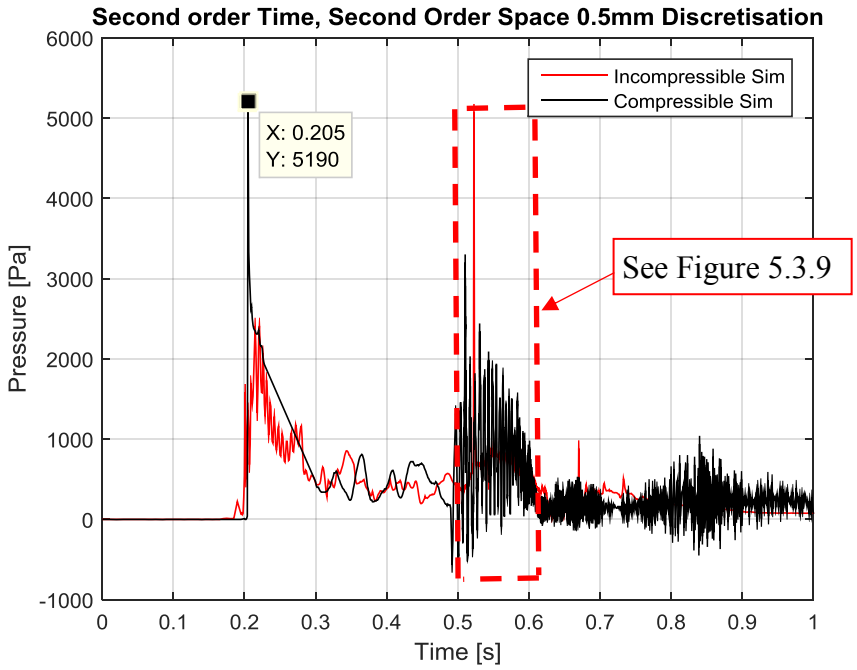

Figure 5.3.7 Pressure records for the second order time and space equation discretisation simulations

In this case there is some high frequency oscillations evident in the incompressible simulation pressure response both immediately before and just after first impact. Also of note is the much reduced impact impulse at approximately 0.205 seconds elapsed simulation time recorded for the incompressible model. These features require further discussion as outlined below.

Figure 5.3.8 (a) and (b) show the free surface profile for the incompressible model and the compressible model respecitvely at approximate wave imact time of t = 0.205, (c) and (d)

show the associated pressure distributions. In this case the pressure is monitored at P1 which is at 8mm above the bed of the numerical tank as in Section 5.3.1.

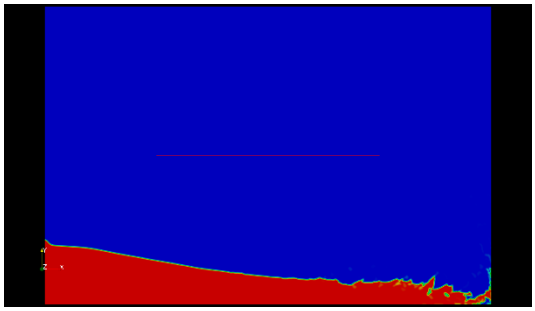

a. Incompressible model free surface profile at t = 0.205 sec

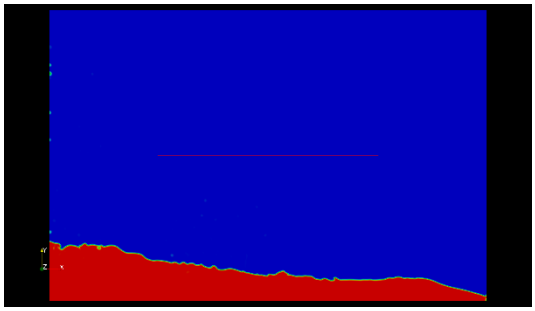

b. Compressible model free surface profile at t = 0.205 sec

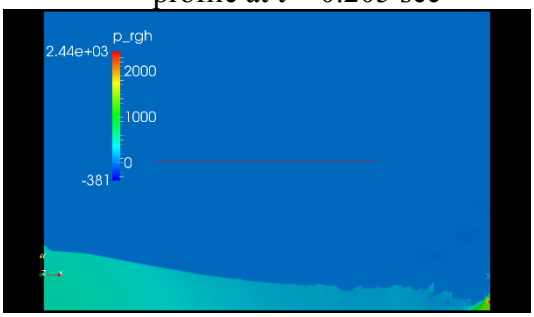

c. Incompressible model pressure distribution at t = 0.205 sec

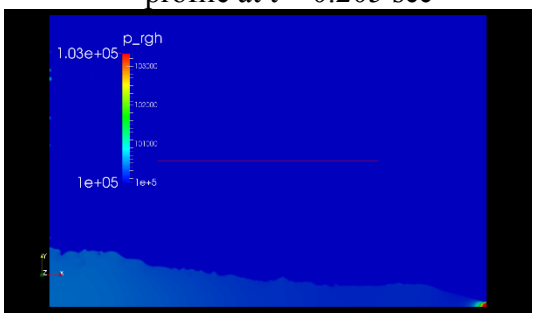

d. Compressible model pressure distribution at t = 0.205 sec

Figure 5.3.8 Free surface profile and pressure contour distribution comparison for incompressible and compressible simulations

In Figure 5.3.8 (a) the leading edge of the wave has already broken prior to impacting the wall. This results in some air entrainment at the wave front and an irregular profile. Consequently some of the wave impact energy is transferred to the wall through the impact of many smaller water droplets. In effect the leading edge of the wave splashes against the wall. Each droplet will result in a pressure impulse, thus giving rise to the oscillating pressure response observed for the incompressible simulation at impact as shown on Figure 5.3.7. Also the highest pressure recorded in the incompressible model occurs about 10mm above P1. In contrast the profile at the leading edge of the flow in the compressible simulation remains intact. This results in the pressure response exhibiting a single impact pulse with a higher energy concentration focussed on P1.

As noted in section 4.2 the atmospheric pressure value in the incompressible simulation is neglected. However in the compressible simulation this value is set to 100kPa. This isobaric pressure may have an influence on the wave leading edge stopping it from breaking before impact in the compressible simulation.

From Figure 5.3.7 there is a good general agreement in pressure trends between the incompressible and compressible simulations. High amplitude oscillations are again recorded in the compressible simulation, most obviously when the jet collapses. However in this case there are two further distinctive time periods in which these oscillations occur, the time period from 0.6-0.7 sec, and 0.75 -0.9 sec. Only the oscillations registered when the jet collapses between 0.475-0.6 seconds will be investigated here. Figure 5.3.9 shows a magnified view of pressure response measured at P1 for this time period.

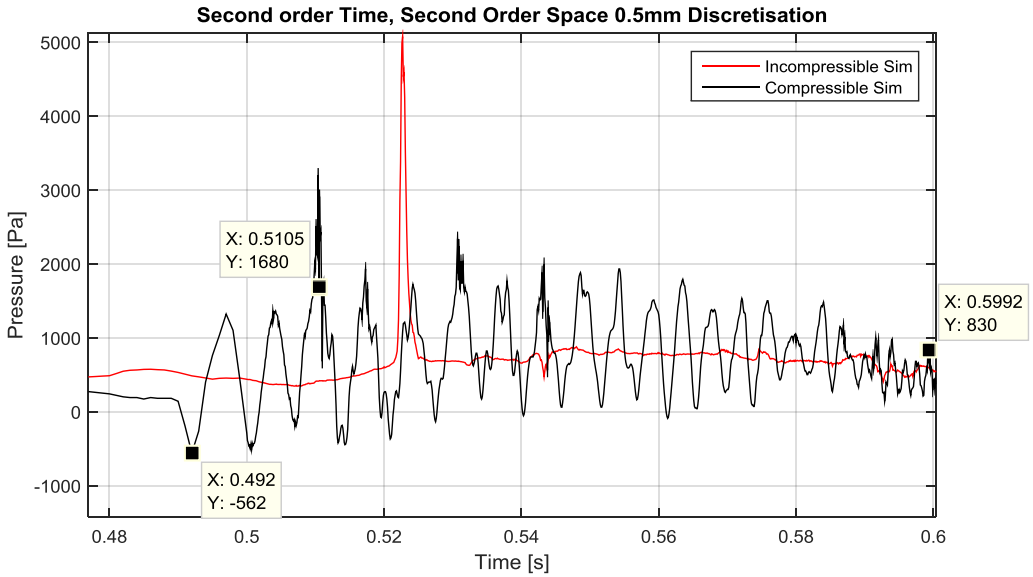

Figure 5.3.9 Pressure response for compressible simulation, temporal range 0.475 sec-0.6sec

Once again these pressure oscillations exhibit a reasonably regular frequency and their onset coincides with the entrainment of air within the liquid phase. Figure 5.3.10(a) shows the free surface profile at 0.492 sec elapsed simulation time for the compressible model. It can be seen that a large, irregularly shaped air void is at the instance of being entrapped. The corresponding pressure distribution (Figure 5.3.10(d)) shows this area to be experiencing low pressure relative to the majority of the region occupied by the water phase, this can be correlated to the low pressure observed at point P1 on Figure 5.3.9.

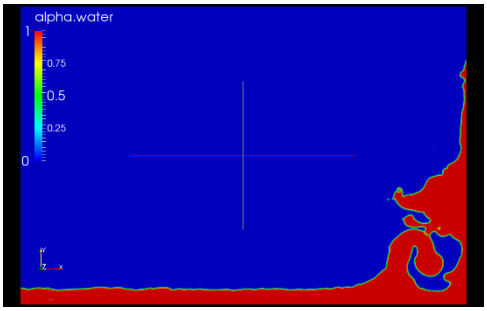

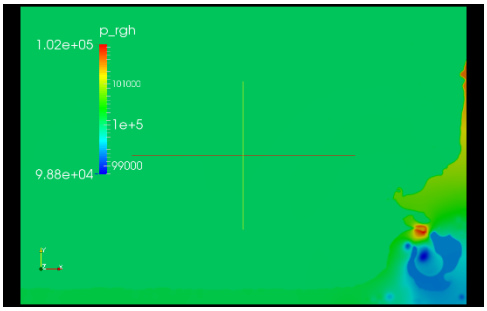

a. Free surface profile at t = 0.492 sec

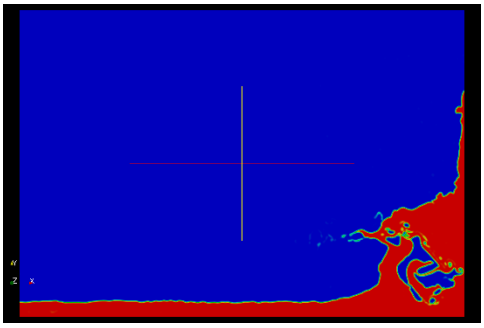

d. Pressure distribution at t = 0.492 sec

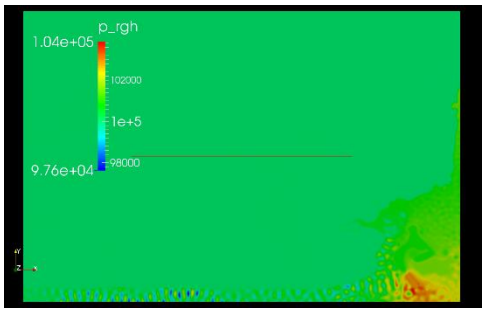

b. Free surface profile at t = 0.5105 sec

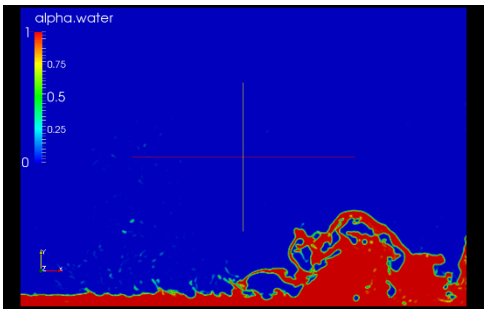

e. Pressure distribution at t = 0.5105 sec

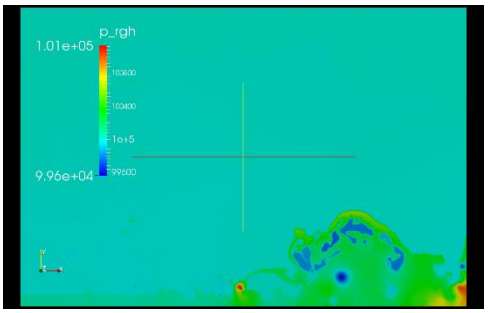

c. Free surface profile at t = 0.5895 sec

f. Pressure distribution at t = 0.5895 sec

Figure 5.3.10 Free surface evolution and associated pressure contour distributions as the water jet collapses

The entrainment of this large bubble coincides with the onset of the pressure oscillations. Because the temporal and spatial equation discretisation schemes are second order and also a higher mesh resolution is applied to the model the flow profile is more accurately represented than the model in Section 5.3.1. Then as the water jet collapses the free surface evolution is more chaotic than in the case of the first order spatial and temporal equation discretisation scheme with 1 mm mesh resolution as was described previously, this is clear if one compares Figure 5.3.3(c) with Figure 5.3.10(c). It can also be noticed that the pressure signal in Figure 5.3.9 is more irregular than that displayed in Figure 5.3.2. This signal irregularity may arise due to the fact that the frequency of oscillation and amplitude of pressure oscillation of each of the smaller entrained bubble is dependent on the individual bubble's size. Figure 5.3.10 (b) shows the free surface profile at 0.5105 seconds, it can be seen that the large bubble in figure 5.3.10 (a) has collapsed to form two main air pockets and some additional smaller bubbles. If one compares this free surface profile with the pressure response shown in Figure 5.3.9 additional higher frequency oscillations are recorded at this time instance. Therefore smaller entrained bubbles exhibit higher pressure frequency oscillations and lower amplitude of pressure oscillation. As the simulation proceeds there is some damping of the pressure signal (Figure 5.3.9) most noticeably from about 0.59-0.6 sec.

This damping is not as pronounced as that which occurred in the first order temporal and spatial discretisation model investigation. This may be explained through the more chaotically evolving flow profile with the constant formation of new bubbles and escape of pre-existing bubbles through the fluid free surface.

5.3.2.1 Frequency domain analysis

Figure 5.3.11 shows the FFT of the pressure signal for the time period 0.5 to 0.6 seconds. When compared to Figure 5.3.5 it can be seen that there are many additional constituent frequency peaks with varying levels of amplitude.

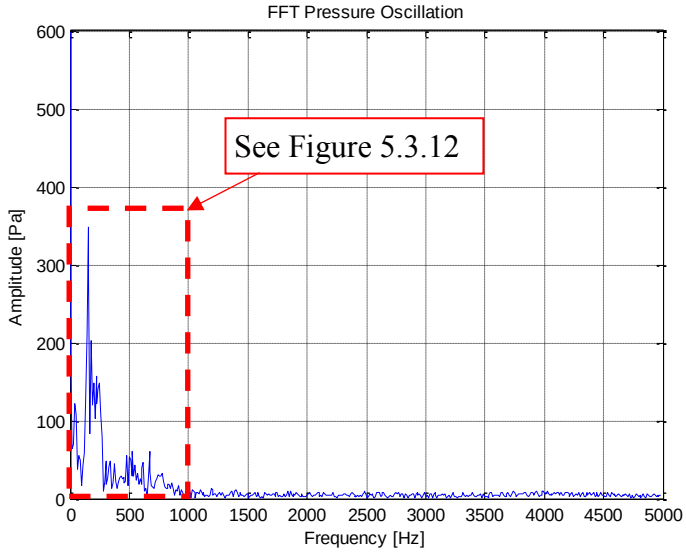

Figure 5.3.11 FFT of pressure oscillation for compressible second order temporal and spatial equation discretisation scheme

The study will concentrate on those frequencies with the largest amplitude which compose the FFT as shown on Figure 5.3.12. There are 5 main frequencies comprising the signal, these occur between 100 and 300 Hz. Table 5.3.2 shows these frequencies and their associated amplitudes. These 5 frequencies should correspond to the resonant frequency of oscillation of the 5 largest bubbles formed between 0.5-0.6 seconds simulation time (larger bubbles oscillate at a low frequency but with a large amplitude). The flow during this time period is very chaotic and the entrained bubbles are constant coalescing, separating and escaping through the free surface, however the five largest bubble sizes measured during the simulation time period 0.5-0.6 seconds are shown in Table 5.3.3. Bubble 2 and 3 form mainly through the separation of bubble 1. Bubble 4 forms through the fragmentation of bubble 2 and bubble 5 forms as bubble 3 merges with some smaller bubbles and is also fragmented. This sequence of free surface flow development is shown on Figure 5.3.13 a-d.

Peak	Frequency [Hz]	Amplitude [Pa]
1	150	348
2	180	203
3	200	148
4	219	157
5	252	148

Table 5.3.2 Main frequencies of interest in pressure signal at P1

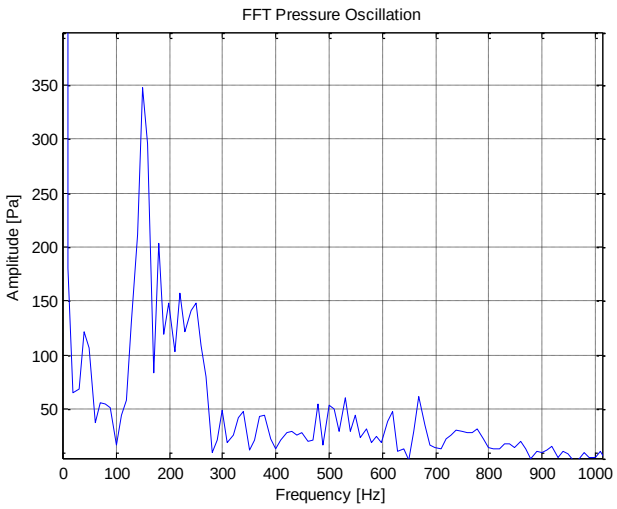

Figure 5.3.12 Main frequencies of interest.

Bubble	Area $[mm]^2$	Equivalent radius [mm]	Time which bubble forms [sec]	Time which bubble size is modified [sec]	Lifetime duration of bubble [sec]
1	1324.5	20	0.492	0.5045	0.0125
2	787	15.8	0.5045	0.5131	0.0086
3	474	12.3	0.5045	0.5231	0.0126
4	483	12.4	0.5131	0.5341	0.0210
5	489	12.5	0.5231	0.5431	0.0260

Table 5.3.3 Bubble formation observed in simulation

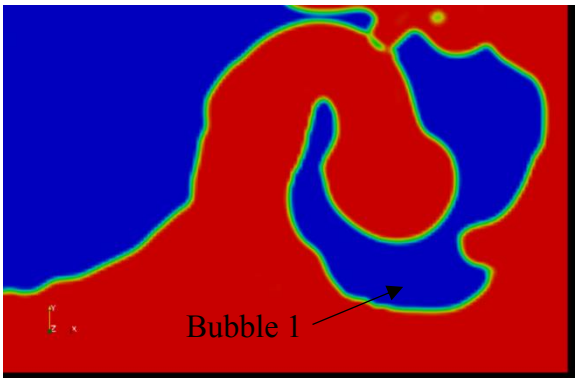

a. Formation of bubble 1

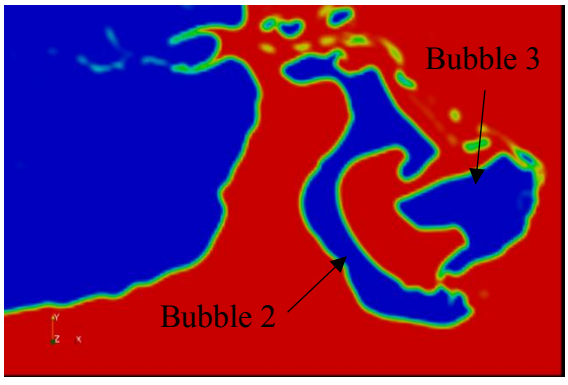

b. Formation of bubbles 2 & 3

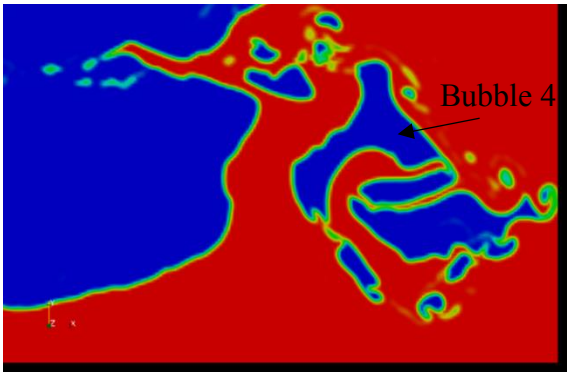

c. Formation of bubble 4

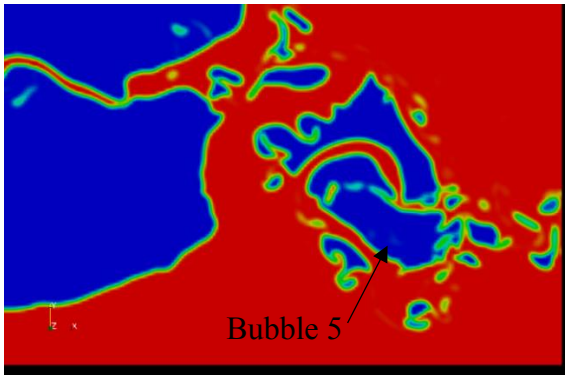

d. Formation of bubble 5

Figure 5.3.13 Fragmentation of entrapped air pockets and formation of smaller bubbles within the flow

Using the five highest amplitude frequencies extracted from the FFT as shown in Table 5.3.2, the analytically predicted entrained bubble sizes calculated using the Minnaert resonance Equation *(5.3.1)* and the Equation *(5.3.2)* formulated by Hattori et al. (1994), are shown in Table 5.3.4.

By comparing the values in Table 5.3.3 with those in Table 5.3.4 it can be seen that there is very good agreement with observed frequency of oscillation for peak 1 and peak 5 on the FFT (150Hz and 252Hz) and the observed equivalent radius of bubble 1 (20 mm) and bubble 5 (12.5 mm) when compared to the Minnaert analytic equation values of 21.7mm and 12.9 respectively. The equation developed by Hattori et al. (1994), consistently underestimates the bubble size. Figure 5.3.14 compares the Minnaert envelope, the Hattori envelope and the observed entrained bubble diameters and the associated resonant frequencies.

Peak	**Minnaert Equation**		**Hattori et al equation**	
	Radius of bubble [mm]	Area of bubble $[mm]^2$	Radius of bubble [mm]	Area of bubble $[mm]^2$
1	21.7	1479	5.5	95
2	18.1	1029	5.0	79
3	16.3	835	4.7	69
4	14.9	697	4.5	64
5	12.9	522	4.2	55

Table 5.3.4 Predicted bubble size according to Minnaert and Hattori equations

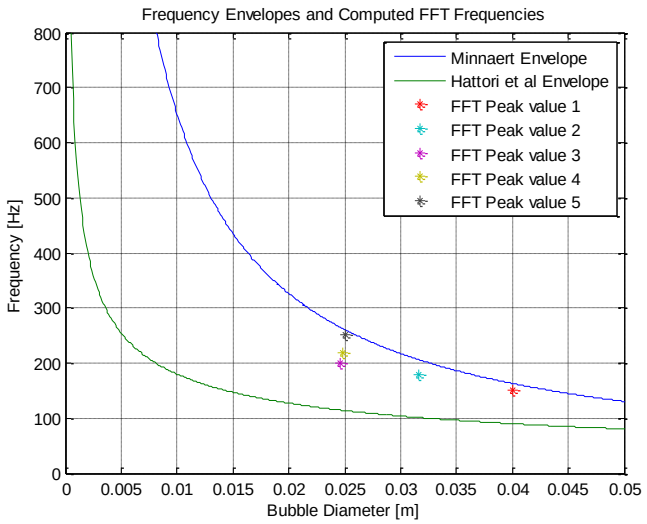

Figure 5.3.14 Analytic frequency curve, experimental bubble frequency curve and simulated bubble oscillatory frequencies

5.3.2.2 Pressure oscillation frequencies recorded within air void

The next stage of the analysis consists of recording the time varying pressures observed within entrapped air pockets during the simulation. For this part of the study two locations, a and b were selected as shown on Figure 5.3.15. These points are located such that a bubble transits across each position during the simulation. It was anticipated that the observed frequency of oscillation and the amplitude of the pressure signal should alter during the time period which the point was located within an air bubble. Figures 5.3.16 (a) and 5.3.16 (b) show the pressure signals measured at each of the points for the time period 0.5-0.6 seconds, also recorded on these graphs is the pressure signal measured at P1. Figure 5.3.16 (c) and 5.3.16 (d) show the FFT of the pressure signal recorded at a and b respectively along with the FFT of the pressure signal measured at point P1 for comparison. Again it is anticipated that those points which are transited by progressively smaller air pockets should exhibit higher constituent frequencies which make up the pressure signal.

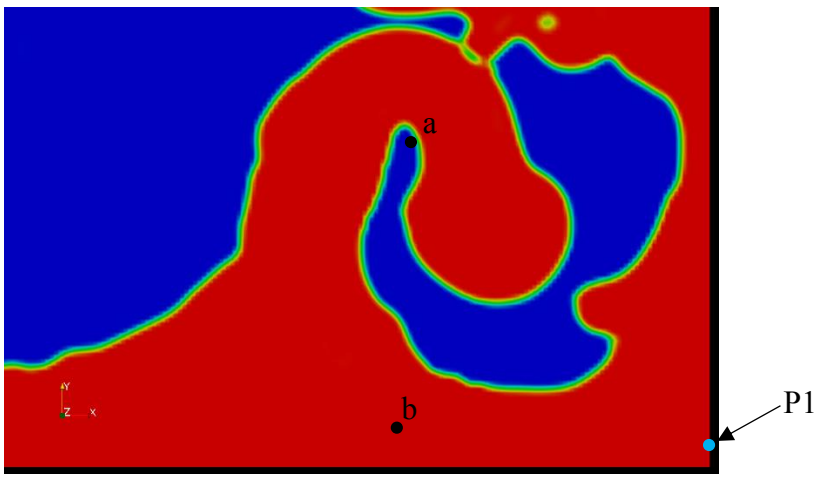

Figure 5.3.15 Flow profile at 0.492 sec. with pressure monitor locations a and b indicated

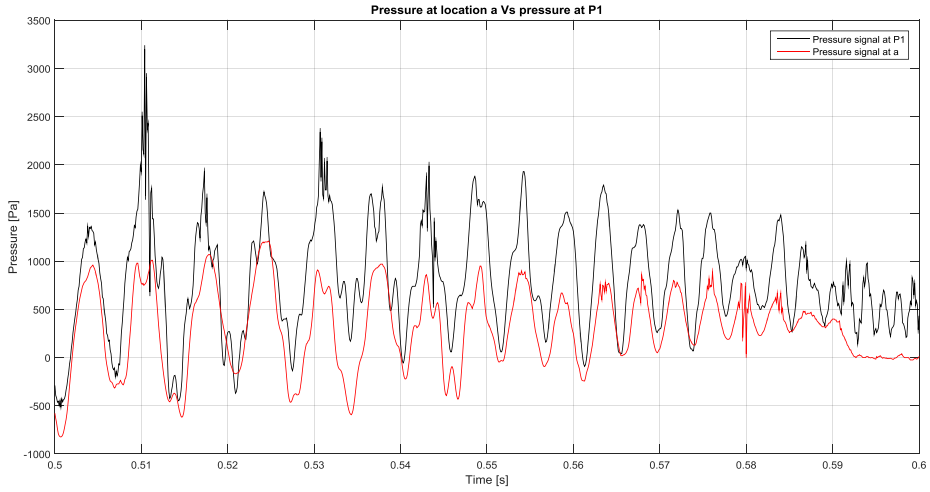

a. Pressure response at a (red)

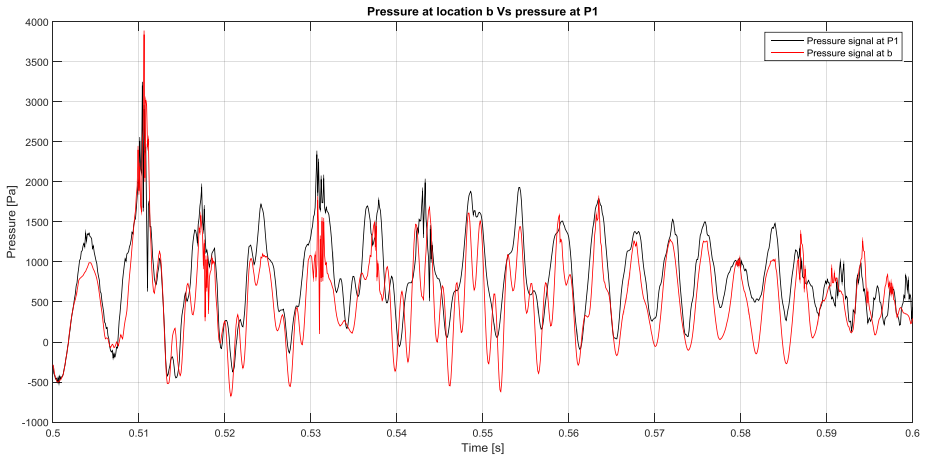

b. Pressure response at b (red)

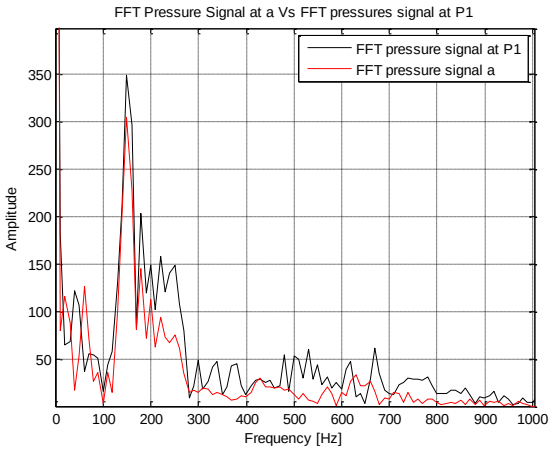

c. FFT of pressure signal at a

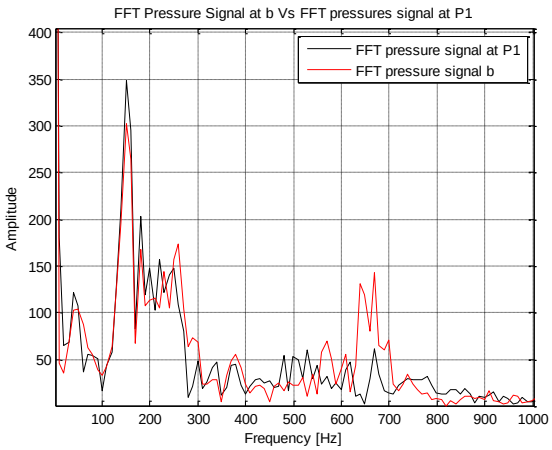

d. FFT of pressure signal at b

Figure 5.3.16 Pressure signal at locations a and b and FFT of pressure signal at a and b

Initially point a is located such that it is positioned within bubble 1 which is formed when the jet collapses and point b is located within the water phase. Comparing Figures 5.3.16 (a) and 5.3.16 (b) it is shown that the pressure signal measured at point b matches the pressure

signal measured at P1 better. As point a is contained within the formed bubble there may be some loss of energy as the pressure wave transmits through the air phase which is compressible. In contrast, the incompressible water phase may conserve the energy of the pressure wave more effectively and the pressure measurement at point b may reflect this. As the simulation progresses bubble 1 bifurcates and point a lies within bubble 2. This happens at approximately 0.5045 sec. There is a slight alteration to the pressure signal at this time. From 0.5095 to 0.5111 seconds bubble 2 loses some of its volume as some smaller bubbles break away. This is reflected as a higher frequency, small amplitude oscillation on figure a around 0.51 sec. Point a is located within the liquid phase from about 0.5181 to 0.5261 and a smooth pressure oscillation results. From 0.5261 to 0.5371 seconds point a is located within bubble 5, the amplitude of oscillation reduces slightly and the oscillation frequency approximately doubles. This supports the data presented in Table 5.3.3 in which the volume of bubble 5 is approximately 63% of bubble 2. Point a is again within the liquid phase from 0.5371 to about 0.5411. From 0.5411 a is situated in a smaller bubble until 0.5481. During this time period when the oscillating frequency increases noticeably. From 0.5481 until about 0.5630 point a is located in the liquid phase on the radial edge of a bubble. Finally point a is located within a thin jet of the liquid phase from 0.5630 until 0.5961 seconds at which time the free surface crosses point a and the pressure drops to zero (neglecting the effects of atmospheric pressure). Also during this time period the amplitude of the pressure oscillations decreases in an under-damped manner.

Point b is located within the liquid phase from 0.5 sec until 0.5451 sec. During this time period the pressure response at b closely resembles the pressure record at point P1, however the amplitude of the signal at b is slightly reduced. From approximately 0.5460 to 0.5550 an air void crosses point b. The pressure signal frequency increases during this time. After 0.5550 point b is located the within the fluid phase and the pressure signal once again closely resembles the pressure response recorded at P1. This supports the suggestion that the presence of air voids are the predominant influence on the frequency of oscillations observed in the pressure signal.

From examination of the FFT of the pressure signal at point a, the five dominant frequencies are shown on Table 5.3.5. Peaks 3, 4 and 5 correspond with the three largest amplitude frequencies observed in the pressure signal at point P1. The component frequencies at 20 Hz and 60 Hz are also the most dominant signals within the pressure response measured at a. Component signals with frequencies greater than about 280 Hz do not feature strongly in the pressure response signal measured at a.

Peak	Frequency [Hz]	Amplitude [Pa]
1	20	116
2	60	127
3	150	304
4	180	145
5	200	112

Table 5.3.5 Dominant frequency components in pressure signal at point a

The five frequency peaks with the largest amplitudes (obtained from the FFT) occurring in the signal recorded at point b are shown in in Table 5.3.6. It can be seen that higher frequency oscillations (most notably between 640 Hz and 700 Hz) feature strongly in the pressure signal recorded at point b. This can be explained by the small entrained air pocket transiting across point b between 0.5460 and 0.5550 seconds simulation time.

Peak	Frequency [Hz]	Amplitude [Pa]
1	150	302
2	180	168
3	230	144
4	260	174
5	670	143

Table 5.3.6 Dominant frequency components in pressure signal at point b

It should be noted that as the simulation progresses, the flow field for both phases transitions into an increasingly chaotic system with some coalescence, but mainly fragmentation of the entrapped air pocket. These smaller bubbles contribute high frequency, low amplitude components to the oscillatory pressure signal.

Chapter 6

Porous structure characterisation and hydraulic conductance

It has long been known that fluid flow in porous media depends on a number of characteristics including porosity, tortuosity, interstitial surface area, solid phase distribution, flow Reynolds number, permeability etc. (Matyka et al., 2008). Many of these parameters are interdependent and by modifying the morphology of the solid material phase one or all of these characteristics may change. In this chapter some of these features of porous media are examined and previous studies which attempt to quantify them and investigate their correlation are reviewed.

6.1 Porous media classification and description

A porous sample in its loosest definition is a material composed of a certain solid volume which contains a proportion of distributed void space. Thus porosity is defined as the fraction of the bulk volume of the sample which is occupied by pore or void space (Dullien, 1992). Porosity can be used as 3 dimensional parameterisation measure for the morphology of the porous structure. Civan (2011) defines porosity mathematically as:

$$\Phi = \frac{\sum_{j \neq s} \Delta V_j}{\Delta V_b} \qquad (6.1)$$

where ΔV_b is the bulk volume of the sample or the total volume occupied by all phases, ΔV_j is the volume occupied by the j'th phase and s denotes the sum of the solid phases forming the porous matrix.

In macroscopic terms according to the classification system of Brewer (1964), this is the fractional volume of a sample which can be occupied by a fluid, either wetting or non-wetting.

Bear (1988) provides a more onerous characterisation of a porous media which suggests that the multiphase matrix must satisfy certain conditions such as level of void space interconnectedness, lower bound limits on interstitial surface areas and uniformity in phase distribution as discussed earlier in Section 2.5. In this study the porous topologies incorporated into the CFD model satisfy the stringent definition as outlined by Bear (1988). Nevertheless other researchers may subscribe to varying definitions of a porous medium and it is a term which is still couched in ambiguity as there is no complete consensus on limits for any of the above conditions.

The study of porosity encompasses many fields of research and each has its own limiting definition on the length scales of porous assembles. It is therefore important at this early point to clearly define the scales at which this porous media analysis is undertaken. For example the International Union of Pure and Applied Chemistry (IUPAC) imposes limits for microscopic, mesoscopic and macroscopic ranges when analysing porous materials. A mesoporous material is one which contains pores with diameters of between 2 and 50 nm and microporous and macroporous materials lie outside these respective ranges. However, the porous samples used in this study all contain voids much larger than 50nm. Therefore using guidelines according to stringent unit measurement limits is not applicable in this investigation. The limit scales must then be established with direct reference to the materials under scrutiny. We use a unit independent method to establish that our sample is in the macroporous scale as presented by Dullien (1992). In his study the lower limiting scale of a macroscopic porous medium sample is that which "may be defined by a smooth porosity variation as a function of the sample volume", (see Figure 6.1.1 below).

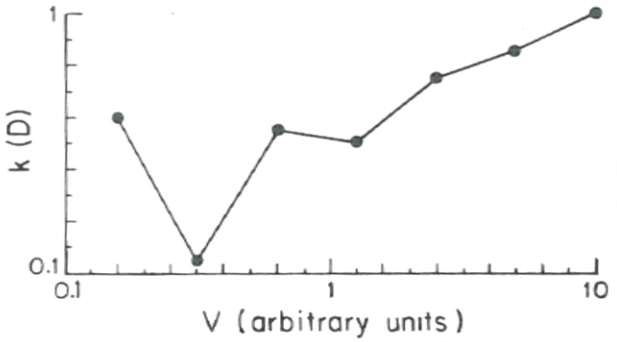

Figure 6.1.1. Illustration of the definition of macroscopic porous medium, (Dullien, 1992)

In Figure 6.1.1, $k(D)$ represents the permeability and V is a volumetric measure of a sample. As the volumetric sample size reduces the permeability is measured over a smaller number of pores and eventually the permeability is no longer statistically independent of the volumetric sample size, either converging on a single pore or on a single solid phase element. At this point we have transitioned into the microscopic scale range. This manner of defining

the limiting macroscopic scale closely resembles the definition of a representative elementary volume (REV) proposed by Bear (1988). The concept of an REV is discussed further in Section 6.5.1.

Porous media may be classified as random or ordered depending on the layout of the voids or the distribution of constituent particles forming the solid matrix within the sample. Random porous materials such as limestone, wood, sandstone etc. occur most frequently in nature. These materials are usually more topologically complex than ordered materials. Ordered porous materials are increasingly finding applications in areas ranging from microelectronics to medical science (Davis, 2002). These materials are usually synthetically manufactured and include zeolites, carbon nanotube and other such material in which the material microstructure is modified or designed, often at the nanoscale.

The morphology of a sample may also be further spatially classified as isotropic or anisotropic, homogenous or heterogeneous, or combinations thereof (see Figure 6.1.2 below). In this study a series of ordered, homogenous, isotropic and also homogenous anisotropic porous structures generated from spheres on varying lattice layout are investigated followed by an examination of a series of highly complex stochastically generated disordered fibrous porous structures.

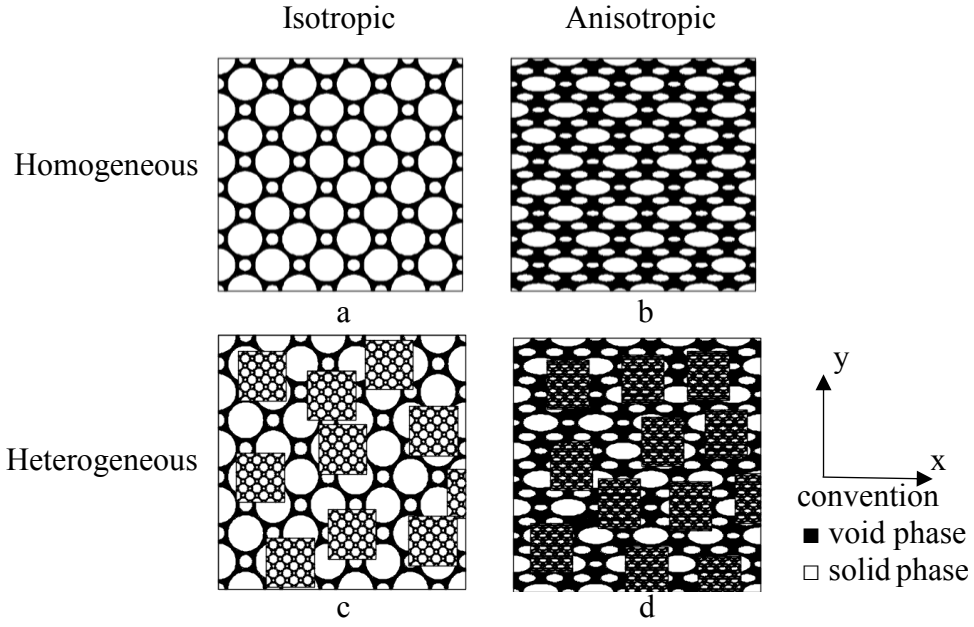

Figure 6.1.2. Types of porous media

Figure 6.1.2 displays various porous media morphologies for an ordered two dimensional porous sample. Figure 6.1.2(a) is both homogeneous and isotropic; the properties of the sample are the same in both the x and y directions, also the distribution of the solid phase is uniform. In 6.1.2(b) the distribution is again uniform, however the sample will have a higher permeability in the x direction as flow streamlines will be less tortuous in this direction, and

thus it is anisotropic. Figure 6.1.2(c) exhibits a heterogeneous isotropic sample. The material is heterogeneous because the distribution of the solid phase is not uniform and contains higher density isolated pockets of solid particles. Heterogeneities in porous media may be defined as a local variation in the pore structure. If these local variations are sufficiently randomly distributed within the sample the material may still behave in an isotropic manner. Figure 6.1.2(d) displays a sample which is both heterogeneous and anisotropic. The above Figure 6.1.2 demonstrates the effects of homogeneity, and isotropy for an ordered material. However the same principals can be applied to a random porous material if the phases are sufficiently stochastically distributed.

The pores within a structure can be classified into effective pore space or isolated pore space. Effective or interconnected pore spaces are those voids which can conduct fluids from one surface of the sample to another surface. Isolated pore spaces are those pores which are either dead end pores of closed pores which do not have a surface opening and therefore cannot contribute to the transport of fluid through the porous sample. A void chamber within a porous structure which is connected to void channels is termed a vugg. The void regions which connect these vuggs are termed pore throats. Figure 6.1.3 shows a flow path thorough a vuggy porous media (Asquith, 1985). Figure 6.1.4 taken from the Recommendations for the characterization of porous solids (Rouquerol et al., 1994) describes the various types of voids within a porous sample.

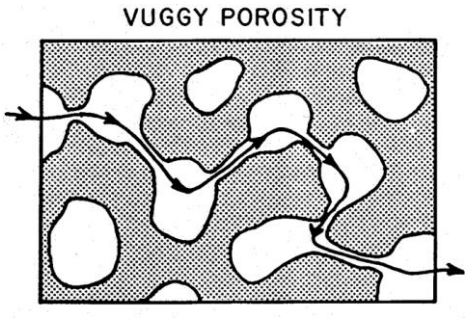

Figure 6.1.3. Flow through vuggy porous media (Asquith, 1985).

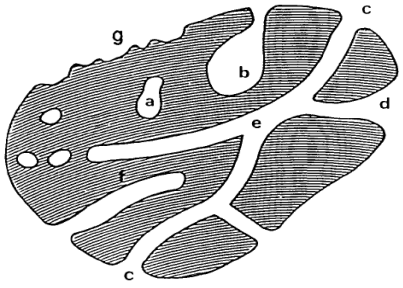

Figure 6.1.4. Cross section through a porous sample showing various types of voids (Rouquerol et al., 1994).

In Figure 6.1.4 above the voids a, b, and f are isolated pores. These cannot contribute to the transport of fluid through the structure. Void paths c to e to c, c to e to d and d to e to c are effective pore spaces as they are continuous through the sample. However there is also a pore space emanating from the vugg at location e which is a dead end. Thus even for this trivial example there are a number of flow paths available.

Whilst the porosity expresses the fractional volume of void space and solid matter contained within a sample, the distribution of both the isolated and the interconnected pores sizes remains a more obscure problem. Additional characteristics of the porous sample must be investigated to determine and categorise the structural morphology of the void space. Tortuosity, surface area and permeability are further parameters which can be used to describe the distribution of the pores or solid phase matrix.

6.2 Tortuosity

Tortuosity is an inherent characteristic of a porous media morphology which in general terms can be described as a ratio of the distance traversed by a fluid element between two fixed points to the straight line distance joining those two points as shown in Figure 6.2.1 (Brus et al., 2014). Tortuosity can be calculated according to:

$$\tau = \frac{L_e}{L_s} \qquad (6.2.1)$$

Where L_e and L_s are shown on Figure 6.2.1.

Whilst there has been a large body of academic research presented on the subject of tortuosity, there is no consensus for a single precise definition of tortuosity. To date a number of different measurements of tortuosity have been advanced for different applications. For example Ghanbarian et al. (2013) in their review paper describe geometric tortuosity, hydraulic tortuosity, electrical tortuosity and diffusive tortuosity.

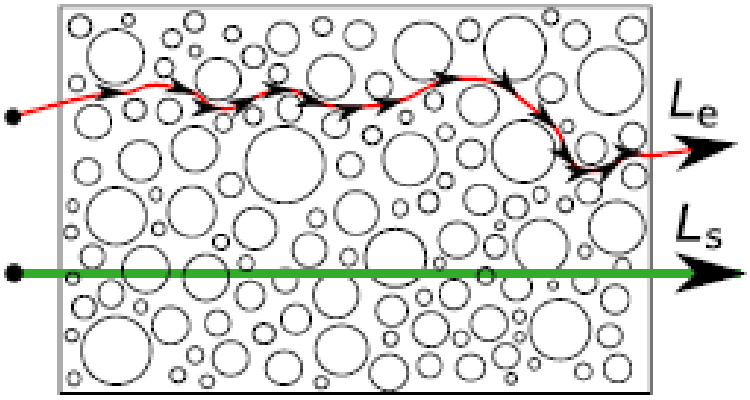

Figure 6.2.1 Tortuosity (Brus et al., 2014)

This difficulty in achieving a unanimous characterisation for tortuosity may be twofold; With the exception of very few materials, e.g. metals, dense rocks and some plastics (Dullien, 1992), most material exhibit porous behaviour to varying degrees at multiscale levels from microscopic through to macroscopic scale. The parameters which govern the tortuosity may vary dramatically within a single material at different scale lengths thus effecting the observed tortuous transport path length. For example a hydrologist may be interested in the transmissive porosity of an aquifer stratum at microscopic levels but a petroleum engineer may be more concerned with developing a network of macroscopic underground porous fissures to allow hydrocarbon accumulations to flow into a drilled well system. In the former case multiphase interfacial parameters such as capillary pressures, surface tension effects and wall friction coefficients may all contribute an important role in the flow rate through the stratum and in the latter case these effects may not warrant consideration due to the bulk of the flow being conveyed through larger fissures where wall friction, capillary and free surface effects are not the limiting constraints on the flow rate. Then, in the case of the hydrologist the hydraulic or streamline tortuosity may be important whereas the geometric tortuosity will be of concern to the petroleum engineer. See Figure 6.2.2 for a comparison between hydraulic and geometric tortuosity.

Secondly the structure of these porous materials can take many forms, and the tortuous paths can vary from being comparatively simple to being highly complicated and sinuous. For instance the porous structure of natural materials such as wood can be somewhat homogenous and anisotropic and in this case the tortuosity can be relatively simply described by reducing it to a model consisting of a bundle of unidirectional capillary tubes. In contrast a material may be much more complex and disordered having multidirectional interweaving fibrous filaments as evidenced within some natural filter material or in paper products for example. Then, the material topology is much more difficult to define and the parameters which can be used to describe the tortuous nature of interconnecting porous voids can be very difficult to determine from the physical sample. In the current study the void throats between the solid particles are relatively narrow such that the flow streamlines are seen to be influenced by the surface of solid phase material in the CFD model.

However, even with the tortuosity scheme specified there may still be some ambiguity in its measurement. Take for example the case of fluid flow through a porous medium consisting of sphere packing on a regular cubic lattice as shown of Figure 6.2.3 (Clennell, 1997) and further analysed in Section 7.1.1. Some of the streamlines will follow a straight line vector path whereby they pass through the centroid of the void spaces having a value of $\tau_{min} = 1$

(Figure 6.2.3 streamline at a), whilst others will closely follow the contours of the solid phase exhibiting a more tortuous flow path with an approximate value of $\tau_{max} = 1.57$ (Figure 6.2.3 streamline at b). For any porous morphology the value of τ_{min} can be determined either through numerical simulations or through experimental means if enough 3D information is available (Bernabe, 1991). It is however much more difficult to determine a value for τ_{max} especially where there are diverging and converging flow path networks or where dead end pores may cause the streamlines to form into eddies in which case the tortuosity may be indeterminate (Clennell, 1997). In this study the minimum tortuosity value is extracted from the numerical simulations.

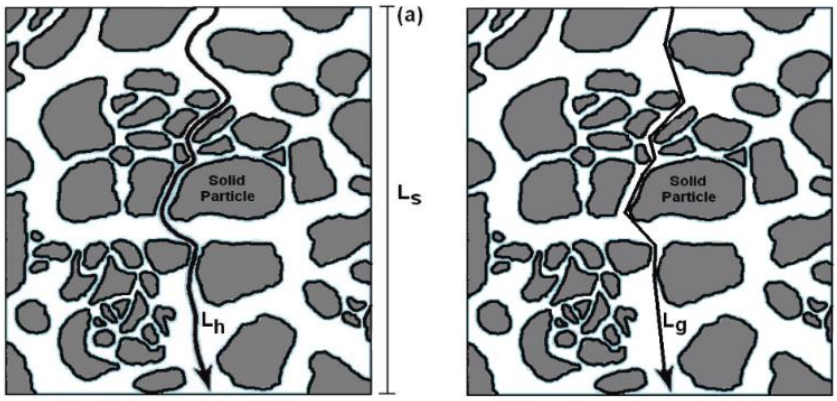

a. Hydraulic tortuous path b. Geometric tortuous path

Figure 6.2.2 Comparison between hydraulic tortuosity and geometric tortuosity (Ghanbarian et al., 2013)

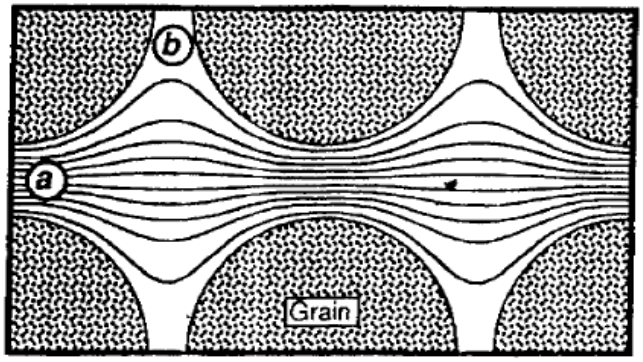

Figure 6.2.3 Hydraulic tortuosity flow streamlines (Clennell, 1997)

Fluid flow through a porous medium is influenced by both the amount and the morphology of the void (pore) space (Vallabh et al., 2010). While the amount of void space is easily quantified by measurement of porosity, the characterisation of the void space structure is often very difficult due to its complex nature (Vallabh et al., 2010). The limiting case of a bundle of parallel, non-interconnected tubes longitudinally orientated in the direction of macroscopic flow, traversing the full thickness, *L*, of the sample presents little resistance to the flow (neglecting frictional effects at the tube wall). In this case a flow streamline tracing

the path of the fluid L_e will have a length similar to the thickness of the sample, i.e. the tortuosity factor following the commonly used engineering definition is:

$$\tau = \frac{L_e}{L} = 1 \qquad (6.2.2)$$

In the case whereby the pore structure is more complex with many converging and diverging channels the streamline path may not follow the liner shortest distance between the bounding surfaces of the sample. Rather, the streamline will follow a sinuous, winding path determined by the morphology of the solid (or void) phase. Then the tortuosity factor must be:

$$\tau = \frac{L_e}{L} > 1 \qquad (6.2.3)$$

Therefore as the tortuosity factor increases above unity the flow streamlines are generally forced to follow a longer path to traverse the sample. This increase in the time taken for the fluid to permeate through the porous media can be manifested in a higher resistance to the flow. Also as the value of tortuosity approaches infinity this represents an internal pore structure (and geometric topology) of increasing complexity. Furthermore, a thorough analysis and understanding of tortuous paths within a sample presents one with a means to quantify the permeability of the sample using the Kozeny-Carman law (Equation 6.4.4) which can be used to calculate the permeability tensor used in Darcy's law (Equation 6.4.1) (Koponen et al., 2017).Tortuosity is usually considered exclusively as a geometrical property of a material, however in this study it is found that there is a temporal aspect to tortuosity which cannot be ignored. This spatio temporal dependent tortuosity is termed kinematic tortuosity. Further discussion on this parameter is contained within Section 8.1.6.

6.3 Specific surface area

The specific surface area of a porous sample is defined as the interstitial void surface area per unit bulk volume having a reciprocal length dimension. In molecular science, specific surface area greatly influences adsorption rates and reactivity processes. However on a macroscale scale it can also be used to characterise the morphology of the porous structure. A higher specific surface area for the same degree of porosity implies a topologically more complex porous medium. Additionally a higher specific surface area will also have the effect of decelerating the flow of fluid through the porous structure as the wall shear stress will have a more pronounced effect with a higher liquid-solid phase interfacial area.

6.4 Permeability and flow regimes

The transport of fluid through porous media is a ubiquitous phenomenon occurring in many natural and engineering processes (Shi et al., 2011). One of the aims of this study is to provide a rigorous numerical analysis which yields data on the permeability of porous breakwater systems.

Common applications and examples of such permeability processes which have been previously investigated include oil reservoir analyses, hydrostratigraphy, food and beverage production and pharmaceutical industries. These applications all rely on the understanding of filtration processes and the manner of conveyance of fluid(s) through a porous structure or membrane. The passage of a Newtonian fluid through the interstices formed within solid skeletal matrix is termed permeation and the ease by which the matrix conveys the fluid is measured by its permeability. Much research has been conducted on the permeability of porous structures, however, due to the highly complex nature of the tortuous, intertwining flow paths within many such materials these studies have mainly been restricted to experimental or theoretical methods. Currently numerical models are being employed more commonly for the study of fluid transport in porous media. Furthermore with recent advances in computational processing power, investigations employing spatially higher resolution numerical simulations are appearing more regularly (Mattila et al., 2016). These numerical approaches allow one to macroscopically simulate the true behaviour of the flow within the voids and interstices of the porous assembly at the pore scale. In contrast, theoretical analyses often employ macroscale continuum approaches which require much model simplification. The continuum approach may require volume averaging smoothing techniques and the use of a representative elementary volume (REV) approach. The REV is defined as the smallest volume which statistically describes the macroscopically averaged properties of the structure based on a sample volume of the material. In his book on porous media Bear (1988) gives an excellent detailed description of the theoretical procedure which is followed in order to define a statistically accurate REV. Experimental studies can often be used to determine coefficients for use in the theoretical approaches. This study takes a macroscale discontinuum approach (Baca et al., 1984) wherein the pore-space transport and interactions between each fluid phase is discretely modelled.

It is important to also identify the different flow regimes which govern the transport of fluid through a porous structure. Flows which are dominated by viscous forces are typically described by the Darcy equation. Inertial flow regimes wherein a boundary layer exists with an inertial flow core within the interstices of the porous structure are described by the Forcheimer equation. There is an additional flow regime in which fully turbulent flow occurs

within the porous structure, however in this study the effects of turbulence within the fluid flow regimes is not considered. Additionally transitional flow regimes exist as boundary layer formation is a gradual process as flow within porous media is a highly complex phenomenon. Fand et al. (1987) provide an in-depth description of these flow regimes and summarised them by Figure 6.4.1.

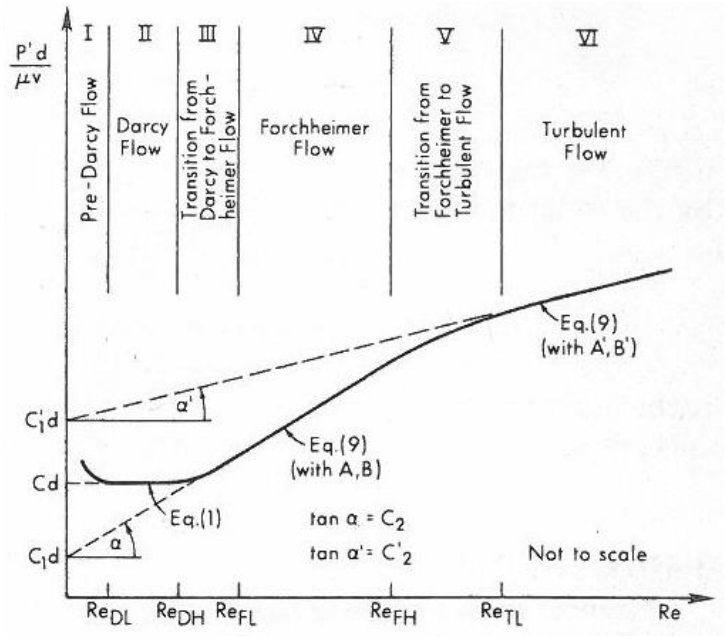

Figure 6.4.1 Porous fluid flow regimes, Fand et al. (1987)

In Figure 6.4.1 the abscissa represents the Reynolds number, the subscripts D, F and T denote the Darcy, Forcheimer and fully turbulent regimes whilst the L and H subscripts represent the lower and higher boundaries of these flows respectively. The ordinate axis has units of length per permeability represented by Cd. P′ is the pressure gradient, μ is the fluid viscosity, ν is the velocity, C is the reciprocal of permeability and d is a characteristic dimension of the porous matrix. The horizontal solid line region labelled Eq. (1) represents Darcy flow. The portion of the line labelled Eq. (9) represents Forcheimer and turbulent flow systems. These different flow models are discussed further in the following sections.

6.4.1 Darcy's Law of flow through porous material

The hydraulic permeability of a porous medium is a measure of the ability of that medium to transport a fluid of a given viscosity through a specific linear distance irrespective of the flow regime. Darcy's law (Darcy, 1856) (Equitation 6.4.1) has been used to describe the flow of fluid through a porous structure at low Reynolds number in a laminar creeping or seepage flow regime:

$$Q = -\frac{\kappa A(P_b - P_a)}{\mu L} \qquad (6.4.1)$$

where Q is the flow rate, κ is a coefficient representing the intrinsic permeability (i.e. it is independent of the fluid characteristics passing through the porous media and is determined only by the structure of the solid matter forming the skeleton of the sample), A is the cross sectional area through which the fluid flows, $(p_b - p_a)$ is the pressure drop across the sample, μ is the fluid viscosity and L is the length over which the pressure drop occurs.
By dividing both sides by the cross sectional area Equation 6.4.1 reduces to:

$$\langle q \rangle = -\frac{\kappa}{\mu}\nabla P \qquad (6.4.2)$$

where $\langle q \rangle$ is the superficial fluid velocity through the porous media and ∇p is the pressure gradient.
Equation 6.4.2 demonstrates that the pressure gradient across the sample is proportional to the seepage velocity. In the above expression there is no explicit term which takes account of the structure of the solid matter within the porous sample. The structure could consist of a bundle of parallel hollow capillary tubes or it may be formed from a more random assemblage of consolidated particles such as occurs within disorganised sphere packing or in most naturally occurring porous media. Various studies have been undertaken to develop a correlation between the permeability and the various parameters describing the morphology of the solid skeleton, however a general equation is still lacking (Koponen et al., 1998). The coefficient κ describing the permeability of a substance in Equation 6.4.2 above is a measure of the fluid conductivity thorough the sample. (Dullien, 1992) has shown through dimensional analysis that the permeability κ of a porous medium can be expressed as:

$$\kappa = \frac{f(\phi, \tau)}{S_v^2} \qquad (6.4.3)$$

where ϕ is the porosity, τ is the tortuosity and S_v is the specific surface area. Various other models have been suggested for the permeability coefficient. The Kozeny capillary model (Kozeny, 1927) based on a porous sample simplification to an assembly of parallel tubes of fixed cross sectional area orientated in the direction of the macroscopic fluid flow expresses the permeability as:

$$\kappa = \frac{\phi^3}{CS^2} \qquad (6.4.4)$$

here C is the Kozeny coefficient which for a series of parallel capillary tubes has a value of 2 (Kozeny, 1927). S is the relative surface area given by $S = S_v(1-\phi)$ where S_v is the specific surface area. It may be noted that the tortuosity does not appear explicitly in Equation 6.4.4 above however if the tubes are orientated in the direction of flow the tortuosity may be assumed to be $\tau = \frac{L_e}{L} = 1$. Equation 6.4.4 was adapted by Carman (1997) to yield

$$\kappa = \frac{1}{cS_0^2}\frac{\phi^3}{\tau^2(1-\phi)^2} \qquad (6.4.5)$$

Where c is the Kozeny-Carman coefficient. Various other equations have been suggested to the compute the permeability coefficient, but it is outside the scope of this study to analyse them all.

6.4.2 Darcy Forcheimer Flow

Whilst Darcy's Law has been shown to accurately predict fluid flow rates through granular porous material of low permeability, typically with flow velocities yielding Reynolds numbers less than 10, it is unsuitable for situations where inertial flow effects should be considered. At these higher flow velocities it has been shown that the linear relationship between flow rate and pressure gradient is no longer applicable (Fourar et al., 2004, Kundu et al., 2016).

Thus the Reynolds number for flow through the porous structure should first be established to characterise the flow regime. This is not an elementary process and there have been a number of different expressions suggested to calculate Reynolds number for flow through a packed fixed bed of contacting spheres, the simplest being:

$$Re = \frac{\rho U d_p}{\mu} \qquad (6.4.6)$$

where ρ is the fluid density, U is the superficial fluid velocity d_p is the characteristic scaling length, which for a packed bed of spheres is often taken as the sphere diameter and μ is the fluid dynamic viscosity. In Equation 6.4.6 there is no attempt to account for different morphologies of the porous structure. For example the spheres may be loosely packed on a homogeneous cubic lattice (simple cubic packing) with a porosity of 0.48 and unobstructed channels through the solid phase. Alternatively the spheres may be more densely packed in a heterogeneous body centred or face centred close cubic packing system with lower porosities and more tortuous paths. Then to account for the varying porosity the Reynolds number can be improved according to:

$$Re = \frac{\rho U d_p}{\mu(1-\varepsilon)} \qquad (6.4.7)$$

where ε is the porosity.

In some regions of the structure the flow velocity will be accelerated or slowed due to constrictions, or cavities, or abrupt changes the flow vectors etc. Thus in determining the Reynolds number for flow through a porous structure it should be acknowledged that the computed value is an averaged quantity over a certain volume (Baker, 2011). Furthermore, unlike flow through a pipe or channel in which a critical Reynolds number defines the transition from laminar to turbulent flow the process has been shown to occur more gradually in porous media (Andrade Jr et al., 1999).In those cases where it has been determined that the flow is influenced by inertial effects the Forcheimer equation is employed. This equation is an extension of the Darcy equation and consists of a liner term for the viscous component of flow and a quadratic term for the inertial component of flow (Rong et al., 2007):

$$-\frac{\Delta P}{L} = \alpha\mu\langle q\rangle + \beta\rho\langle q\rangle^2 \qquad (6.4.8)$$

where α is the viscous coefficient and β is the inertial coefficient.

The Forcheimer equation can be correlated to the Reynolds number for flow through a porous media by the introduction of a friction factor (Andrade Jr et al., 1999) rearranging Equation 6.4.8 in the form,

$$f = \frac{1}{Re'} + 1 \qquad (6.4.9)$$

where $f \equiv -\frac{\Delta P}{L\beta\rho\langle q\rangle^2}$ and $Re' \equiv \frac{\beta\rho\langle q\rangle}{\alpha\mu}$

It should be noted that in the above equations there is no consideration for the tortuosity of the porous structure through which the fluid flows.

6.5 Approaches to modelling transport in porous media

There are two main approaches to modelling fluid transport in porous media. The first approach is the macroscopic continuum method wherein the flow is modelled according to the Navier-Stokes equations with an additional Darcy (or Darcy-Forcheimer) term incorporated into the momentum equation (Higuera et al., 2014), in the region where the porous structure is located. In this method the physics of the flow through the porous medium is governed by phase quantities averaged over control volumes or REV's. The second approach to modelling fluid flow through porous media is a direct modelling approach wherein each phase is explicitly represented and the flow through the porous interstices is modelled by the Navier-Stokes equations. Other methods for modelling flow in porous

media include the smoothed particle hydrodynamic (SPH) method (Vakilha and Manzari, 2008) and lattice Boltzmann methods (Boek and Venturoli, 2010).

6.5.1 Macroscopic volume averaging approach (continuum modelling)

In the continuum modelling method the void space and solid matrix of the porous sample are not explicitly represented (Soulaine, [unpublished]). Instead averaged values of parameters describing the structure, such as the void fraction for a determined volume, are applied to the region in which the porous media is located. Central to the continuum approach of modelling flow through porous media is the characterisation of this control volume which is statistically representative of the porous structure as a whole. This control volume is termed the representative elementary volume or REV. Dullien (1992) provides a definition for the REV as follows "the REV is a prescribed characteristic volume size over which microscopic properties and transport equations can be averaged for consistent description of the macroscopic properties and transport equations in multiphase systems". Much research has been undertaken to determine the REV for a particular porous sample. Bear (1988) provides a concise approach to defining REV (see Figure 6.5.1) for a porous medium. If the size of the REV is too small the sampled volume will be representative of either the void phase or of the solid phase (represented by either 0 or 1 on the ordinate axis). As the REV is enlarged the sampled volume will be representative of both phases but will still be dominated by the phase in which the smaller original REV was first located. The REV will only be representative of the dual phase porous material once its size has exceeded the Domain of macroscopic effects. However whilst the continuum approach is effective for modelling fluid flow through homogenous media (either isotropic or anisotropic) studies have shown that the definition of an REV for a heterogeneous porous sample is a complex process and the size of the REV may not be suitable for all transport characteristics within the same porous sample (Brown et al., 2000). The main benefits of employing this method for flow simulations through porous media include the associated simulation speed up time and reduced storage requirements, both due to the fact that an intricate meshing procedure is not required to represent the complex model void space. However detailed analysis and visualisations of the flow path streamlines within the pore structure are not accessible and the study is restricted to modelling the global flow behaviour within the porous media.

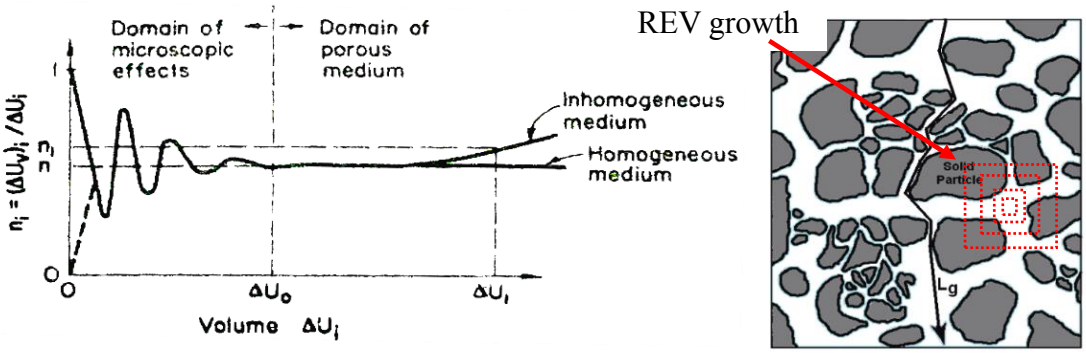

Figure 6.5.1 Definition of REV for porous media, (Bear, 1988), (Ghanbarian et al., 2013)

6.5.2 Direct Numerical Simulation at pore level

In situations where the flow velocities and the flow path vector distribution within the porous medium is required to be determined, direct numerical simulations (DNS) are performed. The solid phase skeleton is accurately represented in the domain and the Navier-Stokes equations(or Stokes equations for capillary flow) are discretised and solved directly using a particular numerical scheme on a mesh representing the pore space (Siena et al., 2015). Then, using this technique the Darcy or Darcy-Forcheimer laws do not need to be incorporated into the governing fluid flow equations.

One of the primary difficulties with this technique is the accurate representation of the solid skeleton. Recently high resolution imaging methods such as X-ray computed micro-tomography and other non-destructive imaging methods have been used to develop computational models of the porous structure which can then be incorporated into the numerical CFD models (Soulaine, [unpublished]).Additionally there are some challenges associated with representing geometries at varying length scales (multiscale analysis), for example the detailed representation of the voids between individual concrete Tetrapod units may not be possible if modelling an extended stretch of coast line. Therefore DNS methods are typically restricted to monoscale numerical simulations. With increasing computational power and storage capacity DNS methods are being employed more frequently. In this study the DNS method is employed.

Additionally, because the void spaces are relatively large within the porous structures adopted in this study, and the flow of fluid through the interstices is dominated by the force of the impact of the wave on the porous structure, the effects of capillarity are negligible in comparison to the gravity dominated flow forces. Nevertheless, air-water and water-solid

contact angles specifications are incorporated into the model in the boundary conditions for each phase but these effects are not influential when compared to the effects of advective flow. The effects of surface tension is important in these models as the oscillatory behaviour of the pulsating air void bubble is central to this study. Thus the surface tension value is specified within the `theromphysicalProperties` in the file contained within the project `constant` directory. The value of the air-water surface tension is set to 0.07 Nm^{-1}.

Chapter 7

3 Dimensional porous model simulation setup

For this phase of the study a number of porous geometries were generated and incorporated into the OpenFOAM CFD model. The structures are defined within the simulation domain such that they are located in path of the collapsing water column. The different porous morphologies and the algorithmic methods employed to generate them are first described. The constituent elements effecting the porous geometries allow the porous structures to be broadly classified as spherical or fibrous in composition. Furthermore these porous structures are modified to assess the influence of constituent element scale and global structural porosity on the flow field. The process of incorporating the porous structures into the CFD simulation software is then explained. The technique by how the computational grid is locally refined to in order that the porous structure can be accurately represented is discussed. A description of the OpenFOAM native mesh generating utility snappyHexMesh which is used for the creation of 3D meshes around irregular topologies is presented. Finally some statistics for the various porous morphologies are tabulated.

7.1 Sphere packing models

In order to isolate and establish the exclusive influence of the various porous morphology characteristics; surface area, porosity, tortuosity, permeability, etc. on the wave impact pressure signal a range of porous structures for which the elemental unit component was a sphere has been created. The porous structures were generated using a short LISP file run in the CAD software package AutoCAD Mechanical. The geometries were then converted, exported and saved as stereolithographic (.stl) files. Each of these porous structures have mono-sized spheres arranged on distinct regular geometric lattices. For each lattice layout the influence of a range of sphere size is examined for both the initial fluid surging wave impact and the subsequent oscillating pressure wave signal observed as a plunging jet is formed. This study is restricted to three different regular lattice layouts; simple cubic packing

having a theoretical porosity of 0.476, simple hexagonal packing with a porosity of 0.395 and rhombohedral packing with a porosity of 0.26. These packing systems encompass the range of minimum to maximum porosities for non-random packing systems on regular lattice layouts. The following subsections describe these packing systems.

7.1.1 Simple cubic packing

This spherical based structure consists of a mono-sized, close packed sphere-swarm arranged on a cubic lattice layout. With the exception of the outermost spheres on the boundary of the lattice (and assuming that there is a minimum of 27 spheres composing the structure), each sphere is in direct contact with its 6 neighbours. This sphere packing arrangement is known as simple cubic packing (see Figure 7.1.1). The porosity of this geometrical arrangement is 0.476, where porosity is defined in Section 6.1. Assuming the bounding box enclosing the lattice structure maintains a fixed volume and the spheres are tightly packed, then the porosity of the assembly is constant for any range of component sphere size. Thus, due to the regular composition of the structure the porosity is maintained with a value of 0.476 for all simulations with the elemental spheres in a simple cubic packing system. This is obvious from Figure 7.1.1. This allows one to investigate the influence of grain size on the flow field while maintaining the structure's overall porosity at a constant value. Furthermore, the tortuosity of the structure which is an inherent characteristic of the porous media and determined by its geometrical composition also retains a constant value irrespective of the definition of tortuosity adopted. If geometric tortuosity is assumed the value of tortuosity is simply $\tau = \frac{L_e}{L} = 1$. If hydraulic tortuosity is employed then it can be easily shown mathematically that the tortuosity varies from a minimum value of $\tau = 1.0$ to a maximum value of tortuosity $\tau = 1.57$ (irrespective of the elemental sphere diameter), assuming the flow streamline remains within the x-y plane of the fluid flow direction and is coincident with the sphere surfaces (see Figure 7.1.2).

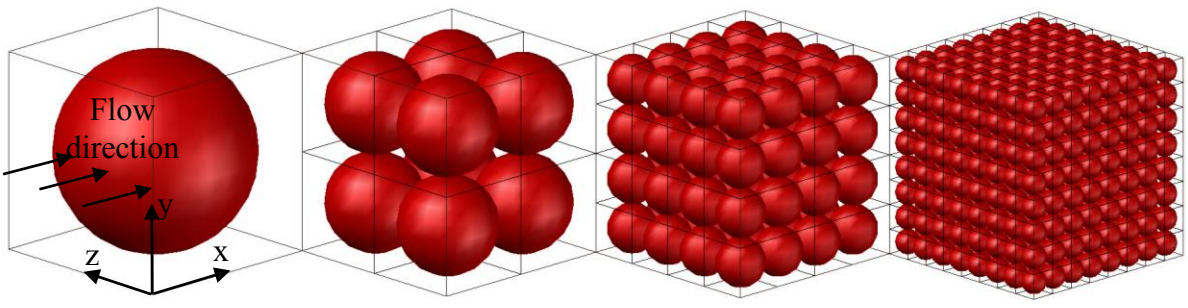

(a) (b) (c) (d)

Figure 7.1.1 Simple cubic packing arrangement

However, as the size of the constituent spheres which composes the overall structure is varied, then the specific surface area is also altered. For example; for a given bounding volume the specific surface area of spheres fitting into that volume will double if the radii of the spheres are halved (assuming cubic packing). The recursive volumetric subdivision of the spheres in this manner results in an octant style decomposition of the cubic lattice grid, See for example Figure 7.1.1. Thus one can derive some inferences relating the specific surface area of the structure to the wave impact pressure signal attenuation by modifying the component sphere size.

In Figure 7.1.1(a) above the radius of the sphere is 50 mm and is enclosed in a cuboid of side 100 mm. In Figure 7.1.1 (b) the cuboid volume is subdivided into 8 sub-volumes with each sub-volume enclosing a sphere. The 8 spheres each have a radius of 25mm. Their combined total surface area of the 8 spheres is twice that of the single sphere enclosed within the same volumetric space. Thus the surface area doubles for each halving of the diameter of the component spheres. This process of recursive volume subdivision and sphere generation with progressive radius halving can be repeated to create the specific surface area values in Table 7.1.1. Geometries consisting of additional, intermediate sphere diameters were also generated to ensure a representative data set of sphere geometries and their influence on the flow field was analysed. Specific surface area is defined in Section 6.3.

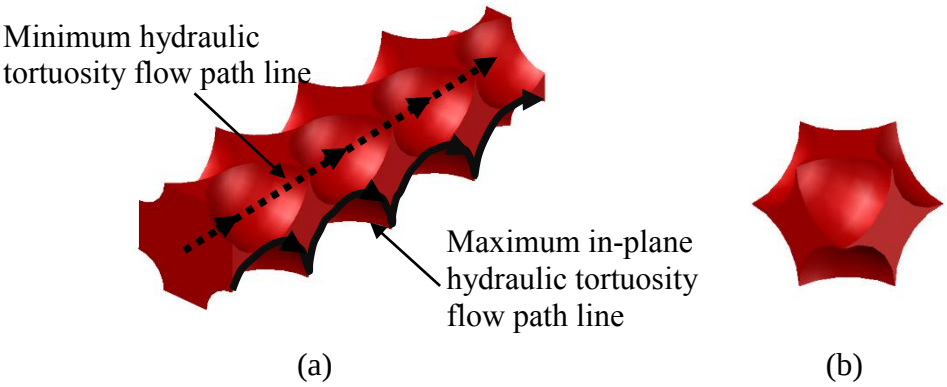

Figure 7.1.2 Simple cubic packing void structure (a) Pore structure for fluid flow path traversing simple cubic packing porous media. (b) Pore structure of single vugg within porous media

Simple cubic packing structure characteristics*												
Sphere diameter	25mm		18.75mm**		12.5 mm		9.375 mm**		6.25 mm		3.125 mm	
Porosity	47.64 %		47.67%		47.64 %		47.64 %		47.64 %		47.64 %	
# of spheres	64		~145		512		~1288		4,096		32,768	
Surface area [mm^2]	125,662		194,471		251,279		355,553		502,558		1,005,116	
Specific surface area [mm^{-1}]	0.1257		0.1945		0.2513		0.3556		0.5026		1.0051	
Coordination number	6		6		6		6		6		6	
In-plane (analytic) Tortuosity	**min**	**max**	**min**	**max**	**min**	**max**	**min**	**max**	**min**	**max**	**min**	**max**
	1	1.57	1	1.57	1	1.57	1	1.57	1	1.57	1	1.57

* Values calculated assuming spheres packed into cube of side 100mm
**Number of spheres approximate as fractional proportion of spheres considered

Table 7.1.1 Simple cubic packed spheres porous structure characteristics

7.1.2 Orthorhombic packing (simple hexagonal packing)

The next sphere packing system which was generated was the orthorhombic packing system. The porosity of this topology is 0.395. This packing system is slightly more complex than the simple cubic packing assembly. Each alternate layer of spheres is displaced by one radial length in one orthogonal spatial direction only. Thus from Figure 7.1.3(a) we can see that layer B is displaced by a distance r in direction y, however the spheres are not displaced in direction x. This allows the spheres to settle into the void space created by the spheres below, i.e. there is also displacement of layer B in the z direction. This is a more stable packing system than the simple cubic packing as each sphere has two support points beneath its centre of mass position. Furthermore, in this packing system each component sphere is in contact with 8 surrounding spheres, the structure has a coordination number of 8. When this porous morphology is incorporated into the CFD model the impact pressure signal will vary depending on whether the flow front impacts in direction x or in direction y as the interfacial surface impact area is has a distinct value for each direction. Furthermore, the permeability of this structure is also influenced by the orientation of the porous assembly as the void structure is direction dependent as shown on Figure 7.1.3(c) and Figure 7.3.1(d). In this case the total surface area of the porous structure does not double as the sphere diameter is halved. This is because each alternate layer (layer B in Figure 7.1.3) packet into the 100mm cubic bounding box now contributes additional surface area from the face of the truncated spheres.

An excellent analysis of sphere packing systems with emphasis on the topological characterisations is given by Graton and Fraser (1935).

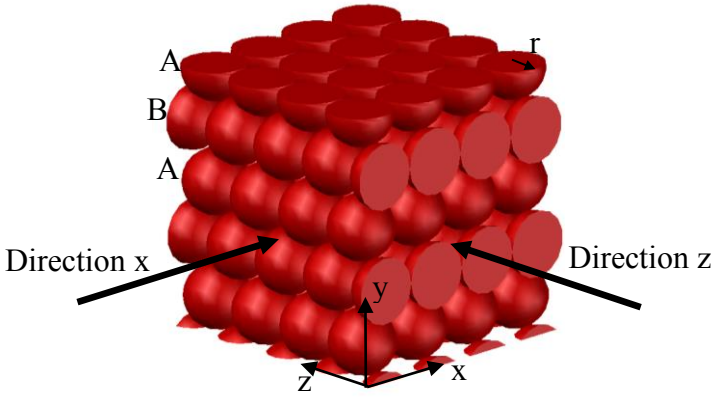

(a) Sphere packing system

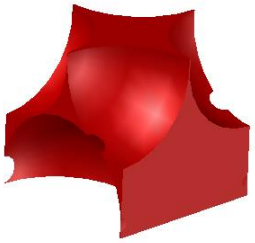

(b) Geometry of single vuggular void

(c) Void structure in orientation x

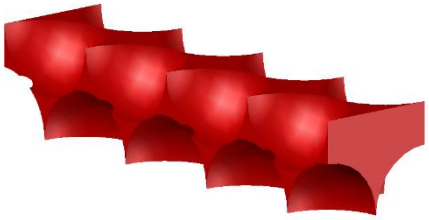

(d) void structure in orientation y

Figure 7.1.3 Orthorhombic packing arrangement and void geometry

Orthorhombic packing structure characteristics										
Sphere Diameter	25mm		18.75mm		12.5 mm		9.375 mm		6.25 mm	
Porosity	39.5 %		39.5 %		39.5 %		39.5 %		39.5 %	
# of spheres (equivalent)	~74		~197		~595		~1519		~4,758	
Surface area [mm^2]	163,644		216,685		306,056		419,332		592,884	
Specific surface area [mm^{-1}]	0.1636		0.2167		0.3061		0.4193		0.5929	
Coordination number	8		8		8		8		8	
In-plane (analytic) Tortuosity	**min**	**max**	**min**	**max**	**min**	**max**	**min**	**max**	**min**	**max**
	1	1.57	1	1.57	1	1.57	1	1.57	1	1.57

Table 7.1.2 Orthorhombic packed spheres porous structure characteristics

7.1.3 Rhombohedral packing (close hexagonal packing)

The final sphere packing porous morphology assembly considered is that of a rhombohedral packing system. This is the densest packing system available for spheres on a regular lattice layout. The porosity of this structure is 0.26, i.e. 74% of the bulk volume is occupied by the solid phase. This is the most stable packing system considered. To create this morphology each alternate layer in the z direction is displace by a distance of r in both the x and y planes. This allows the spheres in every other layer to nestle between 4 spheres in the layer below, i.e. each sphere has 4 support point beneath its centre of mass thus making it the most stable packing system. Additionally each internal sphere is in contact with 4 spheres within its own layer and 4 in the layer above, in total each sphere contacts with 12 other spheres, yielding a coordination number of 12 for this packing system. Unlike the previous orthorhombic packing system the void geometry is not direction dependent in the rhombohedral system, therefore wave impact on either the 0,y,z plane or the x,0,z plane will yield the same pressure signal results.

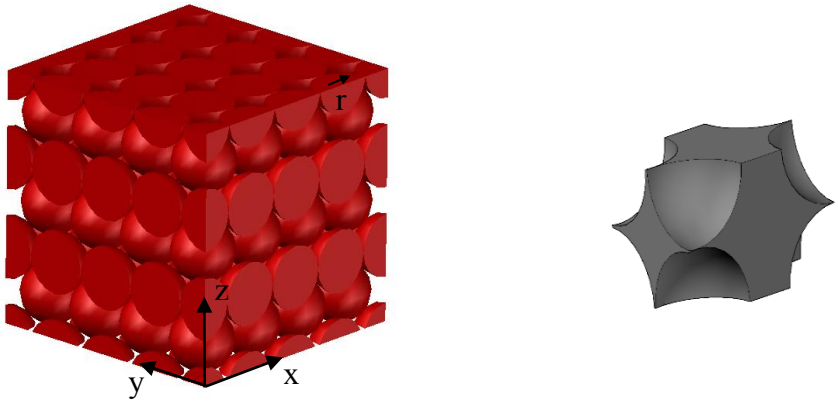

Figure 7.1.4 Rhombohedral packing arrangement and void geometry

Rhombohedral Packing										
Sphere diameter	25mm		18.75 mm		12.5 mm		9.375 mm		6.25 mm	
Porosity	26.0 %		26.0 %		26.0 %		26.0 %		26.0 %	
# of spheres (equivalent)	~90		~257		~724		~1908		~5789	
Surface area [mm^2]	215,599		283,826		374,12		526,779		750,624	
Specific surface area [mm^{-1}]	0.2156		0.2839		0.3741		0.5268		0.7506	
Coordination number	12		12		12		12		12	
In-plane (analytic) Tortuosity	**min**	**max**	**min**	**max**	**min**	**max**	**min**	**max**	**min**	**max**
	1	1.57	1	1.57	1	1.57	1	1.57	1	1.57

Table 7.1.3 Rhombohedral packed spheres porous structure characteristics

7.2 Stochastic fibrous morphology

The fibrous porous structure is generated from a Voronoi tessellation diagram. This is a method of partitioning a plane into a subset of polygonal cells wherein each cell has a seed point. The lines bounding each cell are equidistant between the points of neighbouring cells. Figure 7.2.3 shows a Voronoi diagram. The seed points used to define the vuggular voids are generated randomly in three dimensional space. Then a three dimensional Voronoi diagram is constructed through the implementation of Fortune's Algorithm. This generates the tubular elements which define the fibrous structure. Section 7.2.1 describe the procedural stages of Fortune's Algorithm. The method is first described in a simplified two dimensional domain and then the algorithmic method is extrapolated to three dimensional space is explained.

7.2.1 Fortune's Algorithm

Fortune's Algorithm employs a sweep line approach wherein a straight line (often called the sweep line) advances through a two dimensional bounded domain containing a number of random points or sites. The algorithm generates parabolic locus curves with each site as the focal position and the sweep line acting as the directrix. This is shown in Figure 7.2.1. As the sweep line traverses the domain, the algorithm processes the random sites and a series of parabolas are constructed behind the sweep line (Figure 7.2.2(a)). The portions of these in-

tersecting parabolic curves which are closest to the sweep line form the beach line. The intersection point of two parabolas is termed a break point as shown on Figure 7.2.2(b). These dynamic break points follow the parabola intersections as the sweep line traverses the domain. As the parabolas grow due to the sweep line moving through the domain then the position of the break points also change and they traces out lines which are equidistant between two focal points (the original stochastically generated sites). This delineates the edges of a tessellated pattern. Where three edges or more intersect a tile vertex is formed. The distribution edges and vertices define the individual tessellations which taken together compose the overall Voronoi network. An example is shown in Figure 7.2.3.

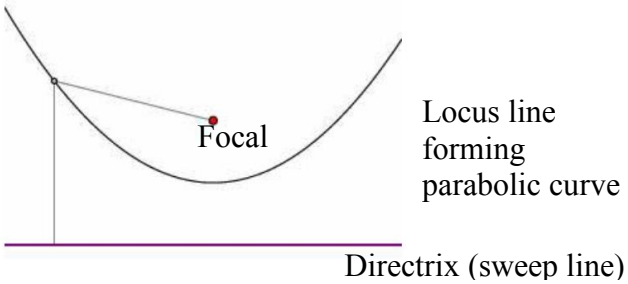

Figure 7.2.1 Parabola construction

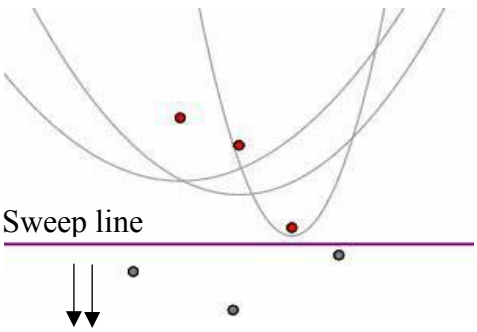

(a) Sweep line and parabolic arcs

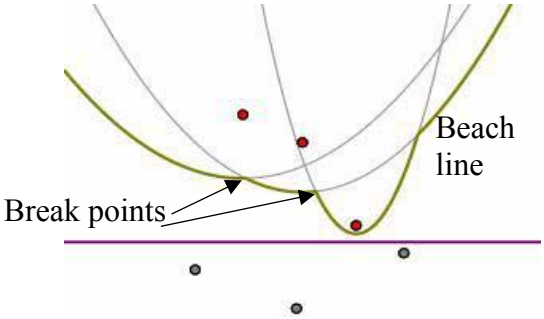

(b) Beach line and break points

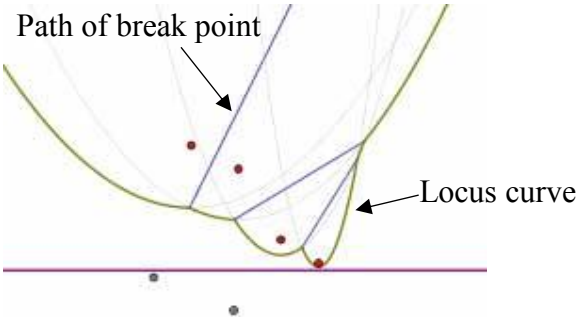

(c) Formation of Voronoi Tessellation edges

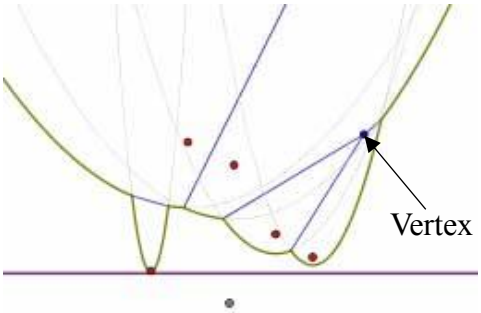

(d) Formation of tessellation vertices

Figure 7.2.2 Voronoi Diagram construction

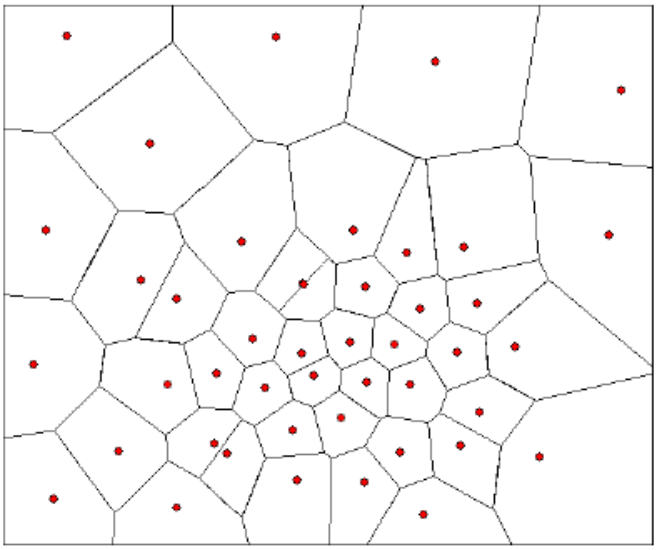

Figure 7.2.3 Voronoi tessellation diagram (Feick and Boots, 2005)

A similar approach can be employed to create tessellated volumetric surfaces in three dimensional space. In this case the sites are stochastically distributed within a three dimensional bounding box. The sites form the focal points for paraboloid surfaces. The directrix is now defined by a planar surface which sweeps through the bounding box. The intersections of the paraboloid surfaces trace out lines which in turn describe planar facets as the directrix moves through the domain and the paraboloid surfaces grow, this is shown on Figure 7.2.4. The edges of these planar facet surfaces can be now be specified as the longitudinal axes for the filaments which form the fibrous porous structure.

This approach can also be used to generate a fragmented, granular porous media with some additional steps incorporated into the algorithm. Each planar surface generated by the intersecting paraboloid surface is common to two component granule fragments, i.e. the structure as a whole is comparable to a fully consolidated conglomerate assembly with zero porosity. By creating 2 new planes offset each side of the original plane and extending (or truncating) these new planes as required, the surface facets of polyhedral non-contacting individual granules are created with interstitial planer spaces around each grain. By varying the number of sites or by varying the offset distance the porosity of the medium can be controlled.

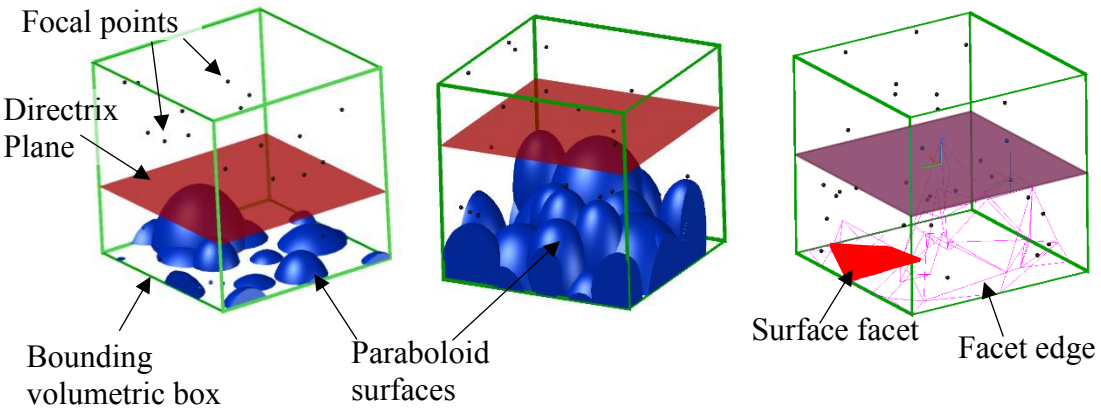

Figure 7.2.4 generation of 3 dimensional Voronoi structure

7.2.2 Fibrous media geometries

An initial tubular solid model composed of 0.82 mm diameter filaments with high porosity of 0.975 (see Figure 7.2.5) was developed from a 3 dimensional Voronoi based structure as described in Section 7.2.1. The structure was imported into a CAD software package (SOLIDWORKS) for processing. Within the CAD software the model was first copied. The copy was then rotated through 90, 180 or 270 degrees about either the x, y or z axis. The copied structure was then superimposed upon the original. A Boolean union operation was then carried out in the CAD software which created a single assembly from the original and the copied structure with slightly less than twice the original density. This process could be recursively repeated to achieve an approximate porosity halving operation. Alternatively if a full density doubling operation was not required the original low density structure could be incorporated into the model to yield a slight decrease in porosity. Using this method a range of porous fibrous structures were constructed with a range of densities. Some of these structures are shown in Figure 7.2.5 and the properties are tabulated on Table 7.2.1. It was found that using the density doubling method outlined above the maximum density (or inversely, the minimum porosity) achievable was a 15.692% solid fibrous structure due to computational limitations on the file size and the practicalities of working with extremely large complex geometric data files.

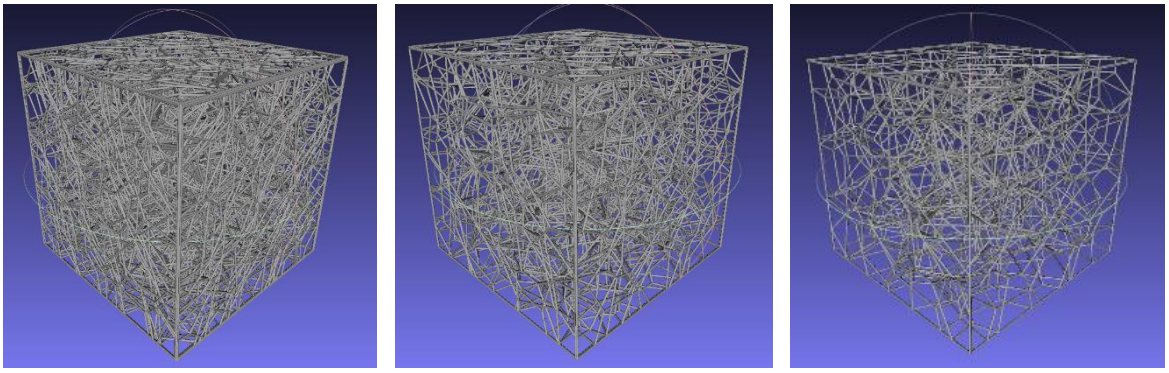

97.527 % porous 95.197 % porous 94.442 % porous

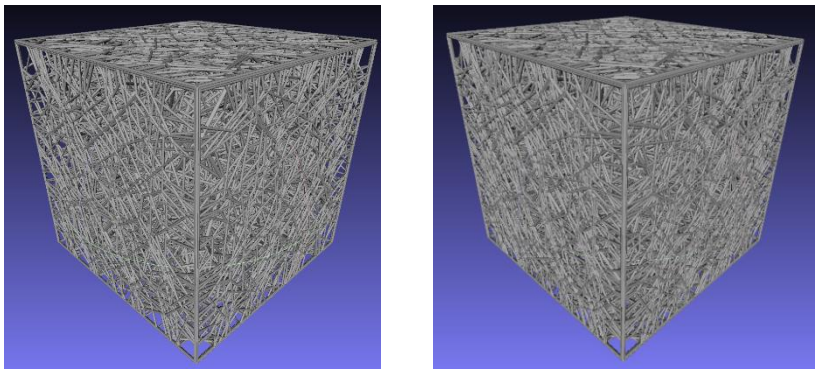

92.154 % porous 84.308 % porous

Figure 7.2.5 Fibrous geometries of varying porosity

Because of the stochastic nature of the fibrous structure the parameterisation of the morphology is not as straightforward as the regular sphere-lattice structures. For example the coordination number and the number of component filament elements comprising the assembly are extremely complex parameters to ascertain, especially as the density of the structure increases (see 84.308 % porous structure in Figure 7.2.5). Instead, we use the number of edges, vertices and faces comprising the .stl file mesh from which the fibrous structure is generated. This process is described in Section 7.4.1. Also, the total length of the edges and the average length of the edges can be extracted from the .stl file using the mesh editing and rendering software MeshLab. It should be noted that the total and the average length of the edges extracted from MeshLab is not the same value as the total and average length the filaments comprising the fibrous structure. In Figure 7.2.6 the triangulated .stl mesh is shown and this contrast is highlighted. The topological .stl file is further discussed in Section 7.4.1 As the density of the fibrous structures increases the number of filament intersections will correspondingly increase thus reducing the individual filament lengths and the corollary .stl file edge lengths. This allows us to use the average edge length in conjunction with the number of edges as a parameter to describe the complexity of the fibrous media.

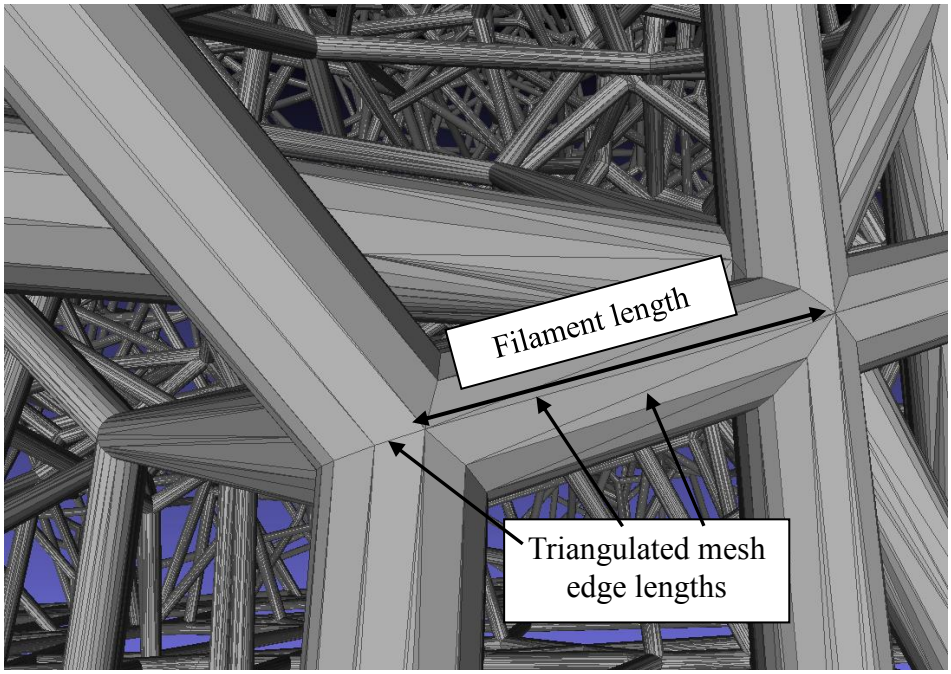

Figure 7.2.6 Filament length and .stl file mesh edge lengths

Fibrous Geometries					
Filament Radius	0.41 mm	0.41 mm	0.41 mm	0.41 mm	0.41 mm
Porosity	97.527 %	95.197	94.442 %	92.154%	84.308%
Surface area	115,656mm^2	218,969mm^2	246,597mm^2	329,511mm^2	659,022 mm^2
Specific surface area	0.1157 mm^{-1}	0.2180 mm^{-1}	0.2466 mm^{-1}	0.3295 mm^{-1}	0.6590 mm^{-1}
# vertices	163,618	441,539	1,591,788	2,570,355	5,140,712
# edges	511,026	1,381,305	4,842,503	7,813,266	15,626,539
#faces	340,684	920,870	3,225,334	5,208,790	10,417,584
Total .stl file edge length	2,393,515 mm	4,745,531 mm	15,911,406 mm	21,681,842 mm	43,364,336 mm
Average edge length	4.684 mm	3.436 mm	3.286 mm	2.775 mm	2.775 mm
Geometric Tortuosity	1	1	1	1	1

Table 7.2.1 Fibrous structure characteristics

7.3 Simulation Geometry

The simulation set-up follows a similar procedure as detailed in Chapter 4 and also as presented in (Mayon et al., 2016). The main modification to the earlier studies is that the domain has been extended to three dimensions. The extension to three dimensions is necessary to account for the variation in the porous structure in the z direction (i.e. in the depth of the simulation domain). The simulation geometry is in the configuration of a dam break flow test case as shown on Figure 7.3.1 below. The numerical wave tank length is increased to 0.4m long and maintained at 0.2m high. The depth of the domain in the third dimension (z direction) is set to 0.1m. The tank contains a water column at the left hand side with the earlier simulation dimensions of width 0.05715m, height 0.0114m maintained. For this three dimensional study the depth of the water column (z direction) is set to 0.1m. A no-slip boundary condition is prescribed at the tank base and at vertical walls at x = 0, z = 0 and z = 0.1. As the top of the tank is considered to be open to the atmosphere, the inflow and outflow of fluid is permitted across this boundary. Thus, at this surface a combination of boundary conditions are specified for the pressure and velocity terms of the fluid flow governing equations to model inflow and outflow behaviour whilst maintaining the PIMPLE algorithm stability. The numerical value of the `fixedValue` boundary condition is set to atmospheric pressure conditions (101 kPa) across the surface which represents the top of the numerical tank. The porous morphologies were incorporated into the model at the right hand side of the domain. There is a 1 mm gap between the bed of the tank and the base of the porous structures, was to facilitate the meshing operation as discussed later in this chapter. Additionally at the right hand side surface (at x = 0.4) the boundary condition applied permits the outflow of fluid from the domain. This allows both fluid phases to pass freely through the porous structure. The pressure signals are sampled at mid height the face of the bottom sphere forming the porous matrix indicated by point P1 on Figure 7.3.1, and also at a point on the face of the fibrous structures close to the bed of the numerical tank. It should be noted that as the constituent sphere sizes reduce, the height of point P1 above the base of the numerical tank will reduce correspondingly.

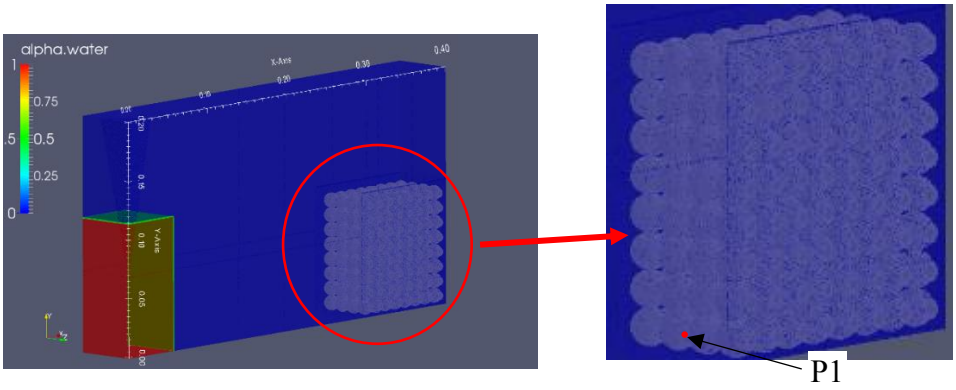

Figure 7.3.1 Section through simulation setup (sphere diameter 12.5mm)

7.4 Incorporation of Porous models into simulation domain

Studies conducted in the early phase of this research established that the OpenFOAM mesh grid discretisation size of 1 millimetre square was sufficiently high resolution to accurately represent the free surface flow, to capture the initial fluid flow impact pressures and also to capture the subsequent high frequency oscillatory pressures. Therefore this 1 mm grid resolution was adopted for the 3 dimensional simulations with fluid flow impact at the porous structure. The

7.4.1 .stl file generation

The porous structures generated using the CAD software are saved in a text based stereolithographic (.stl) file format. This .stl file type contains the minimum amount of information necessary to describe the three dimensional morphology of the structure. All geometrical metadata such as material properties, texture, colour etc. are omitted from the .stl file. A high resolution is necessary to represent the surface curvature of the porous structure. In order to generate an accurate model of the high density fibrous media extremely large .stl files were required (>20 GB). The .stl conversion proceeds by generating an unstructured triangulated mesh to represent the surface of the object. The resolution of this mesh determines how accurately the .stl file captures the surface curvature. The .stl file saves the coordinates of each of the three vertices of each triangular tessellation. In addition, a unit facet normal is also saved for each tessellation. The normal, together with the vertex coordinates allows the orientation and location of each facet to be determined. An excerpt from a .stl file is shown on Figure 7.4.1.

```
solid fibrous
        facet normal 0.268828 0.607833 0.747175
                outer loop
                        vertex 0.31491 0.0288832 0.000819512
                        vertex 0.314884 0.0288985 0.000816383
                        vertex 0.314804 0.0288599 0.000876717
                endloop
        endfacet

        facet normal -0.308322 -0.649325 -0.695208
                outer loop
                        vertex 0.314758 0.028235 0.00033889
                        vertex 0.314718 0.0283192 0.00027813
                        vertex 0.315273 0.028065 0.000269249
                endloop
        endfacet

        facet normal 0.125861 0.256593 -0.958289
                outer loop
                        vertex 0.314763 0.0288403 0.000196822
                        vertex 0.314797 0.0288565 0.000205644
                        vertex 0.31507 0.0285419 0.000157304
                endloop
        endfacet
endsolid fibrous
```

Figure 7.4.1 Sample excerpt from .stl file

7.4.2 Computational domain meshing procedure

The meshing technique initially proceeds in the same manner as described in Chapter 4. The OpenFOAM `blockMesh` utility is first invoked to generate a uniform hexahedral 1 millimetre grid in three dimensions throughout the domain (dimensions 400mm X 300mm X 100mm) at this point there are 12,000,000 grid cells. Thereafter a localised mesh refinement is performed in the region which is to be occupied by the porous media as shown on Figure 7.4.2. By creating this localised higher resolution region, the final stage of meshing the void space in the porous geometry is less computationally demanding. The OpenFOAM `surfaceFeatureExtract` tool is run to detect and extract the tessellation triangle edges from the .stl file. An .emesh file consisting a set of points which are the coordinates of the ends of the tessellated edges and which are on the surface of the porous geometry is created. This data stored in this file allows the `snappyHexMesh` utility to snap to points on the surface of the porous structure.

7.4.3 Local grid refinement

Because the 1 millimetre grid discretisation scheme was too coarse to accurately represent the curvature of either the small diameter sphere's surface or the surface of the fibrous filaments when the .stl file was imported into the simulation domain, a localised grid refinement was performed in the region which the porous morphologies were to be located as show on Figure 7.4.2. A comparison between the CAD file geometry statistics and the .stl file statistics is presented on Table 7.4.1.

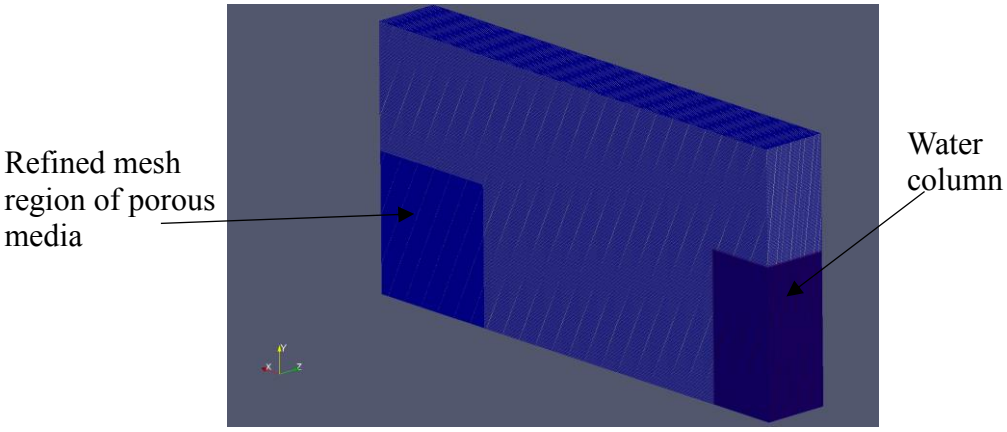

Figure 7.4.2 Localised grid refinement

The local refinement was performed by first employing the `topoSet` tool to generate a cell set topology for the region where the cell splitting procedure was to be performed. Thereafter the `refineMesh` utility was called. By default this utility splits the cells in half in each direction; then in two dimensions each cell is quartered and in 3 dimensions each cell is divided into eight. Then, in the region wherein the porous structure is to be located the hexahedral mesh is reduced from a 1mm grid to a 0.5mm grid. As adaptive time stepping has been has been specified in the `controlDict` file then the CFL condition is enforced through the programme controlled reduction in time step length. Then, the flow of fluid from grid cell to grid cell in this locally refined region will regulate the time step duration for the entire simulation domain.

At this stage of the meshing process the grid cell count was 19,000,000 with no representation of the porous morphology yet defined in the simulation domain. However, by employing the OpenFOAM `snappyHexMesh` utility the porous structure could now be imported from the .stl file and by specifying additional levels of mesh castellation in the `snappyHexMesh` the surface curvature is more accurately represented as shown in Figure 7.4.3. This process is described in Section 7.4.4.

A comparison between the surface areas and porosities for the cubic packed sphere geometries derived from CAD file geometries with the surface areas and porosities for the same structures after they have been converted to .stl files is displayed on Table 7.4.1. It is shown that there is little discrepancy in these attributes before and after conversion to .stl format. By specifying a high level of resolution conversion at all stages of the mesh pre-processing we ensure the accuracy of the mesh geometry. In some cases the surface area differences are positive and in others the areas differences are negative; those porous geometries which fitted exactly into the 100mm domain width (i.e. the 25mm, 12.5mm, 6.25mm and 3.125mm diameter sphere structures) all exhibit an increase in surface area after conversion to .stl format. The outermost layer in those other sphere structures (18.75 and 9.375mm diameter spheres) were required to be truncated to fit within the 100mm domain. Thus the surface area in those geometries was slightly less after the truncation of the outermost spheres to fit within the 100mm domain depth. This is reflected in the reduced surface areas for these .stl files.

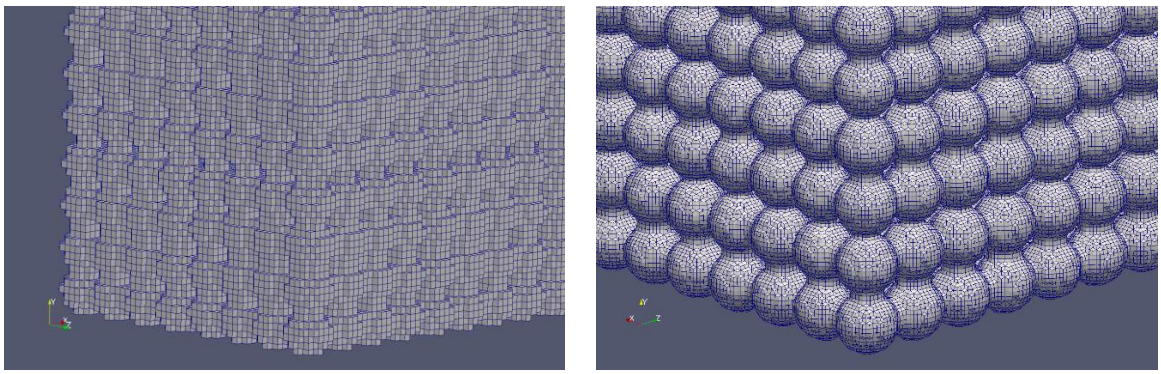

(a) Before local refinement (b) After refinement

Figure 7.4.3 Spheres representation (a) before and (b) after localised grid refinement and specification of mesh castellation

Sphere packing system	Geometric results from CAD file		Results from .stl file structure		% difference	
	Surface area	porosity	Surface area	porosity	Surface area	porosity
Cubic 25 mm	125,662	47.67%	123,855	49.1%	-1.44 %	+3.00%
Cubic 18.75 mm	194,471	47.67%	195,011	47.8%	+0.3%	+0.27%
Cubic 12.5 mm	251,279	47.67%	247,746	49.1%	-1.41 %	+3.00%
Cubic 9.375 mm	355,553	47.67%	357,418	46.2%	+0.52 %	-3.1%
Cubic 6.25 mm	502,558	47.67%	500,481	49.1%	-0.41%	+3.00%
Cubic 3.125 mm	1,005,116	47.67%	1,001,052	49.1 %	-0.4%	+3.00%

Table 7.4.1 Comparison between geometric cubic packed sphere statistics and .stl file cubic packed sphere structures

7.4.4 OpenFOAM SnappyHexMesh utility

The final stage in generating the mesh which represents the interstitial void space between the solid phase of the porous media and consequently the surfaces of the elemental solids forming the structure is implemented by invoking the `snappyHexMesh` utility. There are a number of distinct steps which are completed in a procedural manner when running the `snappyHexMesh` utility. Firstly, a cell splitting or castellation process is performed on those cells which cross an edge of the porous structure as defined in the .emesh file. The user can define the number recursive cell splitting operations. A higher level of castellation will represent the surface of the solid more smoothly but at an additional computational cost, both in terms of algorithm runtime and storage requirements. The next step in the procedure removes all those cells with 50% or more of their volume falling within the solid phase region of the porous morphology. Finally the vertices of castellated cells which remain are snapped to the points representing the surface geometry in the .emesh file. Additional tasks can also be performed such as adding high resolution mesh layers to resolve turbulent boundary layers etc., however these steps were not employed for this study. It should also be noted that due to the high computational cost the meshing procedure was parallelised to run on the Iridis High performance computing (HPC) facility employing 64 cores on duel 2.6GHz Intel Xeon E5-2607 Sandybridge processors.

7.4.5 Volumetric accuracy check for generated porous structures

Subsequent to the mesh generation, the OpenFOAM `checkMesh` utility was invoked to determine the accuracy of the mesh in terms of the representation of the porous structure. The output from the `checkMesh` command is shown below in Figure 7.4.4 for the 25 mm diameter spheres in cubic packing configuration. There are 11,696,299 grid cells with a total volume of 7.537267×10^{-3} m^3. The majority of these cells are hexahedral with a small few polyhedral cells. From the `checkMesh` output we can determine that the bounding mesh box is 0.401m×0.201m×0.1m. This gives a total volume of 8.0601×10^{-3} m^3. By subtracting the grid cells total volume from this figure we can determine the volume of the solid spheres. In this case the solid porous volume is computed to be 5.228×10^{-4} m^3. According to the theoretical porosity value this figure should be 5.24×10^{-4} m^3. Then, in the course of generating these structures, converting them to a .stl file, importing and meshing in OpenFOAM the porosity has been increased from 47.6% to 47.7%. Therefore the procedure of generating the porous structures is very accurate.

```
/*---------------------------------------------------------------------
--------*\
| =========                 |
|
| \\      /  F ield         | OpenFOAM: The Open Source CFD Toolbox
|
|  \\    /   O peration     | Version:  2.3.0
|
|   \\  /    A nd           | Web:      www.OpenFOAM.org
|
|    \\/     M anipulation  |
|
\*---------------------------------------------------------------------
--------*/
Build  : 2.3.0-f5222ca19ce6
Exec   : checkMesh
Date   : Oct 05 2017
Time   : 12:07:32
Host   : "robbie-HP-ENVY-17-Notebook-PC"
PID    : 14319
Case   : /media/robbie/new_8_tera_byte/cubic/diam_25
nProcs : 1
sigFpe : Enabling floating point exception trapping (FOAM_SIGFPE).
fileModificationChecking : Monitoring run-time modified files using
timeStampMaster
allowSystemOperations : Disallowing user-supplied system call opera-
tions

// * * * * * * * * * * * * * * * * * * * * * * * * * * * * * * * * * *
* * * * //
Create time

Create polyMesh for time = 0

Time = 0

Mesh stats
    points:           12292916
    faces:            35690500
    internal faces:   34550594
    cells:            11696299
    faces per cell:   6.005412
    boundary patches: 6
    point zones:      0
    face zones:       0
    cell zones:       0

Overall number of cells of each type:
    hexahedra:     11675099
    prisms:        0
    wedges:        0
    pyramids:      0
    tet wedges:    0
    tetrahedra:    0
    polyhedra:     21200
    Breakdown of polyhedra by number of faces:
        faces   number of cells
            6   100
            9   21100
```

```
Checking topology...
    Boundary definition OK.
    Cell to face addressing OK.
    Point usage OK.
    Upper triangular ordering OK.
    Face vertices OK.
    Number of regions: 1 (OK).

Checking patch topology for multiply connected surfaces...
                   Patch    Faces   Points                  Surface
topology
                leftWall    20100    20402  ok (non-closed singly
connected)
               rightWall    51600    52107  ok (non-closed singly
connected)
               lowerWall    70876    71872  ok (non-closed singly
connected)
        frontandbackWall   225838   228026  ok (non-closed singly
connected)
              atmosphere    40100    40602  ok (non-closed singly
connected)
                  sphere   731392   732080  ok (non-closed singly
connected)

Checking geometry...
    Overall domain bounding box (0 0 0) (0.401 0.201 0.1)
    Mesh (non-empty, non-wedge) directions (1 1 1)
    Mesh (non-empty) directions (1 1 1)
    Boundary openness (6.036057e-16 1.950649e-14 -7.807386e-17) OK.
    Max cell openness = 3.182515e-16 OK.
    Max aspect ratio = 2.636031 OK.
    Minimum face area = 7.52608e-08. Maximum face area = 1.00035e-06.
Face area magnitudes OK.
    Min volume = 3.335611e-11. Max volume = 1.00036e-09.  Total vol-
ume = 0.007537267.  Cell volumes OK.
    Mesh non-orthogonality Max: 26.54876 average: 2.316205
    Non-orthogonality check OK.
    Face pyramids OK.
    Max skewness = 1.515656 OK.
    Coupled point location match (average 0) OK.

Mesh OK.

End
```

Figure 7.4.4 OpenFOAM checkMesh utility output

Chapter 8

3 Dimensional simulation wave impact at porous structure results

The results from the 3 dimensional wave impact simulations at the porous structures are presented. To begin with the sphere based porous structure simulation results are examined followed by the results from the fibrous porous structure analysis. Extensive commentary is given on the cubic packing sphere structure results. The simulation results for the orthorhombic packed spheres, rhombohedral packed spheres and the fibrous porous structure is presented in tabular and in graphical format.

8.1 Simple cubic packing sphere lattice

The results from the simple cubic packing sphere lattice simulations will be investigated in detail in Section 8.1. The results from the orthorhombic and rhombohedral sphere packed structures will be presented and the main simulation results tabulated in Sections 8.2 and 8.3 respectively. The results from the simple cubic packed sphere simulations are summarised in Table 8.1.1 below. The main simulation outputs considered for analysis are the flow profile and free surface evolution, the initial impact impulse values resulting from the surging flow front impinging on the porous structure, the physiognomies of the entrapped air bubble, the characteristics of the oscillatory phase of the pressure signal, the permeability of the structure and the tortuous nature of the flow path through the porous structure. These simulation output parameters are all examined in more detail in the following subsections.

8.1.1 Flow profile and free surface evolution

As the flow simulation progresses, the water column collapses and the flow front advances towards the right hand side (RHS) of the numerical tank where it impacts the porous structure

(Figure 8.1.1 (a)) and is forced vertically upwards through the formation of a thin jet, Figure 8.1.1(b). This initial impact produces the first peak on the pressure history signal (see Figure 8.1.4). The initial impact pressure peaks for each of the component sphere diameter simulations are shown in detail on Figure 8.1.5 (a). As the vertically formed jet collapses (Figure 8.1.1 (c)) it produces a plunging breaker type wave which converges with the fluid below, at this time instant an air bubble is entrapped by the flow. For the 3.125mm diameter cubic packed sphere structure this occurs at t = 0.515 seconds (Figure 8.1.1(d)) and yields the first oscillatory cycle local maximum pressure for each respective simulation as shown on Figure 8.1.6.

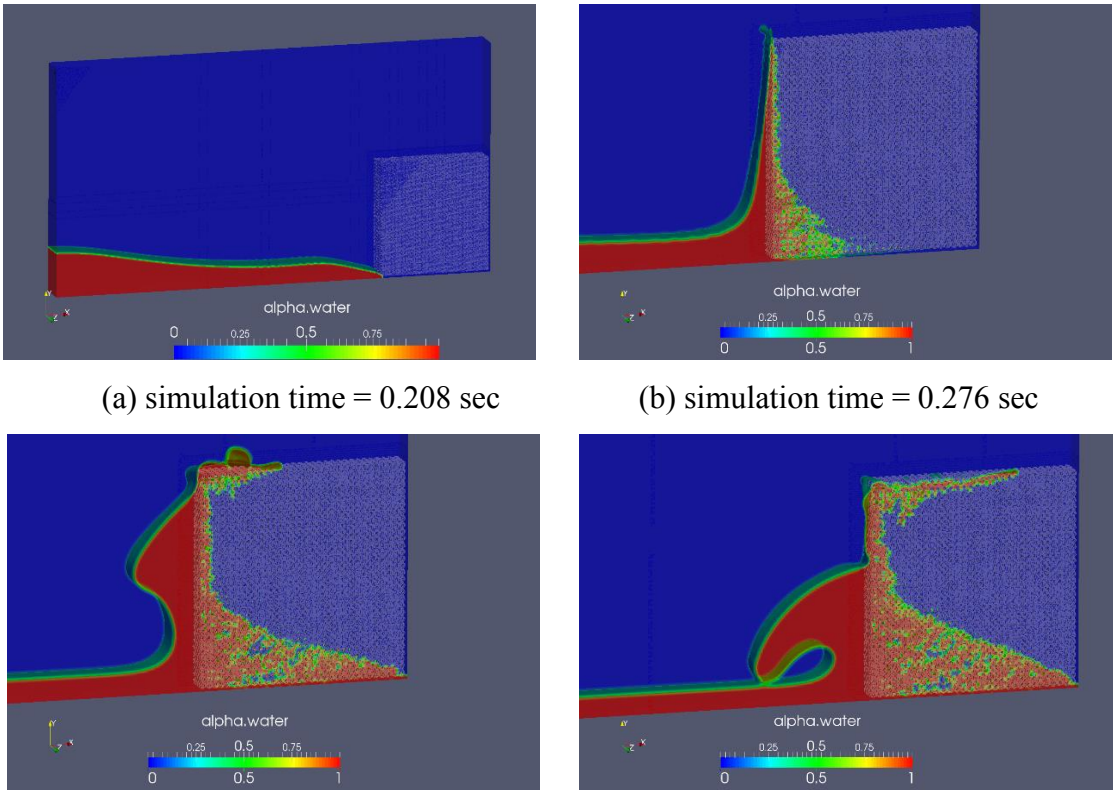

(a) simulation time = 0.208 sec (b) simulation time = 0.276 sec

(c) Simulation time = 0.450 sec (d) Simulation time = 0.515 sec

Figure 8.1.1 F function (phase volume) representation at porous structure (component sphere diameter 3.125mm)

Figure 8.1.2 (a-f) displays slices through each of the cubic packed sphere structures showing the free surface flow profile at simulation time t = 0.5 sec within the porous assemblies. The slices are sampled at mid depth through the model domain (i.e. z = 0.05 m).

As the constituent spheres comprising the porous structure are progressively reduced in size it is found that the liquid phase experiences higher resistance to permeate through the void spaces. This is evidenced by the variations in gradient of the free surface when measured from the outflow face to the point of maximum quasi-hydrostatic pressure within the porous structure as also shown for 4 of the simulations on Figure 8.1.3. The higher specific surface

of the 3 mm diameter spheres also causes a higher vertical jet to form subsequent to the initial surging flow front impact. The jet rises above the porous structure and some of the liquid volume from the formed jet collapses on to the upper surface of the 3mm diameter sphere structure as shown in Figure 8.1.2 (f) and permeates downwards under the influence of gravity.

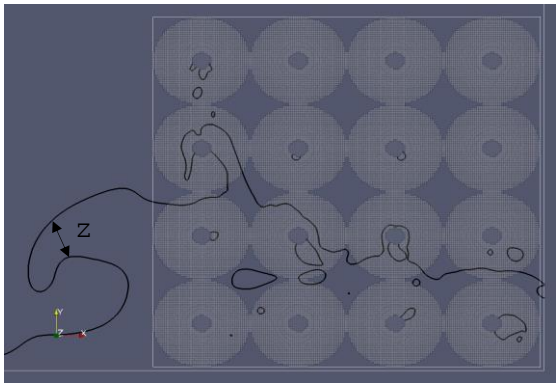

(a) 25 mm diameter sphere structure

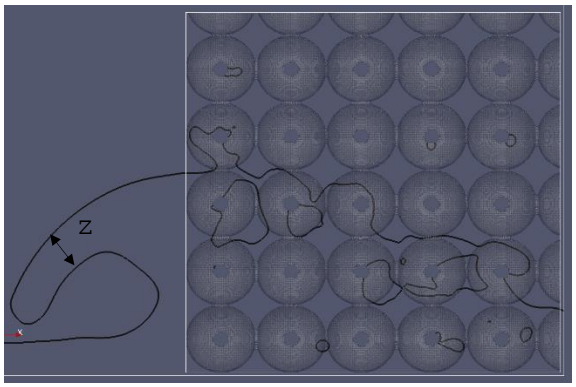

(b) 18.75 mm diameter sphere structure

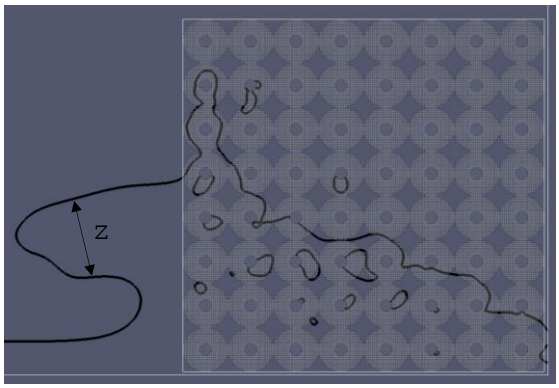

(c) 12.5 mm diameter sphere structure

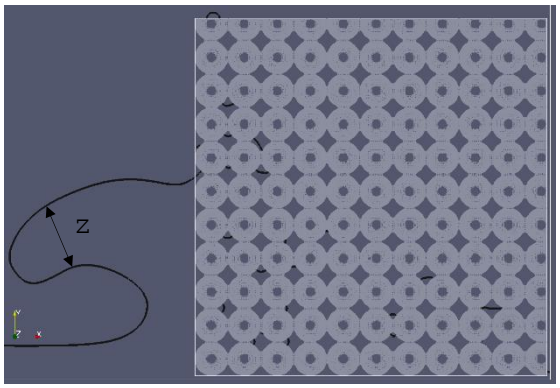

(d) 9.375 mm diameter sphere structure

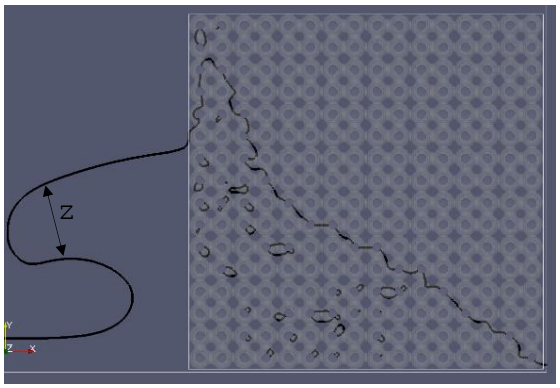

(e) 6.25 mm diameter sphere structure

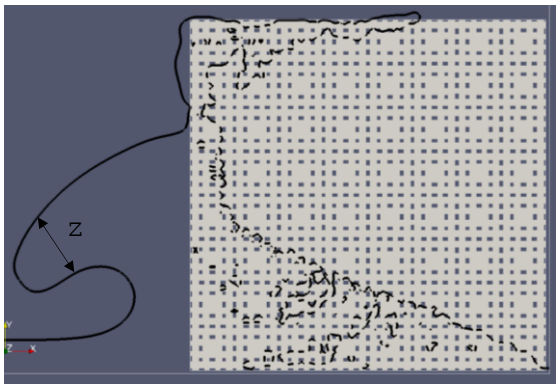

(f) 3.125 mm diameter sphere structure

Figure 8.1.2 Free surface profiles and collapsing jet thickness
at cubic packed porous sphere structures

The effect of the sphere diameter on the free surface profile of the generated plunging breaker wave is also highlighted in Figure 8.1.2. The two largest diameter sphere based structures tend to yield plunging breaker waves with much narrower leading edges (z). Additionally,

the entrapped bubble which is formed subsequently to impact with these larger diameter sphere structures has an increased asymmetrical shape due to the rougher impact interface. These bubbles have a varying cross section in the z axis direction. In contrast the higher specific surface area of the smaller sphere structures effect a smoother surface roughness at the face of the porous morphology and thus a reduced frictional coefficient at the impact interface will result (this allows the formed jet to achieve a larger vertical amplitude for the progressively smaller diameter sphere structures). The plunging breaker which develops as the jet collapses at these small sphere porous models is more uniform through the depth of the domain and this leads to the creation of a more regular, cylindrical tubular shaped air bubble with relatively constant cross section along the z axis.

This cylindrical bubble is bounded at each end in the z direction by the vertical simulation domain faces at z =0 and at z = 0.1. Section 8.1.4 discusses this effect in more detail. The thickness of this plunging jet (z) as shown on Figure 8.1.2 may also influence the oscillation frequency and amplitude of the entrapped air bubble. This is discussed further in Section 8.1.3.

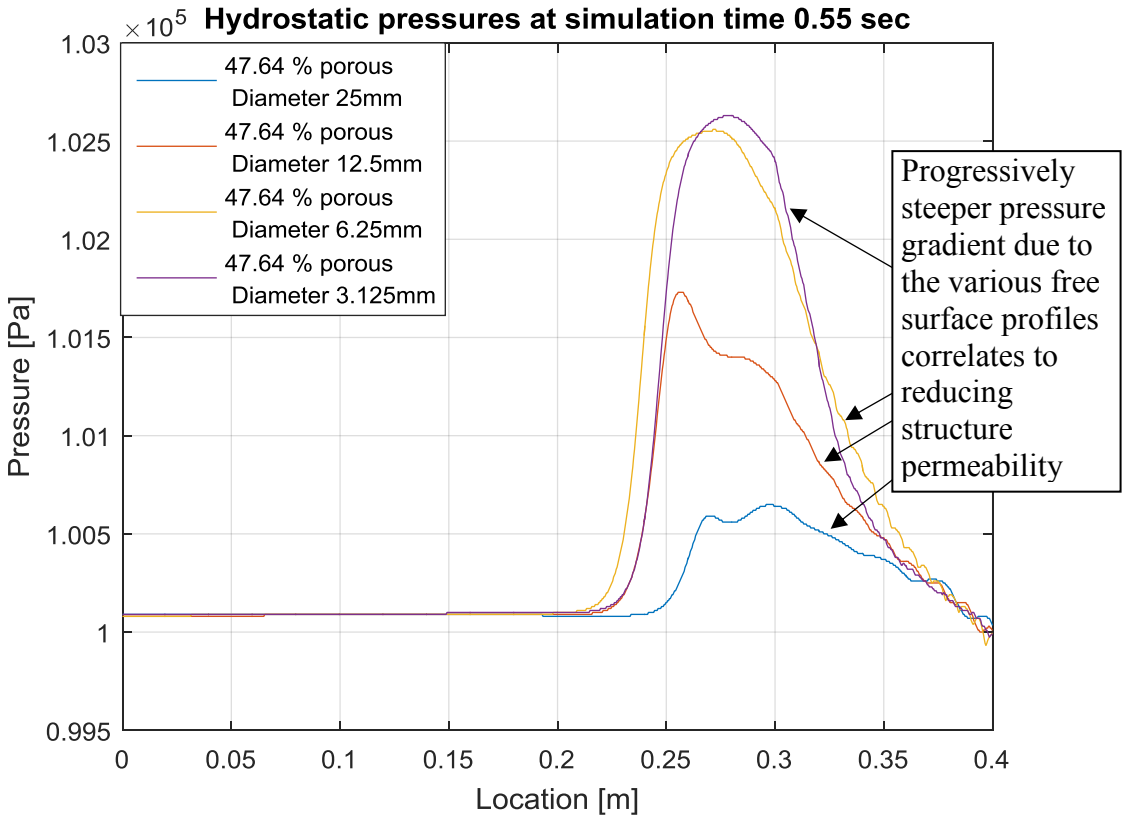

Figure 8.1.3 Quasi-hydrostatic pressure at simulation end time (including atmospheric pressure value)

Simple Cubic Packing Simulation Results						
Structure component sphere diameter	25 mm	18.75 mm	12.5 mm	9.375 mm	6.25 mm	3.125 mm
Impact impulse pressure	1390 Pa	1660 Pa	1990 Pa	1980 Pa	2420 Pa	2840 Pa
Max oscillatory pressure	650 Pa	830 Pa	1370 Pa	2030 Pa	2180 Pa	2440 Pa
Water outflow flow rate (end of simulation)	$8.341e^{-3}$ m^3/sec	$5.380e^{-3}$ m^3/sec	$7.032e^{-3}$ m^3/sec	$4.397e^{-3}$ m^3/sec	$3.143e^{-3}$ m^3/sec	$2.598e^{-3}$ mm^3/sec
Bubble Oscillation Frequency	298.5 Hz	202 Hz	224Hz	175 Hz	199Hz	174Hz
Bubble Oscillation Amplitude	51 Pa	146 Pa	300 Pa	571.8 Pa	557.6 Pa	580 Pa
Entrapped bubble radius (analytic prediction)	10.9 mm	16.2mm	14.6mm	18.7mm	16.4mm	18.8mm
Simulation Bubble Volume	12,284 mm^3	48,000 mm^3	12,190 mm^3	40,914 mm^3	16,423 mm^3	16,396 mm^3
Bubble Surface Area	3,930 mm^2	10,939 mm^2	3,800 mm^2	9,100 mm^2	4,294 mm^2	2,275 mm^2
Bubble (Cylindrical) Length	52 mm	100 mm	52 mm	100 mm	53 mm	54 mm
Bubble Sphericity*	0.6551	0.8552	0.6741	0.9241	0.7227	0.8642
Equivalent entrapped bubble radius (simulation) (c/s)	8.67/14.3 [mm]	22/12.4 [mm]	8.64/14.2 [mm]	21.4/11.4 [mm]	9.93/15.8 [mm]	9.83/15.8 [mm]
Kinematic tortuosity	0.944	0.952	0.952	1.00	1.011	1.003

*using Hakon-Wadell equation (see Section 8.1.4)

Table 8.1.1 Simple cubic packing simulation results

8.1.2 Pressure response at impact interface

Figure 8.1.4 below shows the pressure signal for each of the simulations at the various component sphere diameter porous structures. Also included on the figure is the pressure signal for a wave impact with a solid wall computed in the earlier phase of this study using a geometrically similar simulation setup. The solid wall impact results are also further discussed in Mayon et al. (2016).

Figure 8.1.5 (a) shows the pressure response recorded as the surging flow front impacts the solid and porous walls. There is a slight delay in the impact time for larger spheres as the wave front initially hits these spheres at a level below the position of P1 (see Figure 7.3.1) before flowing vertically up the surface of the sphere thereby inducing a pressure increase at the sampling point P1. This is due to the height of P1 above the numerical tank base being

relative to the sphere diameter; i.e. P1 is located at the 12.5 mm above the tank base of the for the 25 mm diameter spheres and at 6.25 mm above the tank base for the 12.5mm diameter spheres.

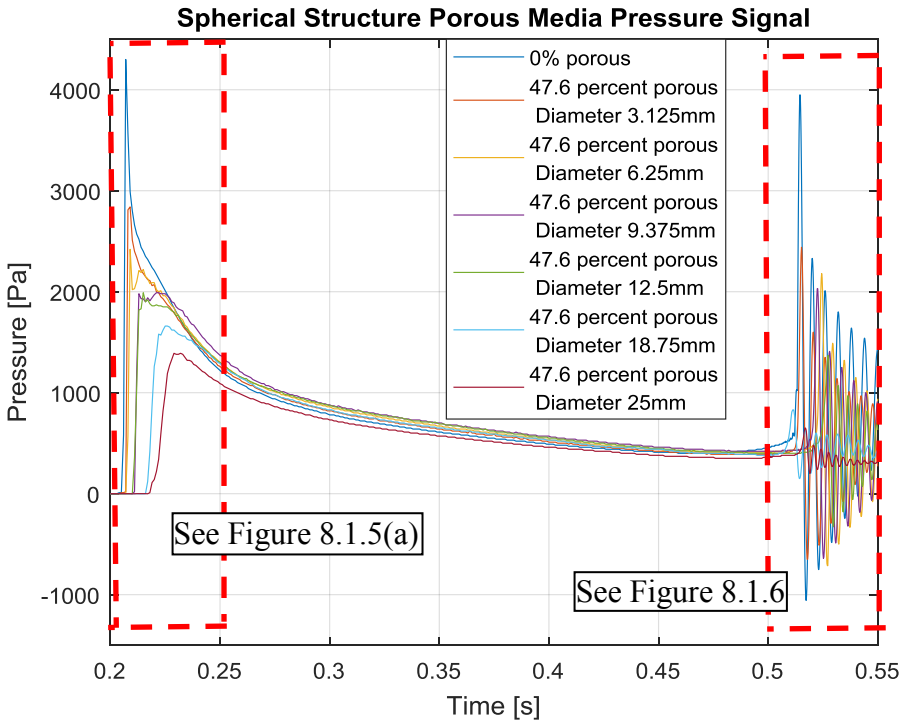

Figure 8.1.4 Cubic packed spheres pressure signal
(atmospheric pressure has been subtracted)

The porous structures composed of the larger spheres also exhibit extended impact durations, termed the rise time as discussed in Section 5.2.1, also see e.g. (Peregrine, 2003), (Mayon et al., 2016). Whilst the porosity of all the cubic packed sphere structures is identical, the void channels between the larger spheres are less numerous but have larger surface area openings in the plane perpendicular to the direction of flow, this allows the fluid to penetrate these void spaces more easily than the structure with more numerous but smaller surface area openings. Additionally, the porous structure assemblages comprising of smaller spheres have an overall larger magnitude wall friction value due to their greater specific surface area. This higher drag force decelerates the flow more rapidly producing a sharper impulse pressure impact force and also reduces the permeability of the porous structure. The result of the longer rise time is a softer, less impulsive impact for the larger sphere structure as shown on Figure 8.1.5(a). The higher flow rate through the larger sphere porous network also supports this assertion of reduced total drag force effect due to smaller specific surface area.

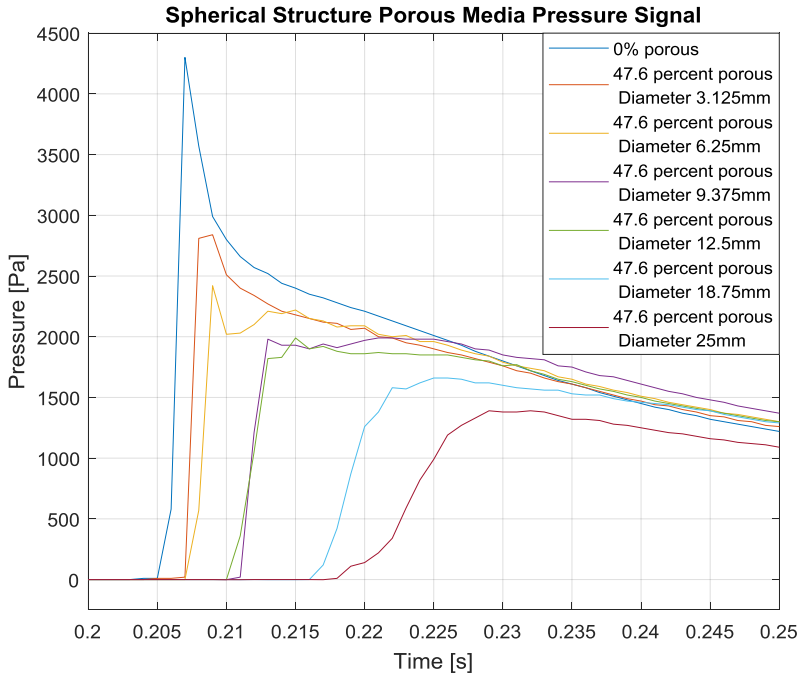

(a) Impulse pressures

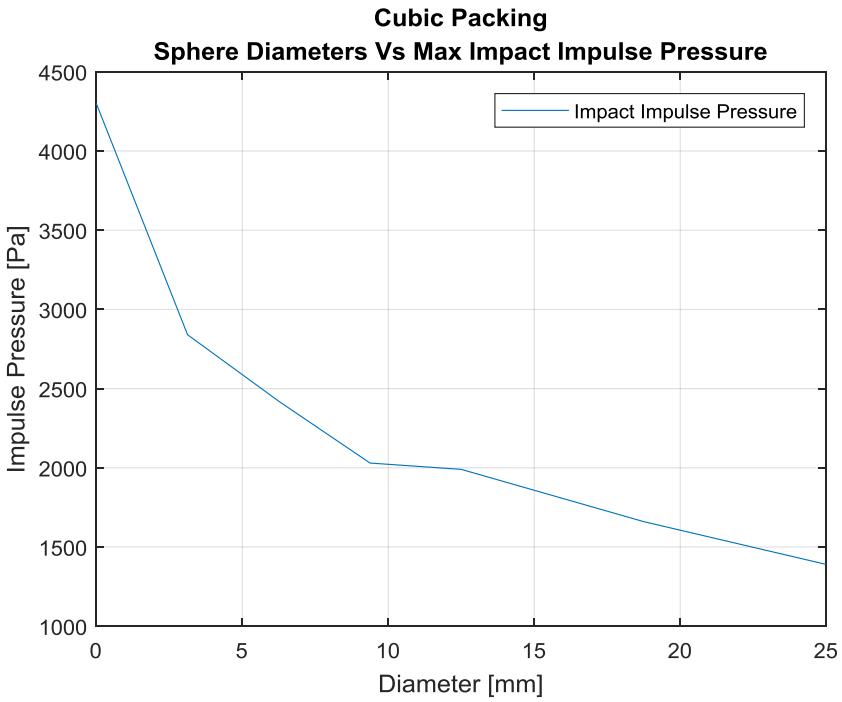

(b) Max Impact Impulse Pressure Vs Sphere diameter

Figure 8.1.5 Initial impact impulse pressure characteristics

Figure 8.1.5 (b) shows the relationship between the sphere diameter and the magnitude of the impulse force. The magnitude of the impulse decreases monotonically as the component sphere diameter increases. The magnitude of the impulse pressures are presented on Table 8.1.2.

Figure 8.1.6 displays a plot of the pressure signals for the various simulations as the formed vertical jet collapses and converges with the fluid in the bed of the domain. As the jet collapses a plunging breaker is formed as shown in Figure 8.1.2 for each of the porous simulations and a large air bubble is entrapped which compresses and dilates in a resonant oscillatory manner yielding the cyclic pressure response shown on Figure 8.1.4 and in detail on Figure 8.1.6.

As air within a bubble is compressible, a larger bubble will resonate with a lower frequency as the radial distance by which it can compress and dilate is volume dependent. Additionally, as these larger bubbles can compress to a greater extent relative to smaller bubbles, the amplitude of the oscillatory signal will be greater for the larger bubbles.

Figure 8.1.7 shows the oscillatory pressure signal for the simulation incorporating the porous structure composed of the 6.25 mm diameter spheres in cubic packing arrangement measured at point P1 in the simulation domain. The local maxima and local minima are indicated on the plot for oscillation cycle. Figure 8.1.8 shows the CFD simulation pressure contours at the corresponding times when these local maxima and minima values occur. By observing the time varying signal trend in Figure 8.1.8 in conjunction with Figure 8.1.7 it is clearly obvious that the entrapped air bubble is the source of oscillatory pressure signal. The contours emanating radially from the centre of the entrapped bubble exhibit increasing and decreasing pressure pulse behaviour in synchronicity with the cyclic pressure signal measured at point P1.

A comparison of the magnitude of the pressures peaks during the initial flow front impact with the maximum magnitude during the first cycle of the oscillatory phase for each respective simulation yields some interesting observations. These comparisons are shown on Table 8.1.2 below. As the porous medium component sphere size reduces the percentage difference between the pressure magnitude at the initial impact impulse and the pressure magnitude of first cycle during the pressure oscillation phase exhibits a generally corresponding reduction. During wave impact at a solid wall, the discrepancy is only 8%, however the reduction in recorded pressure is in excess of 50% with the larger component spheres. This shows that the detrimental effect of air entrainment and associated oscillatory pressures during wave impact can be controlled by modifying the morphology of the porous structure. By reducing the specific surface area of the porous structure (i.e. by constructing it from larger elemental units) a comparatively larger reduction in magnitude of the ensuing oscillatory pressures is obtained however this is at the expense of a higher structure permeability.

Cubic packed spheres pressure analysis							
Structure component sphere diameter	25 mm	18.75 mm	12.5 mm	9.375 mm	6.25 mm*	3.125 mm	Solid wall
Initial impact impulse pressure	1390 Pa	1660 Pa	1990 Pa	2030 Pa	2420 Pa	2840 Pa	4300 Pa
Max oscillatory pressure	650 Pa	830 Pa	1370 Pa	1980 Pa	2180 Pa	2440 Pa	3950 Pa
% increase or reduction	-53	-50	-31	-2	-10	-14	-8

*see Figure 8.1.7 for oscillatory pressure in-depth analysis

Table 8.1.2 Comparison of initial impact pressure with maximum oscillatory pressures

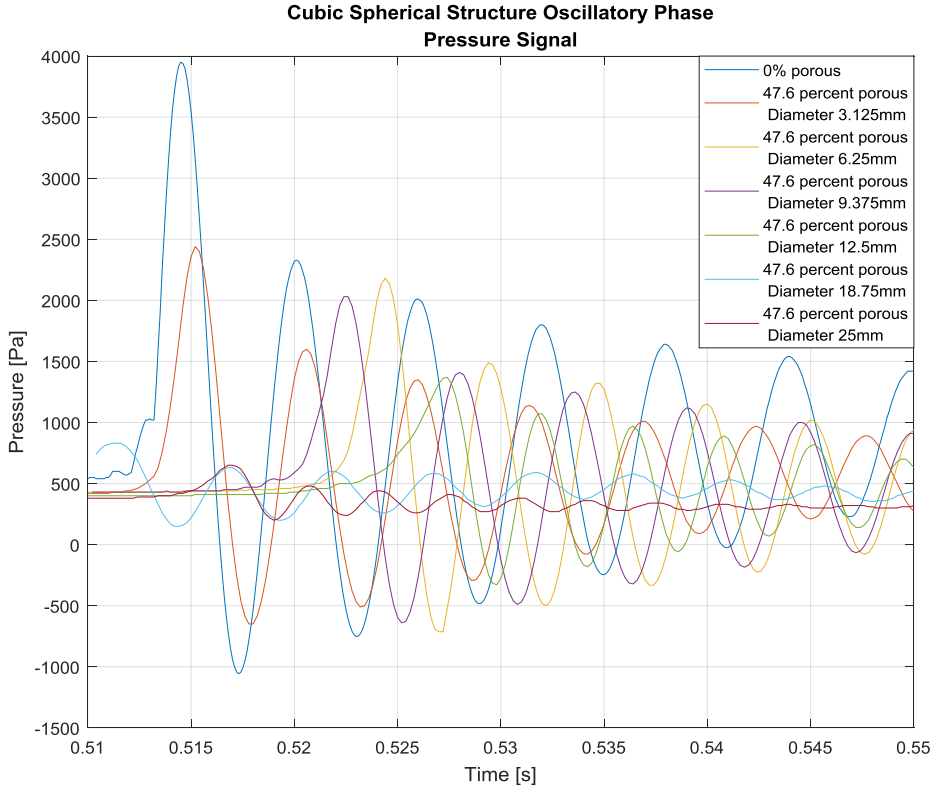

Figure 8.1.6 Oscillatory phase pressure signal for all cubic packed sphere simulations

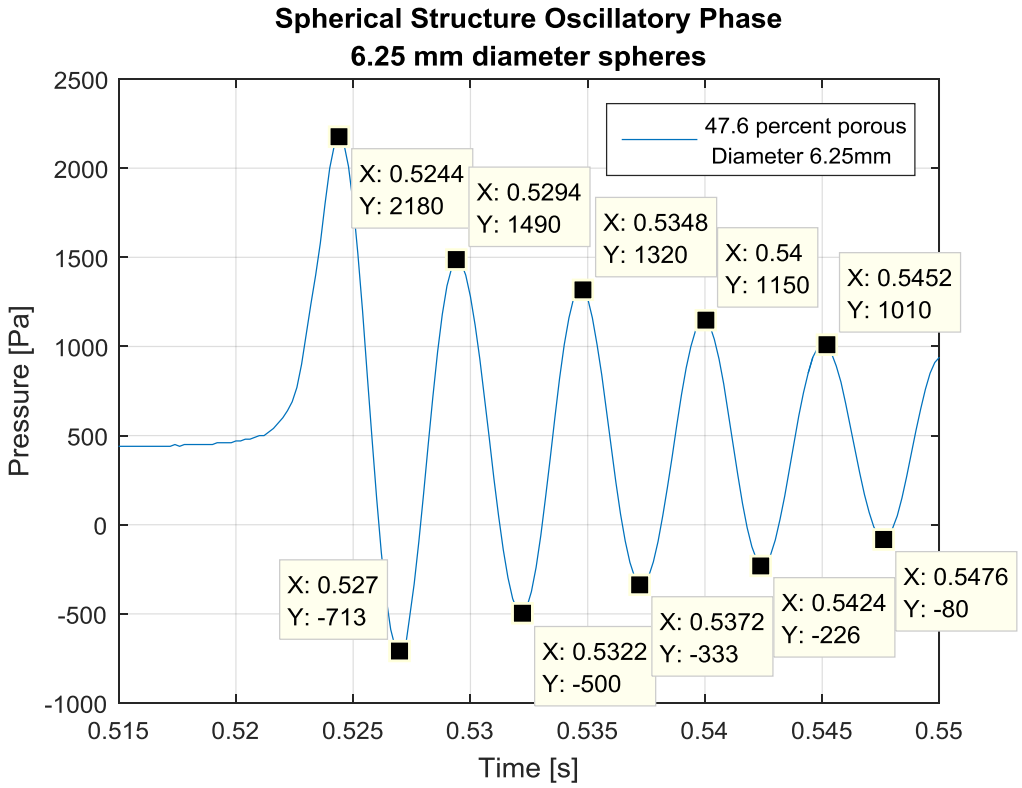

Figure 8.1.7 Oscillatory pressure signal for 6.25mm diameter spheres

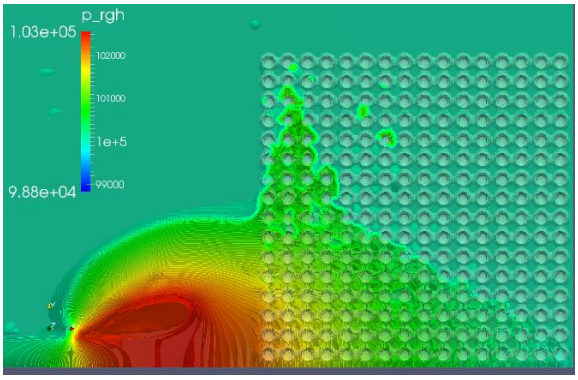

time t = 0.5244

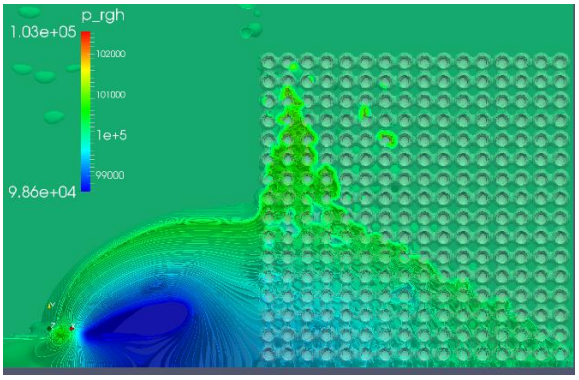

time t = 0.5270

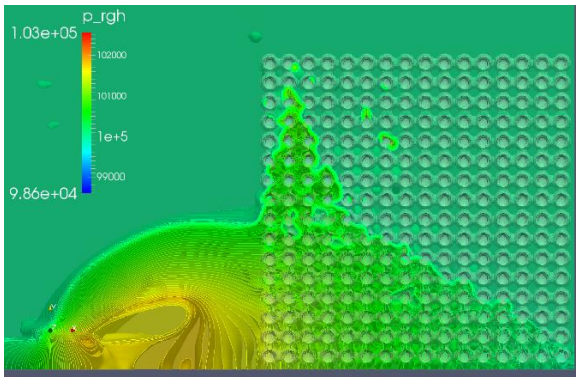

time t = 0.5294

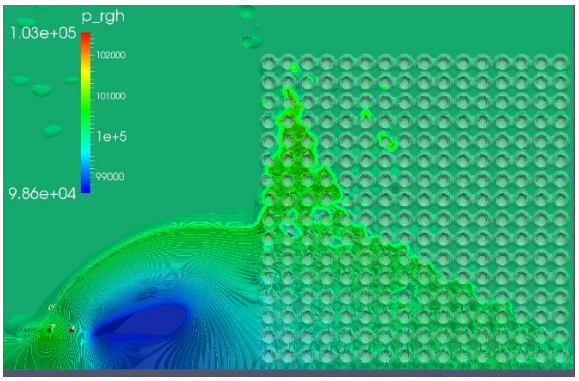

time t = 0.5322

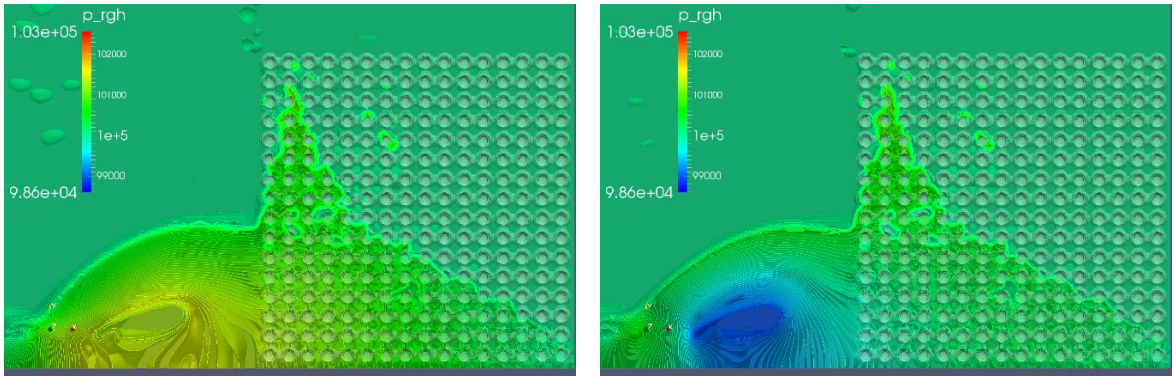

time t = 0.5348 time t = 0.5374

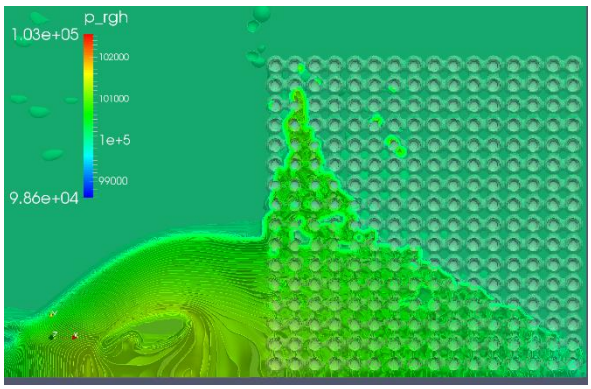

time t = 0.540

Figure 8.1.8 Time varying pressure contours at bubble entrainment for 6.25 mm diameter sphere simulation

8.1.3 Pressure response frequency domain analysis

The pressure signal data is converted from the time domain to the frequency domain by preforming a Fast Fourier Transform (FFT). Figure 8.1.9 shows the results of the transform and each of the dominant simulation signal frequencies and amplitudes are recorded in Table 8.1.1 above. The signal frequencies are plotted against the porous structure component sphere diameters on Figure 8.1.10(a) and the signal amplitudes versus the sphere diameters on Figure 8.1.10(b).

As discussed in Chapter 5 the pressure oscillation frequencies and amplitudes are related to the entrapped bubble size. As shown on Figure 8.1.10 the frequency of oscillation shows a generally increasing trend as the sphere diameter increases. Additionally the amplitude of the oscillation exhibits a decreasing trend. However, as shown in Table 8.1.1 the observed simulated bubble radii does not vary in a corresponding manner when compared to the component sphere diameter comprising the porous structure. This may be explained by a number of possibilities. As previously mentioned the smaller sphere based structure allows less fluid to penetrate. The effect of this is that more fluid will be rejected from passing through the face of the porous structure for these smaller sphere simulations. This in turn will cause a thicker jet to form where the thickness of the jet (z) is shown on Figure 8.1.2.

When this jet collapses it falls further away from the wall entraining a larger bubble. This larger bubble will have a lower pressure oscillation frequency and higher amplitude of pressure oscillation. Additionally, as shown on Figure 8.1.2(d) the small sphere structures may generate a jet which rises higher (due to a lower surface friction coefficient at the impact wall) and some of the fluid may overtop the structure and collapse on the top, permeating down through the voids thus supplying less fluid to the plunging jet. This may also result in a reduced thickness of the collapsing jet. The quantification of this surface friction is outside the scope of this study, nevertheless it is sufficient to say that that as the sphere sizes reduces, the surface of the porous structure which the incident wave impacts will be smoother.

As discussed in Section 5.3.1.1 the analytic relationship between oscillation frequency of a bubble and its radius derived based on the axiom that the bubble is surrounded by a very great water volume (Minnaert, 1933). In Figure 8.1.2 it is shown that the collapsing jet profiles vary greatly with the thickest entraining jets forming during the simulations incorporating the 12.5 mm and 6.25mm diameter component sphere structures. A thicker entraining jet will result in a stiffer bubble wall. Consequently these bubble should resonate with a higher frequency and lower amplitude.

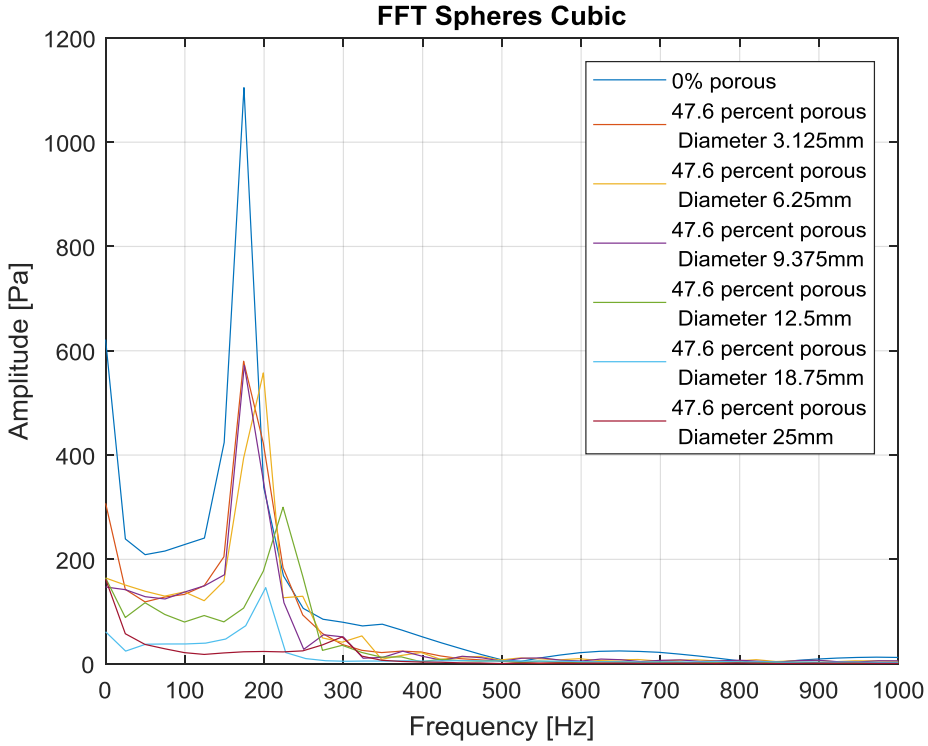

Figure 8.1.9 Oscillatory pressure signal frequency domain results

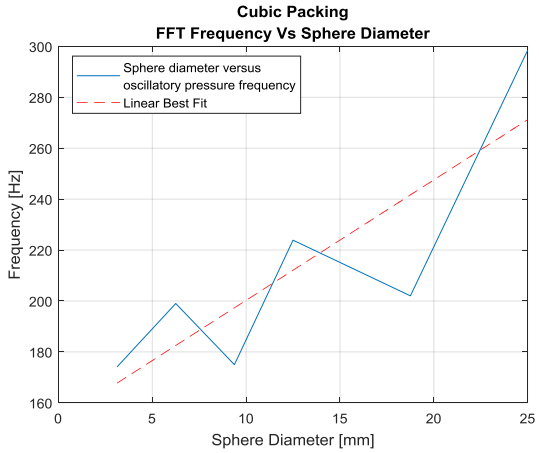

(a) Signal frequency Vs sphere diameter

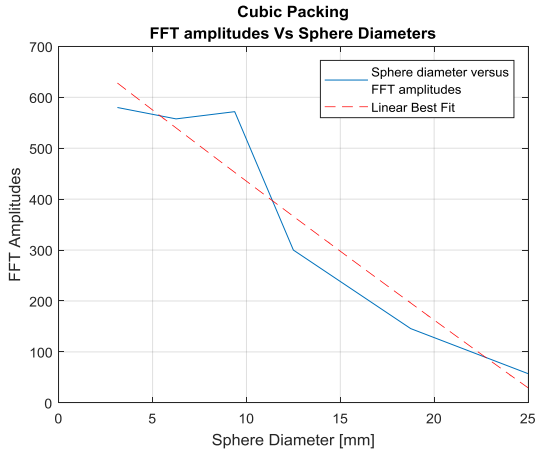

(b) Signal amplitude Vs sphere diameter

Figure 8.1.10 Sphere diameters Vs FFT results

8.1.4 Entrapped air bubble analysis

The discrepancy between the observed bubble volumes, their oscillating frequency and amplitude and the predicted values from the Minnaert equation may be further accounted for by the bubbles' shape. Previous researchers have put forward contrasting opinions on the influence of sphericity on the oscillation frequency of a bubble. Strasberg (1953) states that the oscillation frequency of non-spherical bubbles varies only slightly from the oscillation frequency of spherical bubbles, however both Weston (1966) and Feuillade and Werby (1994) in their studies on non-spherical bubbles (focussing on oblate and prolate spheroid shapes) have shown the frequency of oscillation may increase by up to 40% depending on the degree of non-sphericity. Thus for similar volume bubbles their shape may have a large influence on the observed results. Figure 8.1.11 shows that there is a large variation in the shape of the bubbles generated in the different simulations. Table 8.1.1 records the bubble sphericity for each of the simulations. This is presented as an index originally devised by Wadell (1935). A value of unity indicates a perfect sphere and as the value reduces from 1 the considered shape deviates further from sphericity. An ideal cylinder has an index value of 0.874. The index is calculated according to Equation 8.1 Wadell (1935) :

$$\Psi = \frac{\pi^{\frac{1}{3}}(6V_v)^{\frac{2}{3}}}{A_v} \qquad (8.1)$$

Where V_v and A_v are the volume of the bubble and the surface area of the bubble respectively. The bubble shape tends towards a more uniform cross section (cylindrical) in the plane of the x-y axis as the component sphere size forming the porous structure reduces as shown on Figure 8.1.11 for the final simulation time step. In Table 8.1.1 an entry has been recorded for equivalent entrapped bubble radius (c/s). These values are the calculated radii of perfect

cylinders and spheres computed using the recorded simulation bubble volume. In the cases where the sphericity index calculated using equation 8.1 approaches the ideal cylinder value the analytic bubble radius prediction value (calculated using the Minnaert equation) in Table 8.1.1 agrees quite well with computed equivalent cylinder radius.

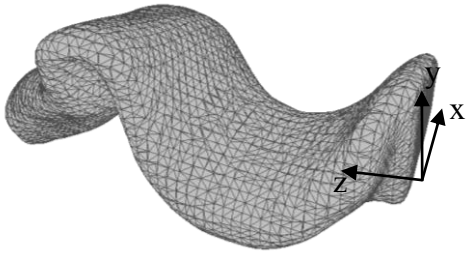

(a) Entrapped Bubble geometry from 25mm sphere diameter simulation

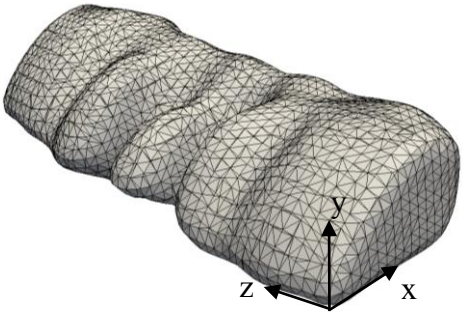

(b) Entrapped Bubble geometry from 18.75mm sphere diameter simulation

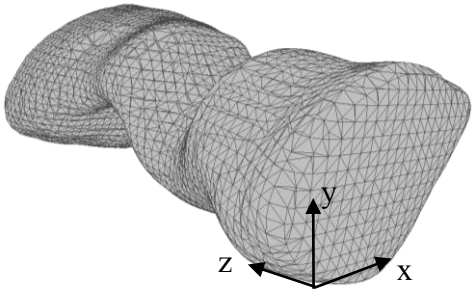

(a) Entrapped Bubble geometry from 12.5mm sphere diameter simulation

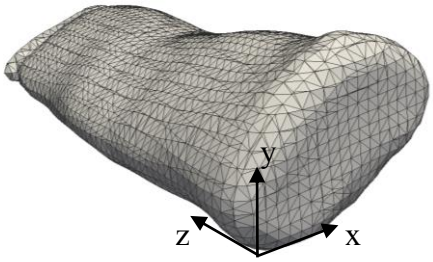

(b) Entrapped Bubble geometry from 9.375mm sphere diameter simulation

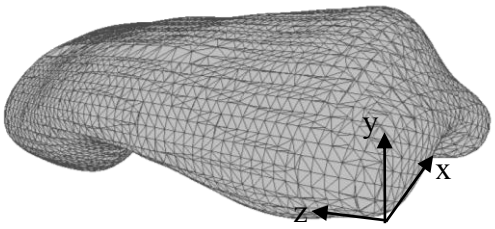

(c) Entrapped Bubble geometry from 6.25mm sphere diameter simulation

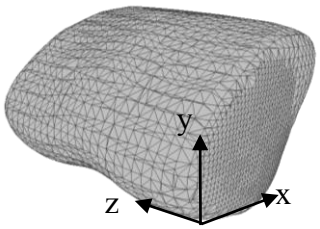

(d) Bubble geometry from 3.125mm sphere diameter simulation

Figure 8.1.11 Entrapped Bubble Geometries

8.1.5 Pressures attenuation at impact surface and within porous sphere structure

Figure 8.1.12 shows the attenuation trends for the oscillatory pressures measured at point P1 computed from the respective simulations for the different component sphere sizes. Also shown on the figure is the 0% porous simulation oscillatory pressure signal (i.e. wave impact with the solid wall). It is clear that the pressure attenuation rate is lower for the larger component spheres porous geometries, indicating that a low amplitude oscillatory pressure

signal is temporally more persistent. The attenuation rates have been mathematically determined for the simulations as single term exponential decays. In order to achieve a good fit, a normalisation and scaling process had to be applied to the exponential decay rate input predictor data. The procedure to normalise the input data required that the vector of time data points were centred at zero mean and scaled to unit standard deviation as shown in Equation 8.2 and described in MATLAB documentation (MathWorks, 2015). Example data for the time normalisation process to determine the exponential decay rate for the 0% porous simulation is shown on Table 8.1.3. By applying this normalisation technique to the input data, an improved accuracy exponential decay rate expression could be obtained for each of the oscillatory signals. This data is presented in Table 8.1.4.

$$t_{new} = \frac{(t - \text{mean(t)})}{std(t)} \tag{8.2}$$

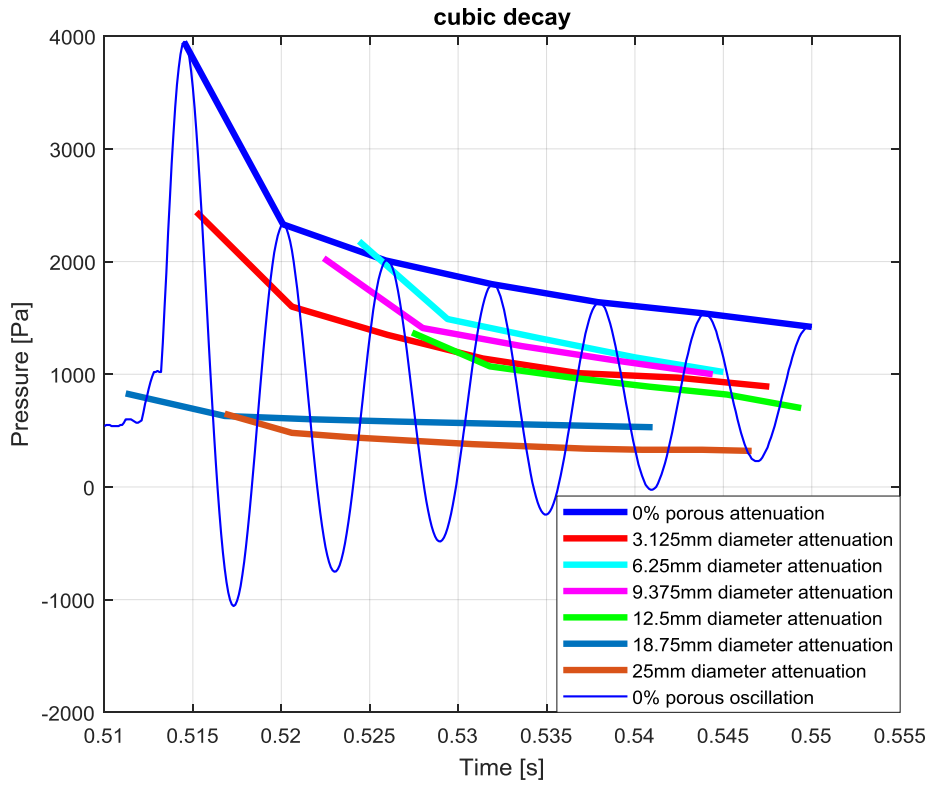

Figure 8.1.12 oscillation decay rates for cubic sphere packed simulations

Normalisation process for 0% porous simulation							
0% porous time data points (t)	0.5145	0.5201	0.5259	0.5319	0.5379	0.5439	0.55
mean (t)	0.532						
Standard deviation (t)	0.01282						
0% porous normalised time data points (t_{new})	-1.3651	-0.9282	-0.4758	-0.0078	0.4602	0.9282	1.4041

Table 8.1.3 normalised inputs for 0% porous simulation

Simple Cubic Packing oscillatory pressure attenuation rates	
Solid wall attenuation (0% porous)	$1938e^{-0.4113t_{new}}$
3.125mm diameter spheres	$1242e^{-0.4107t_{new}}$
6.25mm diameter spheres	$1373e^{-0.3169t_{new}}$
9.375mm diameter spheres	$1314e^{-0.2935t_{new}}$
12.5mm diameter spheres	$946e^{-0.2382t_{new}}$
18.75 mm diameter spheres	$626e^{-0.1703t_{new}}$
25mm diameter spheres	$393e^{-0.2388t_{new}}$

Table 8.1.4 Exponential oscillatory decay rates for cubic packed sphere simulations

The oscillatory pressure signal was also sampled at varying locations within the porous structure. It was observed that in addition to a temporal decay in the amplitude of the pressure signal there was also a spatial reduction in the pressure amplitude as sample point locations receded further away from the impact interface and deeper into the porous matrix. Figure 8.1.13(a-d) shows spatio-temporal pressure signal attenuations within the porous media for four of the cubic sphere packed porous structures. As noted earlier in this section the oscillatory pressures attenuate more rapidly in the temporal dimension within the structures comprised the smaller component sphere sizes. However, as the porous structures composed of the smaller component spheres exhibit a higher specific surface area, a larger volume of fluid is trapped within the void space and this transfers the oscillatory pressures through these porous structure more readily and deeper into the structure. This effect is particularly evident in the 3.125 mm diameter component sphere structure where there is there is very little damping of the pressure signal within the first 30 mm (from the impact interface) of the porous structure.

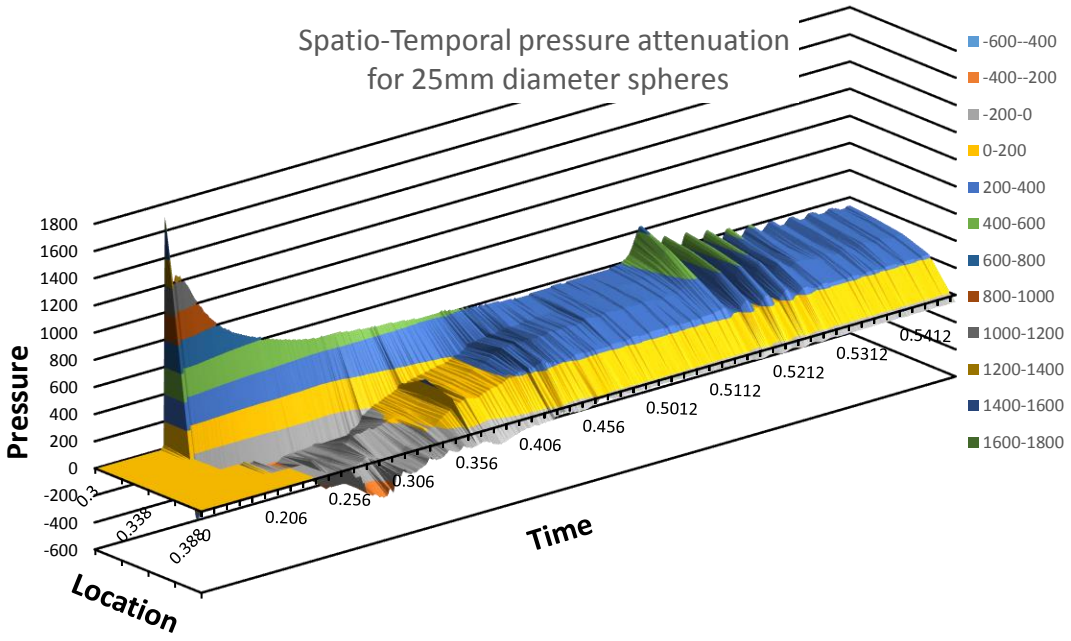

(a) Spatio-temporal pressure attenuation for 25 mm diameter sphere structure

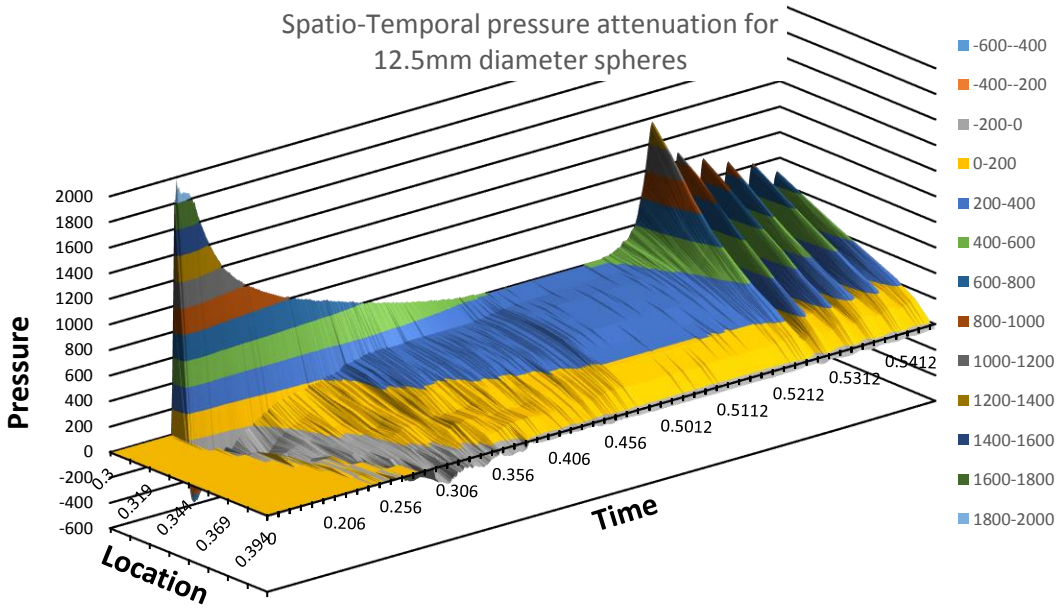

(b) Spatio-temporal pressure attenuation for 12.5 mm diameter sphere structure

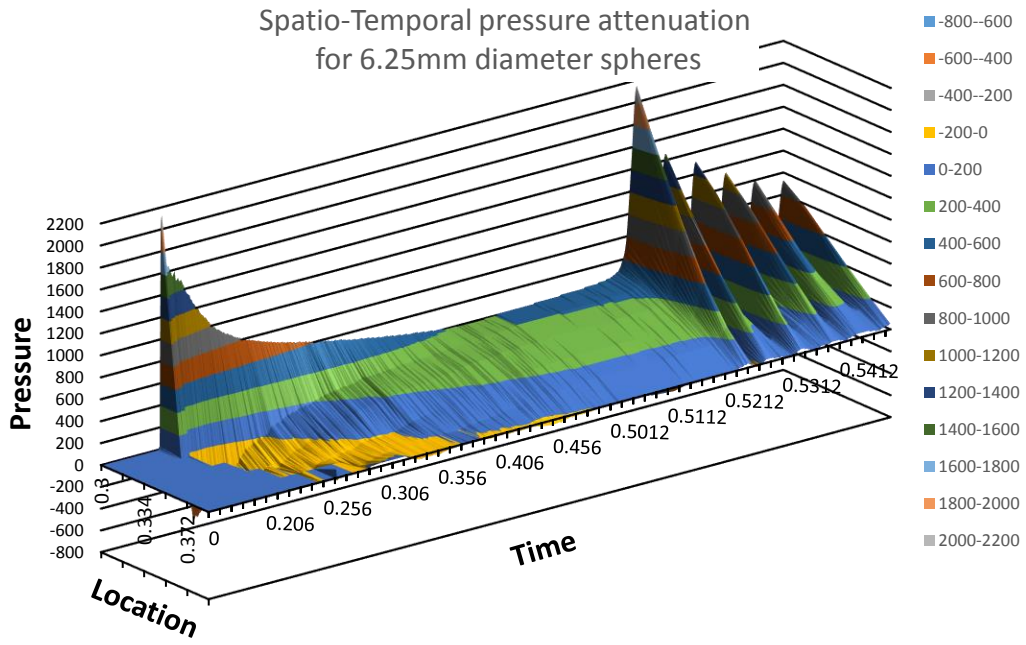

(c) Spatio-temporal pressure attenuation for 6.25 mm diameter sphere structure

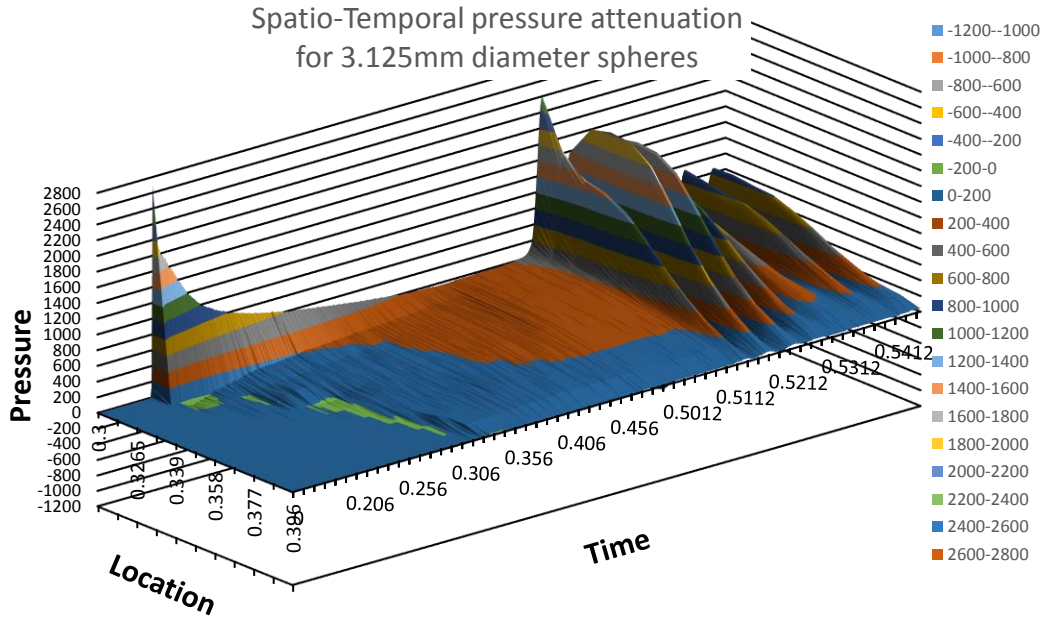

(d) Spatio-temporal pressure attenuation for 3.125mm diameter sphere structure

Figure 8.1.13 Spatio-temporal pressure attenuation
for each cubic sphere packed porous structure simulation

8.1.6 Tortuosity

Earlier experimental investigations on tortuosity using porous sample conductivity measurements by Chen (1973) and later by Wyllie and Rose (1950) in which they focussed on simple cubic packed spheres have suggested tortuosity values of 1.2 and 1.6 respectively

for this morphology. Figure 8.1.14 shows a sampled section through the domain displaying the F-function at the simulation time-step when the liquid phase reaches the outflow boundary for three of the larger component sphere simulations. It should be noted that there is a 1 mm gap between the bed of the tank and the base of the spheres. This is to allow the porous structure to be accurately meshed. Without this gap the meshing algorithm connects the base of the sphere with the numerical tank base causing preferential flow channels to be created at bed of the tank underneath the porous structure. The flow pattern observed at the bed of the tank is shown to follow preferential pathways between the spheres, this phenomenon has been described in earlier studies and is termed unstable infiltration or fingering instability (Gomez et al., 2013). Stable infiltration describes the flow profile wherein the advancing fluid leading edge moves forward with a uniform front. The observed instability patterns in Figure 8.1.14 may be due to drag effects at the base of the spheres. It is also revealed that as the component sphere size reduces, the flow infiltration regime is transitioning from an unstable process to a stable process.

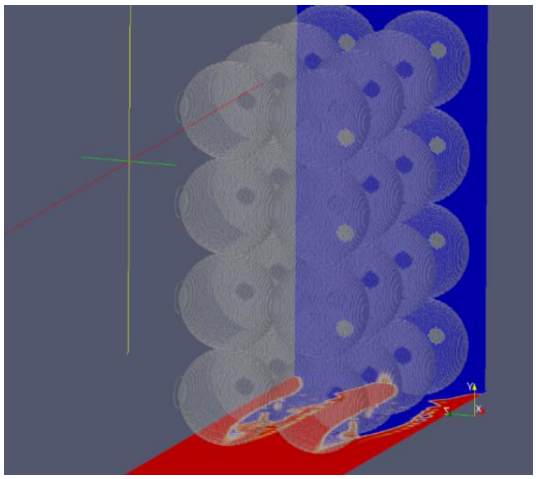

(a) 25mm diameter spheres

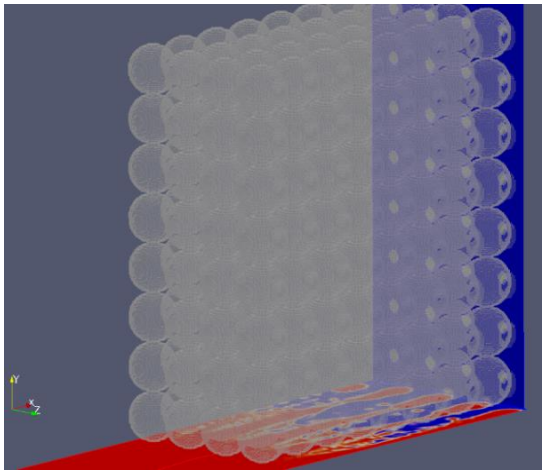

(a) 12.5mm diameter spheres

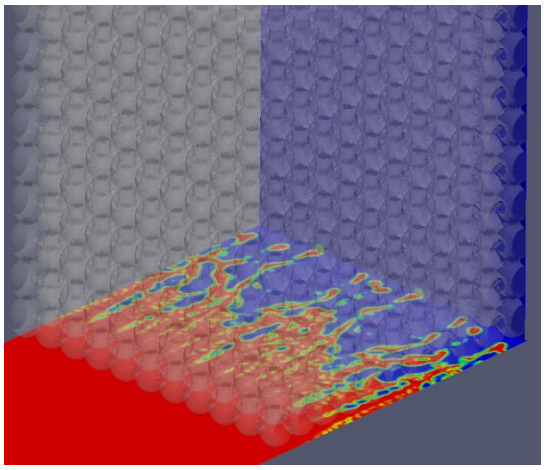

(b) 9.375mm diameter spheres

Figure 8.1.14 unstable infiltration into porous structures

In this numerical study the shortest flow streamline extracted from the simulation results demonstrate that the flow vectors do not deviate significantly from the shortest straight line path when permeating through the porous sphere structure, thus yielding a hydraulic tortuosity value slightly greater than 1. This value is in contrast to the experimental values promulgated by Chen (1973) Wyllie and Rose (1950) of 1.2 and 1.6 respectively. Figure 8.1.15 displays the shortest flow path streamline followed by a fluid element in the 25mm diameter component sphere porous structure simulation. Figure 8.1.15(a) shows the section through the domain perpendicular to the x axis (i.e. perpendicular to the main direction of flow) and Figure 8.1.15 (b) shows a plan view of this streamline. It is obvious from Figure 8.1.15 that the flow streamline does not deviate significantly in the y and z plane thus supporting an approximate unit value for kinematic tortuosity.

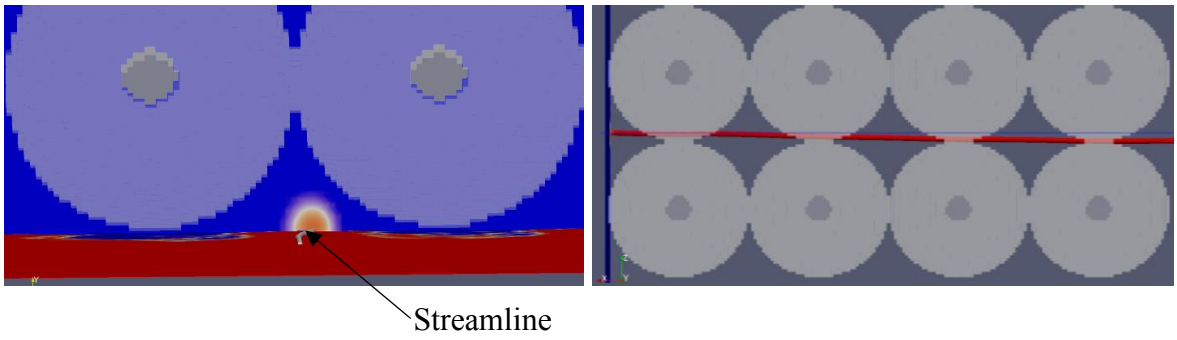

(a) Section perpendicular to x axis showing the streamline (grey line)

(b) Plan view showing the streamline (red line)

Figure 8.1.15 Flow path streamline through 25mm diameter cubic packed sphere structure

In the absence of any obstacle impeding the flow, the surging wave front is projected to reach the outflow boundary at a time of 0.270 seconds. This time is obtained by extrapolating the data from Figure 5.2.5. However as shown on Figure 8.1.16 the water phase reaches the right hand side boundary at reduced times of 0.243 and 0.258 seconds for the 25 mm diameter spheres and the 12.5 mm diameter sphere structures respectively. The 6.25 mm and the 3.125 mm sphere structures have slightly increased the projected time taken for the water to reach the outflow boundary to 0.273 and 0.271 seconds respectively. Therefore, although the shortest flow streamline is longer than the shortest straight line path, the fluid traverses this streamline distance in a shorter time (in the larger sphere structures). The constricting inter-particle void throats in the larger diameter sphere structures may act to accelerate the flow within the porous media through the formation of jets in a similar manner as observed during constricted flow through nozzles. This phenomena may account for the reduced time for the

liquid phase to pass through the larger diameter sphere structure. In contrast, the higher surface area of the smaller sphere structures may decelerate the flow due to higher wall friction and consequently increased drag force, thus the water phase will take longer to reach the outflow boundary. These effects have been previously observed by Bernabe (1991) during experimental studies and he termed it kinematic tortuosity. However he only considered the retarding effects of constrictions on the flow velocity. Clennell (1997) in his review paper on tortuosity also addressed the subject of kinematic tortuosity, again only the decelerating effect of constrictions on the flow were considered. He suggests that kinematic tortuosity is a misnomer and 'local flow divergence' is a better term. This term 'local flow divergence' would seem to suggest that constrictions will always retard the flow velocity which is not the case as demonstrated in this study. Additional analysis is warranted to establish the threshold orifice size which acts to either accelerate or to slow down the flow velocity through the porous geometry.

The minimum theoretical value of hydraulic tortuosity for each these structures is $\tau = 1$ and as previously shown the shortest flow path through the porous assembly follows an approximately linear streamline. Nevertheless using the time taken from the flow to pass from the impact interface to the outflow boundary it has been demonstrated that the geometry acts to accelerate the conductance of fluid in the larger component sphere structures. Then, the value for tortuosity obtained from the numerical simulations is not only spatially dependent but also temporally influenced as a consequence of the acceleration or deceleration of flow through the geometry. In this regard the term kinematic tortuosity, τ_k, is reintroduced for this analysis and its value permitted to possess a value less than unity according to Equation 8.3.

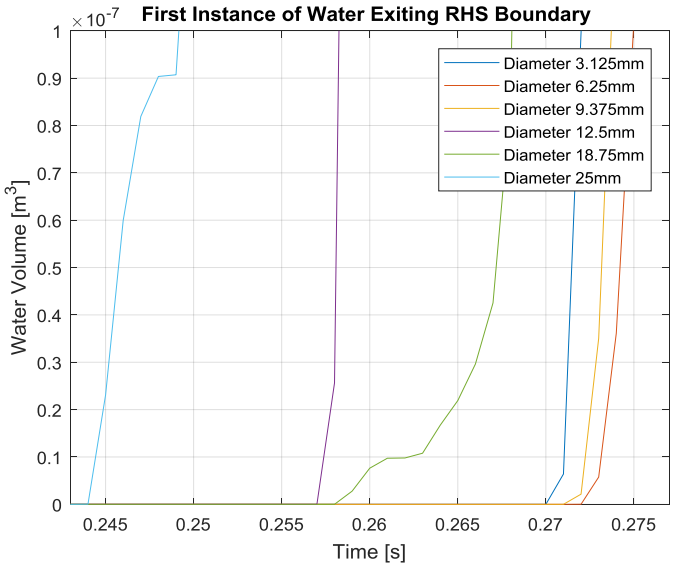

Figure 8.1.16 water phase flow volume at outflow boundary

$$\tau_k = \frac{T_{le}}{T_l} \qquad (8.3)$$

Where T_{le} is the time taken for a fluid element to flow through a porous sample in which the inflow and outflow faces are separated by the distance x and T_l is the time taken for a fluid element to flow through a similar unobstructed distance x.

8.1.7 Permeability

The final topological property which was investigated was the porous structure's permeability. The rate of conveyance of each fluid phase (air and water) through the right hand side boundary for each of the porous structures was determined; this data is shown on Figures 8.1.17a – d. The first plot shows the flow rate for all phases combined.

The second plot shows the flow rate thorough the boundary for the air phase only. The boundary conditions were programmed such that the outflow and inflow of air was permitted across this surface, however, for the water phase only outflow behaviour was permitted. A negative flow rate represents the flow of air into the simulation domain across this boundary. The air flow rate outwards through the boundary increases until approximately the time when the water phase starts to flow out of the domain. At this point outward air flow rate starts to decrease. All but the 3.125 mm diameter sphere simulation exhibit inflow of air into the domain across this boundary. The air flow rate across this boundary also exhibits oscillatory behaviour. These oscillations can be correlated to the cyclic volumetric fluctuations of the entrapped air pocket. As the entrapped air bubble expands air is forced outwards through the boundary and as the bubble contracts air is drawn into the domain.

Figure 8.1.17c shows the outflow rate for the water phase for each of the cubic sphere packed simulations. Although all the structures have identical porosities, those assemblies composed of larger spheres exhibit a higher permeability. The flow rate through these larger diameter sphere structures is relatively irregular in comparison to the smaller diameter sphere component structures. The oscillatory trend in the flow rate for the 25mm diameter sphere simulations indicate that the structure has a large influence on the rate of flow through it. The flow rate is shown to escalate and diminish cyclically as the liquid volume flowing over, under and around the spheres increases and decreases. It is observed that the simulation runtime is not sufficient for the flow to exhibit quasi-steady state behaviour with the observed fluctuations due to the highly vuggy nature of the void space between the spheres controlling the rate of flow through the structure. The 18.75 and 12.5 mm diameter spheres

structures follow a similar trend to the 25 mm spheres structure but they transitions to a quasi-steady state at an earlier time within the simulation. There are some fluctuations in the flow rate record but with much lower amplitudes. The 9.375mm sphere simulation exhibits a reasonably steady state flow rate from 0.375 to 0.45 seconds simulation time, there after there is a large increase in the flow rate. This increase can be correlated to the jet collapsing and forcing a larger volume of water out through the RHS domain boundary.

The 6.25 mm diameter and the 3.125 mm diameter spheres structures exhibit a very similar trend in permeability. The flow rates are more uniform indicating that the vuggy nature of the porous structure is less influential on the permeability and the rate of flow is controlled more effectively by the pore throats. The 3.125 mm diameter spheres structure reaches a relatively constant steady state flow rate at about 0.355 seconds simulation time. However the 6.25 mm diameter sphere simulation takes longer to reach a steady state flow rate and the rate of flow is slightly greater

It is also interesting to note that as the sphere size increases (for the three smallest diameter spheres structures), the quasi-steady flowrates increase correspondingly with a proportionality constant of approximately 2.385. There are no oscillations in the water phase flow rate to correspond to the volumetric fluctuation of the entrapped bubble as the simulation initial conditions did not allow for the inflow of water across this boundary. The final plot on Figure 8.1.17 shows the cumulative volume of water flowing through the outflow boundary.

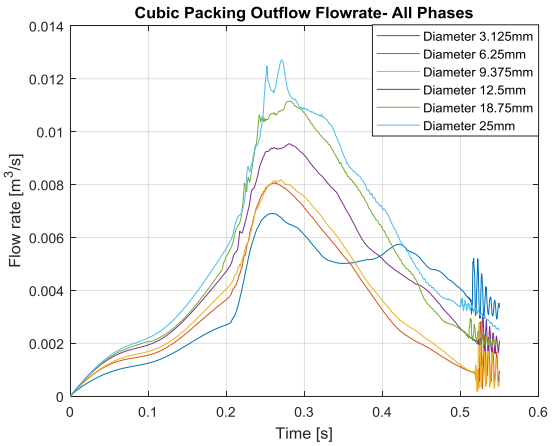

(a) Outflow through RHS boundary (all phases)

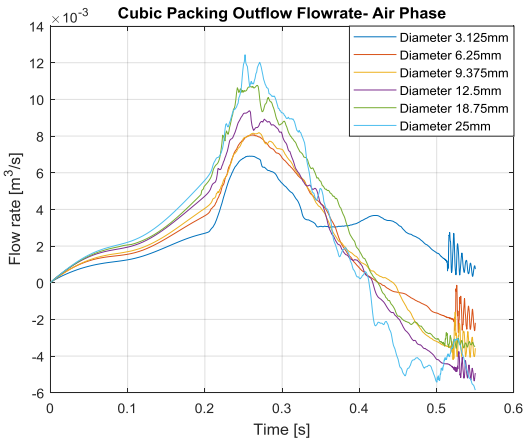

(b) Outflow through RHS boundary (air phase)

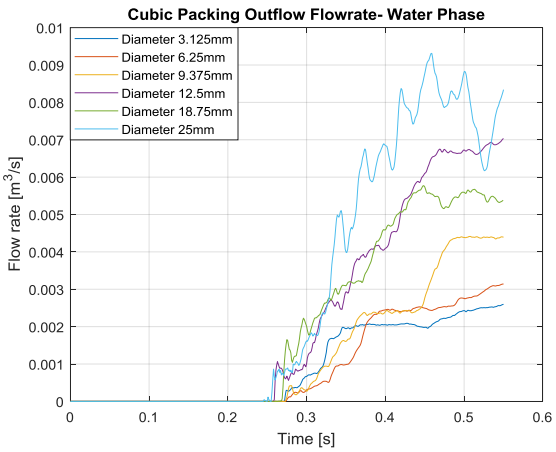

(c) Outflow through RHS boundary (water phase)

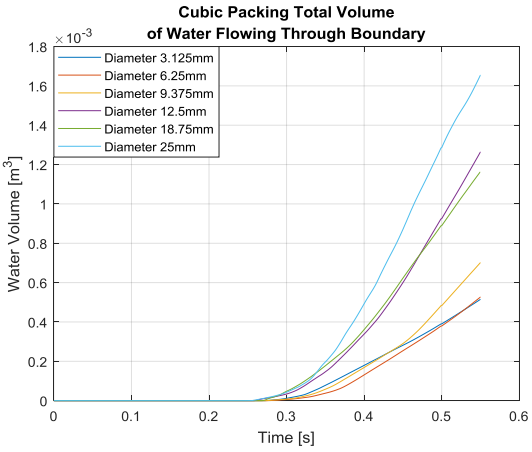

(d) Cumulative Outflow through RHS boundary (water phase)

Figure 8.1.17 Cubic packed spheres structures permeability plots

8.2 Orthorhombic packing sphere lattice

In this section the results from the orthorhombic packing simulations are presented. Similar analysis and arguments can be made as was discussed in the previous section wherein the cubic packed simulations were analysed. Therefore the commentary on the results in this section is restricted to those cases wherein an interesting finding is observed

Orthorhombic packing simulation results					
Structure component sphere diameter	25 mm	18.75 mm	12.5 mm	9.375 mm	6.25 mm
Impact impulse pressure	1290 Pa	1690 Pa	2000 Pa	2450 Pa	2560 Pa
Max oscillatory pressure	2060 Pa	2060 Pa	2320 Pa	2640 Pa	1700 Pa
Water outflow flow rate (end of simulation)	$3.813e^{-3}$ m^3/sec	$2.901e^{-3}$ m^3/sec	$2.140e^{-3}$ m^3/sec	$2.296e^{-3}$ m^3/sec	$1.717e^{-3}$ m^3/sec
Bubble Oscillation Frequency	174 Hz	174 Hz	175 Hz	174 Hz	202 Hz
Bubble Oscillation Amplitude	582 Pa	634 Pa	749 Pa	759 Pa	461 Pa
Entrapped bubble radius (analytic predic-tion)	18.8 mm	18.8 mm	18.7 mm	18.8 mm	16.2 mm
Simulation Bubble Volume	36,092mm^3	40,192 mm^3	30,836 mm^3	34,809 mm^3	10,503mm^3
Bubble Surface Area	7,847 mm^2	8,484 mm^2	6,907 mm^2	7,319 mm^2	3,391mm^2
Bubble Length (Cylindrical)	100 mm	100 mm	88mm	79 mm	46 mm
Bubble Sphericity	0.67	0.67	0.69	0.70	0.68
Equivalent en-trapped bubble ra-dius (simulation) (c/s)	20.5/10.72 [mm]	21.25/11.31 [mm]	19.45/10.56 [mm]	20.26/11.84 [mm]	13.59/8.53 [mm]
Kinematic tortuosity	0.941	0.922	0.963	0.996	0.981

Table 8.2.1 Orthorhombic packing simulation results

8.2.1 Flow profile and free surface evolution

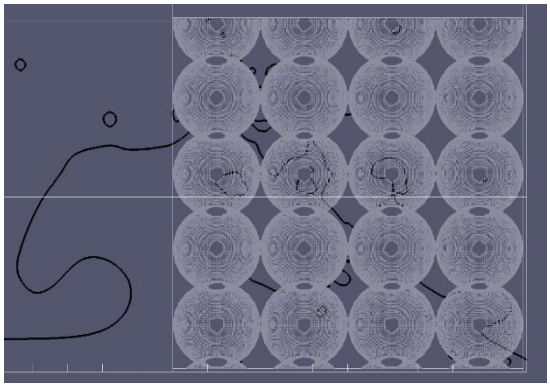

(a) 25 mm diameter sphere structure

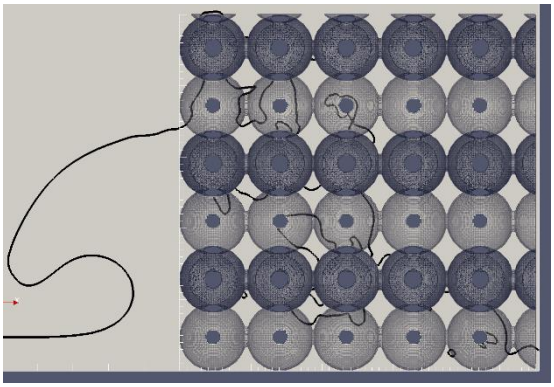

(b) 18.75 mm diameter sphere structure

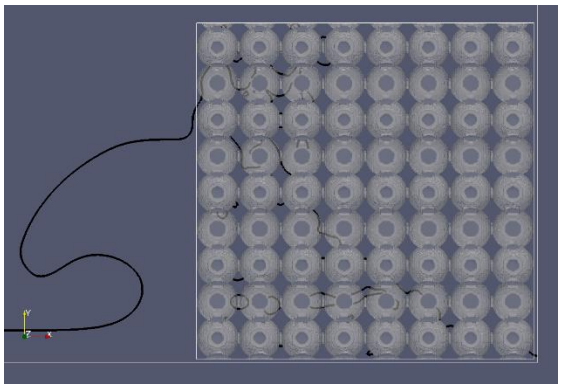

(c) 12.5 mm diameter sphere structure

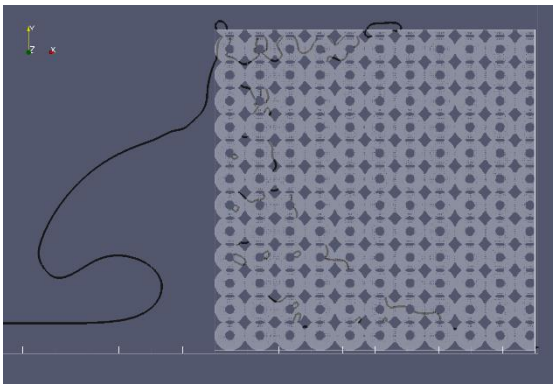

(d) 9.375 mm diameter sphere structure

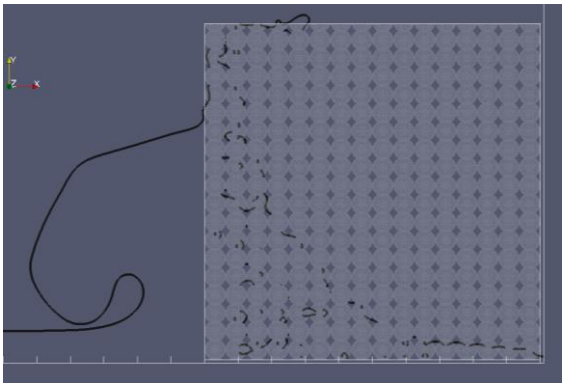

(e) 6.25 mm diameter sphere structure

Figure 8.2.1 Free surface profiles
at orthorhombic packed porous sphere structures

8.2.2 Pressure response at impact interface

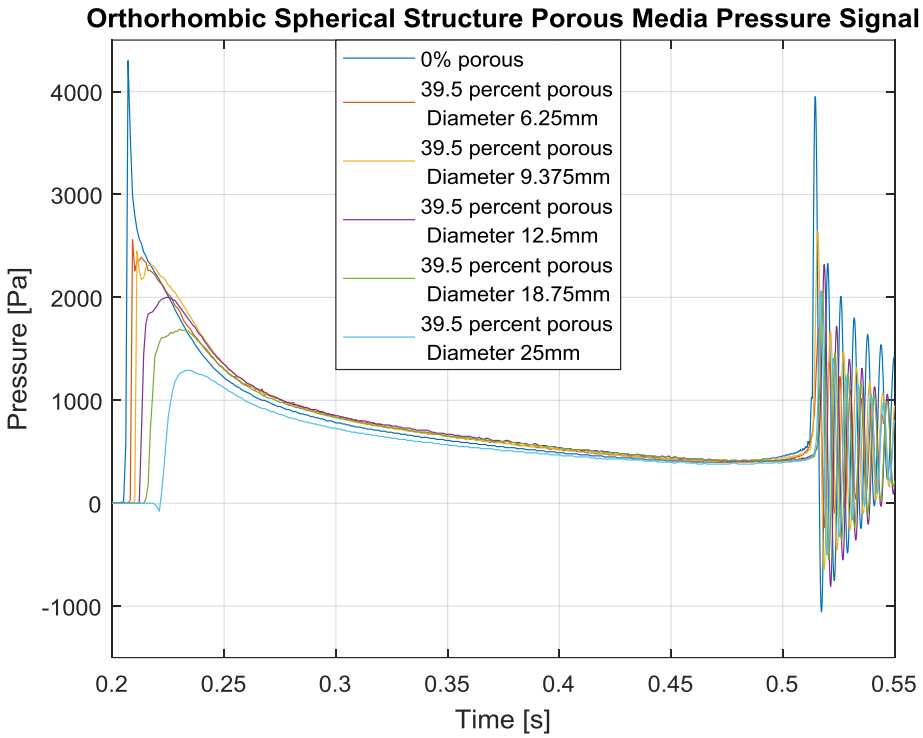

Figure 8.2.2 Orthorhombic packed spheres pressure signal (atmospheric pressure has been subtracted)

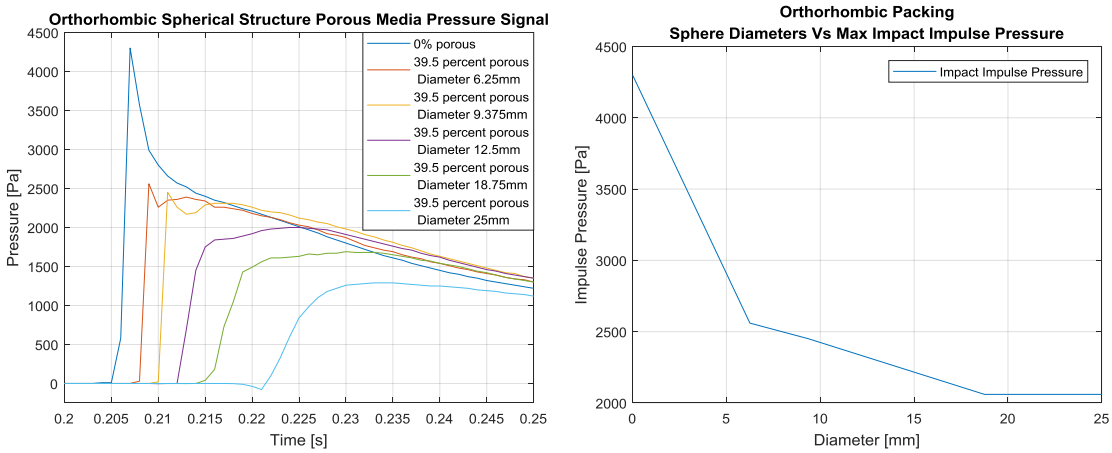

(a)Impulse pressures (b) Max Impact Impulse Pressure Vs Sphere diameter

Figure 8.2.3 Initial impact impulse pressure characteristics

Orthorhombic packed spheres pressure analysis						
Structure component sphere diameter	25 mm	18.75 mm	12.5 mm	9.375 mm	6.25 mm	Solid wall
Initial impact impulse pressure	1290 Pa	1690 Pa	2000 Pa	2450 Pa	2560 Pa	4300 Pa
Max oscillatory pressure	2060 Pa	2060 Pa	2320 Pa	2640 Pa	1700 Pa	3950 Pa
% increase or reduction	60	22	16	8	-34	-8

Table 8.2.2 Comparison of initial impact pressure with maximum oscillatory pressures

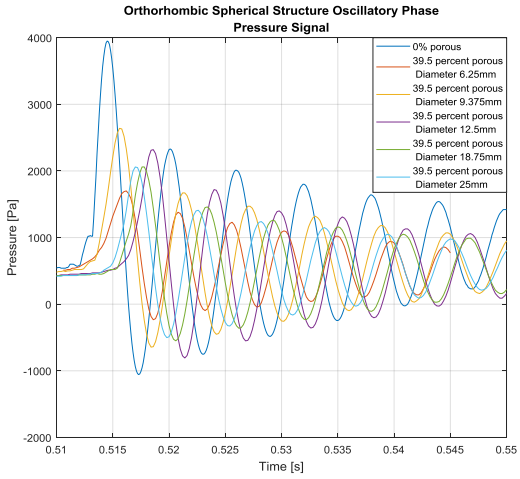

Figure 8.2.4 Oscillatory phase pressure signal for all orthorhombic packed sphere simulations

8.2.3 Pressure response frequency domain analysis

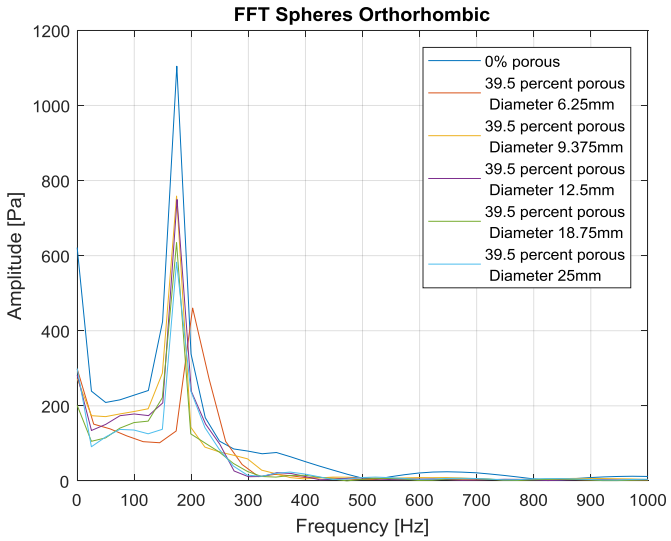

Figure 8.2.5 Oscillatory pressure signal frequency domain results

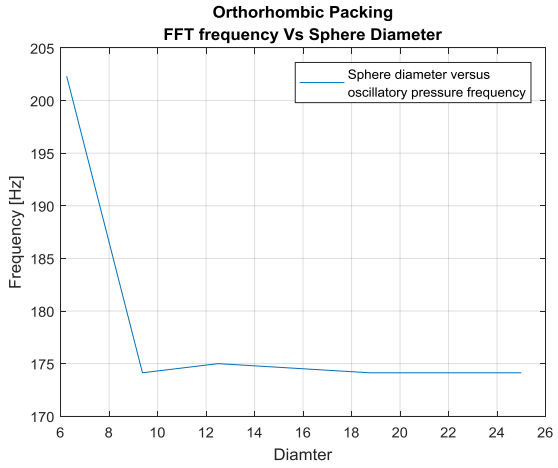

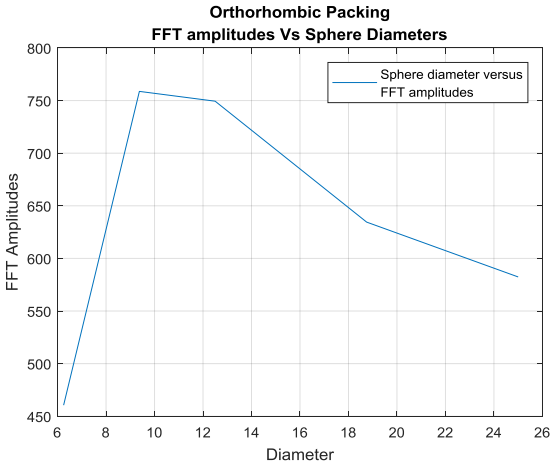

(a) Signal frequency Vs sphere diameter (b) Signal amplitude Vs sphere diameter

Figure 8.2.6 Sphere diameters Vs FFT results

Due to computational limitations significant difficulties were encountered when trying to mesh the interstitial pore space in the 6.25 mm sphere diameter porous structure. Therefore the results from this simulation may not reflect accurately the true behaviour of the pressure oscillations for this model

8.2.4 Pressures attenuation at impact surface

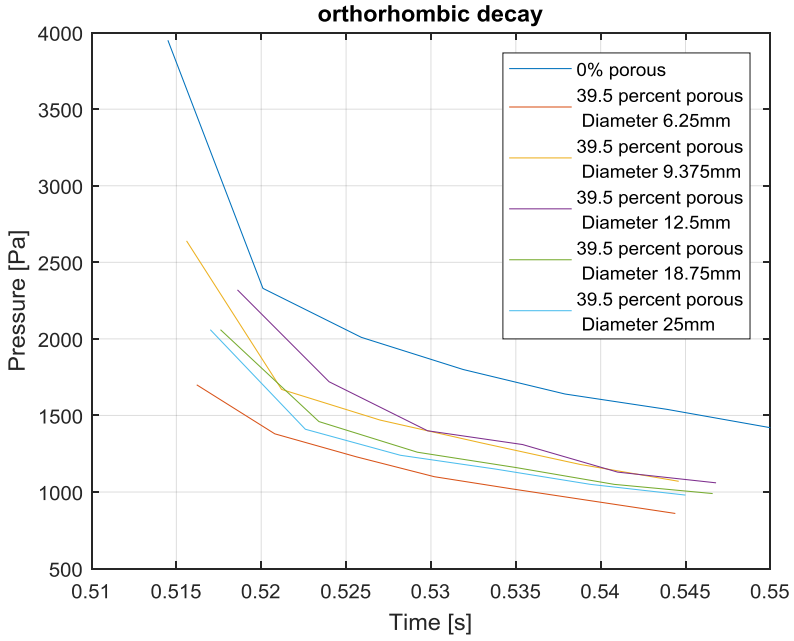

Figure 8.2.7 Oscillation decay rates for orthorhombic sphere packed simulations

Orthorhombic Packing oscillatory pressure attenuation rates	
Solid wall attenuation (0% porous)	$1938e^{-0.4113t_{new}}$
6.25mm diameter spheres	$1119e^{-0.2436t_{new}}$
9.375mm diameter spheres	$1469e^{-0.3634t_{new}}$
12.5mm diameter spheres	$1426e^{-0.3168t_{new}}$
18.75 mm diameter spheres	$1281e^{-0.2929t_{new}}$
25mm diameter spheres	$1125e^{-0.2535t_{new}}$

Table 8.2.3 Exponential oscillatory decay rates for orthorhombic packed sphere simulations

8.2.5 Permeability

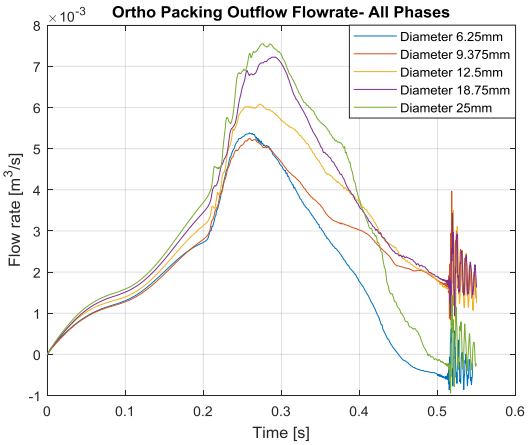

(a) Outflow through RHS boundary (all phases)

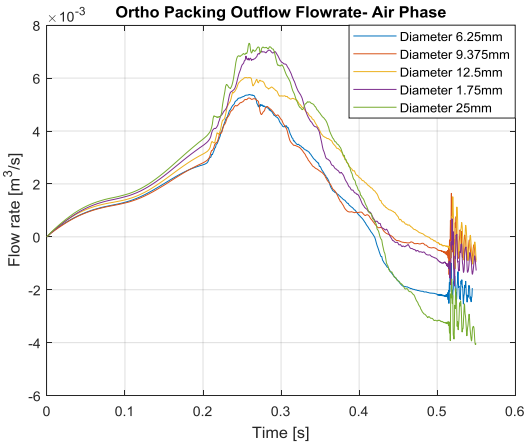

(b) Outflow through RHS boundary (air phase)

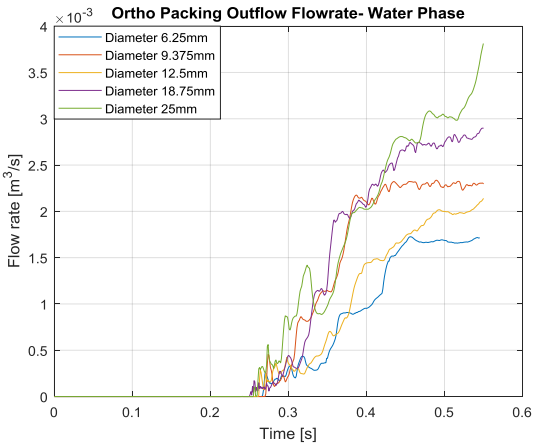

(c) Outflow through RHS boundary (water phase)

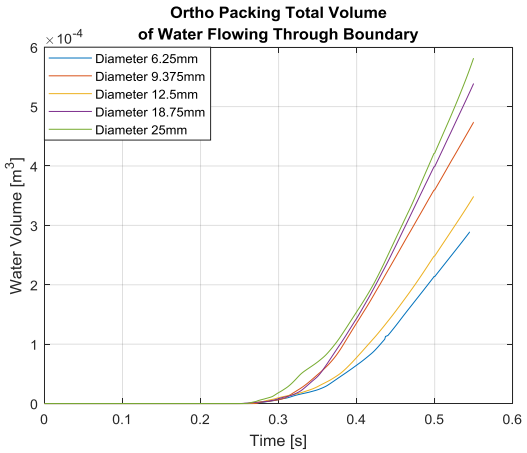

(d) Cumulative Outflow through RHS boundary (water phase)

Figure 8.2.8 Orthorhombic packed spheres structures permeability plots

8.3 Rhombohedral packing sphere lattice

Rhombohedral packing simulation results				
Structure component sphere diameter	25 mm	18.75 mm	12.5 mm	9.375 mm
Impact impulse pressure	1290 Pa	1680 Pa	2080 Pa	2570 Pa
Max oscillatory pressure	2480 Pa	2750 Pa	2880 Pa	3060 Pa
Water outflow flow rate (end of simulation)	$3.57e^{-3}$ m^3/sec	$2.36\ e^{-3}$ m^3/sec	$1.73\ e^{-3}$ m^3/sec	$1.10\ e^{-3}$ m^3/sec
Bubble Oscillation Frequency	174 Hz	174 Hz	174 Hz	175 Hz
Bubble Oscillation Amplitude	722 Pa	782 Pa	822 Pa	920 Pa
Entrapped bubble radius (analytic prediction)	18.8 mm	18.8 mm	18.8 mm	18.7 mm
Simulation Bubble Volume	38,177 mm^3	39,615 mm^3	38,415 mm^3	22,005 mm^3
Bubble Surface Area	8,294 mm^2	8,436 mm^2	8,337 mm^2	5,133 mm^2
Bubble Length (Cylindrical)	100 mm	99 mm	100 mm	60 mm
Bubble Sphericity	0.66	0.67	0.66	0.74
Equivalent entrapped bubble radius (simulation) (c/s)	20.89/11.02 [mm]	21.15/11.29 [mm]	20.93/11.06 [mm]	17.38/10.80 [mm]
Kinematic tortuosity	0.996	0.974	0.989	1.000

Table 8.3.1 Rhombohedral packing simulation results

8.3.1 Flow profile and free surface evolution

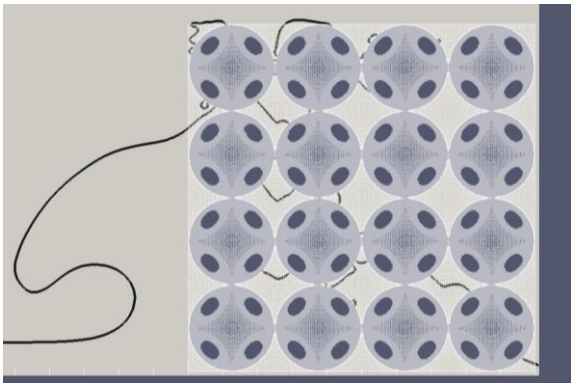

(a) 25 mm diameter sphere structure

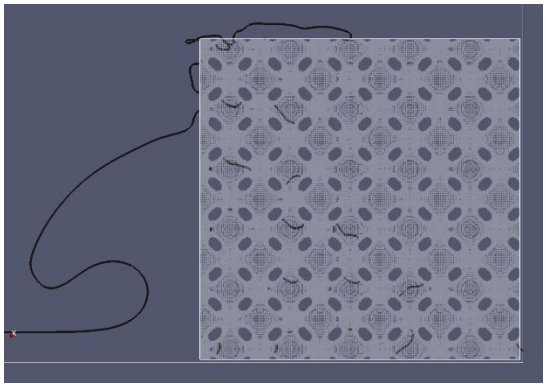

(b) 18.75 mm diameter sphere structure

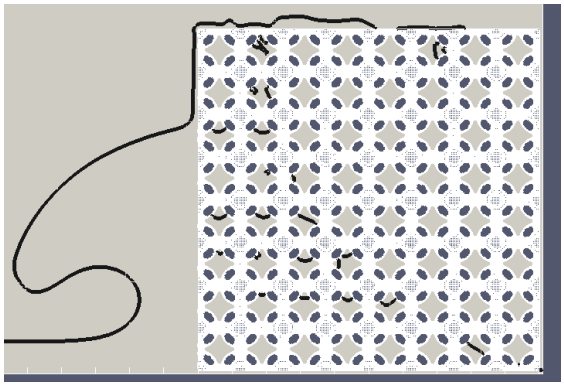

(c) 12.5 mm diameter sphere structure

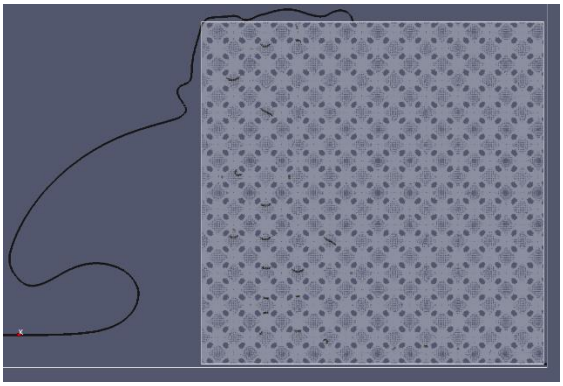

(d) 9.375 mm diameter sphere structure

Figure 8.3.1 Free surface profiles and collapsing jet thickness
at rhombohedral packed porous sphere structures

8.3.2 Pressure response at impact interface

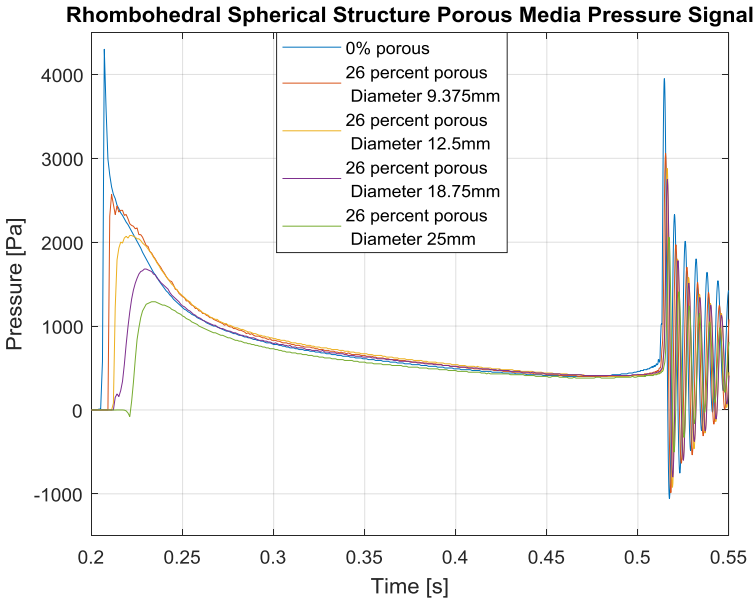

Figure 8.3.2 Rhombohedral packed spheres pressure signal
(atmospheric pressure has been subtracted)

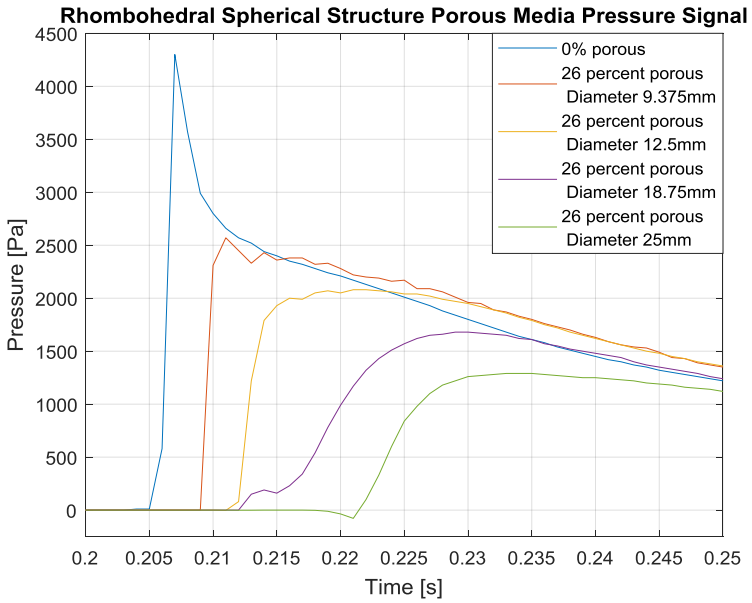

(a) Impulse pressures

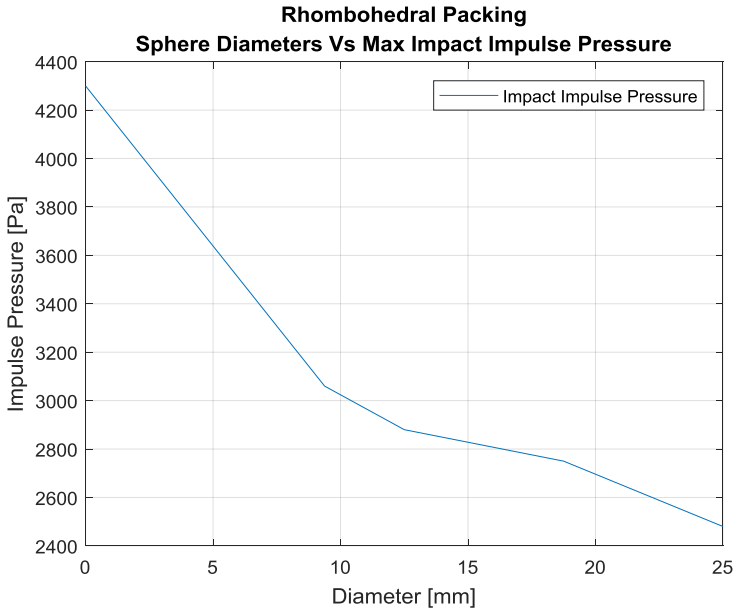

(b) Max Impact Impulse Pressure Vs Sphere diameter

Figure 8.3.3 Initial impact impulse pressure characteristics

Rhombohedral packed spheres pressure analysis					
Structure component sphere diameter	25 mm	18.75 mm	12.5 mm	9.375 mm	Solid wall
Initial impact impulse pressure	1290 Pa	1680 Pa	2080 Pa	2560 Pa	4300 Pa
Max oscillatory pressure	2480 Pa	2750 Pa	2880 Pa	3060 Pa	3950 Pa
% increase or reduction	92	64	38	20	-8

Table 8.3.2 Comparison of initial impact pressure with maximum oscillatory pressures

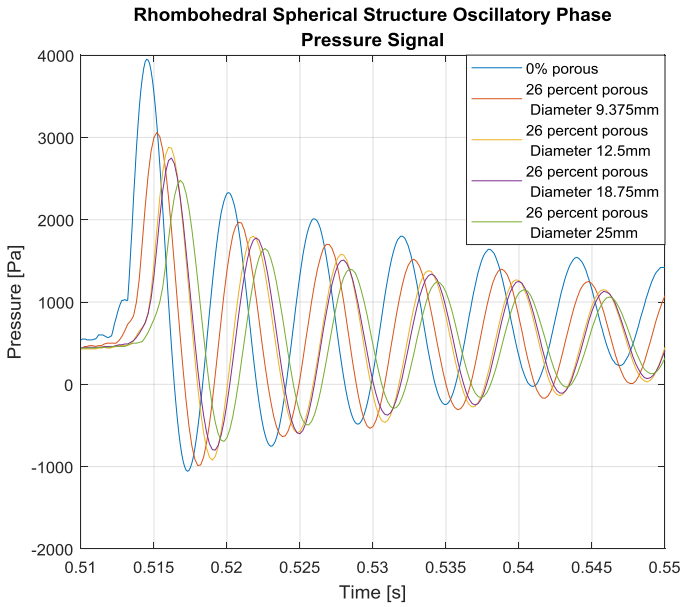

Figure 8.3.4 Oscillatory phase pressure signal for all rhombohedral packed sphere simulations

8.3.3 Pressure response frequency domain analysis

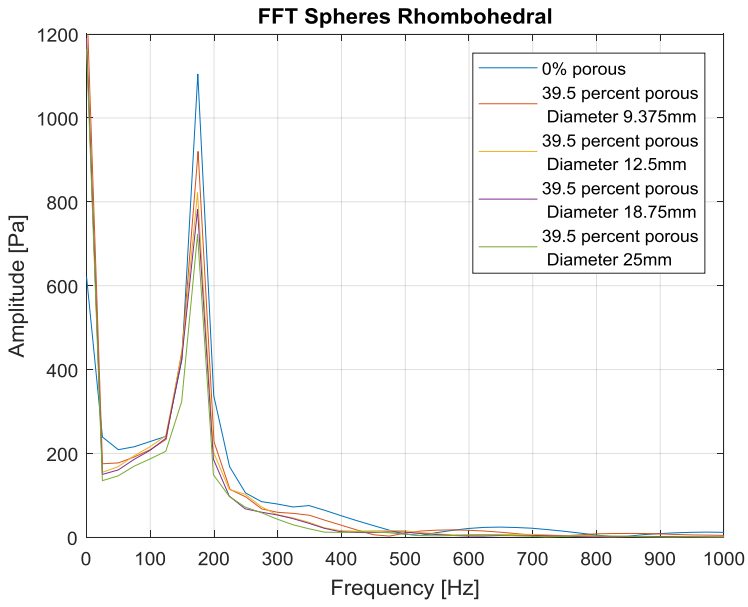

Figure 8.3.5 Oscillatory pressure signal frequency domain results

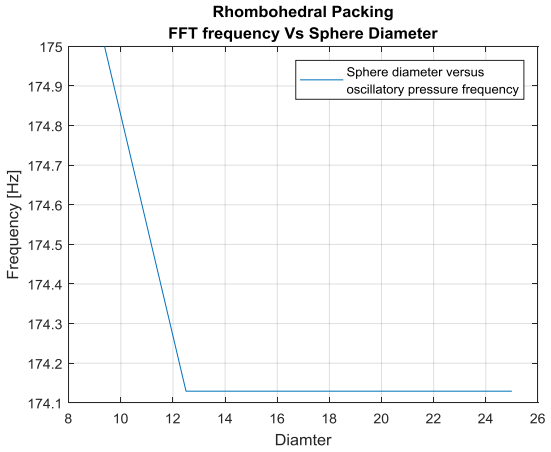

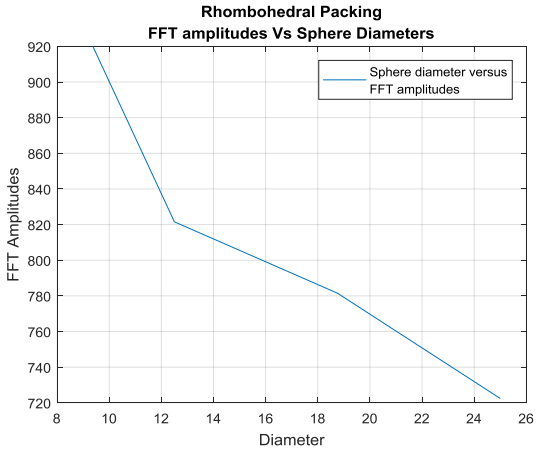

(a) Signal frequency Vs sphere diameter (b) Signal amplitude Vs sphere diameter

Figure 8.3.6 Sphere diameters Vs FFT results

8.3.4 Pressures attenuation at impact surface

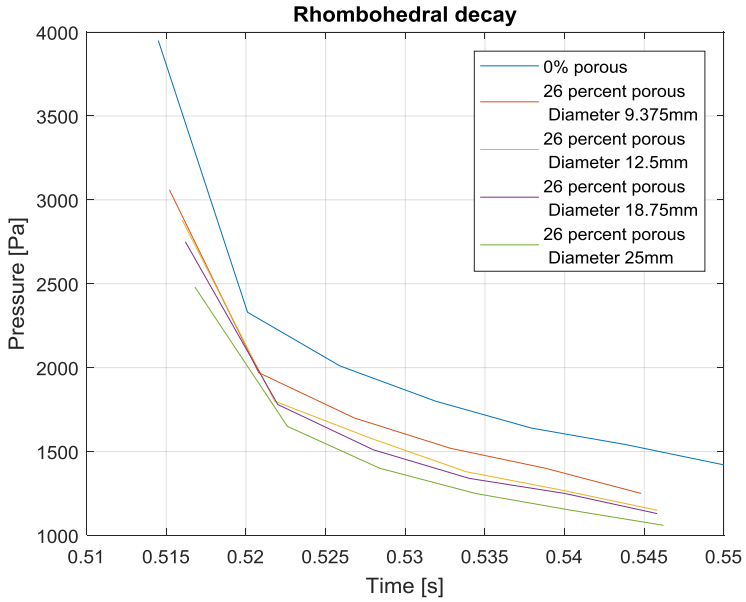

Figure 8.3.7 oscillation decay rates for rhombohedral sphere packed simulations

Rhombohedral Packing oscillatory pressure attenuation rates	
Solid wall attenuation (0% porous)	$1938e^{-0.4113t_{new}}$
9.375mm diameter spheres	$1714e^{-0.3604t_{new}}$
12.5mm diameter spheres	$1574e^{-0.3761t_{new}}$
18.75 mm diameter spheres	$1533e^{-0.3644t_{new}}$
25mm diameter spheres	$1419e^{-0.3487t_{new}}$

Table 8.3.3 Exponential oscillatory decay rates for rhombohedral packed sphere simulations

8.3.5 Permeability

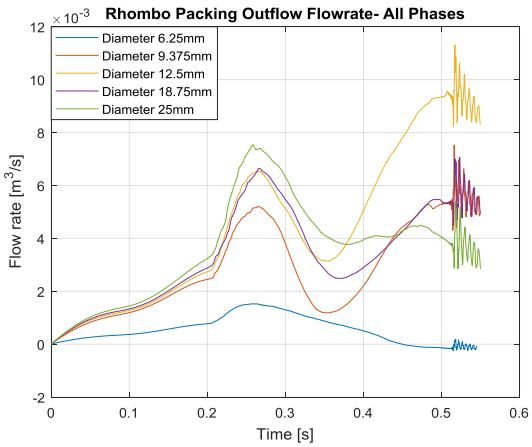

(a) Outflow through RHS boundary (all phases)

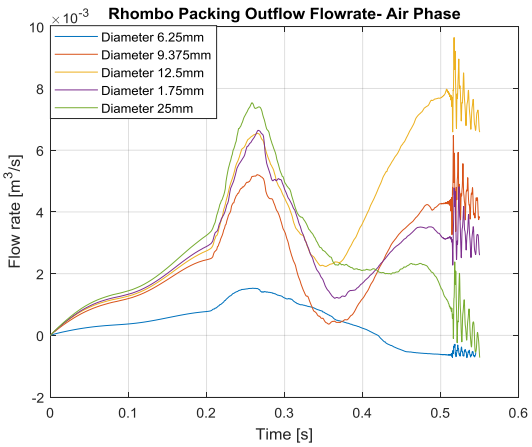

(b) Outflow through RHS boundary (air phase)

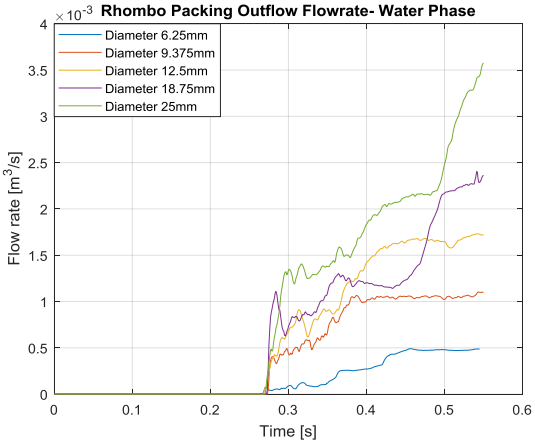

(c) Outflow through RHS boundary (water phase)

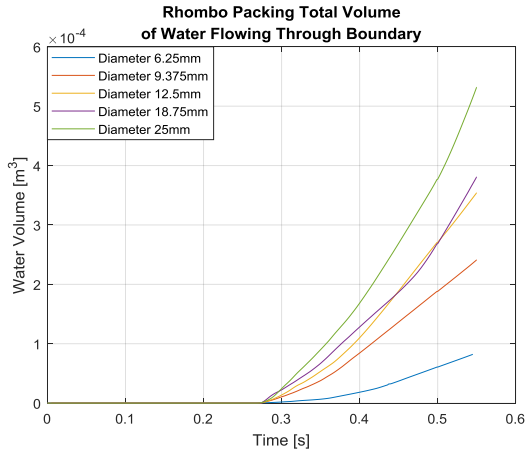

(d) Cumulative Outflow through RHS boundary (water phase)

Figure 8.3.8 Rhombohedral packed spheres structures permeability plots

8.4 Comparison of spherical structure morphology results

Figure 8.4.1 shows the impulse pressures measured at point P1 during the initial wave impact for each of the sphere packing systems and varying sphere diameters. It is shown that both the component sphere diameter size and the packing density influence the magnitude of the observed impact impulse. Larger spheres in a looser packing formation (cubic packing) yield the lowest impact pressures, however this is at the expense of an increased structural permeability.

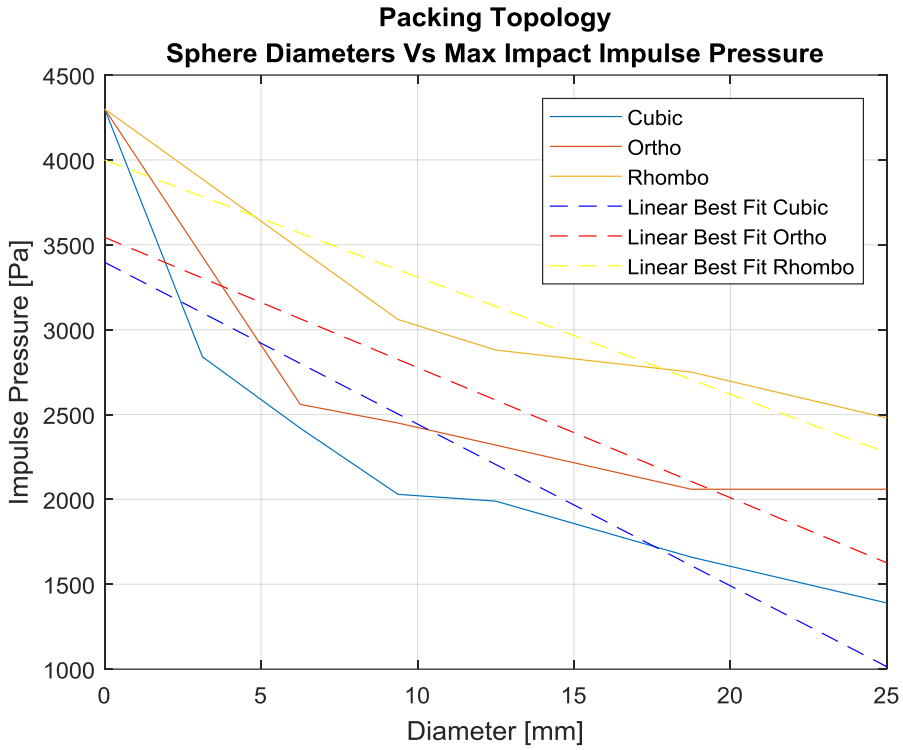

Figure 8.4.1 Impulse pressure at first impact from surging wave for spherical structure morphologies

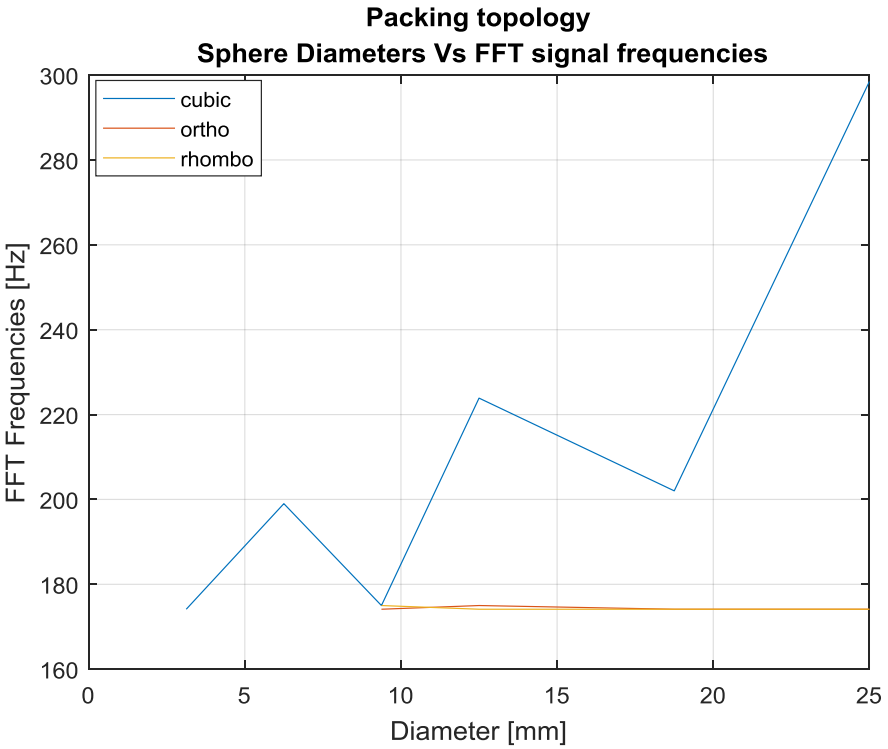

Figure 8.4.2 Oscillation frequencies computed for each of the various spherical structure porous morphologies

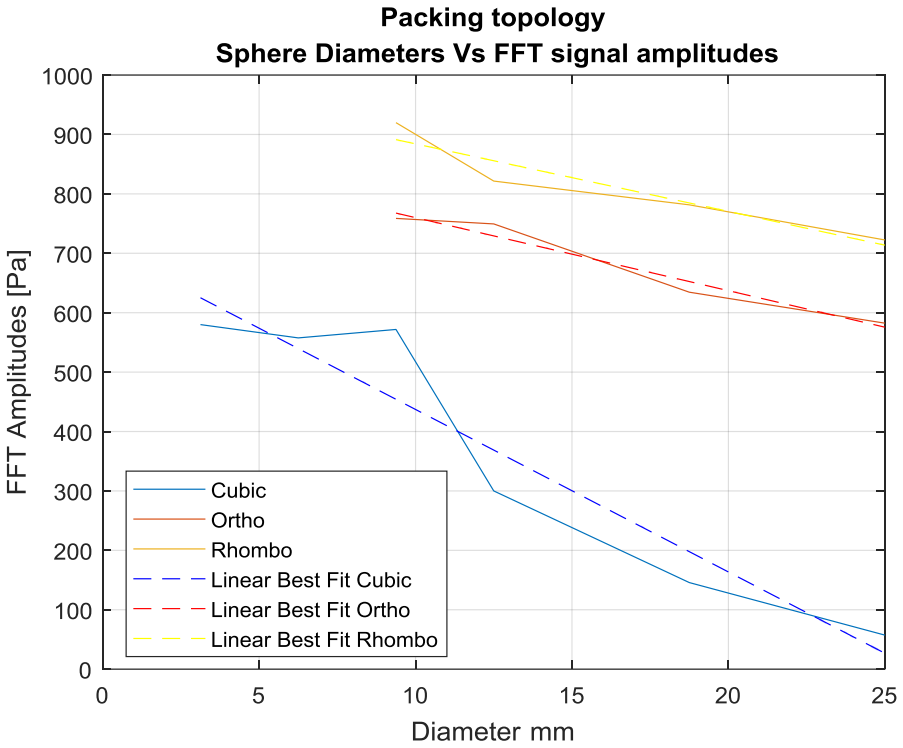

Figure 8.4.3 Oscillation amplitudes computed for each of the various spherical structure porous morphologies

Figures 8.2 and 8.3 present plots of the results obtained from the Fourier Transforms for each of the sphere structure porous morphologies. As discussed in Section 8.2.3 the results from the orthorhombic packed 6.25 mm diameter spheres yielded some spurious results, these results are therefore omitted from these plots. In Figure 8.2 it is shown that the frequency of oscillation is very similar for the orthorhombic and rhombohedral packed sphere and the values do not vary significantly with changing component sphere diameter. In contrast the frequency of pressure oscillation increases significantly with increasing component sphere size for the cubic packed spheres. This suggests that there is a threshold porosity below which the frequency of oscillation is not sensitive to the elemental component size which constitutes the porous structure.

Figure 8.3 demonstrates the influence of changing the porosity and component sphere size on the oscillatory amplitude. Here it is clearly obvious that the low porosity structures with high specific surface yield the highest oscillatory amplitude Thus by using low porosity structures with low specific surface areas a reduction in the oscillation amplitude is observed. However these structures have a high permeability.

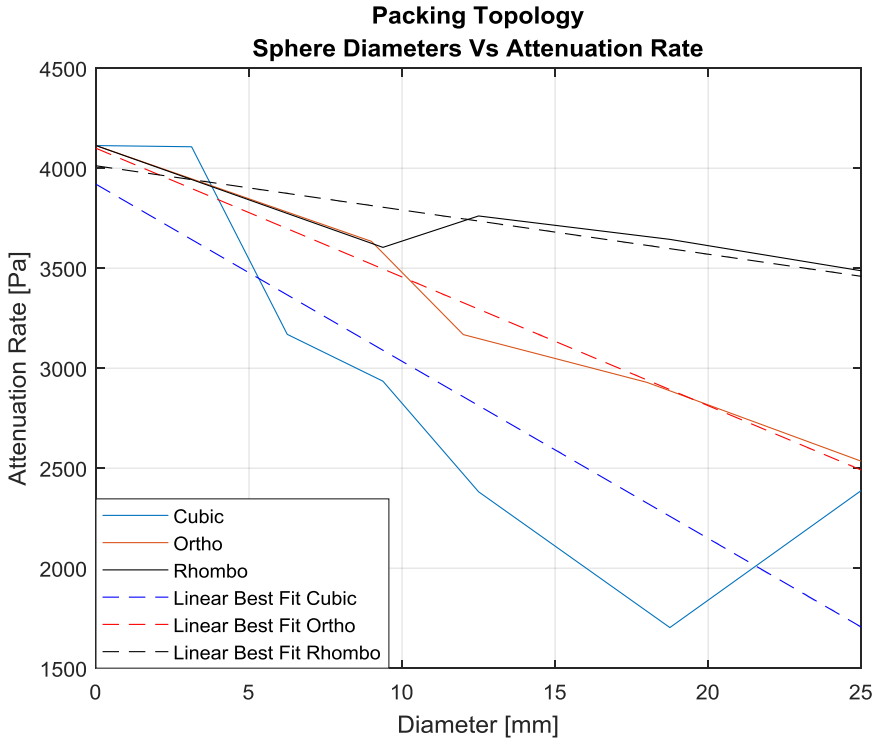

Figure 8.4.4 Oscillatory pressure attenuation rates for each of the spherical structure morphologies

Figure 8.4.4 presents a plot of the absolute value of the oscillatory attenuation rates for the various simulations with different sphere packing formations and different component sphere sizes. From the linear best fits to the data set we clearly show that there is a relationship between the porosity, element sphere size and the attenuation rates. Smaller spheres packed in a tighter formation yield a higher oscillatory pressure attenuation rate. These finding are significant for the design of structures to resist the destructive effects from wave impacts and oscillatory pressures which occur during wave overturning with air entrapment. Based on these findings we can design a bespoke porous topology to resist wave impact forces and oscillatory pressures for coastal regions which are subject to a predominant wave spectrum.

Table 8.4.1 summarises the influence of the sphere packing topology and constituent sphere size on the simulation forces and pressures experienced by the porous structure.

Sphere packing system	porosity		Initial impact impulse		Oscillatory frequencies		Oscillatory amplitude		Rate of oscillatory attenuation
	Large spheres	Small spheres	Large spheres	Small spheres	Large spheres	Small spheres	Large spheres	Small spheres	Sphere size influence
Cubic	High	High	Low	High	High	Low	Low	Medium	High influence
Orthorhombic	Medium	Medium	Low	High	Low	Low	Medium	Medium	High influence
Rhombohedral	Low	Low	Medium	High	Low	Low	Medium	High	Low influence

Table 8.4.1 Summarised sphere packing geometry simulation results

8.5 Fibrous media morphology

Fibrous geometry simulation results					
Simulation Title	2	3	3a	4	5
Porosity %`	97.527	95.197	94.442	92.154	84.308
Impact impulse pressure	760 Pa	760 Pa	760 Pa	1850 Pa	1900 Pa
Max oscillatory pressure	no bubble entrainment	230 Pa	850 Pa	1630 Pa	1850 Pa
Water outflow flow rate (end of simulation)	$4.577e^{-3}$ m^3/sec	$5.0988e^{-3}$ m^3/sec	$3.509e^{-3}$ m^3/sec	$4.710e^{-3}$ m^3/sec	$3.250e^{-3}$ m^3/sec
Bubble Oscillation Frequency	-	259 Hz	199 Hz	224 Hz	202 Hz
Bubble Oscillation Amplitude	-	6 Pa	257 Pa	366 Pa	518 Pa
Entrapped bubble radius (analytic prediction)	-	12.6 mm	16.4 mm	14.6 mm	16.2 mm
Simulation Bubble Volume	-	4,109 mm^3	18,767 mm^3	21,458 mm^3	18,212 mm^3
Bubble Surface Area	-	1,551 mm^2	4,337 mm^2	4,888 mm^2	4,218 mm^2
Bubble (Cylindrical) Length	-	32 mm	52 mm	52 mm	52 mm
Bubble Sphericity	-	0.80	0.787	0.764	0.794
Equivalent Entrapped bubble radius (simulation) (c/s)	-	9.94/6.39 [mm]	16.49/10.71 [mm]	17.24/11.46 [mm]	16.32/10.56 [mm]
Computed kinematic tortuosity	1.07	1.19	1.30	1.39	1.63

Table 8.5.1 Fibrous structure simulation results

8.5.1 Pressure response at impact interface

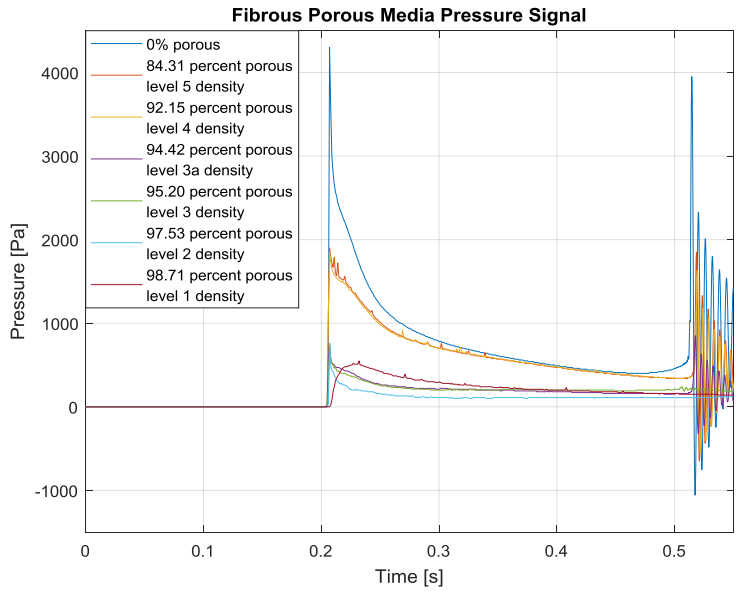

Figure 8.5.1 Fibrous structure pressure signal
(atmospheric pressure has been subtracted)

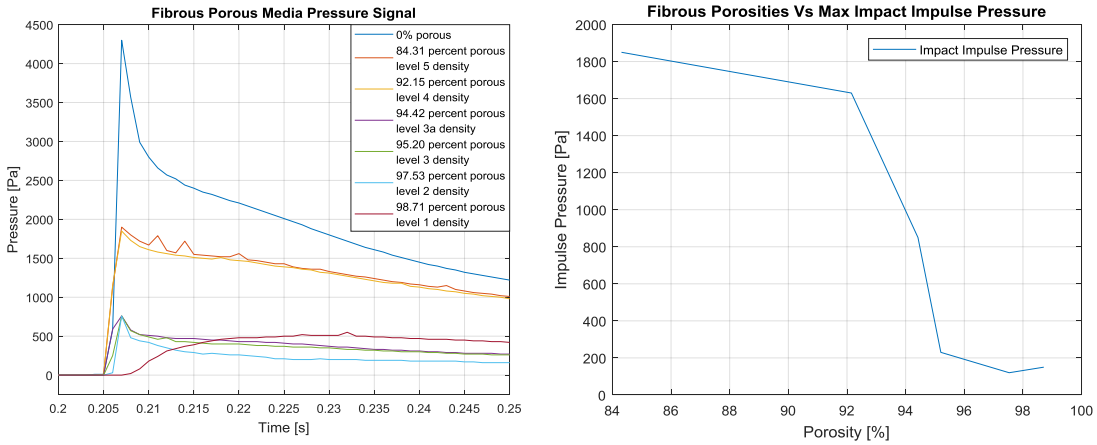

(a) Impulse pressures (b) Max Impact Impulse Pressure Vs Porosity

Figure 8.5.2 Initial impact impulse pressure characteristics

Fibrous porous structure pressure analysis					
Porosity %`	97.527	95.197	94.442	92.154	84.308
Initial impact impulse pressure	760 Pa	760 Pa	760 Pa	1850 Pa	1900 Pa
Max oscillatory pressure	no bubble entrainment	230 Pa	850 Pa	1630 Pa	1850 Pa
% increase or reduction	-	-70	-12	-12	-2

Table 8.5.2 Comparison of initial impact pressure
with maximum oscillatory pressures

8.5.2 Pressure response frequency domain analysis

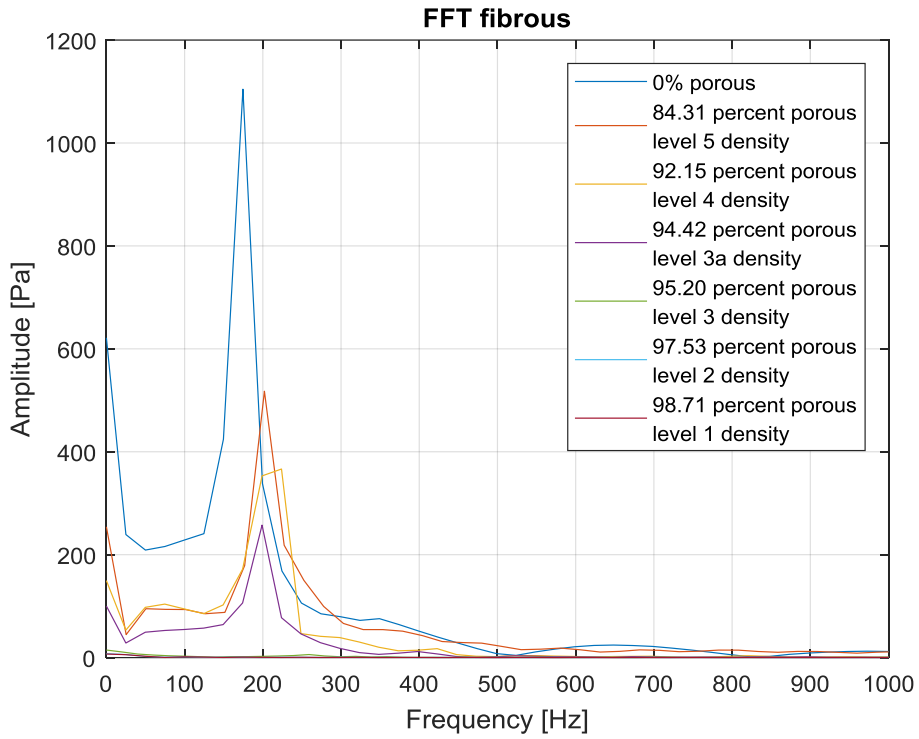

Figure 8.5.3 Oscillatory pressure signal frequency domain results

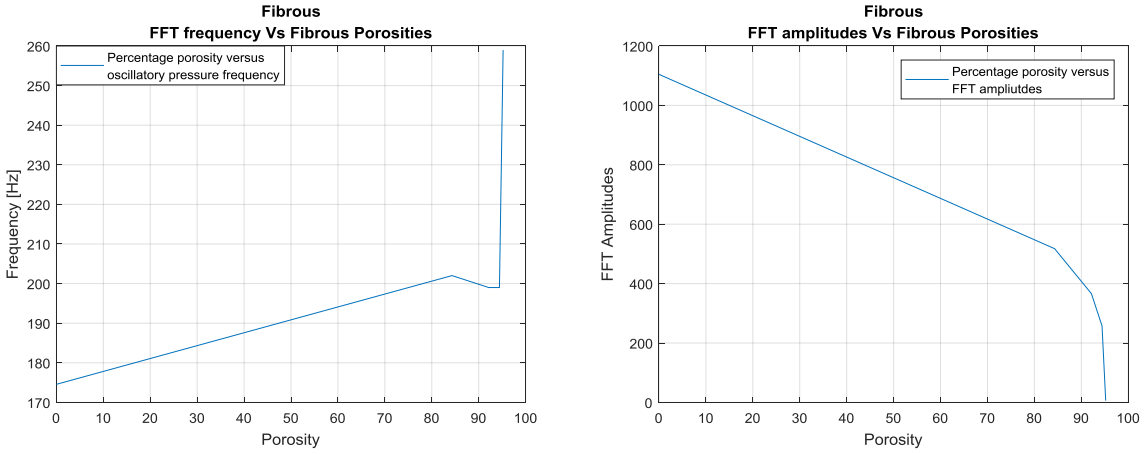

a) Signal frequency Vs structure porosity (b) Signal amplitude Vs structure porosity

Figure 8.5.4 Porosity Vs FFT results

8.5.3 Pressures attenuation at impact surface

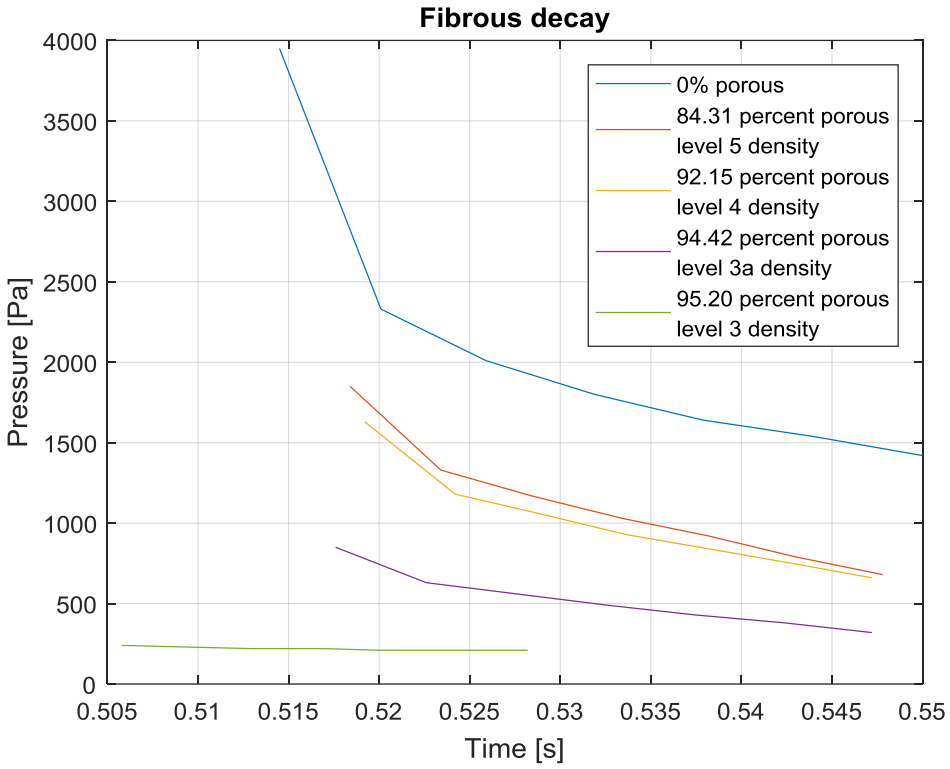

Figure 8.5.5 Oscillation decay rates for fibrous simulations

Fibrous structure oscillatory pressure attenuation rates	
Solid wall attenuation (0% porous)	$1938e^{-0.4113t_{new}}$
84.308 % porous	$1049e^{-0.3575t_{new}}$
92.154 % porous	$961e^{-0.3254t_{new}}$
94.442 % porous	$496e^{-0.3449t_{new}}$
95.197 % porous	$220e^{-0.0493t_{new}}$

Table 8.5.3 Exponential oscillatory decay rates for fibrous structure simulations

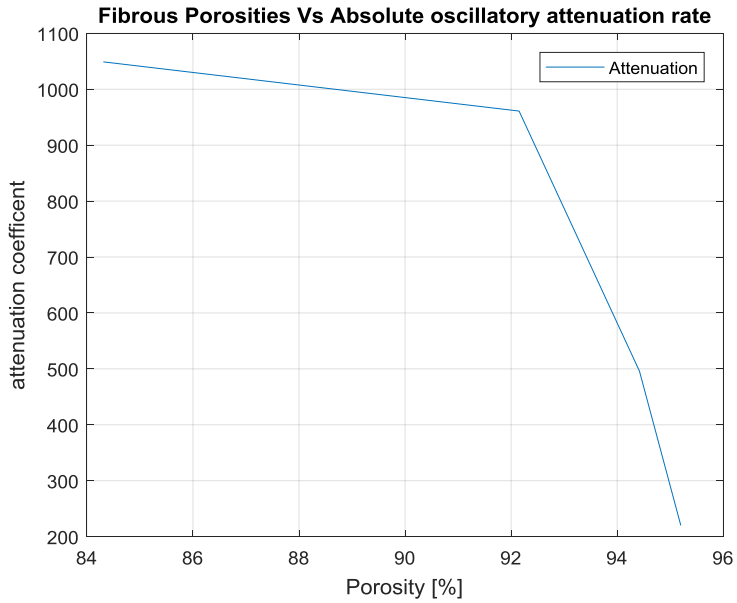

Figure 8.5.6 Fibrous porosity Vs attenuation coefficients

8.5.4 Tortuosity

The tortuosity for the fibrous media has been determined in different manner from the approach described for the sphere lattice morphology. As most of the fluid passes through a localised region at the base of the fibrous structure the analysis to determine the tortuosity of the complete assembly as reported in Section 8.1.6 would not yield a statistically representative value for the fibrous structure as a whole. Therefore an additional set of simulations were performed to determine the tortuosity of the fibrous structures. These simulations and the results obtained are described in the following subsections. These simulation results were then compared with an analytically calculated value to yield a tortuosity value for the fibrous structure. The setup for this additional simulation is shown on Figure 8.5.7.

The time taken for a block of liquid to fall uninhibited through 100mm under gravitational force starting from a stationary position was determined using the equation of motion given in 8.4 below. This time was used as a reference time. It was then compared to the time taken for a similar block of liquid to fall through a 100mm width of the porous structure. Then, by comparing this time to the reference time, the impeding influence of the fibrous structure on fall of the fluid could be determined. Consequently the tortuosity could be inferred for the porous structure.

$$s = ut + \frac{1}{2}at^2 \qquad (8.4)$$

Where *s* is total displacement, *u* is the initial velocity of the water block, *t* is time and *a* is acceleration due to gravity. Using Equation 8.4 the time taken for the water block to fall through 100mm is 0.143 seconds. Because a time component is considered in this method of tortuosity calculation we can still refer to this parameter as a kinematic tortuosity. In order to validate this suggested method for determining the kinematic tortuosity for the fibrous porous structure a bench marking test simulation was conducted with 25mm diameter spheres and 6.25 mm diameter spheres in cubic packed arrangement. This simulation and the results are described in section 8.5.4.2.

8.5.4.1 Simulation geometry for determination of tortuosity of fibrous porous media

Figure 8.5.8 below show the simulation setup to determine the tortuosity for the fibrous porous structures. The structure shown is 84.31% porous. In this case the dimensions of the numerical tank are 0.1m X 0.05m X 0.165m. The water column measures 0.10m X 0.05715m X 0.05715m and the fibrous structure measures 0.1m X 0.05m X 0.1 m. A `zeroGradient` boundary condition with a no slip condition is applied at the vertical walls at x = 0, x = 0.1 and at y = 0, y = 0.05, an `inflowOutflow` boundary condition is prescribed for the air phase at the top of the domain at z = 0 which allows air flow into the domain, and a `zeroGradient` boundary condition applied on the liquid phase. The boundary condition at z = -0.165 allows both the air and water phases to flow out of the domain. The water column displaces vertically downwards under the action of gravitational acceleration.

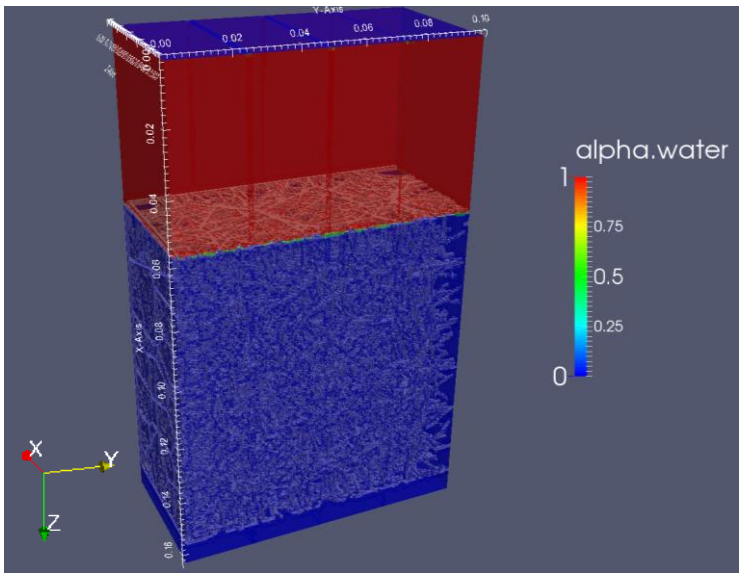

Figure 8.5.7 Simulation setup for fibrous structure tortuosity determination

Figure 8.5.8 below shows the simulation at time t = 0.2. The Figure 8.5.8 (a) shows the both the air and water phases, together with the porous structure, Figure 8.5.8 (b) is a snapshot of the simulation at the same time step with the air-water interface highlighted and finally 8.5.8(c) shows the air-water interface with the fibrous media omitted. Previous studies have shown that areas close to the confining walls of a porous assembly often exhibit higher porosities, and this effect has been studied analytically for sphere swarms in random packing see e.g. (Martin, 1978), (Benenati and Brosilow, 1962). These areas which exhibit a higher permeability are referred to as the wall regions and those areas in which the flow is unaffected by the confining walls are regarded as the core region (Baker, 2011). Because the impervious vertical walls at the perimeter of the domain impede the liquid velocity vectors in the horizontal direction, the water phase percolates downwards through this fibrous porous medium faster adjacent to the walls and in the corners. Additionally the wall and corner regions are locally more porous due to the manner in which the fibrous assembly was created where the bulk of the fibrous are located within the core region. The effect of the more permeable wall regions are obvious from figure 8.5.8(c). In this study a representative value of tortuosity for the porous media it to be determined. Then, those regions where the flow profile is influenced by the boundary walls are not considered and we determine the tortuosity for the core region within the porous structure. Figure 8.5.8(e) shows flow streamlines for fluid elements which have not been constrained in their direction of flow by the tank walls. These streamlines reach the base of the porous structure at 0.299 seconds simulation time. A similar procedure was carried out to determine the tortuosity for each of the fibrous structures. The results for the tortuosities for the fibrous media are recorded in Table 8.5.1

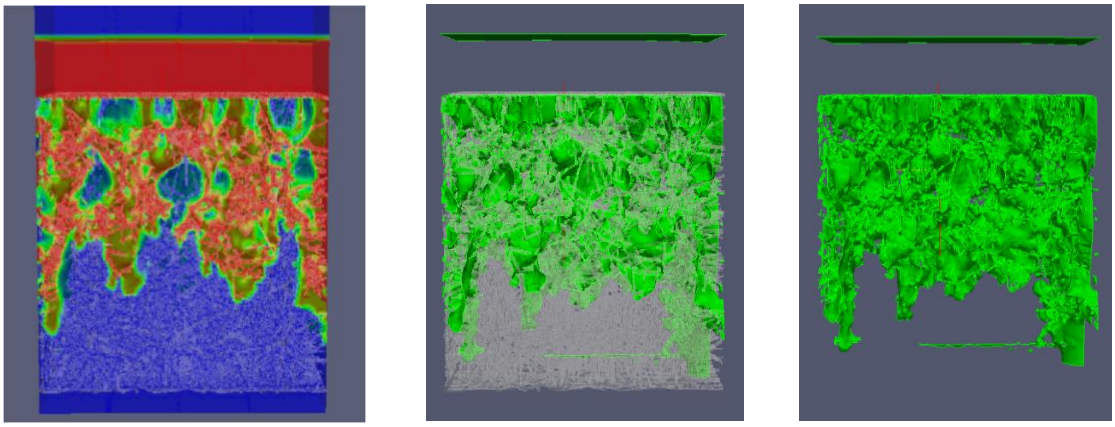

(a) (b) (c)

Figure 8.5.8 Tortuosity determination for the fibrous simulations

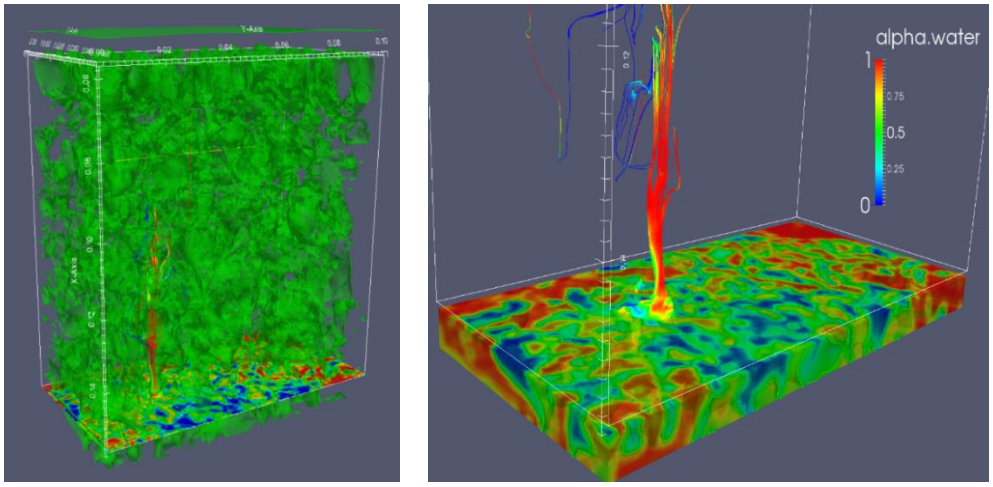

(d) (e)

Figure 8.5.8 Tortuosity determination for the fibrous simulations

8.5.4.2 Simulation geometry for determination of tortuosity of cubic packed spheres porous assembly

Figure 8.5.9 below show the simulation setup to determine the tortuosity for the fibrous porous structures. The structure is assembled from 25mm diameter spheres arranged in a cubic packing system. The setup is similar to that for determining the tortuosity of the fibrous structure. The dimensions of the numerical tank are 0.1m X 0.1m X 0.165m. The water column measures 0.10m X 0.10m X 0.05715m and the porous structure measures 0.1m X 0.1m X 0.1 m. A `zeroGradient` boundary condition with a no slip condition is applied at the vertical walls at x = 0, x = 0.1 and at y = 0, y = 0.1, an `inflowOutflow` boundary condition is prescribed for the air phase at the top of the domain at z = 0 which allows air flow into the domain, and a `zeroGradient` boundary condition applied on the liquid phase. The boundary condition at z = -0.165 allows both the air and water phases to flow out of the domain. The water column displaces vertically downwards under the action of gravitational acceleration.

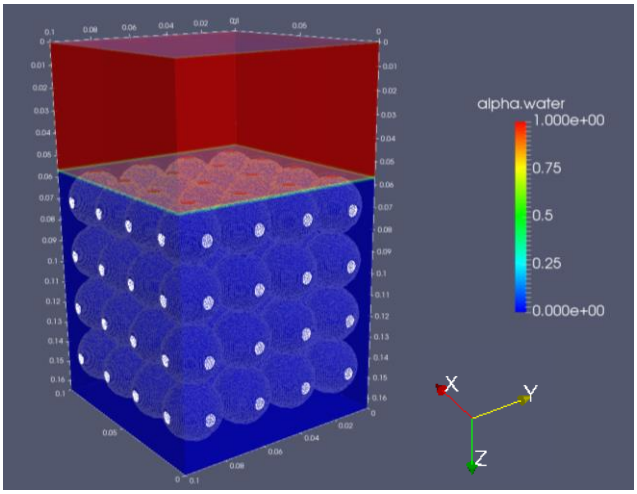

Figure 8.5.9 Simulation setup for sphere structure tortuosity determination

Figure 8.5.10 below shows the simulation at time t = 0.127. The Figure 8.5.10 (a) shows the both the air and water phases, together with the porous structure, Figure 8.5.10 (b) is a snapshot of the simulation at the same time step with the air-water interface highlighted and 8.5.10 (c) shows the air-water interface with the sphere based porous structure omitted. Figure 8.5.10(e) shows flow streamlines for fluid elements which have not been constrained in their direction of flow by the tank walls. These streamlines reach the base of the porous structure at 0.127 seconds simulation time. This time is slightly shorter than the predicted time of 0.143 seconds. However due to the narrow channels between the spheres there may be a pressure increase which may cause a jetting effect as was previously discussed in Section 8.1.6.

A similar procedure was carried out to determine the kinematic tortuosity for the 6.25mm diameter component sphere cubic packed porous structure. The results for the tortuosities for this simulation are recorded on Figure 5.5.11. Although both cubic packed sphere structures have the same porosity, in this case the flow of fluid through is much imped and the fluid takes 0.287 seconds to pass through the fibrous structure.

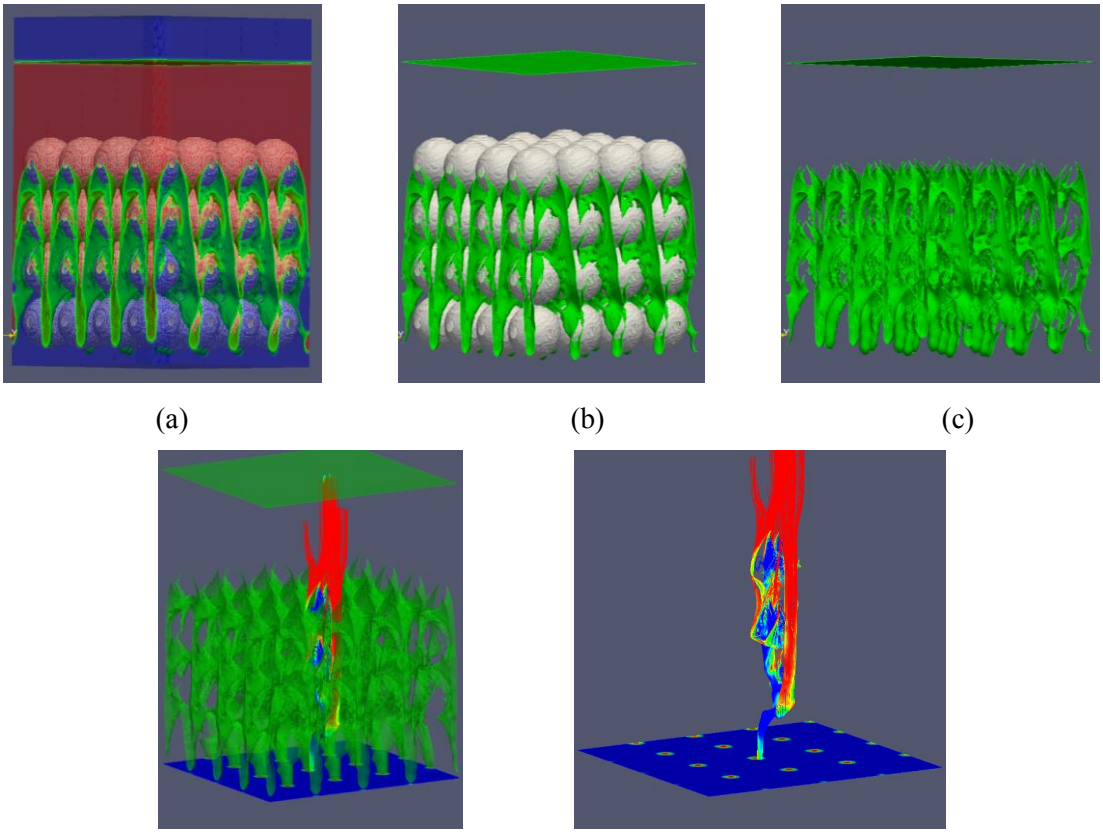

(a) (b) (c)

(d) (e)

Figure 8.5.10 Tortuosity determination for the 25 mm diameter cubic packed sphere simulations at time 0.127 seconds

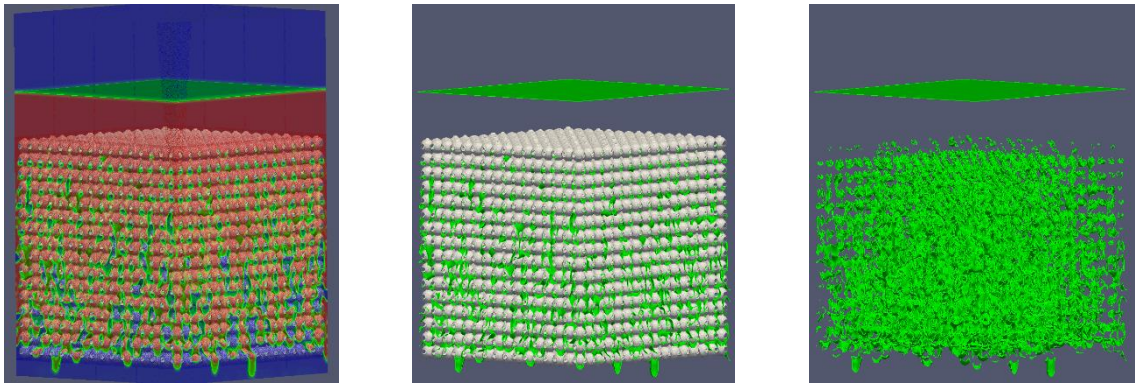

(a) (b) (c)

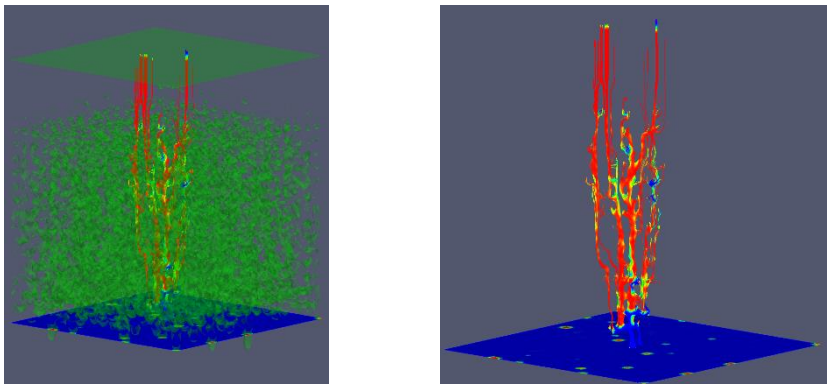

(d) (e)

Figure 8.5.11 Tortuosity determination for the 6.25 mm diameter cubic packed sphere simulations at time 0.287 seconds

8.5.5 Permeability

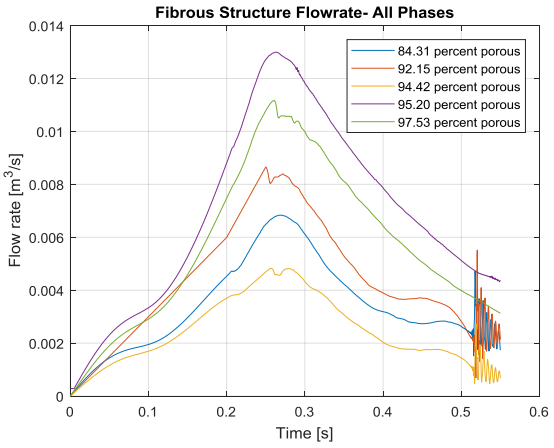

(a) Outflow through RHS boundary (all phases)

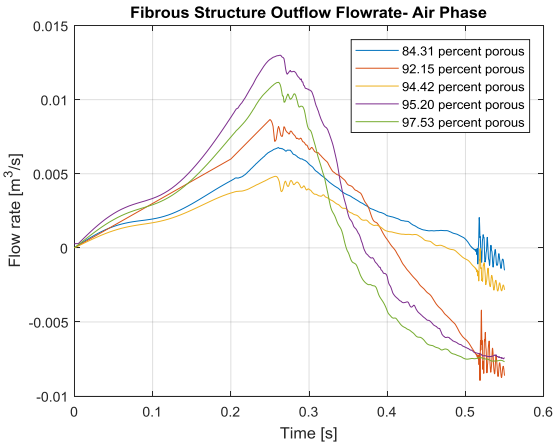

(b) Outflow through RHS boundary (air phase)

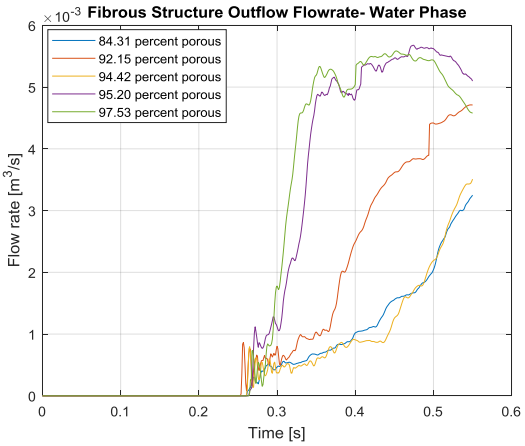

(c) Outflow through RHS boundary (water phase)

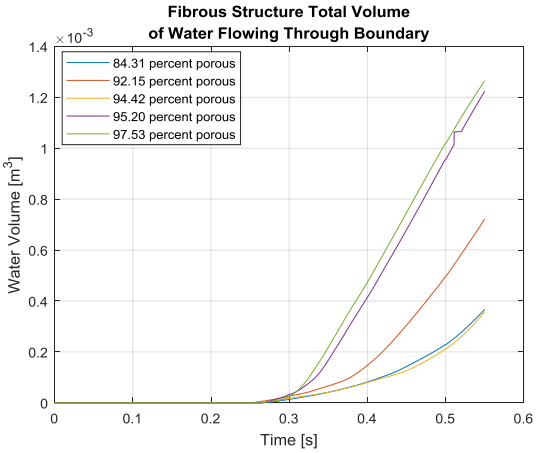

(d) Cumulative Outflow through RHS boundary (water phase)

Figure 8.5.12 Fibrous structures permeability plots

Chapter 9

Conclusion and future work

9.1 Conclusions

A model was developed to simulate the effects of air compressibility during a wave breaking event. The model was verified through a grid independence study and validated through comparison with 2 sets of experimental results. In the verification process it was found that a mesh sizing of 0.5mm X 0.5mm was of a sufficiently high resolution to capture the transient pressure effects during wave impact at the wall.

The first set of results used for validation compared the simulation flow front position with data from an experiment conducted by Martin and Moyce (1952). A second validation of the numerical model was performed by comparing the recorded pressure history a point on the domain wall with results from an experiments conducted at MARIN, (Kleefsman et al., 2005). In both validation cases satisfactory comparisons were observed.

The next stage of the study focussed on verifying the existence of a high frequency pressure oscillation that occurs as a plunging breaker develops. For this phase of the study compressible and incompressible simulation results from the 1mm X 1mm mesh first order spatial, first order temporal equation discretisation schemes,- and the 0.5 mm X 0.5mm second order spatial, second order temporal discretisation schemes were selected for further investigation.

The compressible and incompressible simulation pressure response results for the first order spatial and temporal equation discretisation schemes were first compared. In general, both sets of results showed good agreement. Visually, the free surface flow profile compared well for each of the simulations. However at the point of entrainment of a single large air bubble within the liquid phase the pressure response from the compressible simulation exhibited large amplitude oscillations. These oscillations were absent from the incompressible model simulation. This confirmed that this high frequency oscillation is a direct consequence of air pocket entrapment. This phase of the study was significant as there has been very little

evidence provided in previous literature to attribute the existence of high frequency oscillatory pressures to air entrapment.

A comparison of our simulation results to the Minnaert Analytic Equation (Minnaert, 1933) and results from Hattori et al. (1994) to confirm the existence of a relationship between an entrapped bubble volume and its frequency of oscillation was the performed. Again, the results from our numerical model compared favourably to the analytically and experimentally derived results. Additional analysis was performed in the frequency domain to investigate the effects of air pocket fragmentation and coalescence on the observed pressure signal at the domain wall.

The model was next extended to a three dimensional study. A range of porous structures with varying topologies were developed and incorporated into the simulation domain. An extensive commentary on the parameters to characterise these porous structures was delivered. A number of simulations were performed (24 in total) using the `compressibleInterFoam` solver to model wave impact with air entrainment effects against these structures. A range of results were presented for each model. An extensive analysis of these results was performed. We focussed mainly on the porous structures composed of spheres in three varying packing structures. We clearly demonstrate that there exists relationships between the parameters used to characterise these porous structures and the impact pressures which they are subject to and the frequency and amplitude of pressure oscillation which the structure experiences. Furthermore we confirm that different structures can control and attenuate the frequency and amplitude of the oscillatory signals more effectively.

The main findings from the analysis of the wave impact with the porous structure were;

1. The impulse pressure resulting from a impacting wave varies reasonably linearly with the size of the sphere composing the porous structure irrespective of the packing system used
2. More tightly packed spheres will always yield a higher wave impact impulse pressure
3. There exists a porosity threshold, above which, the frequency of pressure oscillation (due to air entrapment) varies in accordance to the size of the spheres which constitute the porous structure. Below this threshold the size of the spheres constituting the porous structure do not influence the frequency of oscillation.
4. The pressure oscillation amplitude varies reasonably linearly with the size of the sphere composing the porous structure irrespective of the packing system used.

5. However, once again more tightly packed spheres will always yield higher oscillatory pressure wave amplitudes
6. The rate of attenuation of the oscillatory pressure signals resulting from wave impact with air entrainment is most sensitive to sphere size in a loose packed configuration. In the cubic packed spheres it was observed that the rate of attenuation varied significantly as the component sphere size was varied, however the component sphere size had less influence in the more tightly packed orthorhombic or rhombohedral configurations.

It has therefore been shown that by selecting a suitable porous topology for a breakwater structure we can control the forces and pressures of wave impact. Furthermore, the oscillatory pressure energy spectra which results from air entrapment during wave breaking can be efficiently damped by selecting the correct topology for breakwater structures in a given coastal region.

9.2 Future work

Further 3 dimensional wave impacts at sphere based porous structures should be conducted and analysed in order to generate additional datasets which reveal the effects of higher porosities on the impacting wave energy dissipation mechanisms. These simulations can also be used to further analyse the influence of porosity on the oscillatory pressure attenuation. It may be beneficial to perform additional full scale simulations. Nevertheless we have already shown that by performing a non-dimensional analysis of our results, good agreement is obtained with previously conducted experimental research on wave impact with a solid wall.

Further simulations with additional fibrous porous media should be conducted. However during this study computational limitations dictated that 84% porosity was the lowest level of fibrous porous media which could be reliably meshed. By increasing the fibre radii effecting this porous media a lower level of porosity can be achieved.

Studies incorporating irregularly shaped elemental blocks which more accurately reflect the construction of rubble mound breakwaters should also be performed.

Analyses conduced whilst varying the model domain geometry (inclined tank bed, sloping impact interface etc.) can be undertaken in order to simulate the profiles of existing breakwaters. The results from the numerical models can then be validated against existing case study constructions.

This area of research would also benefit from experimental investigation, both at a laboratory and full scale level in order to provide additional validation cases for the wave impacting simulations.

In the future it will be useful to generate a large database of information to provide a robust, reliable design for breakwater structures. Once this is complete, the development of a web-enabled, integrated, inference based software system for the investigation and prediction of coastal defence structural response would be extremely useful to the coastal engineering community.

The energy dissipation mechanism in the porous medium should also be studied in further detail. In this manner a deeper understanding of the relationship can be developed between the wave impact energy attenuation and level of porosity at the impact interface. Additional simulations to generate a range of wave geometries should also be undertaken. This study focussed only on a single wave geometry impacting the porous structure. By performing analyses with a range of varying geometry waves, additional information will be provided which can be used to design bespoke regional breakwaters for areas which experience a prevailing wave spectrum.

References

ALAGAN CHELLA, M., BIHS, H. & MYRHAUG, D. 2015. Characteristics and profile asymmetry properties of waves breaking over an impermeable submerged reef. *Coastal Engineering,* 100**,** 26-36.

AMERICAN INSTITUTE OF AERONAUTICS AND ASTRONAUTICS. 1998. *Guide for the verification and validation of computational fluid dynamics simulations,* Reston, VA, American Institute of Aeronautics and Astronautics.

ANDERSON, J. D. 1995. *Computational fluid dynamics : the basics with applications,* New York, McGraw-Hill.

ANDRADE JR, J., COSTA, U., ALMEIDA, M., MAKSE, H. & STANLEY, H. 1999. Inertial effects on fluid flow through disordered porous media. *Physical Review Letters,* 82**,** 5249.

ANSYS CFX 2013. ANSYS CFX-Solver Theory Guide. *(Release 15) 146-152.*

ASQUITH, G. B. 1985. *Handbook of Log Evaluation Techniques for Carbonate Reservoirs*, American Association of Petroleum Geologists.

BACA, R. G., ARNETT, R. C. & LANGFORD, D. W. 1984. Modelling fluid flow in fractured-porous rock masses by finite-element techniques. *International Journal for Numerical Methods in Fluids,* 4**,** 337-348.

BAGNOLD, R. A. 1939. INTERIM REPORT ON WAVE-PRESSURE RESEARCH. (INCLUDES PLATES AND PHOTOGRAPHS). *Journal of the Institution of Civil Engineers,* 12**,** 202-226.

BAKER, M. J. 2011. *CFD Simulation of Flow through Packed Beds using the Finite Volume Technique.* Ph.D., University of Exeter.

BEAR, J. 1988. *Dynamics of fluids in porous media,* New York, Dover.

BENENATI, R. F. & BROSILOW, C. B. 1962. Void fraction distribution in beds of spheres. *AIChE Journal,* 8**,** 359-361.

BERBEROVIĆ, E., VAN HINSBERG, N. P., JAKIRLIĆ, S., ROISMAN, I. V. & TROPEA, C. 2009. Drop impact onto a liquid layer of finite thickness: Dynamics of the cavity evolution. *Physical Review E,* 79**,** 036306.

BERNABE, Y. 1991. Pore geometry and pressure dependence of the transport properties in sandstones. *GEOPHYSICS,* 56**,** 436-446.

BETONFORM 2015. tetrapod sea defence units. http://www.betonform.co.uk/gallery3/index.php/GANG-MOULDS/tetrapod-sea-defence-units: Accessed [04/09/2015].

BOEK, E. S. & VENTUROLI, M. 2010. Lattice-Boltzmann studies of fluid flow in porous media with realistic rock geometries. *Computers & Mathematics with Applications,* 59**,** 2305-2314.

BREDMOSE, H., PEREGRINE, D. H. & BULLOCK, G. N. 2009. Violent breaking wave impacts. Part 2: Modelling the effect of air. *Journal of Fluid Mechanics,* 641**,** 389-430.

BREWER, R. 1964. *Fabric and mineral analysis of soils,* New York,, Wiley.

BRITISH STANDARDS INSTITUTION 1991. BS 6349-7:1991 Maritime structures. *Part*

7: Guide to the design and construction of breakwaters. Accessed [11/11/2016]: https://bsol.bsigroup.com.
BROWN, G., HSIEH, H. & LUCERO, D. A. 2000. Evaluation of laboratory dolomite core sample size using representative elementary volume concepts. *Water Resources Research,* 36**,** 1199-1207.
BRUS, G., MIYAWAKI, K., IWAI, H., SAITO, M. & YOSHIDA, H. 2014. Tortuosity of an SOFC anode estimated from saturation currents and a mass transport model in comparison with a real micro-structure. *Solid State Ionics,* 265**,** 13-21.
BULLOCK, G. N., OBHRAI, C., MÜLLER, G., WOLTERS, G., PEREGRINE, D. H. & BREDMOSE, H. Advances in the understanding of wave-impact forces. 2006 / 01 / 01 / 2006. 111-120.
BULLOCK, G. N., OBHRAI, C., PEREGRINE, D. H. & BREDMOSE, H. 2007. Violent breaking wave impacts. Part 1: Results from large-scale regular wave tests on vertical and sloping walls. *Coastal Engineering,* 54**,** 602-617.
CARMAN, P. C. 1997. Fluid flow through granular beds. *Chemical Engineering Research and Design,* 75, Supplement**,** S32-S48.
CHAN, E. S. & MELVILLE, W. K. 1988. Deep-Water Plunging Wave Pressures on a Vertical Plane Wall. *Proceedings of the Royal Society of London A: Mathematical, Physical and Engineering Sciences,* 417**,** 95-131.
CHEN, L. L. Y. U. C. 1973. *Binary-Gas Diffusion of Methane - Nitrogen Through Porous Solids, PhD Thesis*, University of MICHIGAN.
CHINI, N., STANSBY, P., LEAKE, J., WOLF, J., ROBERTS-JONES, J. & LOWE, J. 2010. The impact of sea level rise and climate change on inshore wave climate: A case study for East Anglia (UK). *Coastal Engineering,* 57**,** 973-984.
CIVAN, F. 2011. Overview. *Porous Media Transport Phenomena.* John Wiley & Sons, Inc.
CLENNELL, M. B. 1997. Tortuosity: a guide through the maze. *Geological Society, London, Special Publications,* 122**,** 299-344.
COUMOU, D. & RAHMSTORF, S. 2012. A decade of weather extremes. *Nature Clim. Change,* 2**,** 491-496.
DARCY, H. 1856. *Les fontaines publiques de la ville de Dijon: Exposition et application des principes a suivre et des formules a employer dans les questions de distribution d'eau; ouvrage terminé par un appendice relatif aux fournitures d'eau de plusieurs villes au filtrage des eaux et a la fabrication des tuyaux de fonte, de plomb, de tole et de bitume. Atlas*, Victor Dalmont, Libraire des Corps imperiaux des ponts et chaussées et des mines.
DAVIS, M. E. 2002. Ordered porous materials for emerging applications. *Nature,* 417**,** 813-821.
DESHPANDE, S. S., ANUMOLU, L. & TRUJILLO, M. F. 2012. Evaluating the performance of the two-phase flow solver interFoam. *Computational science & discovery,* 5**,** 014016.
DEVIN, C. 1959. Survey of Thermal, Radiation, and Viscous Damping of Pulsating Air Bubbles in Water. *The Journal of the Acoustical Society of America,* 31**,** 1654-1667.
DEWI LE, B., SYBREN, D. & HYLKE DE, V. 2017. A high-end sea level rise probabilistic projection including rapid Antarctic ice sheet mass loss. *Environmental Research Letters,* 12**,** 044013.
DIANAT, M., SKARYSZ, M. & GARMORY, A. 2017. A Coupled Level Set and Volume of Fluid method for automotive exterior water management applications. *International Journal of Multiphase Flow,* 91**,** 19-38.
DOLD, J. W. 1992. An Efficient Surface-Integral Algorithm Applied to Unsteady Gravity-Waves. *Journal of Computational Physics,* 103**,** 90-115.
DULLIEN, F. A. L. 1992. *Porous Media: Fluid Transport and Pore Structure*, Academic Press.

EMANUEL, K. 2005. Increasing destructiveness of tropical cyclones over the past 30 years. *Nature,* 436**,** 686-688.
FAND, R. M., KIM, B. Y. K., LAM, A. C. C. & PHAN, R. T. 1987. Resistance to the Flow of Fluids Through Simple and Complex Porous Media Whose Matrices Are Composed of Randomly Packed Spheres. *Journal of Fluids Engineering,* 109**,** 268-273.
FEICK, R. & BOOTS, B. 2005. Variable Resolution Spatial Interpolation Using the Simple Recursive Point Voronoi Diagram. *Geographical Analysis,* 37**,** 225-243.
FEUILLADE, C. & WERBY, M. F. 1994. Resonances of deformed gas bubbles in liquids. *The Journal of the Acoustical Society of America,* 96**,** 3684-3692.
FOURAR, M., RADILLA, G., LENORMAND, R. & MOYNE, C. 2004. On the non-linear behavior of a laminar single-phase flow through two and three-dimensional porous media. *Advances in Water Resources,* 27**,** 669-677.
GALVIN, C. J. 1968. Breaker type classification on three laboratory beaches. *Journal of Geophysical Research,* 73**,** 3651-3659.
GHANBARIAN, B., HUNT, A. G., EWING, R. P. & SAHIMI, M. 2013. Tortuosity in Porous Media: A Critical Review. *Soil Science Society of America Journal,* 77**,** 1461-1477.
GODDERIDGE, B. 2009. *A phenomenological rapid sloshing model for use as an operator guidance system on Liquid Natural Gas carriers.* PhD, University of Southampton.
GOMEZ, H., CUETO-FELGUEROSO, L. & JUANES, R. 2013. Three-dimensional simulation of unstable gravity-driven infiltration of water into a porous medium. *Journal of Computational Physics,* 238**,** 217-239.
GOSLING, S. N., DUNN, R., CARROL, F., CHRISTIDIS, N., FULLWOOD, J., DE GUSMAO, D., GOLDING, N., GOOD, L., HALL, T. & KENDON, L. 2011. Climate: observations, projections and impacts. . *UK Met Office. Nottingham ePrints: Nottingham, UK*.
GRAHAM, D. I. & HEWSON, P. J. 1992. Measurement of aeration in model-scale breaking waves *Mast G6-S/Project 2, Informal Internal Report*.
GRATON, L. C. & FRASER, H. J. 1935. Systematic Packing of Spheres: With Particular Relation to Porosity and Permeability. *The Journal of Geology,* 43**,** 785-909.
HARLOW, F. H. & WELCH, J. E. 1965. Numerical calculation of time-dependent viscous incompressible flow of fluid with free surface. *Physics of fluids,* 8**,** 2182-2189.
HATTORI, M., ARAMI, A. & YUI, T. 1994. Wave Impact Pressure on Vertical Walls under Breaking Waves of Various Types. *Coastal Engineering,* 22**,** 79-114.
HIGUERA, P., LARA, J. L. & LOSADA, I. J. 2014. Three-dimensional interaction of waves and porous coastal structures using OpenFOAM®. Part I: Formulation and validation. *Coastal Engineering,* 83**,** 243-258.
HIRT, C. W. & NICHOLS, B. D. 1981. Volume of Fluid (VOF) Method for the Dynamics of Free Boundaries. *Journal of Computational Physics,* 39**,** 201-225.
HULME, M. 2016. 1.5 [deg]C and climate research after the Paris Agreement. *Nature Clim. Change,* 6**,** 222-224.
IKEDA, C., O'SHEA, T. T., BRUCKER, K. A., DRAZEN, D. A., DOMMERMUTH, D. G., FU, T., FULLERTON, A. M. & DUNCAN, J. H. 2014. The Impact of a Deep-Water Plunging Breaker. *arXiv preprint arXiv:1410.1915*.
INCROPERA, F. P. & DEWITT, D. P. 2002. *Fundamentals of heat and mass transfer,* New York, J. Wiley.
IVINGS, M. J., LEA, C. J. & LEDIN, H. S. 2004. Outstanding safety questions concerning the analysis of ventilation and gas dispersion in gas turbines enclosures. *Best practice guidelines for CFD.* Health and Safety Laboratory Report CM/03/12.
JENKINS, G. J., PERRY, M. C. & PRIOR, M. J. 2008. The climate of the United Kingdon

and recent trends. *Met Office Hadley Centre, Exeter, UK*.
KISACIK, D., TROCH, P. & VAN BOGAERT, P. 2011. Experimental results of breaking wave impact on a vertical wall with an overhanging horizontal cantilever slab. *Coastal Engineering Proceedings,* 1**,** 26.
KLEEFSMAN, K. M. T., FEKKEN, G., VELDMAN, A. E. P., IWANOWSKI, B. & BUCHNER, B. 2005. A Volume-of-Fluid based simulation method for wave impact problems. *Journal of Computational Physics,* 206**,** 363-393.
KOCH, M., LECHNER, C., REUTER, F., KÖHLER, K., METTIN, R. & LAUTERBORN, W. 2016. Numerical modeling of laser generated cavitation bubbles with the finite volume and volume of fluid method, using OpenFOAM. *Computers & Fluids,* 126**,** 71-90.
KOPONEN, A., EKMAN, A., MATTILA, K., AL-QARARAH, A. M. & TIMONEN, J. 2017. The Effect of Void Structure on the Permeability of Fibrous Networks. *Transport in Porous Media***,** 1-13.
KOPONEN, A., KANDHAI, D., HELLÉN, E., ALAVA, M., HOEKSTRA, A., KATAJA, M., NISKANEN, K., SLOOT, P. & TIMONEN, J. 1998. Permeability of Three-Dimensional Random Fiber Webs. *Physical Review Letters,* 80**,** 716-719.
KOZENY, J. 1927. *Über kapillare Leitung des Wassers im Boden: (Aufstieg, Versickerung u. Anwendung auf die Bewässerg) ; Gedr. mit Unterstütztg aus d. Jerome u. Margaret Stonborsugh-Fonds*, Hölder-Pichler-Tempsky, A.-G. [Abt.:] Akad. d. Wiss.
KUNDU, P., KUMAR, V. & MISHRA, I. M. 2016. Experimental and numerical investigation of fluid flow hydrodynamics in porous media: Characterization of pre-Darcy, Darcy and non-Darcy flow regimes. *Powder Technology,* 303**,** 278-291.
LEIGHTON, T. G. 1994. *The Acoustic Bubble*, Academic Press.
LONGUET-HIGGINS, M. S. & COKELET, E. D. 1976. The Deformation of Steep Surface Waves on Water. I. A Numerical Method of Computation. *Proceedings of the Royal Society of London A: Mathematical, Physical and Engineering Sciences,* 350**,** 1-26.
MARIC, T., HÖPKEN, J. & MOONEY, K. 2015. *The OpenFOAM Technology Primer*, SourceFlux GmbH.
MARTIN, H. 1978. Low peclet number particle-to-fluid heat and mass transfer in packed beds. *Chemical Engineering Science,* 33**,** 913-919.
MARTIN, J. C. & MOYCE, W. J. 1952. Part IV. An Experimental Study of the Collapse of Liquid Columns on a Rigid Horizontal Plane. *Philosophical Transactions of the Royal Society of London A: Mathematical, Physical and Engineering Sciences,* 244**,** 312-324.
MARTÍNEZ FERRER, P. J., CAUSON, D. M., QIAN, L., MINGHAM, C. G. & MA, Z. H. 2016. A multi-region coupling scheme for compressible and incompressible flow solvers for two-phase flow in a numerical wave tank. *Computers & Fluids,* 125**,** 116-129.
MATHWORKS 2015. Curve Fitting Toolbox: User's Guide (R2015b).
MATTILA, K., PUURTINEN, T., HYVÄLUOMA, J., SURMAS, R., MYLLYS, M., TURPEINEN, T., ROBERTSÉN, F., WESTERHOLM, J. & TIMONEN, J. 2016. A prospect for computing in porous materials research: Very large fluid flow simulations. *Journal of Computational Science,* 12**,** 62-76.
MATYKA, M., KHALILI, A. & KOZA, Z. 2008. Tortuosity-porosity relation in porous media flow. *Physical Review E,* 78**,** 026306.
MAYON, R., SABEUR, Z., TAN, M.-Y. & DJIDJELI, K. 2016. Free surface flow and wave impact at complex solid structures. *12th International Conference on Hydrodynamics.*
MINNAERT, M. 1933. XVI. On musical air-bubbles and the sounds of running water. *The*

London, Edinburgh, and Dublin Philosophical Magazine and Journal of Science, 16**,** 235-248.
MITSUYASU, H. 1966. Shock Pressure of Breaking Wave. *Proc. of 10th Int. Conf. Coastal Engineering., Tokyo, Italy,* ASCE, New York**,** 268-248.
NCE 2014. Dawlish rail washout triggers call for inland lines. *In:* ENGINEER, N. C. (ed.). The New Civil Engineer.
OUMERACI, H., KLAMMER, P. & PARTENSCKY, H. W. 1993. Classification of Breaking Wave Loads on Vertical Structures. *Journal of Waterway Port Coastal and Ocean Engineering-Asce,* 119**,** 381-397.
PARRIS, A., BROMIRSKI, P., BURKETT, V., CAYAN, D., CULVER, M., HALL, J., HORTON, R., KNUUTI, K., MOSS, R., OBEYSEKERA, J., SALLENGER, A. & WEISS, J. 2012. Global Sea Level Rise Scenarios for the US National Climate Assessment. *NOAA Tech Memo OARCPO-1*.
PEREGRINE, D. H. 2003. WATER-WAVE IMPACT ON WALLS. *Annual Review of Fluid Mechanics,* 35**,** 23-43.
RICHARDSON, L. F. & GAUNT, J. A. 1927. The Deferred Approach to the Limit. Part I. Single Lattice. Part II. Interpenetrating Lattices. *Philosophical Transactions of the Royal Society of London A: Mathematical, Physical and Engineering Sciences,* 226**,** 299-361.
ROACHE, P. J. 1997. Quantification of uncertainty in computational fluid dynamics. *Annual Review of Fluid Mechanics,* 29**,** 123-160.
RONG, X., HE, G. & QI, D. 2007. Flows with inertia in a three-dimensional random fiber network. *Chemical Engineering Communications,* 194**,** 398-406.
ROQUET, F., MADEC, G., MCDOUGALL, T. J. & BARKER, P. M. 2015. Accurate polynomial expressions for the density and specific volume of seawater using the TEOS-10 standard. *Ocean Modelling,* 90**,** 29-43.
ROSS, C. W. 1955. Laboratory study of shock presures on breaking waves. *BEB Tech. Memo,* No 59**,** 22pp.
ROUQUEROL, J., AVNIR, D., FAIRBRIDGE, C., EVERETT, D., HAYNES, J., PERNICONE, N., RAMSAY, J., SING, K. & UNGER, K. 1994. Recommendations for the characterization of porous solids (Technical Report). *Pure and Applied Chemistry,* 66**,** 1739-1758.
SABEUR, Z. A., ALLSOP, N. W. H., BEALE, R. G. & DENNIS, J. M. Wave dynamics at coastal structures: Development of a numerical model for free surface flow. 1997 / 01 / 01 / 1997. ASCE, 389-402.
SABEUR, Z. A., BEALE, R. G. & BOVOLIN, V. 1996. A full numerical simulation of wave dynamics at coastal structures with the volume of fluid method. *Hydraulic Engineering Software Vi***,** 395-404.
SABEUR, Z. A., COHEN, J. E., STEPHENS, J. R. & VELDMAN, A. E. P. 1998. Investigation on Free Surface Flow Oscillatory Impact Pressures with the Volume of Fluid Method. *in MJ Baines (ed.), Numerical Methods for Fluid Dynamics* VI**,** pp. 493 - 498.
SABEUR, Z. A., ROBERTS, W. & COOPER, A. J. Development and Use of an Advanced Numerical Model using the VOF Method for the Design of Coastal Structures. *In:* MORTON, K. W. & BAINES, M. J., eds. Numerical Methods for Fluid Dynamics V, 1995. Oxford University Press, 565-573.
SCHMIDT, R., OUMERACI, H. & PARTENSCKY, H. W. 1992. Impact loading induced by plunging breakers on vertical structures. *Proc. of 23rd Int. Conf. Coastal Engineering., Venice, Italy,* ASCE, New York 1545-1558.
SEIFFERT, B. R., ERTEKIN, R. C. & ROBERTSON, I. N. 2015. Wave loads on a coastal bridge deck and the role of entrapped air. *Applied Ocean Research,* 53**,** 91-106.
SHI, Y., LEE, Y. T. & KIM, A. S. 2011. Permeability calculation of sphere-packed porous

media using dissipative particle dynamics. *Desalination and Water Treatment,* 34**,** 277-283.
SIENA, M., HYMAN, J. D., RIVA, M., GUADAGNINI, A., WINTER, C. L., SMOLARKIEWICZ, P. K., GOUZE, P., SADHUKHAN, S., INZOLI, F., GUÉDON, G. & COLOMBO, E. 2015. Direct numerical simulation of fully saturated flow in natural porous media at the pore scale: a comparison of three computational systems. *Computational Geosciences,* 19**,** 423-437.
SOULAINE, C. [unpublished]. On the origin of Darcy's Law. Chapter 1.
STAGONAS, D., MARZEDDU, A., COBOS, F. X. G. I., CONEJO, A. S.-A. & MULLER, G. 2016. Measuring wave impact induced pressures with a pressure mapping system. *Coastal Engineering,* 112**,** 44-56.
STRASBERG, M. 1953. The Pulsation Frequency of Nonspherical Gas Bubbles in Liquids. *The Journal of the Acoustical Society of America,* 25**,** 536-537.
THE OPENFOAM FOUNDATION 2013. The Open Source CFD Toolbox, User Guide & Programmer Guide.
TOPLISS, M. E., COOKER, M. J. & PEREGRINE, D. H. Pressure oscillations during wave impact on vertical walls. 1993 / 01 / 01 / 1993. Publ by ASCE, 1639-1650.
VAKILHA, M. & MANZARI, M. T. 2008. Modelling of Power-law Fluid Flow Through Porous Media Using Smoothed Particle Hydrodynamics. *Transport in Porous Media,* 74**,** 331-346.
VALLABH, R., BANKS-LEE, P. & SEYAM, A. F. 2010. New Approach for Determining Tortuosity in Fibrous Porous Media. *Journal of Engineered Fibers and Fabrics,* 5**,** 7-15.
WADELL, H. 1935. Volume, Shape, and Roundness of Quartz Particles. *The Journal of Geology,* 43**,** 250-280.
WEEMS BROTHERS 2013. Marine Construction Riprap Construction. http://www.weemsbrothers.com/Photo_Gallery_Marine_Riprap.html: Accessed [04/09/2015].
WELLER, H. G., TABOR, G., JASAK, H. & FUREBY, C. 1998. A tensorial approach to computational continuum mechanics using object-oriented techniques. *Computers in Physics,* 12**,** 620-631.
WEMMENHOVE, R., LUPPES, R., VELDMAN, A. E. P. & BUNNIK, T. 2015. Numerical simulation of hydrodynamic wave loading by a compressible two-phase flow method. *Computers & Fluids,* 114**,** 218-231.
WESTON, D. E. 1966. Sound propagation in the presence of bladder fish. *Underwater acoustices Vol II,* II**,** pp. 55-58.
WITTE, H. H. 1998. Wave-induced impact loading in deterministic and stochastic reflection. *Mitt. Leichtweiss Inst. Wasserbau, Tech. Univ. Bruaunschweig.,* 102**,** 1-227.
WYLLIE, M. & ROSE, W. D. 1950. Application of the Kozeny equation to consolidated porous media. *Nature,* 165**,** 972-972.
ZHANG, S.-X. & LI, X. 2014. Design formulas of transmission coefficients for permeable breakwaters. *Water Science and Engineering,* 7**,** 457-467.
ZHANG, S. G., YUE, D. K. P. & TANIZAWA, K. 1996. Simulation of plunging wave impact on a vertical wall. *Journal of Fluid Mechanics,* 327**,** 221-254.

Appendix

FREE SURFACE FLOW AND WAVE IMPACT AT COMPLEX SOLID STRUCTRES

Robert Mayon[1, 3]*, Zoheir Sabeur[2, 1], Tan Mingyi[3], Kamal Djidjeli[4]

[1]Southampton Marine and Maritime Institute, University of Southampton, UK
E-mail: r.mayon@soton.ac.uk

[2]IT Innovation Centre, Electronics and Computer Science,
Faculty of Physical Science and Engineering, University of Southampton, UK
E-mail: zas@it-innovation.soton.ac.uk

[3]Fluid Structure Interaction Group,
Faculty of Engineering and the Environment, University of Southampton, UK
E-mail: m.tan@soton.ac.uk

[4]Computational Engineering and Design Group,
Faculty of Engineering and the Environment, University of Southampton, UK
E-mail: kkd@soton.ac.uk

* Corresponding Author

ABSTRACT

Hydrodynamic wave loading at structures is a complex phenomenon to quantify. The design of structures to resist wave loading has been historically and predominantly achieved through empirical and experimental observations. This is due to the challenging understanding and quantification of wave impact energy transfer processes with air entrainment at solid structures. This paper investigates wave loading on such structures with effects of air entrapment. Specifically, it focuses on predicting the multi-modal oscillatory wave impact pressure signals which result from transient waves impinging upon a solid wall. A large dataset of compressible (and incompressible) numerical modelling scenarios have been generated to investigate these processes. The modelling simulation data are verified through a grid scaling analysis and validated against previous studies. Air bubble entrapment oscillatory pressure response trends are observed in the compressible simulation during wave impact. A frequency domain analysis of the impact pressure response is undertaken. The numerical modelling results are found in good agreement with theoretical and experimental observation data. These findings provide good confidence on the robustness of our numerical model foundations particularly for investigating the air bubbles formation, their mechanics and adjusted resonance frequency modes at impact with solid walls.

1. INTRODUCTION

Severe damage can be inflicted on coastal defence structures as a result of high intensity wave forces. Many laboratory experiments have been performed to gain an understanding of the physical processes which occur at the wave impact interface, see e.g. (Topliss et al., 1993), (Bullock et al., 2006), (Bullock et al., 2007), (Bredmose et al., 2009). The damage sustained by coastal defences is often caused by their continuous exposure to transient wave impact pressures which at the present time are not fully understood, e.g. (Oumeraci et al., 1993), (Wemmenhove et al., 2015), (Alagan Chella et al., 2015). Additionally, pulse-like oscillatory pressure signals have been observed in many experimental studies, (Bagnold, 1939), (Hattori et al., 1994), (Peregrine, 2003), (Stagonas et al., 2016). These oscillations manifest themselves subsequent to the initial wave impact with solid walls and may be a source of much serious damage and deterioration to the structural integrity of coastal defences. Experimental studies for the validation of these oscillatory impact pressure response results has proven to be very difficult because of the highly nonlinear, transient nature of the wave breaking process, (Chan and Melville, 1988). This has led researchers to speculate as to the source of the observed oscillations within the pressure response signal. In this study we analyse the impact of a solitary wave with a solid interface while employing a CFD approach.

Experimental work has shown that incident waves on vertical structures can produce impulse pressures which greatly exceed magnitudes of the typical pressures that are expected when employing shallow water wave theory methods for analysis, (Peregrine, 2003). The magnitude of these impulse pressures can commonly exceed:

$$10\rho g(h + H) \tag{1}$$

H is the wave height, h is the water depth, ρ the water density and g the acceleration due to gravity. These higher magnitude impulse pressures have been attributed to a phenomenon often termed as the wave 'flip-through' effect, (Peregrine, 2003). However, additional highly destructive oscillatory pressure effects have been observed in experimental studies. These usually occur when air bubbles are entrained at impact. In this instance, the entrapped air bubbles will compress and dilate with a range of specific oscillatory frequencies. Further, and according to past theoretical, (Minnaert, 1933) and experimental studies, (Hattori et al., 1994), the frequency range with which these bubbles oscillate will be dependent on the size of the entrained air void during their formation.
In this paper, we briefly introduce the theory of free surface fluid flow; and the numerical methods to simulate wave impact at solid structures. We also introduce theories and experiments from the literature which show the relationships between formed sizes of air bubbles in fluid flows and their typical resonance frequencies of oscillation. We investigate numerical dam-break flow simulations with impact at a solid vertical wall and air entrapment. Specifically, the collapsing water column propagates across the model domain and impacts a solid interface. The initial simulation case of a two-phase incompressible flow is described. Our model is then modified to simulate compressible flow case. A large data set of test cases was generated by employing first and second order equation discretisation schemes for both the temporal and spatial terms in the fluid flow governing equations. A range of grid resolutions were also applied to the model to ensure veracity of results.

2. FREE SURFACE FLOW AND BUBBLE OSCILLATION THEORIES

2.1 Numerical Methods

The numerical simulations were preformed using the finite volume technique based open source CFD code OpenFOAM, (The openFOAM Foundation, 2013). This software is compiled as a collection of C++ libraries with dedicated pre-programmed solvers which can be used to model various fluid flow simulation scenarios. In this study, the incompressible two-phase solver `InterFoam` was first used to analyse the flow field development. Subsequently, the `compressibleInterFoam` solver was used to examine the effects of air entrapment in the fluid phase during wave breaking. Both of these solvers use the phase fraction based Volume of Fluid method (VOF), (Hirt and Nichols, 1981), to capture and represent the interface between the two fluids.

2.1.1 Volume of fluid method

The interaction of the individual fluid phase constituents in the model is important as the pressure transfer across the free surface boundary which defines an entrained air bubble is central to this study. In the volume of fluid method a function $\alpha(x, y, t)$, is introduced at each grid cell in the model domain. The value of this function is defined as unity at any cell which is fully occupied by the fluid; and zero at any cell completely devoid of fluid. Cells with intermediate values may contain a droplet, a bubble or are located such that the interface between the two fluids intersects that cell. In the VOF method, the temporal evolution of the phase fraction function and thus the advection of the flow in two dimensional space is governed by the following transport equation:

$$\frac{\partial \alpha}{\partial t} + u\frac{\partial \alpha}{\partial x} + v\frac{\partial \alpha}{\partial y} = 0 \tag{2}$$

Where the phase volume fraction $\alpha \in [0,1]$, and u and v are the fluid velocities in the x and y direction respectively. By calculating the derivatives of the α function at each cell boundary the free surface normal can be established, (Sabeur et al., 1995). The normal direction to the free surface is then the direction in which the α function varies most rapidly (i.e.$\nabla\alpha$). From the value of the α function and the direction of the normal to the fluid interface, a line cutting the cell can be drawn which represents the free surface boundary.

2.1.2 Incompressible model governing equations

The conservation of mass equation for an incompressible fluid is defined as follows:

$$\nabla \cdot \boldsymbol{U} = 0 \tag{3}$$

And the conservation of mass equation for the volume fraction $\alpha \in [0,1]$ can be represented as:

$$\frac{\partial \alpha}{\partial t} + \nabla \cdot \boldsymbol{U}\alpha + \nabla \cdot \boldsymbol{U}_c\alpha(1-\alpha) = 0 \tag{4}$$

Where $\boldsymbol{U}$ is the fluid velocity vector, and $\boldsymbol{U}_c$ is the artificial compression velocity vector given by $\boldsymbol{U}_c = \min[\boldsymbol{U}, \max(\boldsymbol{U})]$. The final term on the left hand side ensures a sharp interface is maintained between the fluid phases. The momentum conservation equation is formulated by summing the averaged fluid properties according to their constituent proportion in the boundary cell. For a two phase flow, density ρ in the cells is given by:

$$\rho = \sum_{\alpha=1}^{2} r_\alpha \rho_\alpha \tag{5}$$

Where r_α is the volumetric fraction of each constituent fluid in the free surface boundary cell.
A single momentum conservation equation for an incompressible fluid can then be defined for the homogeneous mixture as:

$$\frac{\partial(\rho \boldsymbol{U})}{\partial t} + \nabla \cdot (\rho \boldsymbol{U}\boldsymbol{U}) = -\nabla p_h + \nabla \cdot \mu(\nabla \boldsymbol{U} + \nabla \boldsymbol{U}^T) + \boldsymbol{F}_s + \rho \boldsymbol{f}_i \tag{6}$$

Where ρ is given in Equation (5), p_h is the hydrostatic pressure, μ is the fluid viscosity and $\boldsymbol{f}_i$ is the gravitational force. The term $\boldsymbol{F}_s$ represents the surface tension force and is calculated from $\boldsymbol{F}_s = \sigma\kappa\nabla\alpha$, where σ is the interfacial tension and the interface curvature is given by $\kappa = \nabla \cdot (\nabla\alpha/|\nabla\alpha|)$.

2.1.3 Compressible model equations
To include the effects of compressibility within the model an Equation of State (EOS) must be defined for each phase. For the air phase, the ideal gas EOS is specified as follows:

$$\rho_a = p\frac{1}{R_a T} \tag{7}$$

Where ρ_a is the air density, R_a is the specific gas constant for air, T is the air temperature and p is the pressure. For the water phase the perfect fluid EOS is defined as:

$$\rho_W = p\frac{1}{R_W T} + \rho_{W0} \tag{8}$$

Where ρ_{W0} represents the density of water at atmospheric pressure conditions. An additional term must be incorporated into equation (4) in order to allow for air to be modelled as a compressible medium in the interfacial cells.

$$\frac{\partial \alpha}{\partial t} + \nabla \cdot \boldsymbol{U}\alpha + \nabla \cdot \boldsymbol{U}_c\alpha(1-\alpha) = -\frac{\alpha}{\rho_W}\frac{\mathrm{D}\rho_W}{\mathrm{D}t} \tag{9}$$

The Euler compressible mass conservation equation is defined as:

$$\frac{\partial \rho}{\partial t} + \nabla \cdot (\rho \boldsymbol{U}) = 0 \tag{10}$$

The transport equation for the temperature term is derived from the energy conservation equation, (Martínez Ferrer et al., 2016) and is calculated accordingly using equation (11) below:

$$\frac{\partial \rho T}{\partial t} + \nabla \cdot (\rho \boldsymbol{U}T) - \Delta(\mu \mathrm{T}) = -\left(\frac{\alpha}{C_w} + \frac{1-\alpha}{C_a}\right)\left(\frac{\partial \rho k}{\partial t} + \nabla \cdot (\rho \boldsymbol{U}k) + \nabla \cdot (\boldsymbol{U}p)\right) \tag{11}$$

C_w and C_a are the specific heat capacities for water and air respectively, while k is the specific kinetic energy. A flow field solution can be obtained by applying the PIMPLE algorithm which is a pressure-velocity coupling approach derived through combining the PISO and SIMPLE algorithms.

2.2 Resonant Oscillation Frequency of a Single Bubble

2.2.1 Analytical method

The behaviour of a single air bubble which is entrained within an infinite water domain has previously been studied by Minnaert (1933). An analytic expression describing the resonant frequency of a bubble which is subjected to an impulse force is given by:

$$f = \frac{1}{2\pi r}\left(\frac{3\gamma p}{\rho}\right)^{0.5} \tag{12}$$

Where r is the bubble radius and, γ is the polytrophic coefficient of the fluid, and r is the bubble radius.

2.2.2 Laboratory Experimentations

Hattori et al. (1994), have conducted experiments to investigate the influence of air entrainment on impact pressures from a wave impinging on a vertical solid wall. By varying the wall location relative to the breaking wave they were able to capture and analyse the effects of 4 distinct geometries of the breaking wave. High speed video recording at the impact interface was captured, from which still images were provided. The first generated wave broke against the wall while exhibiting flip-through behaviour without the entrainment of bubbles and thus no oscillatory effects in the time-pressure history plot were observed.

The second wave impacted the wall while having developed a vertically flat wave front. This type of breaker yielded a very high impact pressure $p_{max}/\rho g H_b = 109.6$ followed by a series of high frequency (1 kHz) oscillations which decayed rapidly.

The third type of breaking wave geometry analysed was that of a plunging breaker with a thin lens of air trapped at the interface. Again, high amplitude impulse pressures were recorded, $p_{max}/\rho g H_b = 51.9$ with oscillating frequency 250 Hz.

The final wave profile investigated was that of a plunging breaker with a large trapped air bubble. It was found that the increase in the diameter *l*, of the entrained bubble resulted in a decrease in both the peak impulse pressure and an associated decrease in the oscillating pressure frequencies recorded. The relationship between the bubble diameter and peak pressure, and also the bubble diameter and pressure oscillation frequency was found to vary inversely. Hattori et al. (1994) noted that the expression for the oscillating pressure frequency is approximated by:

$$f_{ap} = 180\ (2r)^{-0.5} \tag{13}$$

3. NUMERICAL MODEL

3.1 Geometry and Boundary Conditions

The simulation set-up is in the configuration of a dam break flow test case as shown on Figure 1 below. The numerical wave tank is 0.3m long and 0.2m high. The tank contains a column of water of width 0.05715m and height 0.01143m. A no-slip boundary condition is prescribed at the tank base and at the vertical walls. As the top of the tank is considered to be open to the atmosphere, the inflow and outflow of fluid is permitted across this boundary. Thus, at this edge a combination of boundary conditions are specified for the pressure and velocity terms of the fluid flow governing equations to model inflow and outflow behaviour whilst maintaining the PIMPLE algorithm stability. In the case of the incompressible model a `fixedValue` boundary condition with a value of zero is specified for the pressure term whilst a `pressureInletOutletVelocity` boundary condition is applied to the velocity term at the top edge boundary of the tank. In the case of the compressible simulation, the numerical value of the `fixedValue` boundary condition is set to atmospheric pressure conditions (101 kPa) across the edge which represents the top of the numerical tank. The velocity boundary condition is unchanged from the incompressible case. Pressure is sampled at point P1 on the impact interface where the right hand side wall meets the tank base, (see Figure 1).

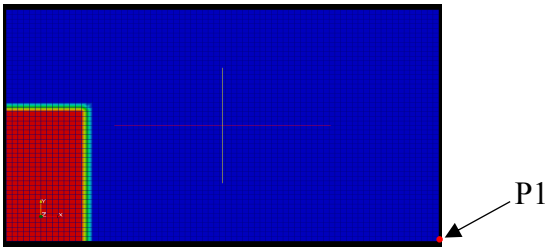

Figure 1: Initial CFD OpenFOAM model setup with 4mm mesh resolution and sampling point P1 indicated.

3.2 Flow Profile and Pressure Field Evolution

As the flow simulation progresses, the water column collapses and the flow front advances towards the right hand side (RHS) of the tank. The flow front impacts the solid RHS wall and is forced vertically upwards through the formation of a thin jet. Figure 2(a) and 2(d) present the α function and pressure distribution respectively as the flow front impacts the wall. This initial impact produces the first pressure peak shown on Figure 6(a) in Section 4.3.1 at time t = 0.205. As the jet collapses and converges with the fluid below, a bubble is entrained in the flow. This occurs at t = 0.492 seconds and yields the first oscillatory cycle local minimum pressure shown on Figure 6(b). The free surface geometry at bubble entrainment is displayed on Figure 2(b) with the associated pressure distribution shown on Figure 2(e).

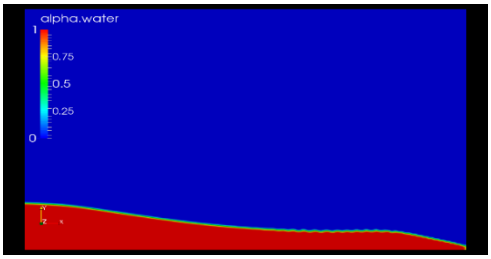

a. Free surface profile at t = 0.205 sec

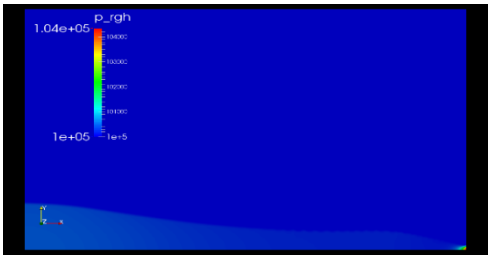

d. Pressure distribution at t = 0.205 sec

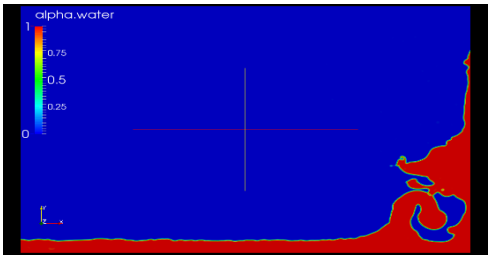

b. Free surface profile at t = 0.492 sec

e. Pressure distribution at t = 0.492 sec

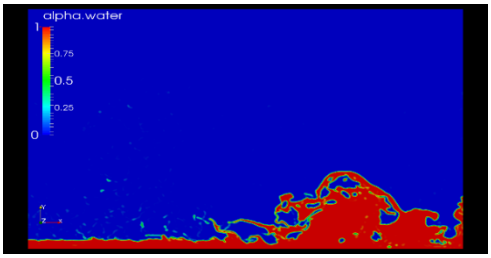

c. Free surface profile at t = 0.610 sec

f. Pressure distribution at t = 0.610 sec

Figure 2: Free surface evolution and associated pressure contour distributions from second order spatial and second order temporal equation discretisation scheme simulation

The amplitude of the oscillating pressure signal decays in an under-damped manner until the oscillations become negligible at approximately t = 0.610 seconds as presented on Figure 6(b). Figure 2(c) and 2(f) above, display the α function and pressure distribution at time t = 0.610 seconds respectively.

3.3 Spatial and Temporal Domain Discretisation

The spatial domain was initially discretised using a structured 4mm square hexahedral mesh. The

mesh resolution was refined three times as part of the grid independence study. Table 1 records the grid resolutions and associated model properties for this section of the study.
Initial simulations were conducted using a specified maximum Courant number of 1.0 and time-step length of 0.00001 sec. For the first order time and spatial discretisation schemes with low level grid resolution this time-step duration was sufficiently short to allow the Courant value to be maintained below 1.0, thus ensuring stability. However as the grid was progressively refined and higher order temporal and spatial equation discretisation schemes were applied to the model, an adaptive time-step control command reduced the time-step duration to ensure convergence of the solution.

Table 1: Grid resolutions

Grid	Δx [mm]	Δy [mm]	No. of nodes	No. of nodes x direction	No. of nodes y direction	No. of elements	No. of elements in x direction	No. of elements in y direction
1	4	4	7752	152	102	3750	75	50
2	2	2	30502	302	202	15000	150	100
3	1	1	121002	602	402	60000	300	200
4	0.5	0.5	482002	1202	802	240000	600	400

4. NUMERICAL SIMULATION RESULTS

4.1 Modelling Scalability Criteria

The grid independence study was established using the grid resolution data from Table 1. The spatial discretisation analysis was performed by calculating the impulse force *I*, at initial wave impact for each level of refinement. The impulse force was obtained for each grid resolution by integrating the maximum impact pressure peak over the rise time (Peregrine, 2003):

$$I(x) = \int_{Rt} p(x,t)dt \tag{14}$$

The duration of impact, which for this study is recorded as the peak rise time measured from a baseline time of 0.19 seconds was determined for each of the four levels of mesh discretisation as shown on Figure 3(a). The impulse force results were then compared to verify that progressive mesh refinement produced a solution trending towards convergence as shown in Figure 3(b). Table 2 records the results from the grid independence study.

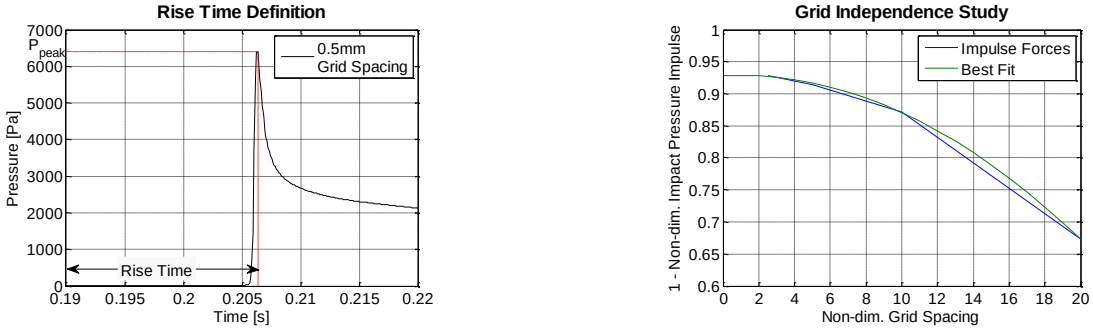

(a) Pressure peak rise time (b) Grid convergence

Figure 3: Model verification (a) pressure peak rise time, (b) grid convergence.

Table 2: Grid independence criteria

Grid	Rise time [R_t] [s]	Non-Dim. Rise time [R_{tnd}]	Peak pressure [p_{max}] [pa]	Non-Dim. Peak pressure [p_{maxnd}]	Non-Dim. impact pressure impulse [p_{ipnd}]
1	0.0233	0.8634	2484.8	2.2160	0.3276
2	0.0170	0.6300	3105.9	2.7700	0.1283
3	0.0169	0.6263	4259.7	3.7990	0.0852
4	0.0163	0.6040	6402.7	5.7102	0.0717

4.2 Model Validation

4.2.1 Collapsing fluid column leading edge position

Numerical model validation was achieved through comparison of the time varying leading edge position of the collapsing fluid column with experimental results from a study performed by Martin and Moyce (1952). The surge front location for the numerical simulation was plotted for each of the four levels of grid resolution. The results are shown on Figure 4. The flow front position shows good agreement between the different mesh resolution models. The 4mm grid spacing simulation reaches the impact interface later than the higher resolution grid simulations (indicated by a sharp change in derivative of the graphs). This is supported by the rise time data presented in Table 2. Also included on Figure 4 is a plot of the flow front leading edge position sampled during experiment 5 conducted by Martin and Moyce (1952). The numerical simulation shows good agreement with the experimental results.

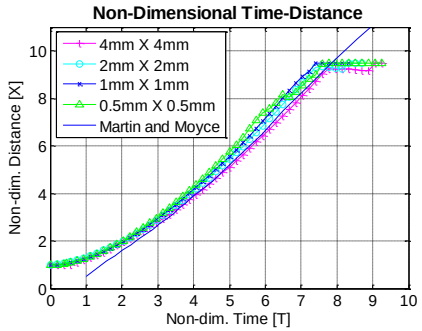

Figure 4: Model validation, flow front position

4.2.2 Transient pressure response comparison

The CFD model is further validated through comparison of the simulation pressure signal results with data from an experimental dam-break study published by Kleefsman et al. (2005).

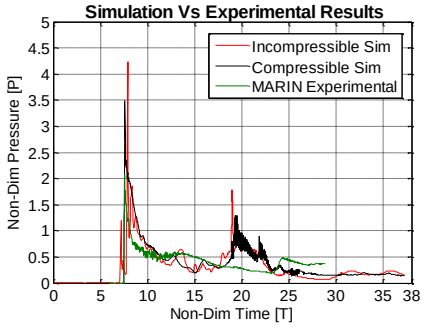

Figure 5: Model validation, transient pressure comparison with experimental results

The geometrical set up for the experiment consisted of a 1.22 metre wide by 0.55 metre high water column which, when released, impacted an obstacle located 1.77 metres from the nearside of the water column. This obstacle measured 0.16 metres wide and 0.16 meter high. By non-dimensionalising the time and pressure response values from the numerical study a direct comparison with the experimental pressure history plots could be made. Figure 5 above, displays a plot of the experimental time pressure history results from the study published by Kleefsman et al. (2005), versus both the incompressible and the compressible numerical simulation results. The pressure signal trend shows good agreement between the experimental and numerical results.

4.3 Simulation Pressure Response Results

The series of simulations performed can be classified according to those in which air compressibility effects were neglected and those in which air was considered as a compressible fluid and also according to the temporal and spatial equation discretisation schemes employed. The second order temporal and spatial scheme results are discussed in Section 4.3.1. Some further discussion on the first order temporal and spatial discretisation results for the 1 mm square grid size resolution for both incompressible and compressible simulations follows in Section 4.3.2.

4.3.1 Second order temporal second order spatial equation discretisation scheme

Figure 2 (Section 3.2) displays the α function and pressure distribution as the flow develops during the simulation. The pressure variation as a function of time for both the incompressible air phase simulation and the compressible air phase simulation is shown on Figure 6 below.

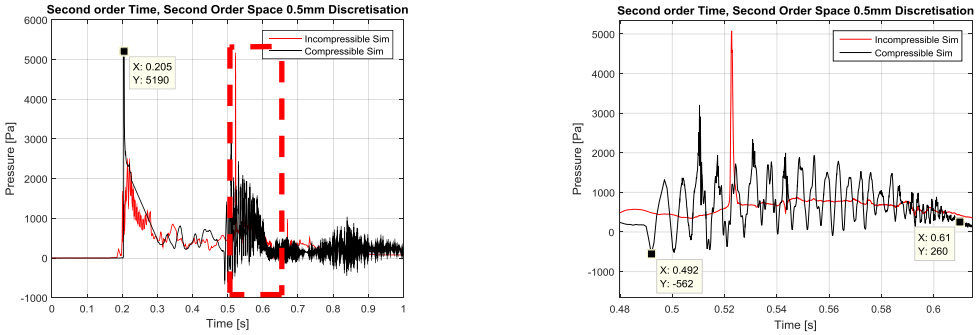

(a) Full pressure response signal (b) Bubble formation phase

Figure 6: Pressure response signal at P1: (a) Full simulation, (b) Oscillation due to air entrainment

It can be observed that between t = 0.492 and t = 0.610 a high amplitude, high frequency, resonant oscillation is recorded in the compressible simulation pressure response at point P1. This is due to the entrapment of a large air bubble which occurs as the vertical jet collapses. The initial entrained air bubble has a cross sectional area of approximately 1324.5 mm^2 which results in an equivalent spherical bubble of approximate radius 20 mm. As the simulation progresses this bubble fragments several times to form smaller bubbles. From Figure 6(b) the pressure signal recorded at P1 can be seen to oscillate with a regular frequency. By applying a Fast Fourier Transform (FFT) to the signal, five principal oscillating frequencies of 150, 180, 200, 219 and 252 Hz were computed. Table 3 summarises the formation of the first 5 bubbles observed during the simulation together with the main oscillatory frequencies.

Table 3: Entrained bubble evolvement and associated frequencies

Bubble	Area [mm]^2	Equivalent radius [mm]	Time which bubble forms [sec]	Time which bubble size is modified [sec]	Lifespan of bubble [sec]	Oscillation frequency [Hz]
1	1324.5	20	0.492	0.5045	0.0125	150
2	787	15.8	0.5045	0.5131	0.0086	180
3	474	12.3	0.5045	0.5231	0.0126	200
4	483	12.4	0.5131	0.5341	0.0210	219
5	489	12.5	0.5231	0.5431	0.0260	252

These frequencies can be compared with the adiabatic Minnaert resonant frequency given by Equation (12) and also with the experimentally derived relationship observed by Hattori et al. (1994) (Equation (13)). These results are presented on Figure 8.

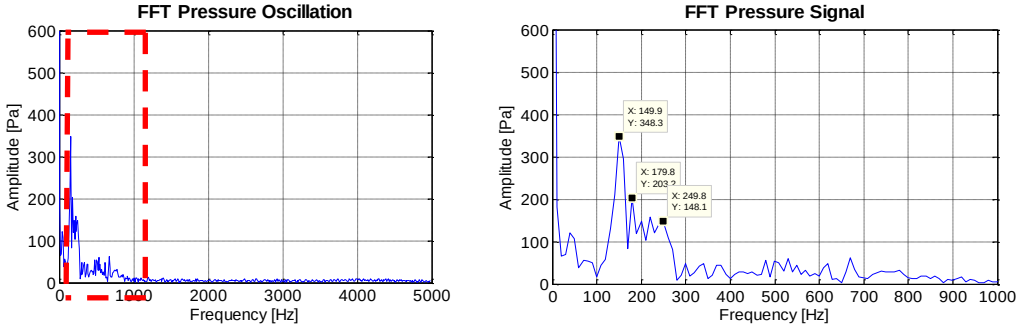

(a) Pressure signal FFT (b) Principal Frequencies

Figure 7: FFT Analysis of pressure oscillation.

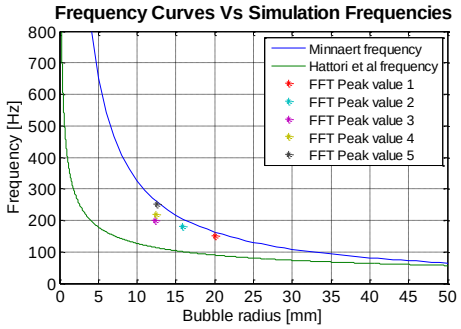

Figure 8: Analytic & Experimental bubble oscillatory frequencies versus numerical model frequency predictions

4.3.2 First order temporal, first order spatial equation discretisation scheme

To further ascertain that the resonant pressure signal oscillations observed at P1 originate from the pulsation of the entrained bubble, analysis was performed on the pressures sampled at a point within the entrapped air bubble.

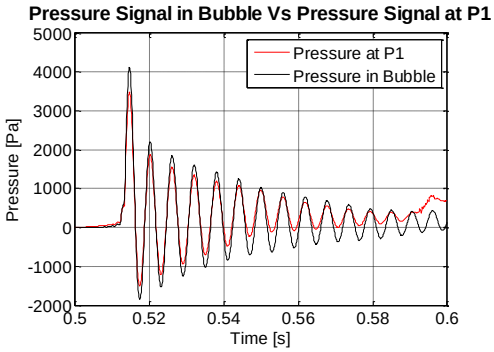

Figure 9: Pressure oscillations at the entrained air bubble vs pressure oscillations at P1

Figure 9 shows the pressure signal inside the air bubble and at position P1 obtained employing the first order temporal and spatial equation discretisation schemes on a 1mm square grid resolution from 0.5 to 0.6 seconds elapsed simulation time. The amplitude of the oscillating pressure signal sampled within the bubble is consistently larger than the pressure recorded at P1. This would imply that the resonant contraction and expansion action of the entrapped bubble is the source of the pressure oscillation. The reduced amplitude of the pressure signal at P1 may be due to energy loss through the free surface and energy loss due to viscous effects within the liquid phase. The pressure oscillation within the bubble also persists for some time after the oscillations at P1 are damped, further supporting the argument that the oscillations emanate from the entrained bubble.

5. CONCLUSIONS AND FUTURE DEVEOPMENTS

The origins of the oscillatory nature of impact pressures at solid walls have been investigated. There is-
clear evidence that the oscillation of the impact pressure at a solid wall is generated from entrapped oscillating air bubbles within the flow. A good size range of entrapped bubbles at the interface with the solid is numerically revealed together with their respective resonant frequencies. The evidenced bubbles respective life spans are found to be finite. One therefore expects the range of bubbles oscillatory frequencies to vary in time as the overall energy of the flow and impact pressures at the wall recede. Further studies of these effects are currently in progress while being applied to complex porous structures. The aim is to quantify the response of the flow at impact at such porous structures together with the manifested oscillatory frequencies of entrapped bubbles as a result.

REFERENCES

Alagan Chella M, Bihs H and Myrhaug D (2015) Characteristics and profile asymmetry properties of waves breaking over an impermeable submerged reef. *Coastal Engineering* 100: 26-36

Bagnold RA (1939) INTERIM REPORT ON WAVE-PRESSURE RESEARCH. (INCLUDES PLATES AND PHOTOGRAPHS). *Journal of the Institution of Civil Engineers* 12(7): 202-226
Bredmose H, Peregrine DH and Bullock GN (2009) Violent breaking wave impacts. Part 2: Modelling the effect of air. *Journal of Fluid Mechanics* 641: 389-430
Bullock GN, Obhrai C, Müller G, Wolters G, Peregrine DH and Bredmose H Advances in the understanding of wave-impact forces. 2006 / 01 / 01 /: 111-120
Bullock GN, Obhrai C, Peregrine DH and Bredmose H (2007) Violent breaking wave impacts. Part 1: Results from large-scale regular wave tests on vertical and sloping walls. *Coastal Engineering* 54(8): 602-617
Chan ES and Melville WK (1988) Deep-Water Plunging Wave Pressures on a Vertical Plane Wall. *Proceedings of the Royal Society of London A: Mathematical, Physical and Engineering Sciences* 417(1852): 95-131
Hattori M, Arami A and Yui T (1994) Wave Impact Pressure on Vertical Walls under Breaking Waves of Various Types. *Coastal Engineering* 22(1-2): 79-114
Hirt CW and Nichols BD (1981) Volume of Fluid (Vof) Method for the Dynamics of Free Boundaries. *J Comput Phys* 39(1): 201-225
Kleefsman KMT, Fekken G, Veldman AEP, Iwanowski B and Buchner B (2005) A Volume-of-Fluid based simulation method for wave impact problems. *J Comput Phys* 206(1): 363-393
Martin JC and Moyce WJ (1952) Part IV. An Experimental Study of the Collapse of Liquid Columns on a Rigid Horizontal Plane. *Philosophical Transactions of the Royal Society of London A: Mathematical, Physical and Engineering Sciences* 244(882): 312-324
Martínez Ferrer PJ, Causon DM, Qian L, Mingham CG and Ma ZH (2016) A multi-region coupling scheme for compressible and incompressible flow solvers for two-phase flow in a numerical wave tank. *Computers & Fluids* 125: 116-129
Minnaert M (1933) XVI. On musical air-bubbles and the sounds of running water. *The London, Edinburgh, and Dublin Philosophical Magazine and Journal of Science* 16(104): 235-248
Oumeraci H, Klammer P and Partenscky HW (1993) Classification of Breaking Wave Loads on Vertical Structures. *J Waterw Port C-Asce* 119(4): 381-397
Peregrine DH (2003) WATER-WAVE IMPACT ON WALLS. *Annual Review of Fluid Mechanics* 35(1): 23-43
Sabeur ZA, Roberts W and Cooper AJ (1995) Development and Use of an Advanced Numerical Model using the VOF Method for the Design of Coastal Structures. IN: Morton KW and Baines MJ (eds) *Numerical Methods for Fluid Dynamics V*: Oxford University Press 565-573
Stagonas D, Marzeddu A, Cobos FXGI, Conejo AS-A and Muller G (2016) Measuring wave impact induced pressures with a pressure mapping system. *Coastal Engineering* 112: 44-56
The Openfoam Foundation (2013) The Open Source CFD Toolbox, User Guide & Programmer Guide.
Topliss ME, Cooker MJ and Peregrine DH Pressure oscillations during wave impact on vertical walls. 1993 / 01 / 01 /: Publ by ASCE 1639-1650
Wemmenhove R, Luppes R, Veldman AEP and Bunnik T (2015) Numerical simulation of hydrodynamic wave loading by a compressible two-phase flow method. *Comput Fluids* 114: 218-231

ACKNOWLEDGEMENT

Thesis work is co-funded by the University of Southampton Marine and Maritime Institute (SMMI), the Faculty of Physical Sciences and Engineering (FPSE) and the Faculty of Engineering and the Environment (FEE).

ANALYSIS OF FLUID FLOW IMPACT OSCILLATORY PRESSURES WITH AIR ENTRAPMENT AT STRUCTURES

Robert Mayon[1]* Zoheir Sabeur[2] Mingyi Tan[3] and Kamal Djidjeli[4]

Hydrodynamic wave loading at coastal structures is a complex phenomenon to experiment, simulate and quantify. The nature of the fluid flow field as waves break against such structures has presented many challenges to scientists and engineers for the design of sustainable coastal defences. The provision of installations such as breakwaters to resist wave loading and protect coastal zones has evolved predominantly through empirical and experimental observations. This is due to the challenging understanding and precise quantification of wave impact energy transfer processes with air entrainment at structures. This paper presents a numerical investigation on wave loading at porous formations including the effects of air entrapment. Porous morphologies generated from cubic packed spheres with varying characteristics representing a breakwater structure are incorporated into the numerical model at the impact interface and the effect on the pressure field is investigated as the wave breaks. We specifically focus on analysing the impulse impact pressure as a surging flow front impacts a porous wall. Thereafter we investigate the multi-modal oscillatory impact pressure signals which result from a transient plunging breaker wave impinging upon a modelled porous coastal structure. The high frequency oscillatory pressure effects resulting from air entrapment are clearly observed in the simulations. A frequency domain analysis of the impact pressure responses is consequently undertaken. We show that the structural morphology of the porous assembly influences the pressure response signal recorded during the impact event. Our findings provide good confidence on the robustness of our numerical model particularly for investigating the air bubbles formation and their mechanics at impact with porous walls.

Keywords: Porous structures; fluid structure interaction; compressible flow; OpenFOAM, computational fluid dynamics

INTRODUCTION

Severe damage can be inflicted on coastal defence structures as a result of high intensity wave forces. Laboratory experiments have previously been performed to gain an understanding of the physical processes which occur at the wave impact interface e.g. (Topliss et al., 1993), (Bullock et al., 2006), (Bullock et al., 2007), (Bredmose et al., 2009). However the validation of these wave impact pressure response results has proven to be very difficult because of the highly nonlinear, transient nature of the wave breaking process (Chan and Melville, 1988).

The progressive damage sustained by coastal defences may be attributed to their continuous exposure to transient and highly oscillatory wave impact pressures. At the present time these forces are not fully understood and the long term durability of coastal defences is difficult to assess (Oumeraci et al., 1993), (Wemmenhove et al., 2015), (Alagan Chella et al., 2015). In addition to these short duration impulse impact pressures, resonant oscillatory pressure signals have been observed in many experimental studies (Bagnold, 1939), (Hattori et al., 1994), (Sabeur et al., 1998), (Peregrine, 2003), (Stagonas et al., 2016). These oscillations manifest themselves subsequent to the initial wave impact with solid or porous walls and may be the main source of deep damage to the structural integrity of coastal defences. Researchers have speculated as to the source of the observed oscillations within the impact pressure response signal (Peregrine, 2003).

Experimental work has shown that incident waves on vertical structures can produce impulse pressures which greatly exceed magnitudes of the typical pressures that are expected when employing shallow water wave theory methods for analysis (Peregrine, 2003). The magnitude of these impulse pressures can commonly exceed:

$$10\rho g(h + H) \qquad (1)$$

Where H is the wave height, h is the water depth, ρ the water density and $\boldsymbol{g}$ the acceleration due to gravity. These higher magnitude impulse pressures have been attributed to a phenomenon often termed as the wave 'flip-through' effect, (Peregrine, 2003). However, additional highly destructive oscillatory pressure effects have been observed in experimental studies, most noticeably when air bubbles are entrained at impact. In this instance, the entrapped air bubbles will compress and dilate with a range of specific oscillatory frequencies. Further, and according to earlier theoretical (Minnaert, 1933), and experimental studies (Hattori et al., 1994), the frequency range with which these bubbles oscillate will be dependent on the size of the entrained air void during their formation. The authors of this study have also observed these effects in previous numerical simulations, see e.g. (Mayon et al., 2016).

In this work we analyse the impact of a solitary wave with a porous interface while employing a CFD approach for numerical simulations. First we briefly introduce the theory for modelling free surface fluid flow;

[1] Southampton Marine and Maritime Institute, University of Southampton, UK
[2] IT Innovation Centre, Department of Electronics and Computer Science, University of Southampton, UK
[3] Fluid Structure Interaction Group, Faculty of Engineering and Environment , University of Southampton, UK
[4] Computational Engineering and Design Group, Faculty of Engineering and Environment, University of Southampton, UK
*Corresponding Author

and the numerical methods to simulate wave impact at porous structures. We also introduce theories and experiments from the literature which show the relationships between formed sizes of air bubbles in fluid flows and their typical resonance frequencies of oscillation. We investigate 3 dimensional numerical dam-break flow simulations with impact at varying morphology porous vertical wall interfaces. The numerical model is stable and capable of capturing the compressible effects of the air phase during bubble formation.

FREE SURFACE FLOW AND BUBBLE OSCILLATION THEORIES

Numerical Methods

The numerical simulations were preformed using the finite volume technique based open source CFD code OpenFOAM (The openFOAM Foundation, 2013). The code is compiled as a collection of C++ libraries with dedicated pre-programmed solvers which can be used to model various fluid flow simulation scenarios. In this study, the *compressibleInterFoam* solver was used to examine the effects of air entrapment in the fluid phase during wave breaking. This solver uses the phase fraction based Volume of Fluid method (VOF) (Hirt and Nichols, 1981), to capture and represent the interface between the two fluids.

Volume of fluid method

The interaction of the individual fluid phase constituents in the model is important as the pressure transfer across the free surface boundary which defines an entrained air bubble is central to this study. In the volume of fluid method a function, $\alpha(x, y, t)$, is introduced at each grid cell in the model domain. The value of this function is defined as unity at any cell which is fully occupied by the fluid; and zero at any cell completely devoid of fluid. Cells with intermediate values may contain a droplet, a bubble or are located such that the interface between the two fluids intersects that cell. In the VOF method, the temporal evolution of the phase fraction function and thus the advection of the flow in two dimensional space is governed by the following transport equation:

$$\frac{\partial \alpha}{\partial t} + u\frac{\partial \alpha}{\partial x} + v\frac{\partial \alpha}{\partial y} = 0 \qquad (2)$$

Where the phase volume fraction $\alpha \in [0, 1]$, and u and v are the fluid velocities in the x and y direction respectively. By calculating the derivatives of the α function at each cell boundary the free surface normal can be established, (Sabeur et al., 1995). The normal direction to the free surface is then the direction in which the α function varies most rapidly (i.e.$\nabla\alpha$). From the value of the α function and the direction of the normal to the fluid interface, a line cutting the cell can be drawn which represents the free surface boundary.

Compressible model governing equations

The conservation of mass equation for an incompressible fluid is defined as follows:

$$\nabla \cdot \boldsymbol{U} = 0 \qquad (3)$$

Using Equation (3) the two phase conservation of mass equation for the volume fraction $\alpha \in [0, 1]$ can then be represented as:

$$\frac{\partial \alpha}{\partial t} + \nabla \cdot \boldsymbol{U}\alpha + \nabla \cdot [\boldsymbol{U}_c \alpha(1-\alpha)] = 0 \qquad (4)$$

Where $\boldsymbol{U}$ is the fluid velocity vector, and $\boldsymbol{U}_c$ is the artificial compression velocity vector given by $\boldsymbol{U}_c = \boldsymbol{U}\alpha_1 - \boldsymbol{U}\alpha_2$, where $\boldsymbol{U}\alpha_1$ and $\boldsymbol{U}\alpha_2$ are the velocity vectors for the liquid and gas phases respectively (Berberović et al., 2009). The final term on the left hand side ensures a sharp interface is maintained between the fluid phases (Berberović et al., 2009). The momentum conservation equation is formulated by summing the averaged fluid properties according to their constituent proportion in the boundary cell. For a two phase flow, density ρ in the cells is given by:

$$\rho = \sum_{\alpha=1}^{2} r_\alpha \rho_\alpha \qquad (5)$$

Where r_α is the volumetric fraction of each constituent fluid in the free surface boundary cell. A single momentum conservation equation for an incompressible fluid can then be defined for the homogeneous mixture as:

$$\frac{\partial(\rho \boldsymbol{U})}{\partial t} + \nabla \cdot (\rho \boldsymbol{U}\boldsymbol{U}) = -\nabla p_h + \nabla \cdot \mu(\nabla \boldsymbol{U} + \nabla \boldsymbol{U}^T) + \boldsymbol{F}_s + \rho \boldsymbol{f}_i \qquad (6)$$

Where ρ is given in Equation (5), p_h is the hydrostatic pressure, μ is the fluid viscosity and $\boldsymbol{f}_i$ is the gravitational force. The term $\boldsymbol{F}_s$ represents the surface tension force and is calculated from $\boldsymbol{F}_s = \sigma\kappa\nabla\alpha$, where σ is the interfacial tension and the interface curvature is given by $\kappa = \nabla\cdot(\nabla\alpha/|\nabla\alpha|)$.

To include the effects of compressibility within the model an Equation of State (EOS) must be defined for each phase. For the air phase, the ideal gas EOS is specified as follows:

$$\rho_a = p\frac{1}{R_a T} \tag{7}$$

Where ρ_a is the air density, R_a is the specific gas constant for air, T is the air temperature and p is the pressure. For the water phase the perfect fluid EOS is defined as:

$$\rho_w = p\frac{1}{R_W T} + \rho_{W0} \tag{8}$$

Where ρ_{W0} represents the density of water at atmospheric pressure conditions. To allow for air to be modelled as a compressible medium an additional term must be incorporated into Equation (4):

$$\frac{\partial \alpha}{\partial t} + \nabla \cdot \boldsymbol{U}\alpha + \nabla \cdot \boldsymbol{U}_c \alpha(1-\alpha) = -\frac{\alpha}{\rho_W}\frac{D\rho_W}{Dt} \tag{9}$$

Equation 3 is modified to yield the Euler compressible mass conservation equation defined as:

$$\frac{\partial \rho}{\partial t} + \nabla \cdot (\rho \boldsymbol{U}) = 0 \tag{10}$$

The transport equation for the temperature term is derived from the energy conservation equation, (Martínez Ferrer et al., 2016), and is calculated accordingly using equation (11) below:

$$\frac{\partial \rho T}{\partial t} + \nabla \cdot (\rho \boldsymbol{U} T) - \Delta(\mu T) = -\left(\frac{\alpha}{C_W} + \frac{1-\alpha}{C_a}\right)\left(\frac{\partial \rho k}{\partial t} + \nabla \cdot (\rho \boldsymbol{U} k) + \nabla.(\boldsymbol{U} p)\right) \tag{11}$$

C_{W} and C_a are the specific heat capacities for water and air respectively, while k is the specific kinetic energy. A flow field solution can be obtained by applying the PIMPLE algorithm which is a pressure-velocity coupling approach derived through combining the PISO and SIMPLE algorithms.

Resonant oscillation Frequency of a single entrained air bubble

The behaviour of a single air bubble which is entrained within an infinite water domain has previously been studied by Minnaert (1933). An analytic expression describing the resonant frequency of a spherical bubble which is subjected to an external impulse force is given by:

$$f = \frac{1}{2\pi r}\sqrt{\left(\frac{3\gamma p}{\rho}\right)} \tag{12}$$

Where r is the bubble radius, γ is the polytrophic coefficient of the fluid, p is the hydrostatic pressure at the depth which the bubble is located in the liquid and ρ is the liquid density.

Hattori et al. (1994), have conducted experiments to investigate the influence of air entrainment on impact pressures from a wave impinging on a vertical solid wall. By varying the wall location relative to the breaking wave they were able to capture and analyse the effects of 4 distinct geometries of the breaking wave. High speed video recording at the impact interface was captured, from which still images were provided. From their experimental analysis the oscillating frequency of an entrained bubble is given by:

$$f_{ap} = 180(2r)^{-0.5} \tag{13}$$

3 DIMENSIONAL POROUS IMPACT INTERFACE SIMULATION

There are two main approaches to modelling fluid transport in porous media. The first approach is the macroscopic continuum method wherein the flow is modelled according to the Navier-Stokes equations with an additional Darcy (or Darcy-Forcheimer) term. This term is incorporated into the momentum equation in the region where the porous structure is located (Higuera et al., 2014). With this method the physics of the flow through the porous medium is governed by phase quantities which are averaged over control volumes across the flow (also known as Representative Elementary Volumes).

The second approach for modelling fluid flow through porous media is a direct modelling approach wherein each phases is explicitly represented and the flow through the porous interstices is modelled explicitly using the Navier-Stokes equations. Other methods for modelling flow in porous media include the Smoothed Particle Hydrodynamic (SPH) method and Lattice Boltzmann methods. In our study the direct modelling approach is employed.

For this investigation a number of porous geometries were generated and incorporated into the OpenFOAM CFD model. Various parameters were used to classify the porous structure according to its morphology. These parameters include porosity, specific surface area, tortuosity and permeability.

Porous structure classification

Porosity

A porous sample in its most basic definition is a material composed of a certain solid volume which contains a proportion of distributed void space. These voids can be occupied by one or more fluids in either a liquid phase, a gaseous phase or both. Thus porosity for the purpose of this investigation is defined as the fraction of the bulk volume of the sample which is occupied by pore or void space. Civan (2011) provides a mathematical definition of porosity as:

$$\Phi = \frac{\sum_{j \neq s} \Delta V_j}{\Delta V_b} \tag{14}$$

Where ΔV_b is the bulk volume of the porous sample or the total volume occupied by all phases, ΔV_j is the volume occupied by the j^{th} phase and s denotes the sum of the solid phases forming the porous matrix.

Bear (1988) provides a more onerous characterisation of a porous media which suggests that the multi-phase matrix must satisfy certain conditions such as level of void space interconnectedness, lower bound limits on interstitial surface areas and uniformity in phase distribution. However the definition of a porous medium is still couched in ambiguity as there is no complete consensus on limits for any of the above conditions.

Specific surface area

The specific surface area of a porous sample is defined as the interstitial void (or solid) surface area per unit bulk volume having a reciprocal length dimension. In molecular science specific surface area greatly influences adsorption rates and reactivity processes. However on a macroscale scale it can also be used to characterise the morphology of the porous structure. A higher specific surface implies a more complex porous media. Additionally a high specific surface area may also decelerate the flow of fluid through the porous structure as the wall shear stress will have a more pronounced effect due to a higher phase interfacial area.

Tortuosity

Tortuosity is an inherent characteristic of a porous media morphology which in general terms can be described as a ratio of the distance traversed by a fluid element between two fixed points to the straight line distance between those two points as shown in Figure 1(Brus et al., 2014). Tortuosity can be calculated from:

$$\tau = \frac{L_e}{L_s} \geq 1 \tag{15}$$

Where L_e and L_s are shown on Figure 1.

Whilst there has been a large body of academic research presented on the subject of tortuosity, there is no general agreement for a single precise definition of tortuosity and to date a number of different measurements of tortuosity have been advanced for different applications. For example Ghanbarian et al. (2013) in their review paper describe geometric tortuosity, hydraulic tortuosity, electrical tortuosity and diffusive tortuosity.

The difficulty in achieving a unanimous characterisation for tortuosity may be twofold; with the exception of very few materials, e.g. metals, dense rocks and some plastics (Dullien, 1992), most materials exhibit porous behaviour to varying degrees at multiscale levels from microscopic through to macroscopic scale. The parameters which govern tortuosity may vary dramatically within a single material at different scale lengths thus effecting the observed tortuous transport path length. Therefore depending on which scale of analysis is being considered, different fluid behavioural effects may dominate the calculated tortuosity ratio.

When analysing the flow of fluid through porous media either the geometric or hydraulic tortuosity is usually considered. Figure 2, Ghanbarian et al. (2013) presents a comparison of a hydraulic tortuous flow path and a geometric tortuous flow path. At the microscale multiphase interfacial parameters such as capillary pressures, surface tension effects and wall friction may all significantly influence the flow rate through a porous structure, however at larger scale lengths these effects may not warrant consideration due to the bulk of the flow being conveyed through larger fissures where wall friction, capillary and free surface effects are not the limiting constraints on the flow rate. Then, it may be more appropriate to use hydraulic tortuosity for microscale analyses and geometrical tortuosity at larger scales.

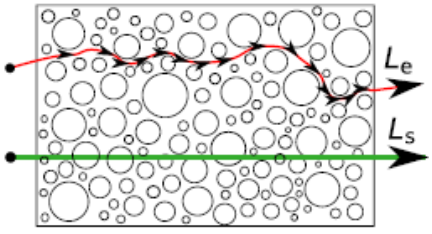

Figure 1 Tortuosity (Brus et al., 2014)

The structure of porous materials can take many forms, and the tortuous paths can vary from being comparatively simple to being highly complicated. For instance the porous structure of a natural material such as wood can be somewhat homogenous and anisotropic and thus the tortuosity can be relatively simply described by reducing the material to a model consisting of a bundle of unidirectional capillary tubes. This limiting case of a bundle of parallel, non-interconnected tubes longitudinally orientated in the direction of macroscopic flow, traversing the full thickness, L_s, of the sample presents little resistance to the flow (neglecting frictional effects at the tube wall). Then, a flow streamline, L_e, tracing the path of the fluid will have a length similar to the thickness of the sample, i.e. the tortuosity factor can be calculated for Equation 15 and will have a value of unity.

In contrast, a material may be much more complex and disordered having multidirectional interweaving fibrous filaments as evidenced within some filter materials or in paper products. Then, the structural morphology is much more difficult to define and the parameters which can be used to describe the tortuous nature of interconnecting porous voids can be very challenging to determine from the physical sample. In this study the void throats between the solid particles are relatively narrow such that the flow streamlines are seen to be influenced by the surface of the solid phase material in the CFD model. The hydraulic tortuosity is therefore adopted in this investigation.

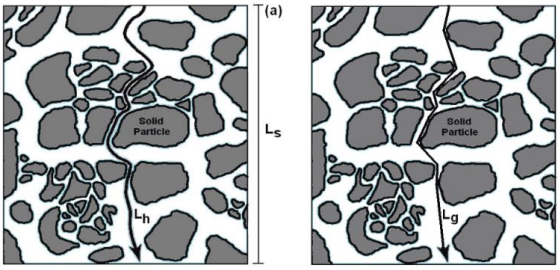

a. Hydraulic tortuous path **b. Geometric tortuous path**

Figure 2 Comparison between hydraulic tortuosity and geometric tortuosity, Ghanbarian et al. (2013)

Fluid flow through a porous medium is influenced by both the amount and morphology of the void (pore) space (Vallabh et al., 2010). While the amount of void space is easily quantified by measurement of porosity, the characterisation of the distribution of the void space structure is often very difficult, especially in complex, irregular porous media (Vallabh et al., 2010). In the case wherein the pore structure is more intricate with many converging and diverging channels the streamline path may not follow the liner shortest distance between the bounding surfaces of the sample. Rather, the streamlines may be forced to follow a sinuous winding path determined by the morphology of the solid (or void) phase. Then the tortuosity factor must be greater than unity. This increases the time taken for the fluid to permeate through the porous media and results in an associated higher resistance to the flow. Thus the tortuosity of a complex sample can be computed as a time dependent variable. Additionally, the higher resistance to flow is manifest in a lower permeability value for the sample. As the value of tortuosity approaches infinity this represents an internal pore structure (and geometric morphology) of increasing complexity. Furthermore, a thorough analysis and understanding of tortuous paths within a sample presents one with a means to quantify the complexity and also the permeability of the sample.

Simulated porous structure morphology

In an earlier study a comprehensive analysis of wave impacts with a solid interface were performed. A range of equation discretisation schemes were employed and the oscillatory behaviour of the resultant bubble(s) were analysed in depth, (Mayon et al., 2016).

In this study wave impact at a single porous morphology with varying component sphere sizes are investigated. The geometry consists of a number of spheres on a regular cubic lattice layout. The porous structures were generated using a short LISP file and the CAD software package AutoCAD Mechanical. The geometries were then exported as stereolithographic files. The OpenFOAM mesh generation utility snappyHexMesh was then used to construct an accurate 3-dimensional split-hex mesh which defined the void geometry within the porous structure.

In order to establish the exclusive influence of the various porous morphology characteristics; surface area, porosity, tortuosity, permeability, etc. on the wave impact pressure signal a range of simulations were conducted whilst varying the component sphere size. Each of these porous structures have mono-sized spheres arranged on a distinct regular geometric lattice. The work presented in this study will be restricted a single regular lattice layout; simple cubic packing. The following subsections describe the porous structure and how it is generated.

Simple cubic packing

This spherical based structure consists of a mono-sized, close packed sphere-swarm arranged on a cubic lattice layout. With the exception of the outermost spheres on the boundary of the lattice (and assuming that

there is a minimum of 27 spheres composing the structure), each sphere is in direct contact with its 6 neighbours, this is also termed the coordination number. This sphere packing arrangement is known as simple cubic packing (see Figure 3).

Assuming the bounding box enclosing the lattice structure maintains a fixed volume and the spheres are tightly packed, then the porosity of the assembly is constant for any range of component sphere size. Thus due to the regular composition of the structure the porosity is maintained with a value of 0.476 for all simulations with the elemental spheres in a simple cubic packing system. The constant porosity is obvious from Figure 3. This allows one to investigate the influence of porous matrix component grain size on the flow field while maintaining the structure's overall density at a constant value. In this study a bounding cube of 100mm length was defined and 4 geometries based on packed sphere sizes of 25mm diameter, 12.5mm diameter, 6.25mm diameter and 3.125mm diameter were investigated.

Furthermore, the theoretical geometric tortuosity of the matrix which is an inherent characteristic of the porous structure and is determined by its geometrical composition also retains a constant value and is calculated according to Equation 15.

However if hydraulic tortuosity is employed then it can be easily shown mathematically that the tortuosity parallel to the flow direction varies from a minimum value of $\tau = 1.0$ to a maximum value of tortuosity $\tau = 1.57$ (irrespective of the elemental sphere diameter), assuming the flow streamline remains within the x-y plane of the fluid flow direction and is coincident with the sphere surfaces. The value of $\tau = 1.0$ is obtained if one considers a streamline which is located at maximum distance from the surface of the spheres, and $\tau = 1.57$ is obtained for a streamline which follows the contour of the spheres surface and assuming the streamline stays in the x-y plane (see Figure 3).

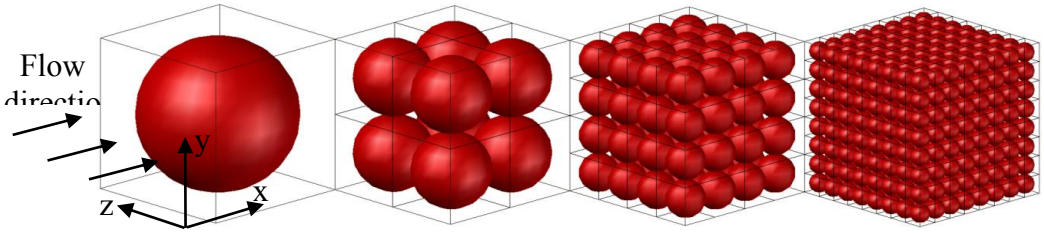

Figure 3: Simple cubic packing arrangement for varying sphere sizes

Table 1. Simple cubic packing structure characteristics*

Sphere diameter	25mm		12.5 mm		6.25 mm		3.125 mm	
Porosity	47.64 %		47.64 %		47.64 %		47.64 %	
# of spheres	64		512		4,096		32,768	
Surface area	125,662mm^2		251,279mm^2		502,558mm^2		1,005,116mm^2	
Specific surface area	0.1257 mm^{-1}		0.2513 mm^{-1}		0.5026 mm^{-1}		1.0051 mm^{-1}	
Coordination number	6		6		6		6	
In-plane (analytic) Tortuosity	**min**	**max**	**min**	**max**	**min**	**max**	**min**	**max**
	1	1.57	1	1.57	1	1.57	1	1.57

*values calculated assuming spheres packed into cube of side 100mm

SIMULATION SETUP

The simulation set-up follows an earlier study presented in Mayon et al. (2016). Model verification and validation data may also be found in Mayon et al. (2016). The geometry is in the configuration of a dam break flow test case as shown on Figure 4 below. The numerical wave tank is 0.4m long and 0.2m high and 0.1m deep. The tank contains a column of water of width 0.05715m, height 0.01143m and depth 0.1m at the left hand side. A no-slip boundary condition is prescribed at the tank base and at vertical walls at x = 0, z = 0 and z = 0.1. As the top of the tank is considered to be open to the atmosphere, the inflow and outflow of fluid is permitted across this boundary. Thus, at this surface a combination of boundary conditions are specified for the pressure and velocity terms of the fluid flow governing equations to model inflow and outflow behaviour whilst maintaining the PIMPLE algorithm stability. The numerical value of the `fixedValue` boundary condition is set to atmospheric pressure conditions (101 kPa) across the surface which represents the top of the numerical tank. The porous morphologies were incorporated into the model at the right hand side of the domain. Additionally at the right hand side surface (at x = 0.4) the boundary condition applied permits the outflow of fluid from the domain. The pressure signals are sampled at mid height the face of the bottom sphere forming the porous matrix indicated by point P1 on Figure 4 below.

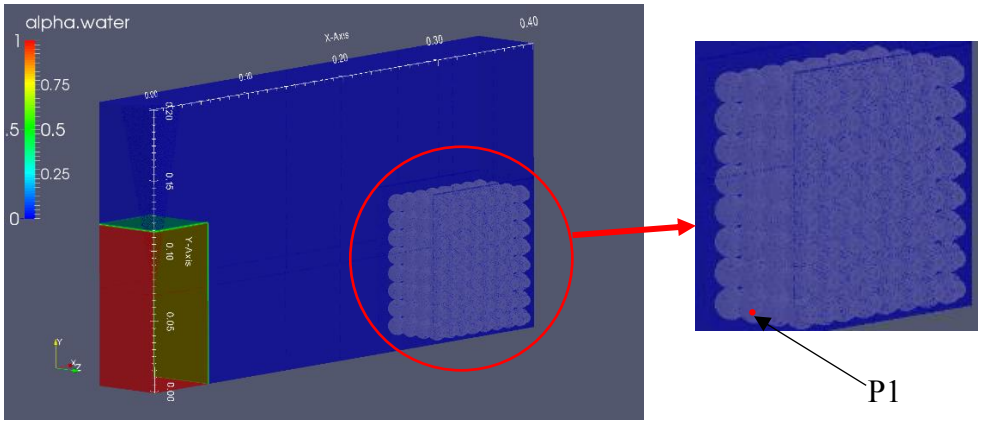

Figure 4: Section through simulation setup (sphere diameter 12.5mm)

As the flow simulation progresses, the water column collapses and the flow front advances towards the right hand side (RHS) of the numerical tank. The surging flow front impacts the porous (Figure 5 (a)) structure and is forced vertically upwards through the formation of a thin jet, Figure 5 (b). Figure 5 (a) presents the α function as the flow front impacts the wall. This initial impact produces the first pressure peak shown on Figure 7 at time t = 0.208. As the vertical jet collapses (Figure 5(c)) it forms a plunging breaker type wave and converges with the fluid below, at this time a bubble is entrained in the flow. For the 3.125mm diameter cubic packed sphere structure this occurs at t = 0.515 seconds (Figure 5(d)) and yields the first oscillatory cycle local maximum pressure shown on Figure 8.

SIMULATION RESULTS

Simulation free surface profile

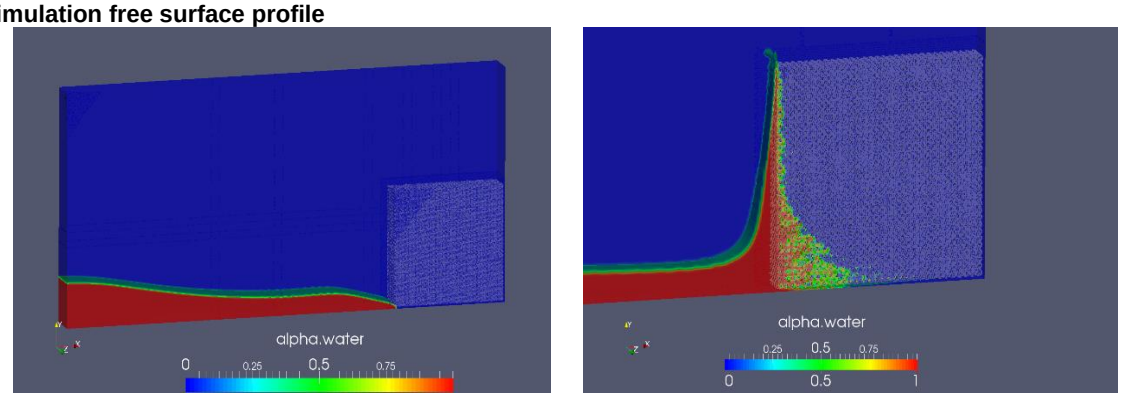

(a) Time = 0.208 sec

(b)
Time = 0.276 sec

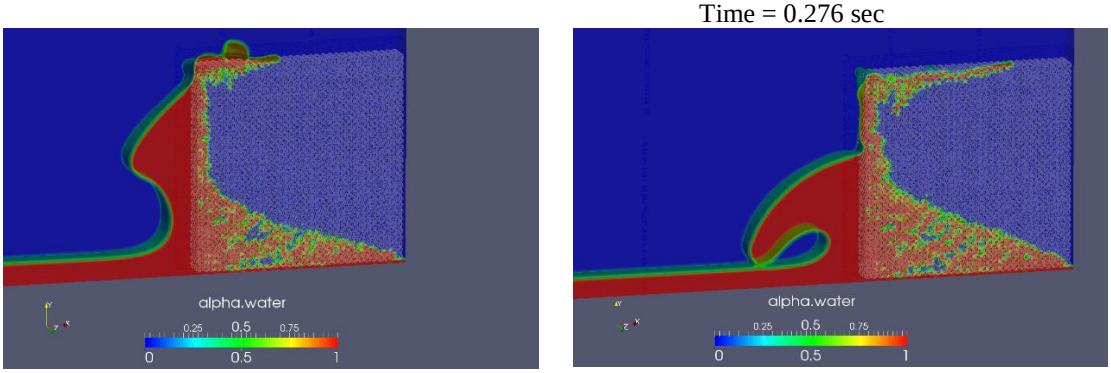

(c) Time = 0.450 sec

(d) Time = 0.515 sec

Figure 5: Free surface flow profile section (sphere diameter 3.125mm)

Table 2. Simple cubic packing simulation results

Spheres Diameter	25mm	12.5 mm	6.25 mm	3.125 mm
Outflow flow rate (end time of simulation)	506,960 mm^3/sec	365,680 mm^3/sec	163,450 mm^3/sec	70,100 mm^3/sec
Bubble Oscillation Frequency	298.5 Hz	224Hz	199Hz	174Hz
Bubble Oscillation Amplitude	51	300	557.6	580
Entrained bubble radius (analytic prediction)	10.9 mm	14.6mm	16.4mm	18.8mm
Observed Simulation Bubble Volume	12,284 mm^3	12,190 mm^3	16,423 mm^3	16,396 mm^3
Bubble Surface Area	3,930 mm^2	3,800 mm^2	4,294 mm^2	3,612 mm^2
Bubble (Cylindrical) Length	50 mm	50 mm	50 mm	50 mm
Bubble Sphericity*	0.6551	0.6741	0.7227	0.8642
Equivalent entrained bubble radius (simulation)	14.31	14.27	15.77	12.51

*calculated following Wadell (1935)

Pressure signal analyses

Figure 6 below shows the pressure signal for each of the simulations with the varying component sphere diameter porous structures. Also included on the figure is the pressure signal for a wave impact with a solid wall computed using a similar simulation setup. The solid wall impact results are taken from the analysis of Mayon et al. (2016).

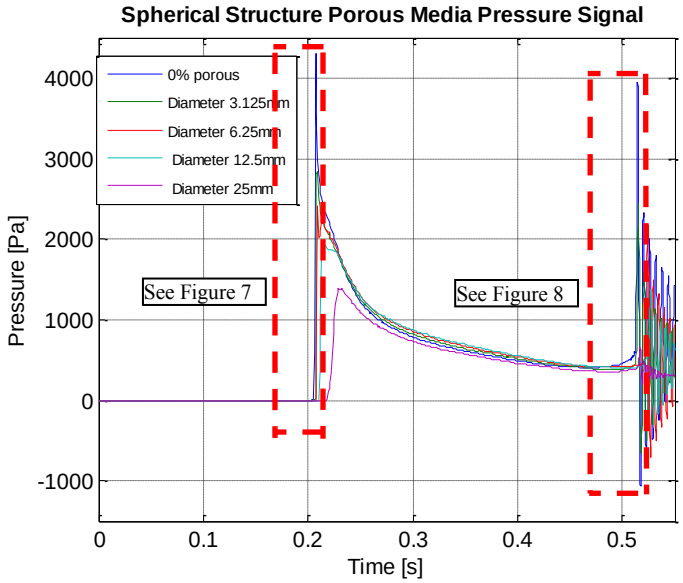

Figure 6: Pressure signals recorded at the interface of the porous structures

Figure 7(a) show the pressure response recorded as the surging flow front impacts the solid and porous walls. There is a slight delay in the impact time for larger spheres as the wave front initially hits the these spheres at a position below P1 (see Figure 4) before flowing vertically up the face of the sphere thereby inducing a pressure increase. The porous structures composed of the larger spheres also exhibit extended impact durations, also termed the rise time, see e.g. (Peregrine, 2003), (Mayon et al., 2016). Whilst the porosity of all the structures is identical the void channels between the larger spheres have a larger surface area opening, this allows the fluid to penetrate these porous structures more easily than the structure with more numerous but smaller surface area openings. This may be explained through the higher wall friction due to the greater specific surface area for the porous assemblages comprising of smaller spheres. The result of this longer rise time is a softer, less impulsive impact for the larger sphere structure. The higher flow rate through the larger sphere porous network supports this assertion.

Figure 7(b) shows the relationship between the sphere diameter and the magnitude of the impulse force. The magnitude of the impulse decreases monotonically as the component sphere diameter increases.

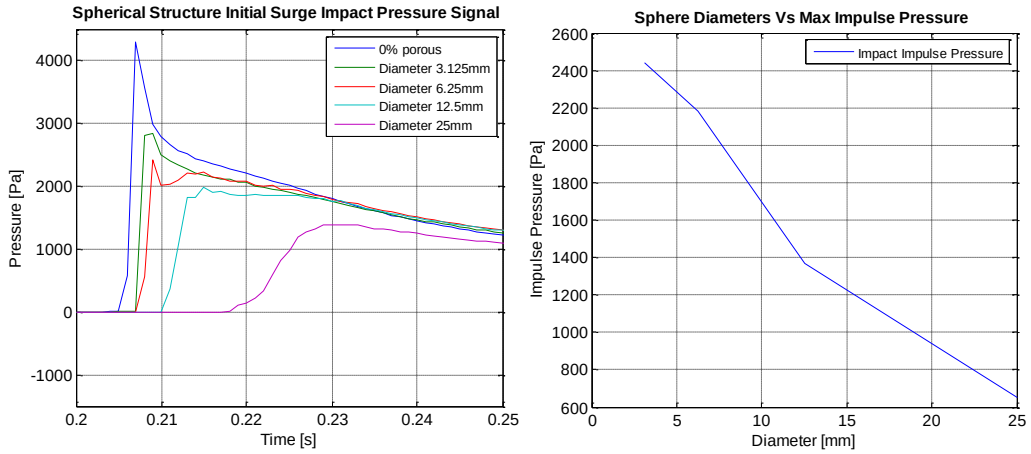

(a) Impact pressure impulse (b) Sphere diameter Vs impulse impact pressure magnitude

Figure 7: Initial impulse impact pressure

Figure 8(a) displays a plot of the pressure signal for the various simulations as the formed vertical jet collapses and converges with the fluid in the bed of the domain. As the jet collapses a plunging breaker is formed as shown in Figure 5(d) and a bubble is entrained which compresses and dilates in a resonant oscillatory manner yielding the cyclic pressure response. As air entrained within a bubble is compressible, a larger bubble will resonate with a lower frequency as the amount by which it can compress and dilate is dependent upon its volume. The larger bubbles can compress to a greater extent relative to smaller bubbles, thus the amplitude of the oscillatory signal will be greater for these larger bubbles.

T he pressure data is converted from the time domain to the frequency domain by preforming a Fourier Transform. Figure 8(b) shows the results of transform and each of the dominant simulation frequencies and amplitudes are recorded in Table 2. The signal frequencies are plotted against the sphere diameters on Figure 9(a) and the signal amplitudes versus the sphere diameters on Figure 9(b).

The frequency of oscillation increases monotonically as the component sphere diameter increases. Additionally the amplitude of oscillation decreases monotonically. The pressure oscillation frequencies and amplitudes are directly related to the entrained bubble size. Nevertheless, as shown in Table 2 the observed simulation bubble volumes do not follow a trend whereby they increase as the sphere diameter decreases. This may be explained by a number of possibilities. As previously mentioned the smaller sphere based structure allows less fluid to penetrate. This means that more fluid will be rejected from the face of the porous structure for these smaller sphere simulations. This in turn will cause a the thicker jet to form. When this jet collapses it falls further away from the wall entraining a larger bubble. This larger bubble will have a lower pressure oscillation frequency and higher amplitude of pressure oscillation. However as shown on Figure 5(c) some of the fluid may collapse on the top of the porous structure and permeate down through the voids.

Another reason for the discrepancy in oscillating frequency and amplitude may be due to the bubble shape. Previous researchers have put forward contrasting opinions on the influence of sphericity on the oscillation frequency of a bubble. Strasberg (1953) states that the oscillation frequency of non-spherical bubbles varies only slightly from the oscillation frequency of spherical bubbles, however both Weston (1966)1966) and Feuillade and Werby (1994) in their studies on non-spherical bubbles (oblate and prolate spheroid shapes) have shown the frequency of oscillation may increase by up to 40% depending on the degree of non-sphericity. Thus for similar volume bubbles their shape may have a large influence on the observed results. Figure 10 shows that there is a large variation in the shape of the bubbles generated in the different simulations. Table 2 records the bubble sphericity for each of the simulations. this is calculated from Equation 16 Wadell (1935):

$$\Psi = \frac{\pi^{\frac{1}{3}}(6V_v)^{\frac{2}{3}}}{A_v} \qquad (16)$$

Where V_v and A_v are the volume of the bubble and the surface area of the bubble respectively.

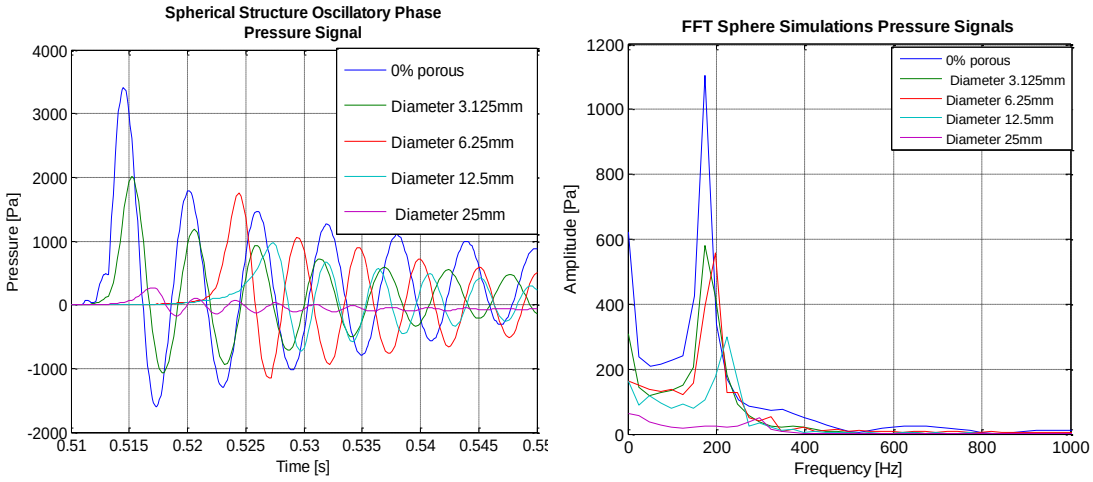

(a) Time domain results

(b)

Frequency domain results

Figure 8:CFD Simulation oscillatory impact pressure responses

Finally Figure 11(a-d) shows spatial and temporal pressure signal attenuations within the porous media for each of the porous structures. The oscillatory pressures attenuate more rapidly within the porous structures with the larger component sphere sizes. As the porous structures composed of the smaller component spheres exhibit a higher specific surface the larger volume of fluid trapped within transfers the oscillatory pressures through these porous structure more readily and deeper into the sturucture.

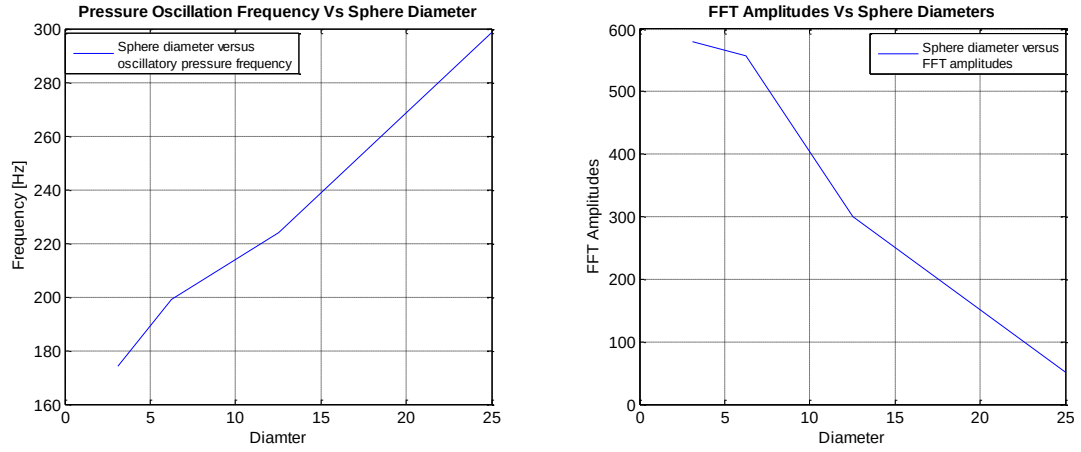

(a) Time domain results

(b)

Frequency domain results

Figure 9: Sphere diameters Vs FFT results

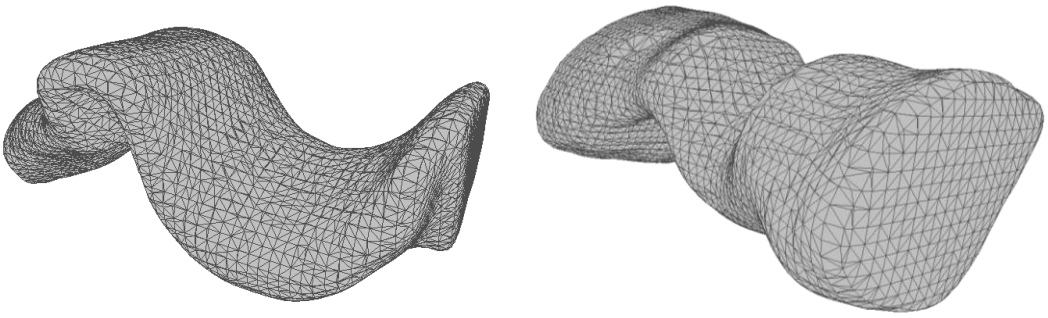

(a) Entrained Bubble geometry from 25mm sphere diameter simulation, at time t = 0.55 sec

(b) Entrained Bubble geometry from 12.5mm sphere diameter simulation, at time t = 0.55 sec

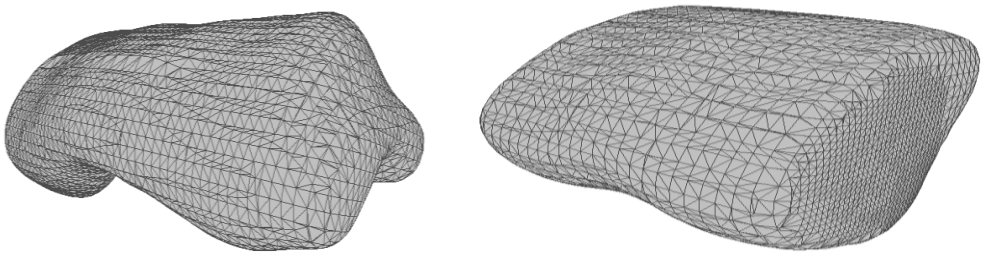

(c) Entrained Bubble geometry from 6.25mm sphere diameter simulation at time t = 0.55 sec

(d) Entrained Bubble geometry from 3.125mm sphere diameter simulation at time t = 0.55 sec

Figure 10: Entrained Bubble Geometries

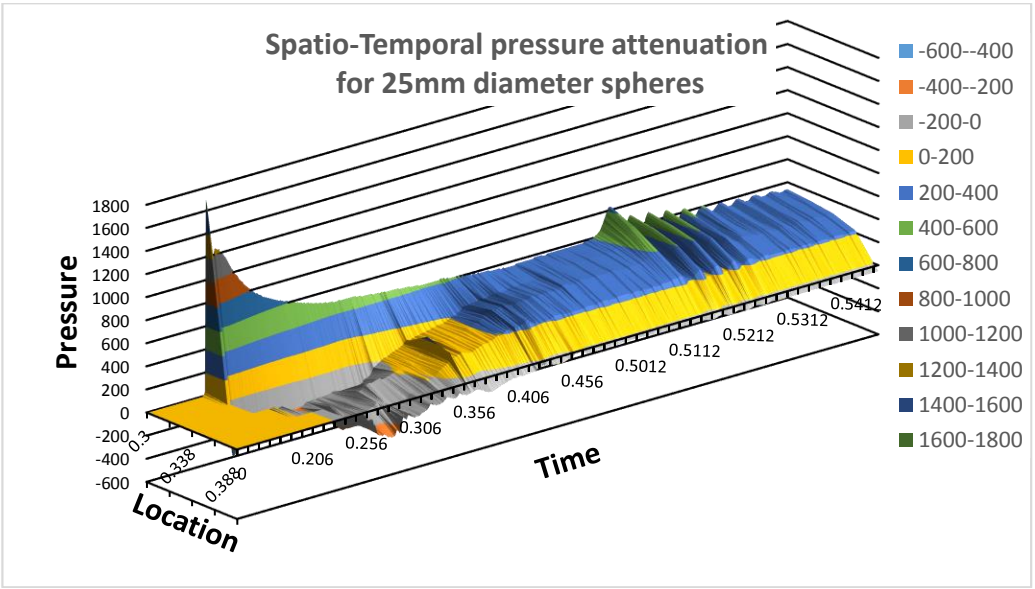

Figure 11(a): Spatio-temporal pressure attenuation for 25mm diameter spheres

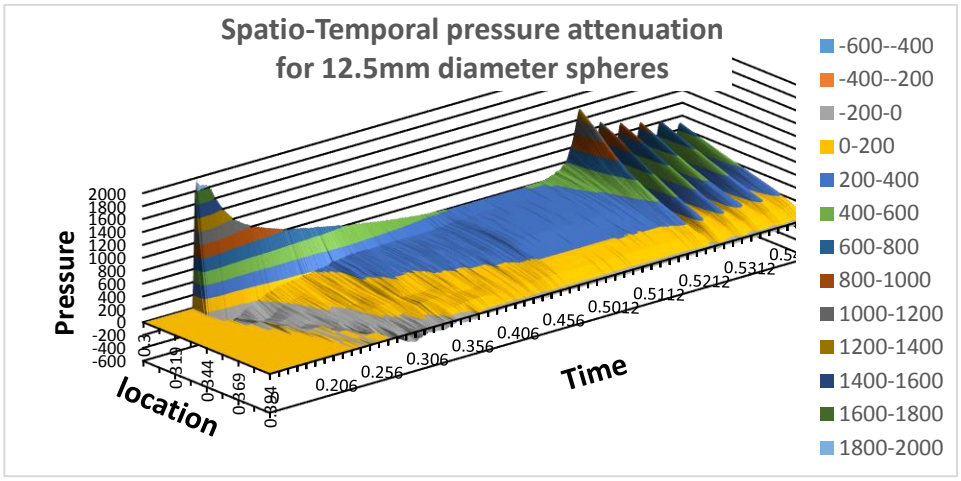

Figure 11(b): Spatio-temporal pressure attenuation for 12.5mm diameter spheres

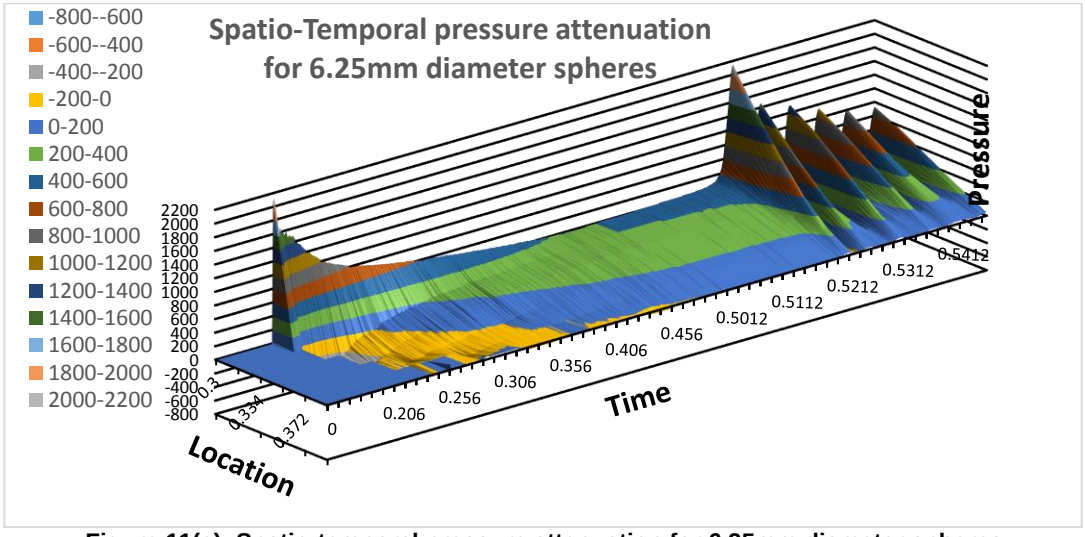

Figure 11(c): Spatio-temporal pressure attenuation for 6.25mm diameter spheres

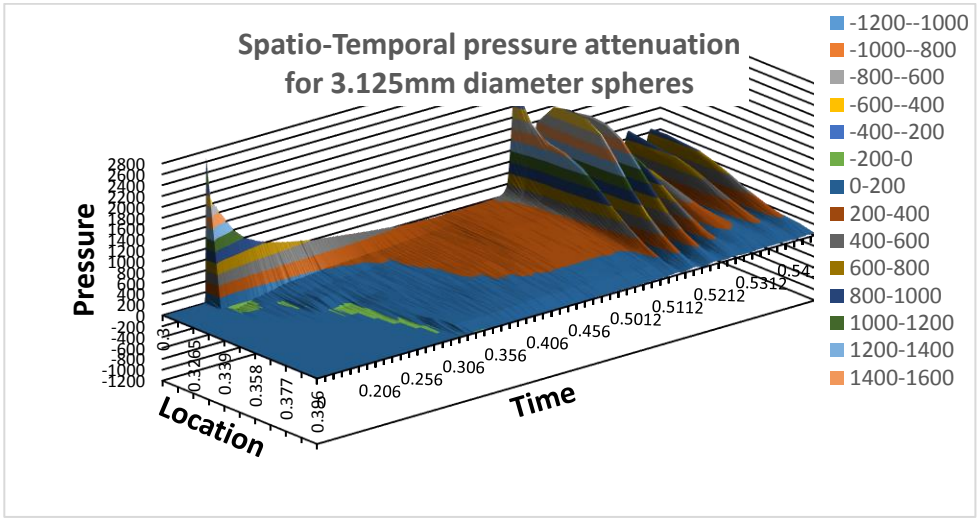

Figure 11(d) Spatio-temporal pressure attenuation for 3.125mm diameter spheres

Figure 11: Spatio-temporal pressure attenuation for each porous structure simulations

CONCLUSIONS AND FUTURE DEVELOPMENTS

Wave impact pressures at a range of varying morphologies of porous structures have been investigated. A thorough parameterisation of the porous media has also been introduced. The influence of the porous structure on the pressure signal resulting from a surging flow front impact has first been analysed. We clearly show that a porous geometry consisting of larger elemental components reduces the magnitude of the impact pressure impulse but results in a longer pressure rise time. We next investigated the effect of varying porous morphology

structures on the pressure signal resulting from a plunging breaker wave impact. Again we demonstrated that a structure with higher specific surface area yielded higher frequency pressure oscillation signals although with lower magnitudes. We also demonstrated that the component sphere size in the porous structure influences the shape, volume and dynamics of the entrained air bubbles. The outflow rate (directly related to permeability) has also been shown to be influenced by the specific surface area of the porous geometry. Finally we have shown that the oscillatory pressure signal persists further into the porous structure comprised of the smaller sphere sizes. As a consequence of this early investigation, we have now successfully demonstrated we could control the impact pressure signals, their respective strengths and persistence in time by accordingly tuning the morphology of the receiving porous structure. Our ongoing and future work currently entails the synthesis of the relationship between such signals characteristics and the receiving impact media representative parameterisations. Specifically, ongoing research is for the discovery of the control of various sphere packing systems and different, more complex porous morphologies (fibrous, granular etc.) on bubble entrapment during wave impact and the resultant oscillatory pressure signals. These are the specific oscillatory forces which inflict the most damage on structures in the long term.

ACKNOWLEDGMENTS

This work is co-funded by the University of Southampton Marine and Maritime Institute (SMMI), the University of Southampton Faculty of Physical Sciences and Engineering (FPSE) and the University of Southampton Faculty of Engineering and the Environment (FEE) .

REFERENCES

ALAGAN CHELLA, M., BIHS, H. & MYRHAUG, D. 2015. Characteristics and profile asymmetry properties of waves breaking over an impermeable submerged reef. Coastal Engineering, 100, 26-36.

BAGNOLD, R. A. 1939. INTERIM REPORT ON WAVE-PRESSURE RESEARCH. (INCLUDES PLATES AND PHOTOGRAPHS). Journal of the Institution of Civil Engineers, 12, 202-226.

BEAR, J. 1988. Dynamics of fluids in porous media, New York, Dover.

BERBEROVIĆ, E., VAN HINSBERG, N. P., JAKIRLIĆ, S., ROISMAN, I. V. & TROPEA, C. 2009. Drop impact onto a liquid layer of finite thickness: Dynamics of the cavity evolution. Physical Review E, 79, 036306.

BREDMOSE, H., PEREGRINE, D. H. & BULLOCK, G. N. 2009. Violent breaking wave impacts. Part 2: Modelling the effect of air. Journal of Fluid Mechanics, 641, 389-430.

BRUS, G., MIYAWAKI, K., IWAI, H., SAITO, M. & YOSHIDA, H. 2014. Tortuosity of an SOFC anode estimated from saturation currents and a mass transport model in comparison with a real microstructure. Solid State Ionics, 265, 13-21.

BULLOCK, G. N., OBHRAI, C., MÜLLER, G., WOLTERS, G., PEREGRINE, D. H. & BREDMOSE, H. Advances in the understanding of wave-impact forces. 2006 / 01 / 01 / 2006. 111-120.

BULLOCK, G. N., OBHRAI, C., PEREGRINE, D. H. & BREDMOSE, H. 2007. Violent breaking wave impacts. Part 1: Results from large-scale regular wave tests on vertical and sloping walls. Coastal Engineering, 54, 602-617.

CHAN, E. S. & MELVILLE, W. K. 1988. Deep-Water Plunging Wave Pressures on a Vertical Plane Wall. Proceedings of the Royal Society of London A: Mathematical, Physical and Engineering Sciences, 417, 95-131.

CIVAN, F. 2011. Overview. Porous Media Transport Phenomena. John Wiley & Sons, Inc.

DULLIEN, F. A. L. 1992. Introduction. Porous Media (Second Edition). San Diego: Academic Press.

FEUILLADE, C. & WERBY, M. F. 1994. Resonances of deformed gas bubbles in liquids. The Journal of the Acoustical Society of America, 96, 3684-3692.

GHANBARIAN, B., HUNT, A. G., EWING, R. P. & SAHIMI, M. 2013. Tortuosity in Porous Media: A Critical Review. Soil Science Society of America Journal, 77, 1461-1477.

HATTORI, M., ARAMI, A. & YUI, T. 1994. Wave Impact Pressure on Vertical Walls under Breaking Waves of Various Types. Coastal Engineering, 22, 79-114.

HIGUERA, P., LARA, J. L. & LOSADA, I. J. 2014. Three-dimensional interaction of waves and porous coastal structures using OpenFOAM®. Part I: Formulation and validation. Coastal Engineering, 83, 243-258.

HIRT, C. W. & NICHOLS, B. D. 1981. Volume of Fluid (Vof) Method for the Dynamics of Free Boundaries. Journal of Computational Physics, 39, 201-225.

MARTÍNEZ FERRER, P. J., CAUSON, D. M., QIAN, L., MINGHAM, C. G. & MA, Z. H. 2016. A multi-region coupling scheme for compressible and incompressible flow solvers for two-phase flow in a numerical wave tank. Computers & Fluids, 125, 116-129.

MAYON, R., SABEUR, Z., TAN, M.-Y. & DJIDJELI, K. 2016. Free surface flow and wave impact at complex solid structures. 12th International Conference on Hydrodynamics.

MINNAERT, M. 1933. XVI. On musical air-bubbles and the sounds of running water. The London,

Edinburgh, and Dublin Philosophical Magazine and Journal of Science, 16, 235-248.
OUMERACI, H., KLAMMER, P. & PARTENSCKY, H. W. 1993. Classification of Breaking Wave Loads on Vertical Structures. Journal of Waterway Port Coastal and Ocean Engineering-Asce, 119, 381-397.
PEREGRINE, D. H. 2003. WATER-WAVE IMPACT ON WALLS. Annual Review of Fluid Mechanics, 35, 23-43.
SABEUR, Z. A., COHEN, J. E., STEPHENS, J. R. & VELDMAN, A. E. P. 1998. Investigation on Free Surface Flow Oscillatory Impact Pressures with the Volume of Fluid Method. in MJ Baines (ed.), Numerical Methods for Fluid Dynamics VI, pp. 493 - 498.
SABEUR, Z. A., ROBERTS, W. & COOPER, A. J. Development and Use of an Advanced Numerical Model using the VOF Method for the Design of Coastal Structures. In: MORTON, K. W. & BAINES, M. J., eds. Numerical Methods for Fluid Dynamics V, 1995. Oxford University Press, 565-573.
STAGONAS, D., MARZEDDU, A., COBOS, F. X. G. I., CONEJO, A. S.-A. & MULLER, G. 2016. Measuring wave impact induced pressures with a pressure mapping system. Coastal Engineering, 112, 44-56.
STRASBERG, M. 1953. The Pulsation Frequency of Nonspherical Gas Bubbles in Liquids. The Journal of the Acoustical Society of America, 25, 536-537.
THE OPENFOAM FOUNDATION 2013. The Open Source CFD Toolbox, User Guide & Programmer Guide.
TOPLISS, M. E., COOKER, M. J. & PEREGRINE, D. H. Pressure oscillations during wave impact on vertical walls. 1993 / 01 / 01 / 1993. Publ by ASCE, 1639-1650.
VALLABH, R., BANKS-LEE, P. & SEYAM, A. F. 2010. New Approach for Determining Tortuosity in Fibrous Porous Media. Journal of Engineered Fibers and Fabrics, 5, 7-15.
WADELL, H. 1935. Volume, Shape, and Roundness of Quartz Particles. The Journal of Geology, 43, 250-280.
WEMMENHOVE, R., LUPPES, R., VELDMAN, A. E. P. & BUNNIK, T. 2015. Numerical simulation of hydrodynamic wave loading by a compressible two-phase flow method. Computers & Fluids, 114, 218-231.
WESTON, D. E. 1967. Sound propagation in the presence of bladder fish. Underwater acoustices Vol II, NATO Advanced Study Instute, Copenhagen. edited by V. M. Albers, Plenum, New York, pp. 55-58.